Boosting the host immune system to fight tuberculosis
Boland, R.

Citation
Boland, R. (2022, April 28). *Boosting the host immune system to fight tuberculosis*. Retrieved from https://hdl.handle.net/1887/3289526

Boosting the host immune system to fight tuberculosis

Ralf Boland

Boosting the host immune system to fight tuberculosis
Ralf Boland

Some figures partly created with BioRender.com
Printed by Gilderpint

Cover: *Mycobacterium marinum* (magenta) and LysoTracker (cyan) in a granulomatous aggregate.

Boosting the host immune system to fight tuberculosis

Proefschrift

ter verkrijging van
de graad van doctor aan de Universiteit Leiden
op gezag van rector magnificus prof. dr. ir. H. Bijl,
volgens besluit van het college voor promoties
te verdedigen op 28 april 2022
klokke 16:15 uur

door

Ralf Boland
geboren te Katwijk, Nederland
in 1986

Promotores

Prof. dr. A.H. Meijer

Prof. dr. H.P. Spaink

Co-promotor

Dr. M. van der Vaart

Promotiecommissie

Prof. dr. G.P. van Wezel

Prof. dr. B.E. Snaar-Jagalska

Prof. dr. M. Barz

Prof. dr. T.H.M. Ottenhoff   (Leids Universitair Medisch Centrum)

Dr. E.N.G. Houben   (Vrije Universiteit Amsterdam)

Table of contents

Aan mijn moeder, Jos, Lotte, Luuk en Mats

1

Introduction and outline of this thesis

Tuberculosis

Tuberculosis (TB) is an increasing global health problem. This infectious disease is ranked as the leading cause of death from a single bacterial infectious agent: *Mycobacterium tuberculosis* (*Mtb*). TB often manifests clinically as a lung infection but it is also common in extrapulmonary forms, such as skeletal and lymphatic infections, meningitis, and miliary TB, which spreads to multiple organs. Characteristic symptoms include coughing, fever, chronic fatigue, and severe weight loss. Globally, 10 million people developed TB and 1.4 million died from the disease in 2019[1]. Furthermore, it is estimated that one third of the global population carries a latent *Mtb* infection, characterized as a clinical state without evidence of disease, but with a positive reaction to the tuberculin skin test. Latent infections can lead to active disease, especially if the host is immune compromised, for example due to HIV infection. Of all people infected with HIV who died in 2019, one third were infected with *Mtb* as well[1].

Current treatment of TB consists of daily doses of first-line antibiotics (isoniazid, rifampicin, ethambutol and pyrazinamide) for six months. In some cases the bacteria are resistant to these first-line antibiotics, and subsequently patients need to be treated with second-line antibiotics that have more side effects and are more costly (i.e. bedaquiline, delamanid, lefloxacin and moxifloxacin)[1,2]. Furthermore, the treatment of latent *Mtb* infection is complicated, because bacteria are dormant and antibiotics disrupting bacterial cell-wall synthesis or other bacterial cell-cycle components are hardly effective in non-dividing bacteria. In addition, the currently used BCG-vaccine, which is a century old, only offers partial protection against TB. While a dozen clinical trials for new vaccines are taking place, an effective vaccine against TB is yet to be developed[3–6].

Developed countries with high standards of living and adequate healthcare systems have eradicated active TB almost completely. However, the rise of multi-drug resistant (MDR) and extensively-drug resistant (XDR) *Mtb* strains is cause for concern. It is believed that poor adherence of patients to first-line antibiotic treatment regiments works in favor of the pathogen developing resistance[7,8]. As conventional treatments become less effective, the threat of TB is becoming larger not just in developing countries, but in countries with better healthcare systems as well. For instance, despite that the overall TB disease burden in the Russian Federation is falling, the incidence of MDR-TB is rising. Moreover, while Europe accounts for only 2,5% of the global disease burden, 17% of new cases in Europe were MDR-TB. Globally, almost half a million TB infections were due to MDR *Mtb* strains in 2019[1].

Ending the epidemic of TB by 2030 is one of the United Nations sustainable development goals[1]. To achieve this ambitious goal, scientists around the world are investigating the disease, the pathogen *Mtb*, and the interaction between the bacterium and its human host. In addition, diverse animal hosts are used to model different aspects of TB[9]. New insights into the disease and host processes involved in the disease are used to find new treatment options. While we aim to fight *Mtb* with new therapeutic strategies, *Mtb* itself has many tricks up its sleeve that make it such a successful pathogen.

Subversion of the immune system

Upon infection, *Mtb* is quickly phagocytosed by professional phagocytes, especially macrophages. Phagocytosed *Mtb* are contained in phagosomes that have to fuse with lysosomes for acidification and degradation of their contents. During the process of phagosome maturation and phagosome-lysosome fusion, bacteria are exposed to a variety of host-defense mechanisms, such as proteases, antimicrobial peptides,

and reactive nitrogen and oxygen species[10–12]. However, *Mtb* and other pathogenic *Mycobacteria* have the remarkable capability of arresting phagosome-lysosome fusion via excreted virulence factors as well as cell envelope components[13,14]. In addition, *Mycobacteria* have evolved mechanisms to protect themselves against phagosomal and lysosomal killing mechanisms[15–17]. Subsequently, they are able to replicate within these vesicles and eventually permeabilize them to escape into the cytosol[18,19]. Escaped cytosolic bacteria or arrested phagosomes can be targeted for autophagy, an intracellular degradation pathway vital to maintaining homeostasis. Via the autophagic pathway, unwanted elements, such as protein aggregates, damaged organelles but also intracellular bacteria, are removed from the cell[20–22]. However, like other host defense mechanisms, also autophagy is inhibited by *Mtb* to some extent[23].

The intracellular presence of *Mtb* causes macrophages to form aggregates, which initiates the formation of tuberculous granulomas. Granulomas are the pathological hallmark of TB and consist of a core of infected macrophages and necrotic cell debris, and a wall of several cell layers that contains various cell types, such as neutrophils, dendritic cells and T- and B-cells[24]. It was long believed that granulomas serve strictly a host-protective function and that granuloma formation represents a host strategy to contain *Mtb* infection. However, this view has been challenged by the findings that *Mycobacteria* actively promote granuloma formation and that directed aggregation of macrophages by *Mycobacterial* virulence factors facilitates dissemination of the bacteria in the infected host[24–26]. These results have shown that *Mycobacteria* benefit from granuloma formation during the early stages of infection. Nevertheless, it is important for the infected host to maintain the structure of mature granulomas, as active TB develops under conditions where granuloma integrity is compromised. For example, this can occur during HIV infection or in patients receiving anti-inflammatory therapy with TNF blockers. It is because of this dual role of granulomas in TB and the intricate interplay between *Mtb* and host-immune-related processes that new therapeutic strategies are desperately needed.

Host-directed therapeutics

Most antibiotic targets are either components of the bacterial cell-wall or involved in cell-wall synthesis[8]. It is believed that resistance to a specific antibiotic can lead to faster developing resistance against other antibiotics with similar targets. The search for new antibiotics continues as more and more pathogens become resistant[27,28]. New antibiotics are sporadically discovered[29], however they are often used as a last-resort, to prevent the rise of resistance against these new antibiotics. Efforts from pharma companies to find new antibiotics are therefore limited, as they are not profitable, in part because of this last-resort policy[30].

Contrary to antibiotics that are directed against the pathogen, host-directed therapeutics (HDTs) aim to modulate host-pathways to potentiate the host-immune response against pathogens such as *Mtb*[31–35]. This can be achieved in several ways: first, HDTs can improve the bactericidal capacity of immune cells. Second, HDTs can limit detrimental effects of inflammation. Third, HDTs can overcome suppressed immune responses by *Mtb* or elicit novel immune responses against *Mtb*. And fourth, HDTs can target host factors that are manipulated by *Mtb* for its own pathogenesis. By enhancing host defense, HDTs have the potential to shorten treatment regimens with conventional first-line antibiotics[36,37]. Importantly, for some HDT candidates, for example imatinib and H89, it was shown that they are effective against antibiotic-resistant *Mycobacteria* offering a possible answer to the rise of MDR and XDR *Mtb* strains[36,38]. It is expected that because HDTs do not directly target bacteria, resistance is less likely to develop[35].

In the search for HDTs for TB and other infectious diseases, drug repurposing screens are often employed. The principle behind drug repurposing is that drugs that have been approved for clinical use may have additional effects besides those for which they are registered, and therefore these drugs may be utilized for other therapeutic applications. Similarly, there is a large unexplored potential in candidate drugs that did not pass phase-II clinical trials for efficacy assessment but may prove effective in other disease treatments than the one they were originally tested for. One advantage of drug repurposing compared to the development of novel HDTs, is that most of these compounds have already passed phase-I clinical trials for safety assessment. When these compounds are proven to work in in animal models for TB, they could potentially be tested immediately in phase-II trials and the development time for new therapies is greatly reduced.

In recent years, several laboratories have reported on results of large-scale screening of compound libraries and genetic targets, in which many potential candidate HDTs for TB treatment have been identified[38–42]. The majority of these screens are performed *in vitro* with cultured cells or monocyte derived macrophages, but they also can be performed using a suitable *in vivo* model, such as the zebrafish model for TB[43]. Several excellent reviews have described the current status of HDT identification for TB[31,33,35,44]. In this chapter we highlight HDT strategies that focus on autophagy and (auto)phagolysosomal pathways. In addition, we discuss how the zebrafish model can contribute to HDT screening and be used to translate *in vitro* effects of HDTs to a straightforward *in vivo* model of TB.

Autophagy

The most common arm of the autophagy pathway is called macroautophagy (hitherto autophagy) and describes the clearance of intracellular waste or cargo, such as organelles, lipids and proteins via autophagosomes (Figure 1). These double membraned compartments fuse with lysosomes to form autolysosomes in which the cargo is digested into cellular building blocks such as fatty acids and amino acids[45]. At the beginning of this century, it was reported that induction of autophagy in macrophages leads to protection against *Mtb*[20,46]. It has now become well established that autophagy plays an important role in the clearance of intracellular bacteria and other microbes. First, the induction of bulk, or non-specific, autophagy by starvation or by inhibition of mTOR (mammalian target of rapamycin) signaling can lead to increased intracellular bacterial killing[21]. In addition, autophagy can also reduce bacterial growth because it limits inflammation[21] and promotes antigen presentation to T-cells[47].

Recent studies have highlighted that autophagy often occurs as a selective, receptor-mediated process[48,49]. Selective autophagy is classified depending on the cytoplasmic material that it targets. For example, xenophagy targets microbes, mitophagy targets damaged mitochondria, and aggrephagy targets protein aggregates[50,51]. Specific receptors mediate selective autophagy by linking the cargo directly to the microtubule-associated light chain 3 protein (LC3), which is conjugated to the membrane of nascent and mature autophagosomes[48]. In the case of xenophagy, microbes that have escaped the phagosome are ubiquitinated and recognized by members of the Sequestosome (p62/SQSTM1)-like receptor (SLR) family, a family of selective autophagy receptors that includes p62, NDP52, NBR1, TAX1BP1, and OPTN (optineurin). Xenophagy has been well established as an important effector of innate immunity. For instance, p62 and optineurin have been shown to be required for the autophagic defense against mycobacterial infection in the zebrafish model for TB[52]. Furthermore, it is believed that the generation of neo-antimicrobial peptides, which are effective in killing *Mtb*, is
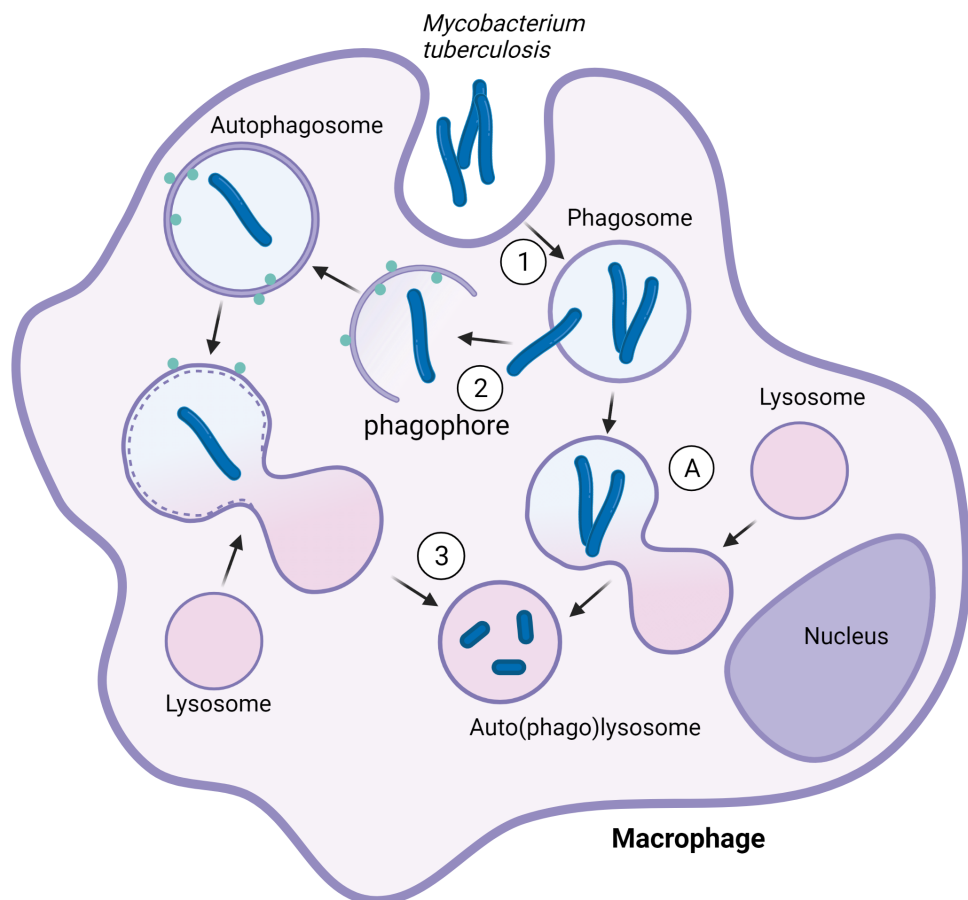
Figure 1. Role of the autophagic pathway in *Mycobacterium tuberculosis* clearance
Mtb is phagocytosed (1) and contained in a phagosome from which it can escape (2). Following phagosomal escape, the bacteria are targeted to the autophagic pathway via LC3 (green dots). After the bacteria is contained in an autophagosome, the autophagosome fuses with a lysosome and the contents is degraded. Alternatively, bacteria can remain contained in the phagosome, which fuses with a lysosome (A) after which the contents is degraded.

mediated by ubiquitination and delivery of proteins to microbe-containing compartments by p62 and related receptors[53].

Although autophagy is recognized as an important host-protective pathway[21,22], the interplay between *Mtb* and autophagy is complex. A recent study showed no effect on susceptibility to *Mtb* in mice with mutations in different autophagy proteins and has therefore questioned the role of autophagy in the immune response to *Mtb*[54]. In this study, only a mutation in ATG5 led to increased susceptibility to *Mtb*, confirming a previously shown antimycobacterial effect of this autophagy protein[55]. However, Kimmey *et al* did not attribute this antimycobacterial effect to the role of ATG5 in autophagy, but to the prevention of an immuno-pathological neutrophil response via ATG5. Furthermore, they did not see an increase in susceptibility in *p62* loss-of-function mutants, which is in contrast with other studies[52,56]. Together, these studies suggests that the impact of autophagy on infection outcome depends critically on experimental conditions. The complexity of the interplay between *Mtb* and autophagy is further demonstrated by the

ability of *Mtb* to inhibit LC3-associated phagocytosis (LAP)[57], which is an autophagy-related process contributing to host defence[58]. During LAP, the phagosome membrane is directly decorated with LC3 resulting in fusion of the so-called LAPosomes with lysosomes. However, *Mtb* is well known for its capability to evade immune defences, including autophagy and LAP, which could also explain why autophagy mutations had limited effect on susceptibility in some studies[54]. Boosting autophagy levels using HDTs could be a way to overcome the pathogen's autophagy evasion strategies and could therefore be a promising therapeutic route[23].

HDTs strategies to boost autophagy and lysosomal degradation

One of the best-known autophagy modulating drugs is Rapamycin, which can induce autophagy by inhibiting the negative autophagy regulator mTOR. However, rapamycin has properties beyond autophagy induction and it is used as an immuno-suppressive drug during organ transplants[59]. Due to its immuno-suppressive effects, Rapamycin is not well suited for clinical use against TB, although targeted delivery to macrophages may be considered[60]. Furthermore, Rapamycin is metabolized by CYP3A4[61], a hepatic enzyme that is greatly induced by the antibiotic Rifampicin, which is an important first-line drug used in TB treatment. In the zebrafish model for TB, inducing autophagy using Rapamycin was also shown to be detrimental for the defense against mycobacteria, presumably due to its immunosuppressive effects or due to toxic side effects[62]. Similarly, mTOR inhibition by molecules related to Rapamycin might be ineffective. In fact, the small-molecule inhibitor Torin 1 increased susceptibility to *Mtb* infection in human macrophages, most likely due to reduction of phagosome acidification which led to increased *Mtb* replication[63]. In contrast, the mTOR inhibitor Everolimus showed promising results in a study using an *in vitro* TB granuloma mode[64]. Single-drug treatment using Everolimus increased levels of autophagy and decreased *Mtb* burden and oxidative stress. In addition, Everolimus was also effective in a combinatorial treatment regime with the antibiotics, Isoniazid and Pyrazinamide, important first-line drugs used in TB treatment.

Autophagy can also by induced by drugs acting on signaling molecules upstream of mTOR. A promising drug for TB treatment is Metformin, which promotes the expression of the energy sensor AMP-activated protein kinase (AMPK), resulting in inhibition of mTOR. Metformin is used in the treatment of adult-onset diabetes. Of note, diabetes is known to increase the risk of developing TB as well as complicating its treatment[65]. Therefore, the antimycobacterial effect of Metformin is particularly relevant. Metformin was shown to be able to increase phagolysosome fusion as well as mitochondrial ROS production, thereby inhibiting *Mtb* growth *in vitro*[37]. Combinatorial treatment of Metformin and the first-line antibiotic Isoniazid showed a minor, but significant, inhibition on mycobacterial burden as compared to Isoniazid alone. Furthermore, Metformin treatment decreased the inflammatory response, thus reducing negative effects of inflammation such as tissue damage. Metformin was also found to enhance the adaptive immunity response to mycobacterial infection[66].

A number of other autophagy modulating drugs have emerged from high-content and high-throughput screens of small molecules. Using a microscopy-based assay, Stanley et al. identified Gefitinib to induce autophagy and inhibit *Mtb* in macrophages[67]. Gefitinib is an anti-cancer epidermal growth factor receptor (EGFR) tyrosine kinase inhibitor and induces autophagy potentially in an EGFR unrelated manner[68]. Not only did Gefitinib reduce *Mtb* in human cultured macrophages, it also reduced bacterial replication in a murine model for TB. The same study identified Fluoxetine as an antimycobacterial compound. Fluoxetine is a selective serotine reuptake inhibitor and is widely known as an

anti-depressant under the name Prozac. Treatment of *Mtb* infected human macrophages led to a significant increase in TNF-a and induction of autophagy. TNF-a induction can indeed induce autophagy and is highly relevant for the immune response to numerous bacterial infections, including TB[69]. Interestingly, the anti-psychotic drugs Haloperidol, Nortriptyline and Prochlorperazine have all been shown to induce *in vitro* killing of *Mtb*[70]. Prochlorperazine and Nortriptyline activate autophagy via mTOR inhibition, while the same study showed Haloperidol to enhance endosomal progression. While other underlying mechanisms could be at play, the induction of autophagic degradation by these anti-psychotic drugs could be a common explanation for their effect against *Mtb*.

Anticonvulsant drugs, including Carbamazepine and Valproic acid, are another class of anti-TB compounds revealed by drug screening[41]. Among these drugs, Carbamazepine was shown to stimulate autophagy and decrease intracellular mycobacteria in both *in vitro* and *in vivo,* using macrophages, zebrafish, and mice models of TB[41]. Carbamazepine induces autophagy independently of mTOR by reducing myo-inositol uptake by macrophages, inducing autophagy through increased phosphorylation of AMP kinase and ULK1

Kinases are among the most frequently used drug targets in general and are also explored as HDTs for TB. The tyrosine kinase inhibitor, Imatinib, is used as a therapeutic in cancer treatment and has been shown to reduce *Mtb* burden by promoting phagolysosomal processes[36]. Mechanistically, Imatinib inhibits tyrosine kinases ABL1 and ABL2 and ABL family tyrosine kinases can regulate autophagy. Napier *et al* showed that Imatinib treatment leads to reduced bacterial burden, increased acidification of vesicles and increased percentages of mycobacteria in lysosomes. Furthermore, the AKT1 kinase inhibitor H89 has been shown to be effective in inducing phagosomal maturation to phagolysosomes and reducing intracellular bacterial growth of both *Salmonella* and *Mtb*[38].

Finally, an interesting class of drugs that mediate phagolysosmal degradation are statins, clinically used to reduce cholesterol levels. Paradoxically, statins can inhibit phagosomal acidification, which is expected to prolong survival of *Mtb*. However, statins are also found to prevent phagosome escape by *Mtb*, thereby increasing (auto)phagolysosomes containing *Mtb* and promoting bacterial degradation[71–73]. Increasing autophagy or enhancing lysosomal processes are closely related drug effects, which we also show in chapters 4 and 5, where Tamoxifen and Amiodarone, besides increasing autophagy, also increase (auto)phagolysosomal processes. Figure 2 contains an overview of the above described HDTs and how they function.

The zebrafish model for tuberculosis and autophagy research

The zebrafish (*Danio rerio*) is a small sub-tropical fish originating from south-east Asia[74]. It has become widely used as a model animal with its roots in developmental research[75]. Since the early 2000s its potential as a vertebrate model in biomedical research became apparent[76,77]. Today, the zebrafish model is an invaluable addition for disease and translational biomedical research as an intermediate between *in vitro* models and mammalian animal models[78]. Zebrafish are highly suitable for this purpose as they possess several distinct qualities beneficial for biomedical research. First, they are optically transparent in early embryonic and larval stages. This is ideal for imaging using fluorescent microscopy and confocal microscopy to gain biomolecular insights that could not have been achieved using adult animals (Figure 3), even to the point where correlative light and electron microscopy is possible[77,79]. Second, genes are highly conserved between zebrafish and humans, especially those associated
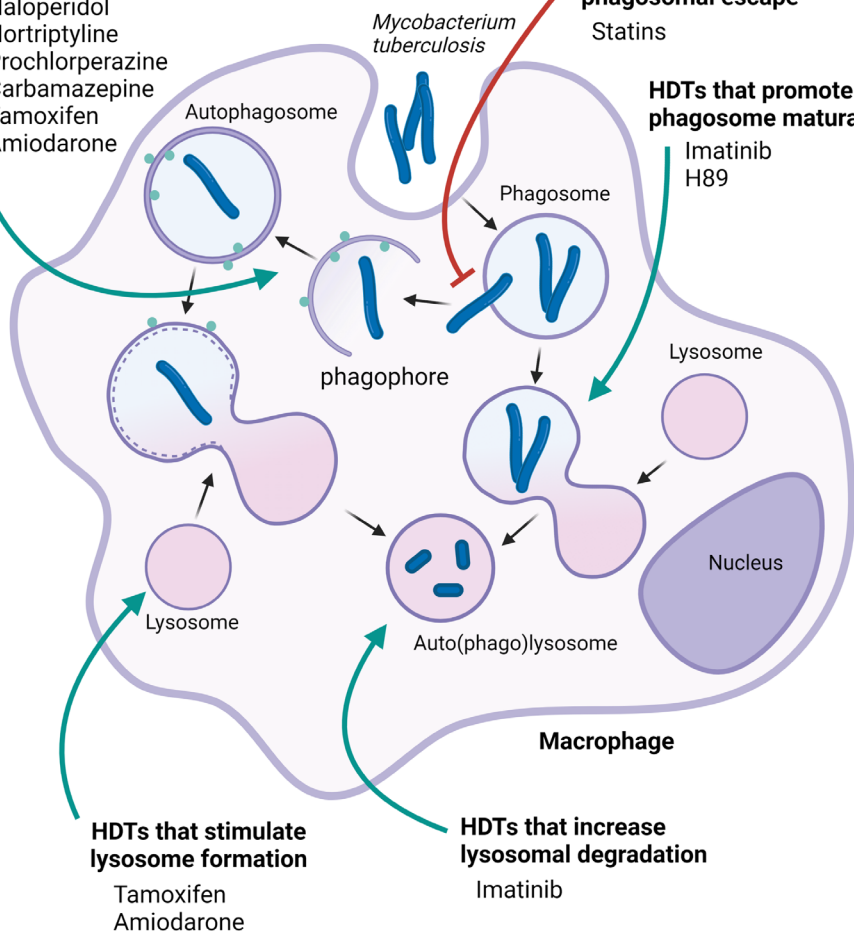
HDTs that stimulate autophagy
Everolimus
Metformin
Gefitinib
Fluoxetine
Haloperidol
Nortriptyline
Prochlorperazine
Carbamazepine
Tamoxifen
Amiodarone

HDTs that inhibit phagosomal escape
Statins

HDTs that promote phagosome maturation
Imatinib
H89

Mycobacterium tuberculosis

Autophagosome

Phagosome

phagophore

Lysosome

Lysosome

Nucleus

Auto(phago)lysosome

Macrophage

HDTs that stimulate lysosome formation
Tamoxifen
Amiodarone

HDTs that increase lysosomal degradation
Imatinib

Figure 2. Overview of HDTs and how they modulate the autophagic-, phagosomal- and lysosmal-pathway
Green lines denotes a stimulating effect while the red line denotes an inhibiting effect.

with disease phenotypes where 84% of human genes have identified counterpart in zebrafish[80]. Third, because of external fertilization, genetic modification can be easily performed by injecting DNA constructs or knockdown/knockout reagents into the zebrafish eggs at the one-cell stage, and precise genome editing has become even more straight-forward with CRISPR/Cas9 techniques[78,81,82]. As a result, a wide variety of knock-out and reporter lines are available in the zebrafish research community. Fourth, zebrafish are relatively easy to maintain compared to mammalian models and they take up far less space, making it also an economically interesting model[77]. Fifth, innate and adaptive immunity are separated in development by 2 to 3 weeks, making it possible to study host-pathogen interactions exclusively during the innate immune response in zebrafish embryos and larvae[83,84]. Sixth, zebrafish embryos and larvae are especially
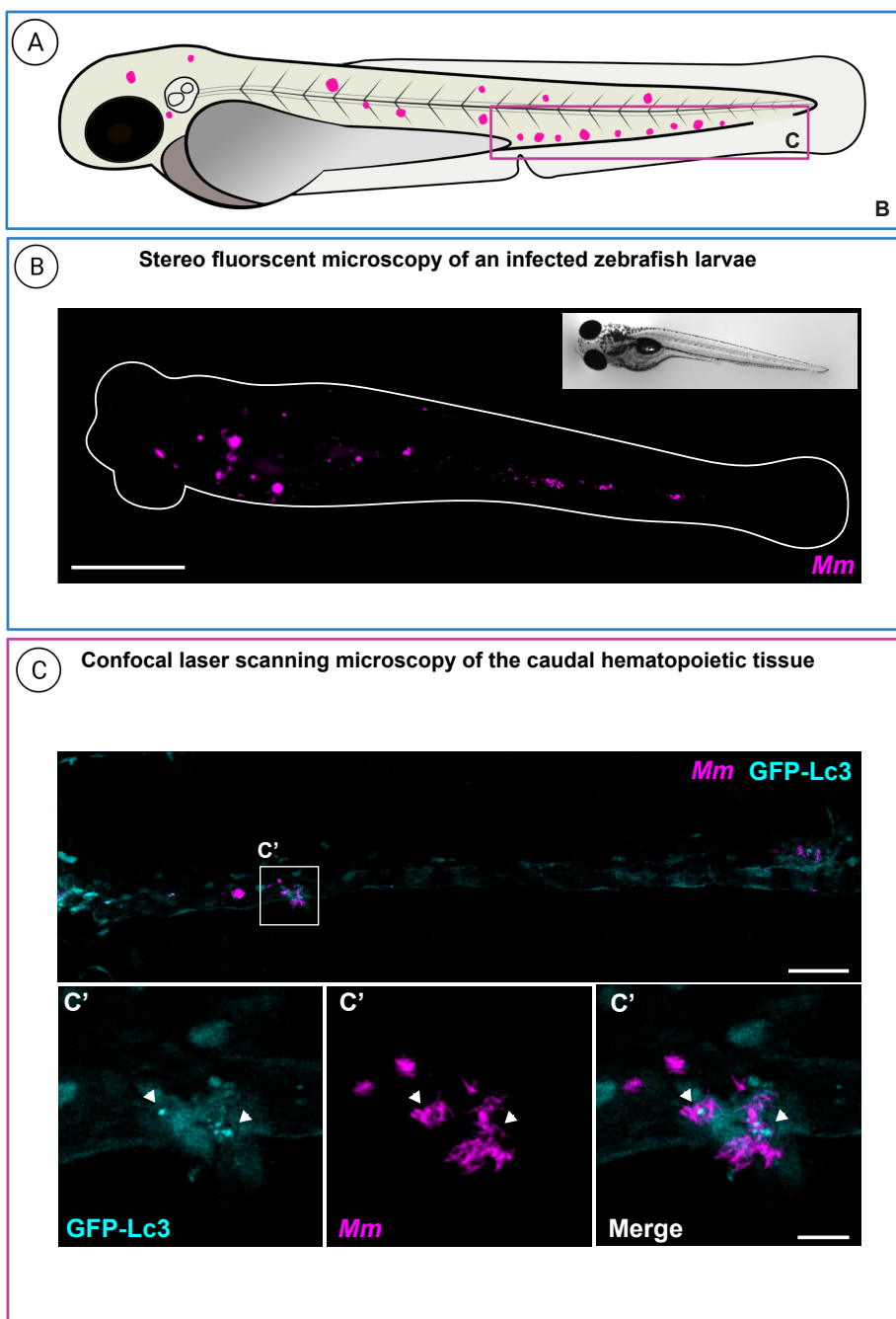
Figure 3. Examples of two imaging techniques using the zebrafish model

A. Representation of an infected zebrafish larvae, 5 days post fertilization. Magenta dots indicate *Mm* clusters.

B. Example of stereo fluorescent image of whole larvae infected with mWasabi-expressing *Mm*. Magenta shows *Mm*. Scale bar annotates 1 mm.

C. Example of confocal microscopy max projection images of the caudal hematopoietic tissue (CHT) region of an infected transgenic GFP-Lc3 zebrafish larvae. Cyan shows GFP-Lc3 positive vesicles and magenta shows *Mm*. Scale bar annotates 50 µm.

suitable for screening drugs, which can be easily administered via the water and are taken up through the skin[85]. Finally, adult zebrafish share physiology and anatomy with vertebrates, including humans, and many processes in disease are similar to that in humans[78]. All these advantages make the zebrafish an attractive model animal to study mechanisms of disease, metabolic disorders, genetic disorders, cancer, infections, behaviour, and to apply zebrafish in drug discovery pipelines.

Infection of zebrafish with the natural fish pathogen *Mycobacterium marinum* (*Mm*), a close relative of *Mtb*, leads to pathogenesis remarkably similar to TB-pathogenesis[24,86,87]. Using the zebrafish model for TB, important insights have been obtained for example on the role of granulomas that are characteristic for TB pathology. Though it was long thought that the granulomatous aggregates of leukocytes are mainly a host defence structure, encapsulating the bacteria, it was the zebrafish model that provided evidence that these aggregates are dynamic structures that aid dissemination of bacteria, especially at the early stages of their development that can be visualized in zebrafish larvae[26]. Important virulence factors, including those that promote granuloma formation, are similar in *Mtb* and *Mm*[25,88]. Adult zebrafish can be used as a TB model by intraperitoneal injection of *Mm* and they can be used to model latent TB disease, overcoming an important limitation of other TB animal models[89,90]. However, the versatility and possibilities of the embryonic and larval stages are the biggest contributors to the popularity of zebrafish as a vertebrate model for TB[87]. Experimentally, embryos can be injected with bacteria as early as 1 day post fertilization and both systemic or local infections can be achieved using micro-injection techniques[91]. Because there is no need for feeding during the first week of development and development is normal even under anesthesia, the embryos and larvae are ideal for non-invasive imaging. The zebrafish-*Mm* model has therefore proven highly useful to study host-pathogen dynamics during the early stages of infection using specific phagocyte-lineage reporter lines[92–95]. Of particular interest for this thesis is the use of the zebrafish embryo model for autophagy research in the context of TB.

Zebrafish have been used to study autophagy in the context of development and disease, including infection. Using both genetic knockdown of autophagy genes and chemical modulation of autophagy, using commonly used autophagy inhibitors or inducers, zebrafish have helped elucidate the role autophagy machinery in various developmental and disease contexts[96–99]. To study anti-mycobacterial autophagy *in vivo* we have used the zebrafish embryo model for TB in combination with a GFP-Lc3 reporter line developed in the Klionsky lab[99,100]. By correlative light electron microscopy studies using the GFP-Lc3 autophagy reporter line we demonstrated the delivery of Mm to autophagic compartments[79]. Furthermore, we observed using electron microscopy that double membraned autophagic vesicles fuse with larger *Mm*-containing degrading compartments, a mechanism proposed to enhance the microbicidal capacity[53,62]. We have also shown the protective role of the DNA-damage regulated autophagy modulator Dram1, which is upregulated during infection by the central Myd88-NFκB signalling pathway[62,101]. Moreover, using CRISPR/Cas9-mediated mutagenesis, we showed the requirement of selective autophagy receptors Optineurin and p62 for host resistance to mycobacterial infection[52]. For this thesis we took advantage of the possibilities of the zebrafish embryo model for TB and the available zebrafish toolkit to study several autophagy-modulating HDTs as potential anti-TB drugs.

Outline of this thesis
New drugs for use as TB treatment are needed due to the constrains of classical antibiotics against TB and the rise of antibiotic-resistant strains, making TB a harder

and harder disease to treat. This thesis is focused on using the *in vivo* whole animal zebrafish embryo model for TB to evaluate potential anti-TB HDTs arising from *in vitro* screens and gain more mechanistic insights into the molecular function of these potential drugs. Although *in vitro* screens for HDTs using cellular models can be performed at high throughput, a limiting step is the validation in whole animal models and translation of results to clinical applications.

The zebrafish model is highly suitable as an intermediate for translational research as it fills the gap between *in vitro* research and mammalian animal models. Research into enhancing the potential of the zebrafish model, such as robotic injection of zebrafish eggs and rapid screening based on automated fluorescence assessment and sorting has led to new developments that make the zebrafish a moderate to high throughput model. In **chapter 2** we used machine learning to improve robotic injection efficiency and effectivity for genetic manipulation of zebrafish larvae using morpholinos, Tol2 transgenesis and the CRISPR/Cas9 system. Robotic injection has similar efficiency as manual injections, but due to its higher throughput leads to a higher yield. This allows for high throughput knock-out or knock-in applications using the zebrafish model.

Due to the complex infection dynamics of mycobacteria, the use of whole animal models is indispensable in research into TB and the zebrafish model has contributed key findings about host-pathogen dynamics during mycobacterial infection. In **chapter 3** we tested several variations of established zebrafish infection protocols to determine which robotic or manual injection conditions are the most suitable to do an initial whole animal screen of potential anti-TB HDTs. We concluded that the manual intravenous injection of *Mm* into one day old embryos gave the most robust results. We then continued with a pilot screen and confirmed the anti-TB activity of Trifluoperazine, Amiodarone and Tamoxifen, first shown in *Mtb*-infected human macrophages, in the zebrafish model for TB.

One of the most promising host targets of HDTs is autophagy. Besides the role of autophagy in cellular homeostasis, the role of autophagy in the immune system has become more and more clear in the last two decades. Intracellular pathogens, such as *Mtb*, are degraded by the autophagy pathway. However, *Mtb* has remarkable strategies to evade degradation and escape from (auto)phagosomes. Therefore, enhancing the autophagic capabilities of professional phagocytes, such as macrophages, is a highly interesting strategy to combat intracellular pathogens and in particular *Mtb*. We used both a primary human macrophage *Mtb* infection model and the zebrafish-*Mm* TB infection model to demonstrate the potential of Tamoxifen as an anti-TB HDT in **chapter 4**. We show the anti-mycobacterial effects are independent of the well-known target of Tamoxifen, the estrogen receptor, and show that Tamoxifen modulates autophagy and in particular the lysosomal pathway. Transcriptome analysis and co-localization studies using fluorescent microscopy show lysosomal activation after treatment with Tamoxifen, as well as increased localization of mycobacteria in lysosomes.

Another potential drug that is interesting as a potential HDT against TB is Amiodarone. This antiarrhythmic medication can induce autophagy and stimulates nitric oxide release. Nitric oxide plays a key role in immunity and inflammation and mycobacteria have been shown to be highly susceptible to reactive nitrogen species. In **chapter 5**, Amiodarone is confirmed to restrict mycobacterial infection in the zebrafish embryo model for TB. We then unravel aspects of host-mechanisms involved in the anti-mycobacterial effect of Amiodarone. We start by investigating the involvement of the nitric oxide host defence

pathway. Furthermore, we use transcriptome analysis and co-localization studies using fluorescent microscopy which point towards alteration by Amiodarone of host pathways related to autophagy and lysosomal function beneficial for the host during mycobacterial infection. Finally, the findings presented in this thesis are put into the perspective of current knowledge in **chapter 6**.

References

1. WHO. *Global Tuberculosis Report 2020*. (2020).

2. Lawn, S. D. & Zumla, A. I. Tuberculosis. *Lancet* **378**, 57–72 (2011).

3. Kaufmann, S. H. E. *et al.* Progress in tuberculosis vaccine development and host-directed therapies-a state of the art review. *Lancet Respir. Med.* **2**, 301–320 (2014).

4. da Costa, C., Walker, B. & Bonavia, A. Tuberculosis Vaccines - state of the art, and novel approaches to vaccine development. *Int. J. Infect. Dis.* **32**, 5–12 (2015).

5. Evans, T. G., Schrager, L. & Thole, J. Status of vaccine research and development of vaccines for tuberculosis. *Vaccine* **34**, 2911–2914 (2016).

6. Khoshnood, S. *et al.* Novel vaccine candidates against Mycobacterium tuberculosis. *Int. J. Biol. Macromol.* #pagerange# (2018) doi:10.1016/J.IJBIOMAC.2018.08.037.

7. Nazir, T., Abraham, S. & Islam, A. Emergence of Potential Superbug Mycobacterium Tuberculosis, Lessons from New Delhi Mutant-1 Bacterial Strains. *Int. J. Heal. …* **6**, 87–94 (2012).

8. Islam, M. M. *et al.* Drug resistance mechanisms and novel drug targets for tuberculosis therapy. *J. Genet. Genomics* **44**, 21–37 (2017).

9. Yang, H.-J., Wang, D., Wen, X., Weiner, D. M. & Via, L. E. One Size Fits All? Not in In Vivo Modeling of Tuberculosis Chemotherapeutics. *Front. Cell. Infect. Microbiol.* **0**, 134 (2021).

10. Chan, J., Yun, X., Magliozzo, R. S. & Bloom, B. R. Killing of virulent Mycobacterium tuberculosis by reactive nitrogen intermediates produced by activated murine macrophages. *J. Exp. Med.* **175**, 1111–1122 (1992).

11. Minakami, R. & Sumimotoa, H. Phagocytosis-Coupled Activation of the Superoxide-Producing Phagocyte Oxidase, a Member of the NADPH Oxidase (Nox) Family. *Int. J. Hematol.* **84**, 193–198 (2006).

12. Elks, P. M. *et al.* Hypoxia Inducible Factor Signaling Modulates Susceptibility to Mycobacterial Infection via a Nitric Oxide Dependent Mechanism. *PLoS Pathog.* **9**, 1–16 (2013).

13. Vergne, I., Chua, J., Singh, S. B. & Deretic, V. CELL BIOLOGY OF MYCOBACTERIUM TUBERCULOSIS PHAGOSOME. *Annu. Rev. Cell Dev. Biol.* **20**, 367–394 (2004).

14. Vergne, I., Gilleron, M. & Nigou, J. Manipulation of the endocytic pathway and phagocyte functions by Mycobacterium tuberculosis lipoarabinomannan. *Front. Cell. Infect. Microbiol.* **4**, 1–9 (2015).

15. Vandal, O. H., Pierini, L. M., Schnappinger, D., Nathan, C. F. & Ehrt, S. A membrane protein preserves intrabacterial pH in intraphagosomal Mycobacterium tuberculosis. *Nat. Med.* **14**, 849–854 (2008).

16. Levitte, S. *et al.* Mycobacterial Acid Tolerance Enables Phagolysosomal Survival and Establishment of Tuberculous Infection In Vivo. *Cell Host Microbe* **20**, 250–258 (2016).

17. Zulauf, K. E., Sullivan, J. T. & Braunstein, M. The SecA2 pathway of Mycobacterium tuberculosis exports effectors that work in concert to arrest phagosome and autophagosome maturation. *PLOS Pathog.* **14**, e1007011 (2018).

18. van der Wel, N. *et al*. M. tuberculosis and M. leprae translocate from the phagolysosome to the cytosol in myeloid cells. *Cell* **129**, 1287–1298 (2007).

19. Simeone, R., Bottai, D., Frigui, W., Majlessi, L. & Brosch, R. ESX/type VII secretion systems of mycobacteria: Insights into evolution, pathogenicity and protection. *Tuberculosis (Edinb)*. **95 Suppl 1**, S150–S154 (2015).

20. Deretic, V. *et al*. Mycobacterium tuberculosis inhibition of phagolysosome biogenesis and autophagy as a host defence mechanism. *Cell. Microbiol*. **8**, 719–727 (2006).

21. Deretic, V., Saitoh, T. & Akira, S. Autophagy in infection, inflammation and immunity. *Nat. Rev. Immunol*. **13**, 722–37 (2013).

22. Gomes, L. C. & Dikic, I. Autophagy in antimicrobial immunity. *Mol. Cell* **54**, 224–233 (2014).

23. Kimmey, J. M. & Stallings, C. L. Bacterial Pathogens versus Autophagy: Implications for Therapeutic Interventions. *Trends Mol. Med*. **22**, 1060–1076 (2016).

24. Ramakrishnan, L. Revisiting the role of the granuloma in tuberculosis. *Nat. Rev. Immunol*. **12**, 352–366 (2012).

25. Volkman, H. E. *et al*. Tuberculous granuloma formation is enhanced by a Mycobacterium virulence determinant. *PLoS Biol*. **2**, (2004).

26. Davis, J. M. & Ramakrishnan, L. The Role of the Granuloma in Expansion and Dissemination of Early Tuberculous Infection. *Cell* **136**, 37–49 (2009).

27. Barry, C. E. & Blanchard, J. S. The chemical biology of new drugs in the development for tuberculosis. *Curr. Opin. Chem. Biol*. **14**, 456–466 (2010).

28. Zhu, H. *et al*. Eliciting antibiotics active against the ESKAPE pathogens in a collection of actinomycetes isolated from mountain soils. *Microbiol. (United Kingdom)* **160**, 1714–1726 (2014).

29. Makarov, V. *et al*. Benzothiazinones Kill Mycobacterium tuberculosis by blocking Arabinan synthesis. *Science (80-.)*. **324**, 801–804 (2009).

30. Norrby, S. R., Nord, C. E. & Finch, R. Lack of development of new antimicrobial drugs: a potential serious threat to public health. *Lancet Infect. Dis*. **5**, 115–119 (2005).

31. Hawn, T. R., Matheson, A. I., Maley, S. N. & Vandal, O. Host-directed therapeutics for tuberculosis: can we harness the host? *Microbiol. Mol. Biol. Rev*. **77**, 608–27 (2013).

32. Zumla, A. *et al*. Towards host-directed therapies for tuberculosis. *Nat. Rev. Drug Discov*. **1**, (2015).

33. Wallis, R. S. & Hafner, R. Advancing host-directed therapy for tuberculosis. *Nature Reviews Immunology* vol. 15 255–263 (2015).

34. Machelart, A., Song, O. R., Hoffmann, E. & Brodin, P. Host-directed therapies offer novel opportunities for the fight against tuberculosis. *Drug Discov. Today* **22**, 1250–1257 (2017).

35. Kilinç, G., Saris, A., Ottenhoff, T. H. M. & Haks, M. C. Host-directed therapy to combat mycobacterial infections*. *Immunological Reviews* vol. 301 62–83 (2021).

36. Napier, R. J. *et al*. Imatinib-Sensitive tyrosine kinases regulate mycobacterial pathogenesis and represent therapeutic targets against tuberculosis. *Cell Host Microbe* **10**, 475–485 (2011).

37. Singhal, A. *et al*. Metformin as adjunct antituberculosis therapy. *Sci. Transl. Med.* **6**, 263ra159-263ra159 (2014).

38. Kuijl, C., Savage, N., Marsman, M. & Tuin, A. Intracellular bacterial growth is controlled by a kinase network around PKB/AKT1 (supplementary figures). *Nature* 1–27 (2007) doi:10.1038/nature0.

39. Kumar, D. *et al*. Genome-wide analysis of the host intracellular network that regulates survival of Mycobacterium tuberculosis. *Cell* **140**, 731–43 (2010).

40. Wilkinson, G. F. & Pritchard, K. In vitro screening for drug repositioning. *J. Biomol. Screen.* **20**, 167–179 (2015).

41. Schiebler, M. *et al*. Functional drug screening reveals anticonvulsants as enhancers of mTOR-independent autophagic killing of Mycobacterium tuberculosis through inositol depletion. *EMBO Mol. Med.* **7**, 127–139 (2015).

42. Korbee, C. J. *et al*. Combined chemical genetics and data-driven bioinformatics approach identifies receptor tyrosine kinase inhibitors as host-directed antimicrobials. *Nat. Commun.* **9**, 358 (2018).

43. Matty, M. A. *et al*. Potentiation of P2RX7 as a host-directed strategy for control of mycobacterial infection. *Elife* **8**, 1–27 (2019).

44. Tobin, D. M. Host-Directed Therapies for Tuberculosis. *Cold Spring Harb. Perspect. Med.* **5**, a021196 (2015).

45. Eskelinen, E.-L., Reggiori, F., Baba, M., Kovács, A. L. & Seglen, P. O. Seeing is believing: The impact of electron microscopy on autophagy research. *Autophagy* **7**, 935–956 (2011).

46. Gutierrez, M. G. *et al*. Autophagy is a defense mechanism inhibiting BCG and Mycobacterium tuberculosis survival in infected macrophages. *Cell* **119**, 753–766 (2004).

47. Rubinsztein, D. C., Codogno, P. & Levine, B. Autophagy modulation as a potential therapeutic target for diverse diseases. *Nat. Rev. Drug Discov.* **11**, 709–730 (2012).

48. Boyle, K. B. & Randow, F. The role of 'eat-me' signals and autophagy cargo receptors in innate immunity. *Curr. Opin. Microbiol.* **16**, 339–348 (2013).

49. Bradfute, S. B. *et al*. Autophagy as an immune effector against tuberculosis. *Curr. Opin. Microbiol.* **16**, 355–365 (2013).

50. Johansen, T. & Lamark, T. Selective autophagy mediated by autophagic adapter proteins. *Autophagy* **7**, 279–296 (2011).

51. Kirkin, V. & Rogov, V. V. A Diversity of Selective Autophagy Receptors Determines the Specificity of the Autophagy Pathway. *Mol. Cell* **76**, 268–285 (2019).

52. Zhang, R. *et al*. The selective autophagy receptors Optineurin and p62 are both required for zebrafish host resistance to mycobacterial infection. *PLOS Pathog.* **15**, e1007329 (2019).

53. Ponpuak, M. & Deretic, V. Autophagy and p62/sequestosome 1 generate neo-antimicrobial peptides (cryptides) from cytosolic proteins. *Autophagy* **7**, 336–337 (2011).

54. Kimmey, J. M. *et al*. Unique role for ATG5 in neutrophil-mediated immunopathology during M. tuberculosis infection. *Nature* **528**, 565–569 (2015).

55. Castillo, E. F. *et al.* Autophagy protects against active tuberculosis by suppressing bacterial burden and inflammation. *Proc. Natl. Acad. Sci.* **109**, E3168–E3176 (2012).

56. Ponpuak, M. *et al.* Delivery of Cytosolic Components by Autophagic Adaptor Protein p62 Endows Autophagosomes with Unique Antimicrobial Properties. *Immunity* **32**, 329–341 (2010).

57. Köster, S. *et al.* Mycobacterium tuberculosis is protected from NADPH oxidase and LC3-associated phagocytosis by the LCP protein CpsA. *Proc. Natl. Acad. Sci. U. S. A.* **114**, E8711–E8720 (2017).

58. Martinez, J. LAP it up, fuzz ball: a short history of LC3-associated phagocytosis. *Curr. Opin. Immunol.* **55**, 54–61 (2018).

59. Li, J., Kim, S. G. & Blenis, J. Rapamycin: One drug, many effects. *Cell Metab.* **19**, 373–379 (2014).

60. Kim, Y. S., Silwal, P., Kim, S. Y., Yoshimori, T. & Jo, E. K. Autophagy-activating strategies to promote innate defense against mycobacteria. *Exp. Mol. Med. 2019 5112* **51**, 1–10 (2019).

61. Tortorici, M. A., Matschke, K., Korth-Bradley, J. M., Dilea, C. & Lasseter, K. C. The effect of rifampin on the pharmacokinetics of sirolimus in healthy volunteers. *Clin. Pharmacol. drug Dev.* **3**, 51–56 (2014).

62. van der Vaart, M. *et al.* The DNA Damage-Regulated Autophagy Modulator DRAM1 Links Mycobacterial Recognition via TLR-MYD88 to Autophagic Defense. *Cell Host Microbe* **15**, 753–767 (2014).

63. Andersson, A. M. *et al.* Autophagy induction targeting mTORC1 enhances Mycobacterium tuberculosis replication in HIV co-infected human macrophages. *Sci. Rep.* **6**, 1–15 (2016).

64. Ashley, D. *et al.* Antimycobacterial Effects of Everolimus in a Human Granuloma Model. *J. Clin. Med.* **9**, 1–14 (2020).

65. Crevel, R. van & Critchley, J. A. The Interaction of Diabetes and Tuberculosis: Translating Research to Policy and Practice. *Trop. Med. Infect. Dis. 2021, Vol. 6, Page 8* **6**, 8 (2021).

66. Böhme, J. *et al.* Metformin enhances anti-mycobacterial responses by educating CD8+ T-cell immunometabolic circuits. *Nat. Commun.* (2020) doi:10.1038/s41467-020-19095-z.

67. Stanley, S. a *et al.* Identification of host-targeted small molecules that restrict intracellular Mycobacterium tuberculosis growth. *PLoS Pathog.* **10**, e1003946 (2014).

68. Sugita, S. *et al.* EGFR-independent autophagy induction with gefitinib and enhancement of its cytotoxic effect by targeting autophagy with clarithromycin in non-small cell lung cancer cells. *Biochem. Biophys. Res. Commun.* **461**, 28–34 (2015).

69. Harris, J. & Keane, J. How tumour necrosis factor blockers interfere with tuberculosis immunity. *Clin. Exp. Immunol.* **161**, 1–9 (2010).

70. Sundaramurthy, V. *et al.* Integration of chemical and RNAi multiparametric profiles identifies triggers of intracellular mycobacterial killing. *Cell Host Microbe* **13**, 129–42 (2013).

71. Parihar, S. P. *et al.* Statin therapy reduces the mycobacterium tuberculosis burden in human macrophages and in mice by enhancing autophagy and phagosome maturation. *J. Infect. Dis.* **209**, 754–763 (2014).

72. Guerra-De-Blas, P. D. C. *et al.* Simvastatin Enhances the Immune Response Against Mycobacterium tuberculosis. *Front. Microbiol.* **10**, (2019).

73. Dutta, N. K. *et al*. Adjunctive Host-Directed Therapy With Statins Improves Tuberculosis-Related Outcomes in Mice. *J. Infect. Dis*. **221**, 1079–1087 (2020).

74. Engeszer, R. E., Patterson, L. B., Rao, A. A. & Parichy, D. M. Zebrafish in The Wild: A Review of Natural History And New Notes from The Field. *Zebrafish* **4**, 21–40 (2007).

75. Kimmel, C. B., Ballard, W. W., Kimmel, S. R., Ullmann, B. & Schilling, T. F. Stages of embryonic development of the zebrafish. *Dev. Dyn*. **203**, 253–310 (1995).

76. Traver, D. *et al*. The zebrafish as a model organism to study development of the immune system. *Adv. Immunol*. **81**, 253–330 (2003).

77. Lieschke, G. J. & Currie, P. D. Animal models of human disease: Zebrafish swim into view. *Nat. Rev. Genet*. **8**, 353–367 (2007).

78. Patton, E. E. & Tobin, D. M. Spotlight on zebrafish: the next wave of translational research. *Dis. Model. Mech*. **12**, dmm039370 (2019).

79. Hosseini, R. *et al*. Correlative light and electron microscopy imaging of autophagy in a zebrafish infection model. *Autophagy* **10**, 1844–1857 (2014).

80. Howe, K. *et al*. The zebrafish reference genome sequence and its relationship to the human genome. *Nat. 2013 4967446* **496**, 498–503 (2013).

81. Stainier, D. Y. R. *et al*. Guidelines for morpholino use in zebrafish. *PLoS Genet*. **13**, 6–10 (2017).

82. Cornet, C., Di Donato, V. & Terriente, J. Combining Zebrafish and CRISPR/Cas9: Toward a more efficient drug discovery pipeline. *Front. Pharmacol*. **9**, 1–11 (2018).

83. Meijer, A. & Spaink, H. Host-pathogen interactions made transparent with the zebrafish model. *Curr. Drug Targets* 1000–1017 (2011).

84. Page, D. M. *et al*. An evolutionarily conserved program of B-cell development and activation in zebrafish. *Blood* **122**, 1–12 (2013).

85. Kantae, V. *et al*. Pharmacokinetic Modeling of Paracetamol Uptake and Clearance in Zebrafish Larvae: Expanding the Allometric Scale in Vertebrates with Five Orders of Magnitude. *Zebrafish* **13**, 504–510 (2016).

86. Davis, J. M. *et al*. Real-time visualization of Mycobacterium-macrophage interactions leading to initiation of granuloma formation in zebrafish embryos. *Immunity* **17**, 693–702 (2002).

87. Meijer, A. H. Protection and pathology in TB: learning from the zebrafish model. *Semin. Immunopathol*. **38**, 261–273 (2016).

88. Stamm, L. M. & Brown, E. J. Mycobacterium marinum: the generalization and specialization of a pathogenic mycobacterium. *Microbes Infect*. **6**, 1418–1428 (2004).

89. Prouty, M. G., Correa, N. E., Barker, L. P., Jagadeeswaran, P. & Klose, K. E. Zebrafish-Mycobacterium marinum model for mycobacterial pathogenesis. *FEMS Microbiol. Lett*. **225**, 177–182 (2003).

90. Parikka, M. *et al*. Mycobacterium marinum Causes a Latent Infection that Can Be Reactivated by Gamma Irradiation in Adult Zebrafish. *PLoS Pathog*. **8**, (2012).

91. Benard, E. L., Rougeot, J., Racz, P. I., Spaink, H. P. & Meijer, A. H. *Transcriptomic Approaches in the Zebrafish Model for Tuberculosis—Insights Into Host- and Pathogen-specific Determinants of the Innate Immune Response. Advances in Genetics* vol. 95 (Elsevier Ltd, 2016).

92. Tobin, D. M., May, R. C. & Wheeler, R. T. Zebrafish: A See-Through Host and a Fluorescent Toolbox to Probe Host–Pathogen Interaction. *PLoS Pathog.* **8**, e1002349 (2012).

93. Ramakrishnan, L. The Zebrafish Guide to Tuberculosis Immunity and Treatment. *Cold Spring Harb. Symp. Quant. Biol.* **78**, 179–192 (2013).

94. Torraca, V., Masud, S., Spaink, H. P. & Meijer, A. H. Macrophage-pathogen interactions in infectious diseases: new therapeutic insights from the zebrafish host model. *Dis. Model. Mech.* **7**, 785–97 (2014).

95. Yoshida, N., Frickel, E. M. & Mostowy, S. Macrophage-microbe interactions: Lessons from the Zebrafish model. *Front. Immunol.* **8**, (2017).

96. Varga, M., Fodor, E. & Vellai, T. Autophagy in zebrafish. *Methods* **75**, 172–180 (2015).

97. Mathai, B., Meijer, A. & Simonsen, A. Studying Autophagy in Zebrafish. *Cells* **6**, 21 (2017).

98. Lopez, A., Fleming, A. & Rubinsztein, D. C. Seeing is believing: methods to monitor vertebrate autophagy in vivo. *Open Biol.* **8**, (2018).

99. Muñoz-Sánchez, S., van der Vaart, M. & Meijer, A. H. Autophagy and Lc3-Associated Phagocytosis in Zebrafish Models of Bacterial Infections. *Cells* **9**, 2372 (2020).

100. He, C., Bartholomew, C. R., Zhou, W. & Klionsky, D. J. Assaying autophagic activity in transgenic GFP-Lc3 and GFP-Gabarap zebrafish embryos. *Autophagy* **5**, 520–526 (2009).

101. Zhang, R. *et al.* Deficiency in the autophagy modulator Dram1 exacerbates pyroptotic cell death of Mycobacteria-infected macrophages. *Cell Death Dis. 2020 114* **11**, 1–16 (2020).

2

Deep learning image recognition enables efficient genome editing in zebrafish by automated injections

Maria Lorena Cordero-Maldonado[1*], Simon Perathoner[1*], Kees-Jan van der Kolk[2*], **Ralf Boland**[3], Ursula Heins-Marroquin[1], Herman P. Spaink[3], Annemarie H. Meijer[3], Alexander D. Crawford[1], Jan de Sonneville[2]

1. Luxembourg Centre for Systems Biomedicine, University of Luxembourg, Belvaux, Luxembourg
2. Life Science Methods BV, Leiden, the Netherlands
3. Institute of Biology, Leiden University, Leiden, the Netherlands
* Equal contribution

Abstract

One of the most popular techniques in zebrafish research is microinjection. This is a rapid and efficient way to genetically manipulate early developing embryos, and to introduce microbes, chemical compounds, nanoparticles or tracers at larval stages. Here we demonstrate the development of a machine learning software that allows for microinjection at a trained target site in zebrafish eggs at unprecedented speed. The software is based on the open-source deep-learning library Inception v3. In a first step, the software distinguishes wells containing embryos at one-cell stage from wells to be skipped with an accuracy of 93%. A second step was developed to pinpoint the injection site. Deep learning allows to predict this location on average within 42 μm to manually annotated sites. Using a Graphics Processing Unit (GPU), both steps together take less than 100 milliseconds. We first tested our system by injecting a morpholino into the middle of the yolk and found that the automated injection efficiency is as efficient as manual injection (~ 80%). Next, we tested both CRISPR/Cas9 and DNA construct injections into the zygote and obtained a comparable efficiency to that of an experienced experimentalist. Combined with a higher throughput, this results in a higher yield. Hence, the automated injection of CRISPR/Cas9 will allow high-throughput applications to knock out and knock in relevant genes to study their mechanisms or pathways of interest in diverse areas of biomedical research.

Introduction

Microinjection is one of the most powerful techniques used in zebrafish (*Danio rerio*), as it allows to follow cell fate[1], evaluate pathogenesis of bacteria[2], produce chimeric individuals[3], study tumour progression[4,5], manipulate protein levels[6,7] and create genetically altered lines[8]. In addition, it is also a suitable technique to introduce chemical compounds that otherwise do not readily enter the embryo due to the compound lipophilicity properties and the protection function of the chorion[9]. More recently, microinjections have been also used in the fields of toxicology and nanomedicine to evaluate nanoparticles toxicity at different functional levels and to inject nanoparticles encapsulating genetic material or therapeutic drugs to specific tissues in older embryos and/or larvae[10-13].

The intrinsic biological properties of zebrafish make it particularly amenable to this technique, since these cyprinids are highly fecund, a spawning pair typically producing more than 400 eggs at a time. Moreover, fertilization is external and spawning is confined to a brief period at dawn (natural or artificial), allowing for timing of the experiments. Furthermore, the chorion of zebrafish eggs is supple and easy to pierce.

Classically, injection of tracer dyes is used to identify single cell populations[14,15], to follow cell lineages and to build fate maps in zebrafish[1,16]. The development of molecular methods for the zebrafish model enabled functional studies by manipulating the expression of specific genes. Injection of messenger RNA (mRNA) can be used to overexpress and misexpress a specific protein[17], while morpholino antisense oligonucleotides (MOs) can be employed to knock down a given target gene[18]. In zebrafish mRNA and MO injections are simply performed by introducing a fine-tipped needle into the yolk of one-cell stage eggs and delivering nanoliter volumes of the injection material into it[19]. As cytoplasmic streaming will move the mRNA or MOs into the cytoplasm, it is not necessary that the injection targets the cell. While injection into the yolk requires

some skill, it can usually be learned within a few weeks. Nevertheless, injections of mRNAs and MOs have their drawbacks. First of all, the effect is only transient, *i.e.* the injected molecules will be degraded and/or diluted with time. Moreover, in the case of mRNA injection, tissue-specific upregulation is not possible and a given mRNA will be expressed in all tissues indiscriminately. Also, the specificity of MO antisense technology has recently been questioned as MOs can sometimes lead to misleading results due to toxicity and off-target effects[20]. In a recent study[21], loss-of-function mutations for ten different genes previously thought to have an essential role in development failed to recapitulate the corresponding morpholino-induced phenotypes. In several cases, the discrepancy between mutant and morphant phenotypes, could be explained by genetic compensation mechanisms that occur in mutants[22], however, undoubtedly rigorous controls are required to ascertain the reliability of MO-induced phenotypes[20,23,24].

In the last years, with the implementation of targeted nuclease techniques in the zebrafish, the demand for genetic evidence to define gene function has greatly increased. Fortunately, after a somewhat slow start using zinc-finger nucleases (ZFNs)[25] and transcription activator-like effector nucleases (TALENs)[26], the adaptation of the prokaryotic CRISPR/Cas9 (clustered regularly interspaced short palindromic repeats/ CRISPR associated protein 9) defence system to engineer genomes has revolutionized reverse genetics in zebrafish[27].

Recently the CRISPR/Cas9 system was adapted and optimised to engineer genomes. A single synthetic guide RNA (gRNA) directs Cas9-mediated cleavage of target DNA [27,28], and the method was implemented in multiple systems including zebrafish[29,30], finally paving the road for knock-ins in this model[31]. Along with *Tol2* mediated transgenesis, a transposon system based on the *Tol2* element of medaka (*Oryzias latipes*) widely used in zebrafish to create transgenic lines[8], the CRISPR/Cas9 system has become an essential tool for genome editing in zebrafish. In this context microinjection is an essential technique. For the creation of genetically altered lines in zebrafish, be it through *Tol2* transgenesis or by means of zinc finger nucleases, TALEN or Cas9 nucleases, it is critical to inject the solution directly into the blastomere at the one-cell stage or at least at the interface between blastomere and yolk[32-35]. Contrary to RNA or MOs, DNA appears not to be transported into the blastomere via cytoplasmic streaming. Moreover, efficiency of all these genome editing techniques is much lower compared to mRNA or MOs injections. Therefore, in order to create genetically altered zebrafish lines it is essential to master microinjections into the cell. This can be challenging as this type of injection requires long training and excellent technical skills

Automated microinjection system

One of the first reports attempting to establish an automated microinjection system was published by Wang and colleagues in 2007[36]. This microrobotic system based on computer vision and motion control was able to inject zebrafish embryos at an average speed of 25 seconds per embryo. Although quite innovative, this system is limited by the low batch size (only up to 24 embryos per plate) and low injection speed compared to the first version of our microinjection system[33,37,38]. This automated microinjection system featured half-spherical wells, moulded in agarose gel, which allowed for high-throughput microinjection into the yolk of zebrafish eggs at fast speed (1 embryo in 1.8 seconds). This was used for microinjection of bacteria, morpholinos and cancer cells[37,38]. The great advantage over other systems was the higher batch size and speed of the injections allowing to inject up to 2000 embryos per hour and up to 2580 embryos per plate. As the initial cell division steps in zebrafish embryos occur in intervals of 20-40 minutes, speed is crucial for the accuracy, reproducibility and number of experiments.

In our experience, it is apparent that injections into the middle of the yolk are less suitable for DNA injections. Therefore as a first step, the program "click-to-inject" was developed to test the efficiency of injections closer to the first cell[38]. With this, we noticed that we could achieve a great increase in efficiency, similar to manual injections done into the first cell. Therefore, we set out to automate this procedure.

In this study we demonstrate the results of autonomous site selection and injection for CRISPR/Cas9 and DNA manipulation of the zebrafish genome.

Results and discussion

Manual and automated injections of slc45a2-MO

In order to test MO efficiency of manual and automated injections we employed a translation-blocking MO against *slc45a2* (solute carrier family 45 member 2). Downregulation of this gene induces albino and/or hypo-pigmented morphants, as the melanophores are unable to produce melanin[41]. Manual and automated yolk microinjections were performed in parallel, and in both cases the induced albino phenotype was assessed in larvae at 3 dpf (Figure 1). The results obtained with both microinjection approaches are comparable and show that downregulation of *slc45a2* is highly efficient using morpholino antisense technology (Figure 1A). Additionally, the manual injections were performed by two different experimentalists (Figure 1B) and this shows that efficiency and variation of efficiency obtained by manual morpholino injections differs from person to person and that the variation of the efficiency of the automated injections is slightly larger.

Semi-automated "click-to-inject"

After demonstrating that automated injection into the yolk is an efficient way to generate morphants, we sought to apply the robotic injector for generating CRISPR/
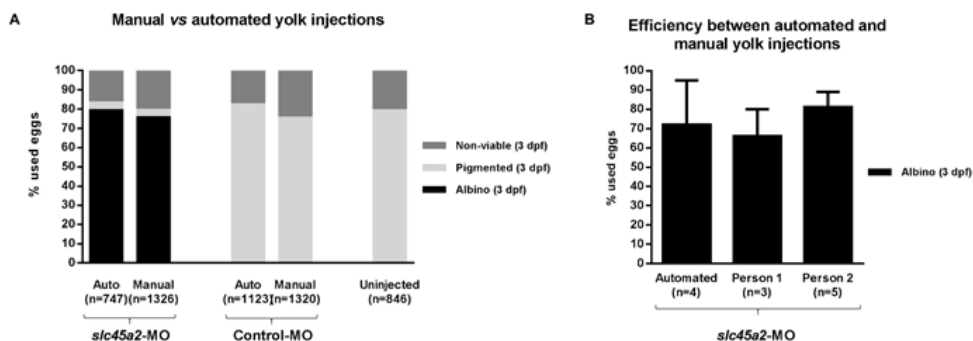
Figure 1. Morpholino knockdown efficiency with manual and automated injections.

A. The survival and knockdown efficiency of slc45a2-MO manual and automated (auto) microinjections were measured as the number of larvae displaying an albino phenotype at 3 days post-fertilization (dpf). Control-MO injected larvae and uninjected larvae were processed in parallel and the resulting pigmented (wild-type) larvae were also counted at 3 dpf. "n=" indicates the number of eggs used to obtain this cumulative result.

B. Efficiency comparison between the automated injection into the yolk and manual injections performed by two independent experimentalists (P1: experienced and P2: expert; not statistically significant). "n=" indicates the number of experiments used to calculate the average and standard deviation. Each experiment refers to different technical and biological experiments.

Cas9 mutants for *slc45a2*. To investigate the dependence on the injection location we used the "click-to-inject" program to test the efficiency of injections closer to the first cell. In the "click-to-inject" program the injection depth is set, but the (x y) position is chosen by the operator[38]. To inject, the operator moves the mouse pointer to a specific site (*e.g.* the first cell) and clicks to trigger an injection and a subsequent movement to the next egg. Based on this, next we set out to develop an automated image recognition to more precisely identify the first cell and to automate CRISPR/Cas9 injections.

Imaging conditions

In manual microinjection setups, as well as in standard microscopy, near-perfect imaging conditions are applied with lighting from the bottom and imaging from the top, or vice versa. As the zebrafish egg is very transparent, epi illumination from below is not suitable; most contrast and edges are then lost. As the egg is spherical, a ring-light displays a very bright circle on top of the egg. Therefore, to obtain better and more reproducible imaging conditions in different locations, we placed a large (L x B = 60 x 80 cm^2) diffuse light source above the robotic injector. Five different classes were used to annotate the images (Figure 2). In the "Inject" class the ideal injection position for automated microinjection is also annotated. Instead of injecting directly into the zygote, we have chosen to inject in the yolk, close to the visible zygote. The reason is that injections in a thin zygote (less ideal orientation, or very early stage) would often cause a rotation of the egg, and bounce the needle off. Injections into the yolk-blastomere boundary almost never show this problem, and thus gave a higher yield.

Machine learning

Initially, we tried a classic approach of machine vision on these images. The Hough
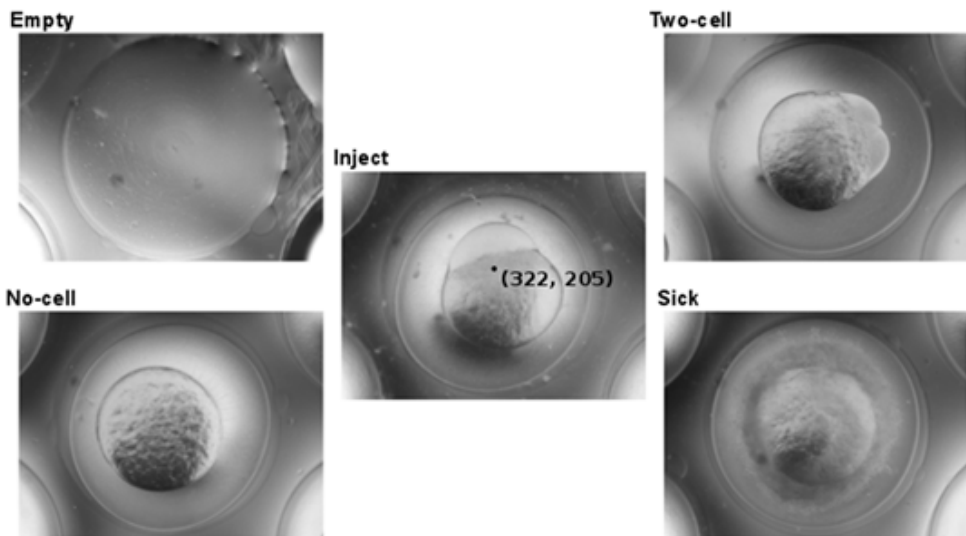
Figure 2. Imaging classification for injection.
Representative digital images measured from below of an agarose grid ("Empty") that supports zebrafish eggs with the first cell visible ("Inject") or not visible ("No cell"), eggs in a two- or higher cell stage ("Two cell") or non-viable eggs ("Sick"). In the "Inject" image an injection location is indicated by a black dot with (x y) coordinates.

circle transform allowed us to detect the yolk with an above 90% accuracy[36]. However, the next step to find the first cell was problematic. In cases where the shadow of the micromanipulator overlapped with the first cell, the edge detection algorithm failed. As an alternative to edge detection, we annotated a database of images with injection positions. We used a Fast Fourier Transform (FFT) algorithm to find a closest matching egg in this database and used that image to infer an injection position. This worked reasonably well with a peak error (distance between calculated position and annotated position) of 20 μm. However, when a good match could not be found, the error was quite high, and as a result the tail of the error was quite large. An explanation for the large variation in results is that there is also a large variation in first cell shapes, especially when looking from an arbitrary angle. It can be an early very thin line up to about a third of the yolk depending on the developmental stage and orientation of the egg. To overcome this variation, we could make the annotated database larger, to increase the chance of a close match. Nevertheless, the downside of this solution is that more images have to be compared, and this takes more processing time during injection. Thus, we sought to apply a better approach based on deep learning.

Using a database of annotated images as input, one can also train a deep learning network. Instead of comparing images during runtime, one trains an algorithm that is afterwards used to interpret new images. The execution time of this algorithm is independent of the size of the training image set. Thus, roughly speaking, the larger the number of annotated images, the higher the accuracy of the algorithm. We used the Inception v3 open source deep learning software[46]. This software has been built and tested to categorize images, based on a large training database of images, initially for the annual ImageNet Large Scale Visual Recognition Challenge (ILSVRC; www.image-net.org). The Inception v3 architecture uses a neural network that takes the pixels of images as input and extracts features. Many features are subsequently built on top of features, in different layers of neurons, in higher and higher levels of abstraction, until the neurons reach an output of defined categories[47]. One advantage of the Inception v3 software is that one can reuse the first layers of feature extraction for a different set of images. This is built on the idea that the basic features, *e.g.* lines and simple patterns, can be used in all higher-level features that are used to train new categories with new sets of images. Within eight hours of training time we reached a 93% accuracy, with an execution time in the order of tens of milliseconds.

After finding the images with a visible first cell, the next step was to determine the injection location. To enable the use of deep learning for this problem, we had to modify the output from categories into an ideal location. When just the pixel (x y) coordinate is used as output, only one pixel of the whole image is correct. With this output the neuronal network cannot easily distinguish between locations closer to the annotated location and further away, and this makes learning impossible. Therefore, we translated the (x y) coordinates to a barycentric coordinate system[48]. The Greek word "*barys*" means heavy and refers to the centre of gravity. In a barycentric coordinate system a grid of triangles is used, with a weight assigned to each vertex. This is used as follows. A chosen grid of triangles is placed on top of each image. The annotated injection position will fall within one triangle; then the weights of these triangle vertices are given a value according to the location within that triangle. These weights sum up to one, whereas the other vertices in the grid are all zero. This vertices output vector then represents the ideal outcome. The advantage is now that a small deviation from this ideal output vector can be scored gradually instead of binary. This then allows for efficient training. A more detailed explanation is available in S1 Text. After eight hours of training we created a table of (x y) coordinates using validation images. We calculated the distance between

the annotated injection position and the position as predicted by the deep learning network (Figure 3). The average distance is 42 μm, as depicted in Figure 3B, and for 83% of the images this distance is smaller than 60 μm.
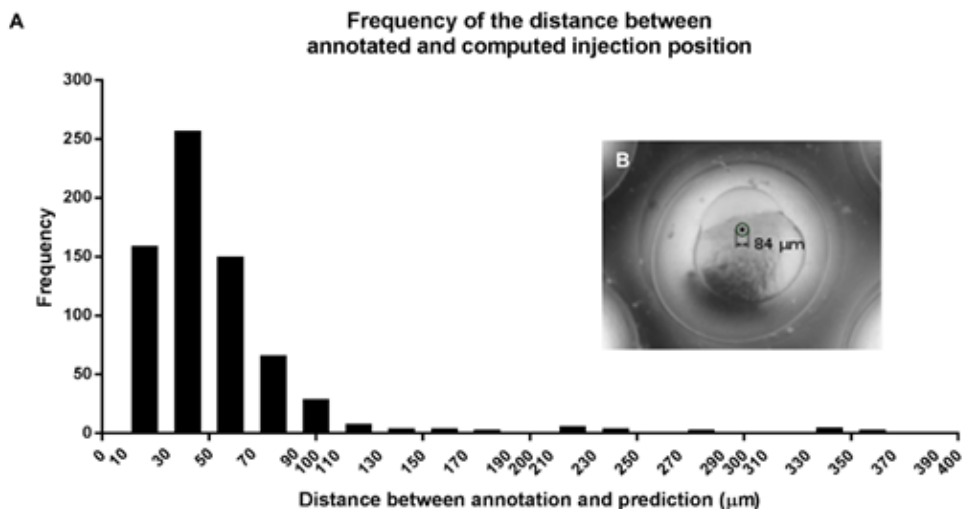
Figure 3. Distance between annotated and computed injection location.
A. Bar graph depicting the frequency of the distance between annotated and computed injection position (prediction).
B. Digital image with a circle around an annotated injection point to illustrate the average distance between annotation and prediction.

Automated injection of slc45a2 gRNA/Cas9

Trial and error in many laboratories have led to a best practice of injecting into the first cell for the application of the CRISPR/Cas9 editing technique. In our robotic microinjection system, injecting in the middle of the yolk gives the highest speed. Image recognition used to customise an injection location takes time but can increase the injection efficiency. To balance efficiency and speed, and to be able to monitor improvements of our image recognition model, we started by measuring efficiency of CRISPR/Cas9 injections performed in the yolk. Both manual and automated yolk injections gave a very low efficiency of 12% (Figure 4A). Then, with the "click-to-inject" program (semi-auto), resulting in injections closer to the first cell we could generate albino larvae at an almost three times higher efficiency than with the injections in the middle of the yolk (Figure 4A). Next, using deep learning (auto), we could automate this procedure and with this we reached a slightly lower efficiency when comparing it the "click-to-inject" injections but a higher efficiency than the one obtained with automated and manual injections in the middle of the yolk (Figure 4A). Still, manual injections into the first cell reached the highest efficiency of 43% (Figure 4A). Figure 4B shows that both the efficiency and the variation between experiments differs considerably depending on the experimentalist (displayed as P1: experienced, P2: expert and P3: novice). In contrast, here, the automated injections show relatively little variation, also when compare them to the "click-to-inject" (semi-auto) injections (Figure 4B). Also, it can be seen that the efficiency is quickly surpassed by humans given enough experience (P1 and P2). This lower efficiency achieved with the robot can be explained by the injection location – close-to-cell instead of into the zygote – and by the fact that not all the eggs

are oriented with a cell visible on the side, despite the fact that they are oriented in the agar grid. Hence, the automated injections tend to be a mixture of injections into the middle of the yolk, and close to the first cell, when the first cell was detected. With this we obtained an efficiency of 24% on average (Figure 4B).
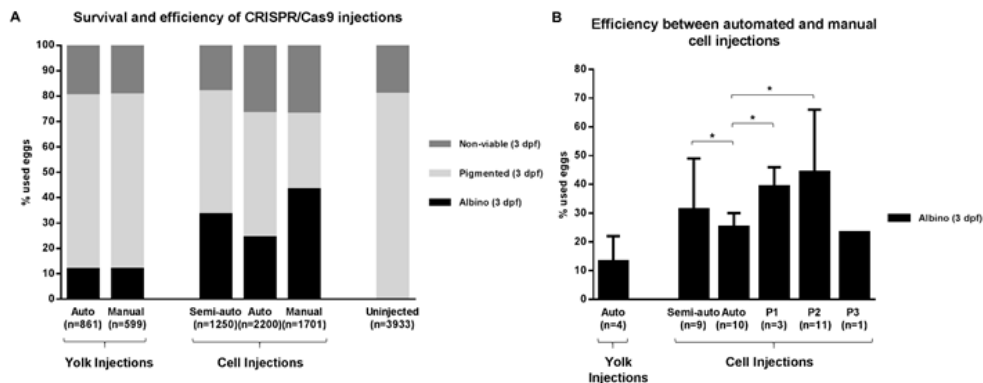
Figure 4. Automated injections of CRISPR/Cas9.
A. Survival and average efficiency of slc45a2 gRNA/Cas9 manual, click-to-inject (semi-auto) and automated (auto) microinjections both in the yolk and in the cell were measured as the number of larvae displaying an albino phenotype at 3 days post-fertilization (dpf). Uninjected larvae were processed as controls and the resulting pigmented (wild-type) larvae were also counted at 3 dpf. "n=" indicates the number of eggs that were used to obtain the cumulative results.
B. Comparison of the average efficiency and standard deviation between the automated (auto), click-to-inject (semi-auto) and manual injections performed by three independent experimentalists (P1: experienced, P2: expert and P3: novice). "n=" indicates the number of experiments that were used to calculate the average and standard deviation. Each experiment refers to different technical and biological experiments. (* $p<0.05$).
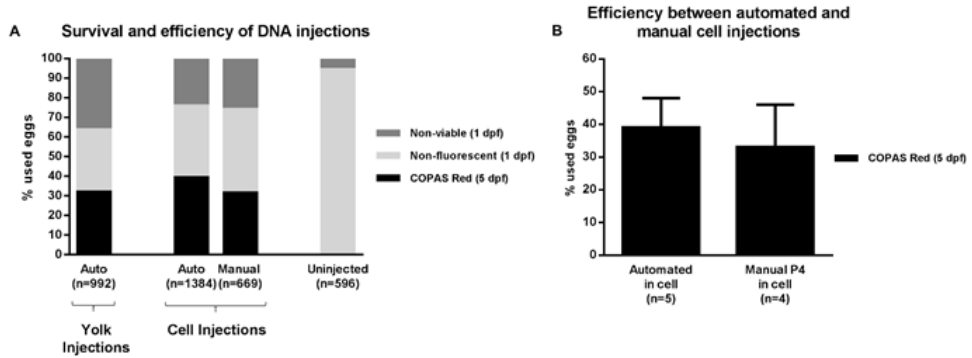
Automated injection of DNA

For the injections with DNA we used a COPAS (Complex Object Parameter Analyzer and Sorter) system to measure the efficiency of the injections (Figure 5A). For this, we first measured the highest red fluorescence signal of the uninjected control larvae and took the highest signal as a threshold at 5 dpf. Then we measured the DNA-injected larvae and counted the larvae that passed this threshold. The survival was measured at 1 dpf to focus on differences as a result of the injection. Prior to placing the larvae into the COPAS system, larvae with visible developmental defects were removed. Both the manual and automated injected eggs had a similar relative number of malformed embryos (4% on average).

These results show that DNA injections are less demanding in terms of injection location. Injections into the middle of the yolk reached an average efficiency of 32%. This can be improved by injecting close to the first cell, when possible, to reach an efficiency of 39%. Surprisingly, here manual injections close to the first cell (personal preference) had a lower efficiency than could be obtained by automated injections and gave on average the same efficiency as injections into the middle of the yolk.

Microinjection throughput

To calculate the microinjection throughput, we divided the average injection time by the average efficiency. This results in the average time needed for one successfully injected larva. We measured and compared the throughput for the different genetic

Figure 5. Automated injections of DNA.
A. Average survival and efficiency of DNA automated (auto) and manual injections as measured by the COPAS system. "n=" indicates the number of eggs that were used to obtain the cumulative results.
B. Comparison of the average efficiency and standard deviation between the automated and manual cell injections. P4 indicates a different experienced experimentalist and "n=" indicates the number of experiments that were used to calculate the average and standard deviation.

modifications and experimental setups described in this article, *i.e.* automated and manual injections for gene knockdown by morpholino antisense, gene knockout by CRISPR/Cas9 and transgenesis by *Tol2* (Figure 6).

In the case of the manual injections, the throughput differs greatly depending on the experimentalist, as experience can lead to a higher throughput by increasing both the efficiency and speed of the injection process. It can also be seen that the robot is on par with fast human performance in case of the morpholino injections, but 1.5 times as fast as average human performance.
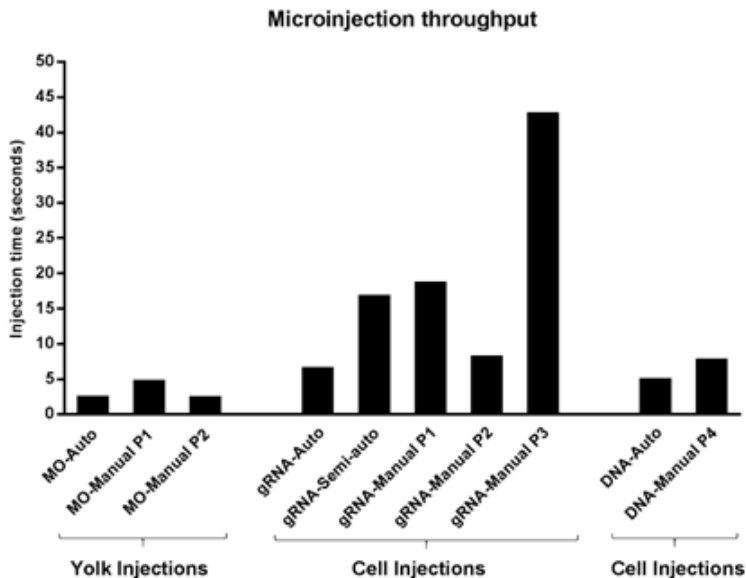
Figure 6. Average injection time required to obtain one positive genetically modified larva.
Abbreviations: MO, slc45a2 morpholino; gRNA, slc45a2 gRNA/Cas9; DNA, Tol2 construct; Auto, automated injections; P1-4, four different experimentalists.

With deep learning, a robot can outperform humans on the more complex cell injections. With CRISPR/Cas9 samples the robot needs 6 seconds of injection time to obtain a positive larva, and humans need 8 up to 43 seconds. On average, the robot is more than three times (3.6x) faster. Manual injections of DNA constructs close to the cell are faster to perform than injections into the cell (2.5 seconds *vs* 6.8 seconds). However, this also reduces the manual efficiency, resulting in a 1.5 times higher throughput of the robot. A movie showing the robotic injection process in real-time is available in S1 File. The movie shows that the time between capturing the image and placing the cross (demonstrating the calculated injection location) is only about 100 milliseconds.

Efficiency dependence on the injection location

Contrary to what might be expected, the efficiency of injections into the middle of the yolk to alter the genome were not negligible as the efficiency was 12% for CRISPR/Cas9, 32% for DNA injections and 80% for morpholino injections. Using the measured efficiencies and statistics of image classification we can calculate the efficiencies of injections close to the first cell. During the injections of CRISPR/Cas9, on average 65% of the eggs were oriented with a first cell visible, and 35% were injected into the middle of the yolk. The increase in efficiency, 24%, was caused by 65% of the eggs being injected with efficiency much higher than 12%. Using the efficiency of the yolk injections we can predict the efficiency of injections close to the first cell. Solving the equation $0.65*X+0.35*0.12 = 0.24$ for X results in an efficiency of around 30% for injections close to the first cell. For DNA injections we have chosen to not orient the eggs after placing them in a grid, and therefore less eggs, 46%, were injected close to the first cell. Solving the equation $0.46*X + 0.54*0.32 = 0.39$ for X results in a predicted efficiency of 47% for injections close to the first cell. Surprisingly, this is much higher than what was obtained by manual injections close to the first cell. The higher efficiency of DNA injections (47%) versus CRISPR/Cas9 injections (24%) can be partially explained by the fact that the integration of a single copy of DNA construct can still be detected, while the readout of the CRISPR/Cas9 injection requires a non-synonymous mutation to occur on both alleles in order to have a visible phenotype, the albino phenotype being recessive. A non-synonymous mutation in one copy of *slc45a2* would not be detected in our assay. Hence, we expect that the actual number of induced CRISPR/Cas9 mutations is underestimated.

These measured and calculated efficiencies can also be used to make a prediction of the positive embryos, directly after the injection.

Conclusion and perspectives

In this study we have demonstrated how we improved an automated injection robot to inject close to the first cell using image recognition in order to enable efficient genome editing in zebrafish embryos. This was accomplished using a modified open-source deep-learning software and annotation of thousands of images. A step-by-step approach of first testing an annotation strategy and efficiency helped to predict the increase in efficiency that can be obtained. Initially we tested the efficiency with a semi-automated click-to-inject program. This click-to-inject approach is also suitable as a first step for other microinjection applications, such as injections into older zebrafish larvae or different organisms.

Because of its transparency, rapid development and easy genetic manipulation, zebrafish

have become a key vertebrate model organism for the elucidation of developmental processes. With the advent of CRISPR/Cas9 technology, zebrafish are becoming an even more powerful tool for the study of diverse human disorders. The CRISPR/Cas9 system achieves mutagenesis rate of around 80% for generation of knockout lines[31], and has proven to have fewer side effects than other genome editing technologies. However, generation of specific hereditable mutations or epitope tagging of chromosomal genes in zebrafish is still challenging. Unfortunately, genome editing in zebrafish is unpredictable and efficiency sometimes drops to 3.5%[49]. Therefore, higher number of eggs should be injected for the generation of the expected mutation. Creation of zebrafish mutant lines using CRISPR/Cas9 requires precise injections into or close to the zygote. These types of injections take time to master and are tedious if many batches of hundreds of eggs have to be injected, particularly for the generation of knock-in lines. Our results have shown that efficiency and reproducibility of manual cell injections highly depend on the training stage of the person performing the experiment, making it more difficult to have this technique as a routine procedure in the laboratory. Here, we show the establishment of automated injections as a reliable tool for the generation of CRISPR/Cas9 mutants. Automated microinjections are simple to learn and allow the cell injection of 100 embryos in 2.5 minutes with comparable efficiency to manual cell injections. This method could also be used for high-throughput gene overexpression studies by microinjection of mRNA.

The need for high-throughput genome manipulation

To date there have been almost 9,000 morpholinos used in zebrafish research. In addition, the adaption of CRISPR/Cas9 editing technology is progressing faster than any other gene silencing method, and even faster than the adoption of morpholino knockdown technology (statistics on zfin.org). However, injections of mRNAs or DNA must be more precise and are more time consuming. Therefore injection can be a limiting step for high-throughput genetic studies. For the moment, there are about 30,000 known gene loci that could be interesting to manipulate in order to investigate their function in development, disease or expressed phenotype (zfin.org). Multiplied with 300 injections that are typically used to obtain a mutant, and multiple mutants per gene, this brings us to tens of millions of injections. Much time and efforts would be saved if this tedious but needed task can be performed mostly by robotic systems.

Acknowledgements

Materials and methods

Animals

Wild type adult zebrafish (AB or TL strain) are maintained in the Aquatic Facility of the Luxembourg Centre for Systems Biomedicine and the Institute of Biology, Leiden University, according to standard protocols[39]. Zebrafish eggs were obtained by natural spawning on the day of each experiment, kept in 0.3X Danieau's solution (14 mM NaCl, 2 mM KCl, 0.12 mM $MgSO_4$, 1.8 mM $Ca(NO_3)_2$, 1.5 mM HEPES pH 7.5 and 0.03 M methylene

blue) or egg water (60 µg/ml sea salt, Sera Marin, Heinsberg, Germany), and staged by morphology (one-cell stage) for the injections. After each series of injections, the eggs were incubated at 28 °C (±0.5) and evaluated up to 5 days post-fertilization (dpf). Anaesthesia of larvae used for live imaging and COPAS analysis was done with 0.02% buffered Tricaine (3-aminobenzoic acid ethyl ester, Sigma-Aldrich) in egg water[37,40].

Ethics statement

The Luxembourg Centre for Systems Biomedicine is registered as an authorized breeder, supplier and user of zebrafish (*Danio rerio*) with Grand-Ducal decree of 20 January 2016. Zebrafish lines used at the Institute of Biology, Leiden University were handled in compliance with local animal welfare regulations as overseen by the Animal Welfare Body of Leiden University (license number: 10612). All practices involving zebrafish were performed in accordance with European laws, guidelines and policies for animal experimentation, housing and care (European Directive 2010/63/EU on the protection of animals used for scientific purposes). The present study did not involve any procedures within the meaning of Article 3 of Directive 2010/63/EU and as such it is not subject to authorization by an ethics committee.

Morpholino antisense oligonucleotide

The translation blocking morpholino for *slc45a2* (solute carrier family 45 member 2) was obtained from Gene Tools according to Dooley *et al*., 2012 with the following sequence: 5'-GCTGGTCCTCAGTAAGAAGAGTCAT-3' [41]. In addition, a 3' fluorescein modification was included, which allowed fluorescent differentiation of injected eggs. A standard MO with sequence 5'-CCTCTTACCTCAGTTACAATTTATA-3' was used as an injection control. In both cases, stock solutions (1 mM ~ 8 ng/nL) were prepared according to the specifications of the provider and titrated working solutions were freshly prepared for each experiment.

Preparation of Cas9 mRNA, slc45a2 sgRNA and DNA construct

Both *slc45a2* sgRNA and Cas9 mRNA were prepared according to Gagnon *et al*., 2014[34]. Briefly, the *slc45a2* DNA template was synthetized with T4 DNA polymerase (New England BioLabs) using the oligonucleotides: *slc45a2*-specific (taa tac gac tca cta taG GTT TGG GAA CCG GTC TGA Tgt ttt aga gct aga aat agc aag) and constant (AAA AGC ACC GAC TCG GTG CCA CTT TTT CAA GTT GAT AAC GGA CTA GCCTTA TTT TAA CTT GCT ATT TCT AGC TCT AAA AC). The sgRNA was synthetized using T7 RNA polymerase (Ambion MEGAscript) and then diluted to 400 ng/µl. Cas9 mRNA was synthetized using the pCS2-Cas9 plasmid[42], transcribed using the SP6 mMessage mMachine kit (Ambion) and finally diluted to 600 ng/µl.

The DNA plasmid was constructed using standard methods[43]. Briefly, a GFP reporter (*Tol*2kit construct 389) and mCherry reporter (*Tol*2kit construct 233) expressed under a constitutive promoter (*Tol*2kit construct 299) was constructed (final construct actb:-NLSmCherry-IRES-GFP) in the Gateway *Tol*2 vector (pDestTol2pA2). The plasmid was transfected in *E. coli*, isolated from an overnight liquid culture and diluted to 25 ng/µl. The *Tol*2 transposase RNA was synthetized using SP6 RNA polymerase (Ambion mMESSAGE mMACHINE) and then diluted to 25ng/µl.

Manual microinjections

Manual microinjections of *slc45a2*-MO, *slc45a2* sgRNA/Cas9 and the DNA construct in zebrafish embryos were performed following standard methods using Eppendorf FemtoJet microinjectors and both in-house pulled needles, prepared with thin-wall capillaries (World Precision Instruments) and a P-1000 Micropipette Puller (Sutter

Instrument, USA), and commercially available ready-to-use 10 μm tip needles (Qvotek, Mississauga, Canada)[19,44]. The needles for each round of injections were calibrated according to well-established methods using a stage micrometer slide (Carl Zeiss)[19]. Ultimately, the required bolus size for injection was achieved and controlled by regulating the pressure in the microinjector. After each series of microinjections, the embryos were incubated at 28 °C (±0.5) and evaluated daily until 5 dpf to record non-viable embryos, (*i.e.* non-fertilized, fluorescent negative, dead and dysmorphic embryos/larvae from 1 to 5 dpf), and the efficiency of injection. Table 1 shows the specifications of the different types of manual injections that were performed in this study.

	slc45a2 MO & control MO	*slc45a2* gRNA + Cas9 RNA	DNA construct + *Tol2* RNA
Injection type	Manual	Manual	Manual
Developmental stage at injection	One- to two-cell	One-cell	One-cell
Injection location	Middle of the yolk	Middle of the yolk	Blastomere/yolk boundary
Sample concentration	230 μM	400 ng/μL + 600 ng/μL	25 ng/μL + 25 ng/μL
Injection volume	2 nL	4 nL	1 nL
Injection time(per 100 embryos)	P1: 5 min P2: 3 min	P1: 17 min P2: 10 min P3: 19 min	P4: 4 min
Microinjector type	EppendorfFemtoJet 4X	EppendorfFemtoJet 4X	Eppendorf FemtoJet
Evaluation lapse	From 6 hpf to 5 dpf	From 6 hpf to 5 dpf	From 6 hpf to 5 dpf
Sorting criteria	GFP positive and albino phenotype	Albino phenotype	GFP positive
Exclusion criteria	Non-fertilized, GFP negative, dysmorphic and dead embryos / larvae	Non-fertilized, no albino phenotype, dysmorphic and dead embryos / larvae	Non-fertilized, GFP negative, dysmorphic and dead embryos / larvae
Place of the experiments	LCSB	LCSB	Leiden University

Table 1. Technical specification for the manual microinjections
Abbreviations: P1, experienced experimentalist; P2, expert experimentalist; P3, novice experimentalist; P4, experienced experimentalist; hpf, hours post-fertilization; dpf, days post-fertilization; GFP, green fluorescent protein.

Automated microinjections

Automated microinjections of *slc45a2*-MO, *slc45a2* sgRNA/Cas9 and the DNA construct in zebrafish embryos were performed using the robotic injector (Life Science Methods BV) following guidelines described in Spaink *et al*. 2013[38]. Briefly, all components of the robotic injector are connected to a controlling computer that is equipped with a software control program written in Python. The robot uses Eppendorf FemtoJet 4X microinjectors in combination with both in-house pulled needles and commercially available ready-to-use 10 μm tip needles as described in the section above. The established parameters for each needle (*i.e.* pressure and time) were then used for the microinjector linked to the robot injector. Zebrafish embryos were carefully arranged in each well of a 1% agarose covered grid (9 blocks x 100 wells) with the help of an artist brush. Particularly for RNA injections, each embryo was also oriented (with the artist brush) to put the one-cell visible for injection. The grid was then placed in the motorized stage coupled to a controlled and motorized micro-manipulator. After the

robotic injector was properly set (position of grid and needle) automated injections occurred at high speed (Table 2). For RNA and DNA injections in the robotic injector we used an image classification algorithm (see section below) to recognize each embryo *i.e.* "First-cell", "No-cell", "Empty", "Two-Cell", and "Sick", and to decide if triggering an injection. The total count of injected embryos (*i.e.* classified as "First-cell" and "No-cell") and of non-injected wells (classified as "Empty", "Two-Cell", and "Sick") was obtained at the end of each injection round. After each series of microinjections, the embryos were incubated at 28 °C (±0.5) and evaluated daily until 5 dpf to record non-viable embryos, (*i.e.* non-fertilized and fluorescent negative at 6 hpf, dead and dysmorphic embryos/larvae from 1 to 5 dpf), and the efficiency of injection. Table 2 shows the specifications of the different types of automated injections that were performed in this study.

	slc45a2 MO & control MO	*slc45a2* gRNA + Cas9 RNA	DNA construct + *Tol2* RNA
Injection type	Automated	Automated	Automated
Developmental stage at injection	One- to two-cell	One-cell	One-cell
Injection location	Middle of the yolk	Depending on image classification	Depending on image classification
Injection volume	2 nL	4 nL	1 nL
Injection concentration	230 µM	400 ng/µL + 600 ng/µL	25 ng/µL + 25 ng/µL
Microinjector type	Robotic injector + Eppendorf FemtoJet 4X	Robotic injector + Eppendorf FemtoJet 4X	Robotic injector + Eppendorf FemtoJet 4X
Injection time (per 100 embryos)	2 – 3 minutes	3 minutes	3 minutes
Evaluation lapse	From 6 hpf to 5 dpf	From 6 hpf to 5 dpf	From 6 hpf to 5 dpf
Sorting criteria	GFP positive and albino phenotype	Albino phenotype	GFP positive
Exclusion criteria	Non-fertilized, GFP negative, dysmorphic and dead embryos / larvae	Non-fertilized, no albino phenotype, dysmorphic and dead embryos / larvae	Non-fertilized, GFP negative, dysmorphic and dead embryos / larvae
Place of the experiments	LCSB	LCSB	Leiden University

Table 2. Technical specifications for the automated microinjections
Abbreviations: hpf, hours post-fertilization; dpf, days post-fertilization; GFP, green fluorescent protein.

Deep learning algorithm for image classification

As a first step we used the Inception v3 network to learn to distinguish between five different categories: "Empty", "No-Cell", "First-Cell", "Two-Cell", "Sick" (this term is used to refer to non-viable eggs). We used a total of 11,000 annotated images. To prevent overfitting, we artificially increased the number of training samples by performing four types of image transformation: *1)* rotations about the center of the image; *2)* zooming by a factor 0.9-1.1; *3)* shifting by 28 pixels orthogonally in the +/- x and y direction, and *4)* flipping the image horizontally. The neural network architecture consisted of: *1)* the top part of the Inception v3 network (containing all inception blocks); *2)* a 2D global spatial average pooling layer; *3)* a fully connected layer of 1024 nodes with ReLU activation function, and *4)* a fully connected layer of 5 nodes, with softmax activation function. Training of the classification step was done using the Adam stochastic optimizer[45], with a learning rate of 10^{-4}. For a more in-depth description see S1 Text.

Deep learning algorithm for finding the injection site

For the injection point determination, we translated the (x y) coordinates to a vector in a triangular mesh using a barycentric coordinate system. We let the outputs of the neural net correspond to vertices in the mesh. In our case, we used 160 vertices.

The neural network architecture consists of: *1)* the top part of the Inception v3 network (containing all inception blocks); *2)* a 2D global spatial average pooling layer; *3)* a fully connected layer of 1024 nodes with ReLU activation function, and *4)* a fully connected layer of 160 nodes, with softmax activation function. We used 2724 images for training and 674 images for validation (these are the same images as used for label "first-cell" in the classification step). Training of the injection point determination step was done using the Adam optimizer, with a learning rate varying from 10^{-3} to 10^{-5}. More details can be found in S1 Text.

Software and hardware

For deep learning and robot control we used a Shuttle SZ170R8 equipped with an Intel Core i3 6100 CPU, 16 GB kit Kingston DDR4 2133Mhz, ECC memory and an NVidia GeForce GTX 1070 GPU. Installed software are: Keras 1.2.2, Theano 0.9.0, NumPy 1.11.0, SciPy 0.17.0. For the analysis of the data, raw data for all the series of microinjections was processed in excel. Statistical analysis was done using excel and GraphPad Prism 6 followed by unpaired *t*-test with Welch's correction for single comparisons (when applicable). The criterion for statistical significance was $P < 0.05$. Graphs were plotted using GraphPad Prism 6 and error bars on all graphs represent standard deviation.

Microscopy and fluorescent analysis

At the Institute of Biology, Leiden University, representative pictures were taken using a Leica M205 FA stereo fluorescence microscope equipped with a DFC345 FX monochrome camera. Fluorescent signal was quantified using a Complex Object Parameter Analyzer and Sorter (COPAS, Union Biometrica). At the Luxembourg Centre for Systems Biomedicine, fluorescent sorting of fluorescein positive embryos (for *slc45a2*-MO injections) was done using a Nikon SMZ25 stereomicroscope. Representative pictures of control larvae and injected larvae displaying an albino phenotype were taken using the Nikon SMZ25 stereomicroscope equipped with a Nikon Digital Sight DS-Ri1 camera

Supplementary information

S1 Text. Deep learning supplement.
S1 File. Movie demonstrating robotic injections with deep learning.
S2 File. Demo source code and demo images.
S3 File. Data set used for plotting the graphs.

The supporting information can be found here:
https://doi.org/10.1371/journal.pone.0202377

References

1. Kimmel CB, Warga RM, Schilling TF. Origin and organization of the zebrafish fate map. Development. 1990; 108(4): 581-594.

2. Takaki K, Davis JM, Winglee K, Ramakrishnan L. Evaluation of the pathogenesis and treatment of Mycobacterium marinum infection in zebrafish. Nature protocols. 2013; 8(6): 1114-1124.

3. Lin S, Long W, Chen J, Hopkins N. Production of germ-line chimeras in zebrafish by cell transplants from genetically pigmented to albino embryos. Proceedings of the National Academy of Sciences. 1992; 89(10): 4519-4523.

4. Jung DW, Oh ES, Park SH, Chang YT, Kim CH, Choi SY, et al. A novel zebrafish human tumor xenograft model validated for anti-cancer drug screening. Molecular BioSystems. 2012; 8(7): 1930-1939.

5. Nicoli S, Presta M. The zebrafish/tumor xenograft angiogenesis assay. Nature protocols. 2007; 2(11): 2918-2923.

6. Nasevicius A, Ekker SC. Effective targeted gene 'knockdown' in zebrafish. Nature genetics. 2000; 26(2): 216- 20.

7. Toyama R, O'Connell ML, Wright CV, Kuehn MR, Dawid IB. Nodal induces ectopic goosecoid and lim1 expression and axis duplication in zebrafish. Development. 1995; 121(2): 383-391.

8. Suster ML, Kikuta H, Urasaki A, Asakawa K, Kawakami K. Transgenesis in zebrafish with the tol2 transposon system. Transgenesis Techniques: Principles and Protocols. 2009: 41-63.

9. Braunbeck T, Boettcher M, Hollert H, Kosmehl T, Lammer E, Leist E, et al. Towards an alternative for the acute fish LC(50) test in chemical assessment: the fish embryo toxicity test goes multi-species -- an update. ALTEX. 2005; 22: 87-102.

10. Veneman W, Spaink HP, Brun NR, Bosker T, Vijver M. Pathway analysis of systemic transcriptome responses to injected polystyrene particles in zebrafish larvae. Aquatic Toxicology. 2017; 190: 112-120.

11. Hague E, Ward AC. Zebrafish as a model to evaluate nanoparticle toxicity. Nanomaterials. 2018; 8: 1-18.

12. Chen L, Watson C, Morsch M, Cole NJ, Chung RS, Saunders DN, et al. Improving the delivery of SOD1 antisense oligonucleotides to motor neurons using calcium phosphate-lipid nanoparticles. Frontiers in Neuroscience. 2017; 11: 1-12.

13. Craig MP, Gilday SD, Dabiri D, Hove JR. An optimized method for delivering flow tracer particles to intravital fluid environments in the developing zebrafish. Zebrafish. 2012; 9: 108-119.

14. Kaethner RJ, Stürmer C. Dynamics of process formation during differentiation of tectal neurons in embryonic zebrafish. Journal of Neurobiology. 1997; 32(6): 627-639.

15. Van Asselt E, De Graaf F, Smit-Onel MJ, Van Raamsdonk W. Spinal neurons in the zebrafish labeled with fluoro-gold and wheat-germ agglutinin. Neuroscience. 1991; 43(2): 611-622.

16. Stainier DY, Lee RK, Fishman MC. Cardiovascular development in the zebrafish. I. Myocardial fate map and heart tube formation. Development. 1993; 119(1): 31-40.

17. Kim CH, Bae YK, Yamanaka Y, Yamashita S, Shimizu T, Fujii R, et al. Overexpression of neurogenin induces ectopic expression of HuC in zebrafish. Neuroscience letters. 1997; 239(2): 113-116.

18. Gore AV, Maegawa S, Cheong A, Gilligan PC, Weinberg ES, Sampath K. The zebrafish dorsal axis is apparent at the four-cell stage. Nature. 2005; 438(7070): 1030-1035.

19. Rosen JN, Sweeney MF, Mably JD. Microinjection of zebrafish embryos to analyze gene function. Journal of visualized experiments: JoVE. 2009 (25).

20. Eisen JS, Smith JC. Controlling morpholino experiments: don't stop making antisense. Development. 2008; 135(10): 1735-1743.

21. Kok FO, Shin M, Ni CW, Gupta A, Grosse AS, van Impel A, et al. Reverse genetic screening reveals poor correlation between morpholino-induced and mutant phenotypes in zebrafish. Developmental cell. 2015; 32(1): 97-108.

22. Rossi A, Kontarakis Z, Gerri C, Nolte H, Hölper S, Krüger M, et al. Genetic compensation induced by deleterious mutations but not gene knockdowns. Nature. 2015; 524(7564): 230-233.

23. Stainier DY, Kontarakis Z, Rossi A. Making sense of anti-sense data. Developmental cell. 2015; 32(1): 7-8.

24. Stainier DY, Raz E, Lawson ND, Ekker SC, Burdine RD, Eisen JS, et al. Guidelines for morpholino use in zebrafish. PLOS Genetics. 2017; 13(10): e1007000. doi: 10.1371/journal.pgen.1007000

25. Urnov FD, Rebar EJ, Holmes MC, Zhang HS, Gregory PD. Genome editing with engineered zinc finger nucleases. Nature Reviews Genetics. 2010; 11(9): 636-646.

26. Hwang WY, Peterson RT, Yeh JR. Methods for targeted mutagenesis in zebrafish using TALENs. Methods. 2014; 69(1): 76-84.

27. Jinek M, Chylinski K, Fonfara I, Hauer M, Doudna JA, Charpentier E. A programmable dual-RNA–guided DNA endonuclease in adaptive bacterial immunity. Science. 2012; 337(6096): 816-821.

28. Mali P, Yang L, Esvelt KM, Aach J, Guell M, DiCarlo JE, et al. RNA-guided human genome engineering via Cas9. Science. 2013; 339(6121): 823-826.

29. Hwang WY, Fu Y, Reyon D, Maeder ML, Tsai SQ, Sander JD, et al. Efficient genome editing in zebrafish using a CRISPR-Cas system. Nature biotechnology. 2013; 31(3): 227-229.

30. Sander JD, Joung JK. CRISPR-Cas systems for editing, regulating and targeting genomes. Nature biotechnology. 2014; 32(4): 347-355.

31. Auer TO, Del Bene F. CRISPR/Cas9 and TALEN-mediated knock-in approaches in zebrafish. Methods. 2014; 69(2): 142-150.

32. Clark KJ, Voytas DF, Ekker SC. A TALE of two nucleases: gene targeting for the masses?. Zebrafish. 2011; 8(3): 147-149.

33. Foley JE, Yeh JR, Maeder ML, Reyon D, Sander JD, Peterson RT, et al. Rapid mutation of endogenous zebrafish genes using zinc finger nucleases made by Oligomerized Pool ENgineering (OPEN). PloS one. 2009; 4(2):e4348. doi: 10.1371/journal.pone.0004348

34. Gagnon JA, Valen E, Thyme SB, Huang P, Ahkmetova L, Pauli A, et al. Efficient mutagenesis by Cas9 protein-mediated oligonucleotide insertion and large-scale assessment of single-guide RNAs. PloS one. 2014; 9(5):e98186. doi: 10.1371/journal.pone.0098186

35. Gupta A, Hall VL, Kok FO, Shin M, McNulty JC, Lawson ND, et al. Targeted chromosomal deletions and inversions in zebrafish. Genome research. 2013; 23(6): 1008-1017.

36. Wang W, Liu X, Gelinas D, Ciruna B, Sun Y. A fully automated robotic system for microinjection of zebrafish embryos. PloS one. 2007; 2(9):e862.

37. Carvalho R, de Sonneville J, Stockhammer OW, Savage ND, Veneman WJ, Ottenhoff TH, et al. A high-throughput screen for tuberculosis progression. PloS one. 2011; 6(2):e16779. doi: 10.1371/journal.pone.0016779.

38. Spaink HP, Cui C, Wiweger MI, Jansen HJ, Veneman WJ, Marín-Juez R, et al. Robotic injection of zebrafish embryos for high-throughput screening in disease models. Methods. 2013; 62(3): 246-254.

39. Westerfield, M. The zebrafish book. A guide for the laboratory use of zebrafish (Danio rerio). 4th ed., Univ. of Oregon Press, Eugene. 2000

40. Dove A. Screening for content—the evolution of high throughput. Nature biotechnology. 2003; 21(8): 859-864.

41. Dooley CM, Schwarz H, Mueller KP, Mongera A, Konantz M, Neuhauss S, et al. Slc45a2 and C-ATPase are regulators of melanosomal pH homeostasis in zebrafish, providing a mechanism for human pigment evolution and disease. Pigment Cell Melanoma Res. 2012; 26: 205-217.

42. Irion U, Krauss J, Nüsslein-Volhard C. Precise and efficient genome editing in zebrafish using the CRISPR/Cas9 system. Development. 2014; 141, 4827-4830.

43. Kwan KM, Fujimoto E, Grabher C, Mangum BD, Hardy ME, Campbell DS, et al. The Tol2kit: A multisite gateway-based construction kit for Tol2 transposon transgenesis construct. Developmental Dynamics. 2007; 11: 3088-3099.

44. Lieschke G. Zebrafish: Methods and Protocols. Springer protocols, Heidelberg. 2008.

45. Kingma D, Ba J. Adam: A method for stochastic optimization. arXiv:1412.6980. 2014.

46. Szegedy C, Vanhoucke V, Ioffe S, Shlens J, Wojna Z. Rethinking the inception architecture for computer vision. In Proceedings of the IEEE Conference on Computer Vision and Pattern Recognition 2016; 2818-2826.

47. LeCun Y, Bengio Y, Hinton G. Deep learning. Nature. 2015; 521(7553): 436-444.

48. Ungar AA. Barycentric calculus in Euclidean and hyperbolic geometry: A comparative introduction. 2010.

49. Hruscha A, Krawitz P, Rechenberg A, Heinrich V, Hecht J, Haass C, et al. Efficient CRISPR/Cas9 genome editing with low off-target effects in zebrafish. Development. 2013; 140(24): 4982-4987.
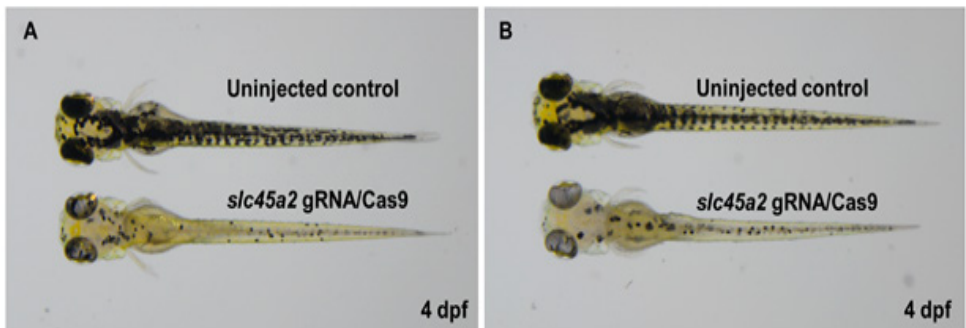
Supplementary figures
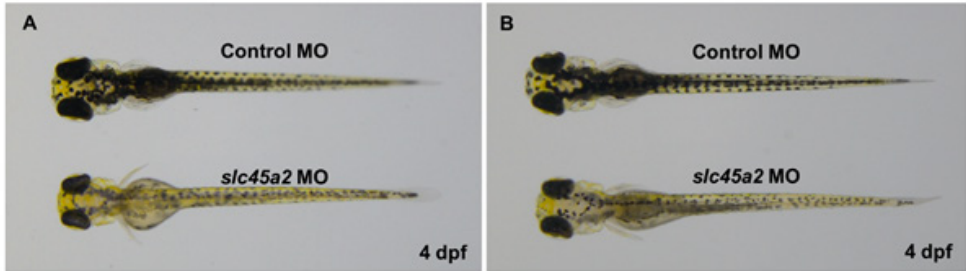
Figure S1. Representative images of manual and automated yolk injections with *slc45a2* morpholino.
The images show four days post-fertilization (dpf) larvae that were injected manually (A) or injected by the automated robot (B) with control morpholino (top) and *slc45a2* morpholino (bottom). In both cases the albino phenotype is evident in the morphant larvae (bottom), in which pigmentation is significantly reduced compared to the control morpholino (top).
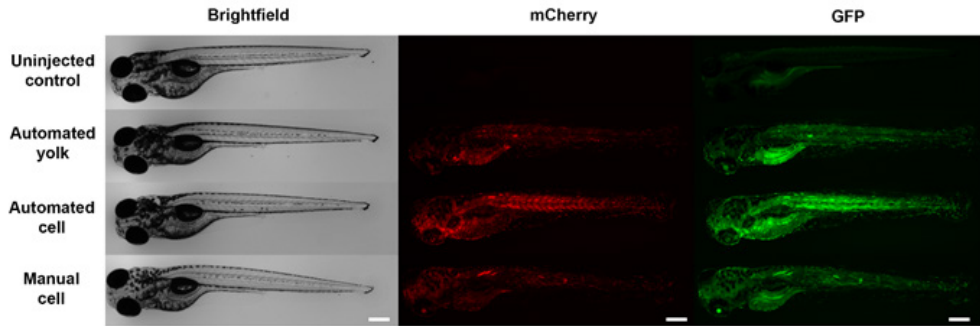
Figure S2. Representative images of manual and automated injections with (*act:*-NLSmCherry-IRES-GFP) *Tol2* construct.
The images show five days post-fertilization (dpf) larvae that were subjected to manual cell injections or automated yolk or cell injections with a (*act:*-NLSmCherry-IRES-GFP) *Tol2* DNA construct and *Tol2* transposase RNA. In all three cases the phenotype is evident as fluorescent signal is significantly increased compared to the uninjected control (top row). White scale bar = 250μm.

Figure S3. Representative images of manual and automated cell injections with *slc45a2* gRNA/Cas9.
The images show four days post-fertilization (dpf) larvae that were subjected to manual cell injections (A) or automated cell injections (B) with *slc45a2* gRNA/Cas9. In both cases the albino phenotype (bottom) is evident as pigmentation is significantly reduced compared to the uninjected controls (top).

3

Identifying host-directed therapeutics against tuberculosis in the zebrafish model

Ralf Boland[1], Michiel van der Vaart[1], Matthias Heemskerk[2], Tom Ottenhoff[2], Herman P. Spaink[1], Annemarie H. Meijer[1]

1. Institute of Biology Leiden, Leiden University, Leiden, The Netherlands
2. Department of Infectious Diseases, Leiden University Medical Center, Leiden, The Netherlands

Abstract

Tuberculosis (TB) remains a global health threat to date, in part because of the rise in multi-drug-resistant *Mycobacterium tuberculosis* (*Mtb*) strains. Host-directed therapeutics (HDTs), currently under investigation as adjunctive therapy for TB, aim to increase the ability of the host-immune system to resist the infection. HDTs have the potential to shorten treatment length with conventional antibiotics and combat multi-drug-resistant TB (MDR-TB). While screens for HDTs using cultured cells can be performed at high-throughput level, the rate limiting step is subsequent validation in whole organism models to translate results to clinical applications. The zebrafish model fills the gap between *in vitro* research and mammalian animal models and is therefore a useful intermediate for translational research. In this study we evaluated a preselected set of compounds with demonstrated anti-TB activity in human cells for a host-directed effect against mycobacterial infection using the zebrafish embryo model for TB. In this well-established model, zebrafish embryos are infected with *Mycobacterium marinum* (*Mm*), a close relative of *Mtb* that displays similar pathogenesis in its poikilothermic hosts. We optimized the infection protocol to determine the most suitable screening conditions. Subsequently, we performed a pilot screen of potential anti-TB HDTs and found Trifluoperazine, Amiodarone-HCl and Tamoxifen-citrate to be effective in the zebrafish model for TB, showing that these compounds not only have anti-TB activity in *Mtb*-infected human macrophages but also in a whole organism test system.

Introduction

Ever advancing technological possibilities have greatly facilitated large-scale *in vitro* screens aimed at the identification of new drugs or cellular pathways as therapeutic targets. An increasing number of screens are performed for a wide range of applications, for example the treatment of cancer and infectious diseases, such as tuberculosis (TB)[1–4]. Furthermore, it has become common practice to re-screen available compound libraries, including FDA-approved compounds, in an effort to repurpose compounds used in therapies for different diseases or not having passed phase-II clinical trials for the disease that they were originally intended for[5–8]. However, research using a whole organism model is always needed to validate discoveries from these *in vitro* screens because disease phenotypes generally result from complex interactions between different cell types. In addition, toxic effects and pharmacokinetics are difficult to assess *in vitro*[9,10]. Furthermore, using a whole organism model could lead to discoveries that would be missed using only *in vitro* screening methods, because of the context of cellular cross-talk in tissues or elaborate pathogen-host dynamics not present when only screening in one cell type. While mammalian models are of great importance for translating research results to clinical applications, the zebrafish model is an effective intermediate for translational research, filling the gap between *in vitro* research and mammalian models[11].

The zebrafish has emerged as an alternative whole organism vertebrate model with a wide range of possibilities, especially for intravital imaging, genetics, and drug efficacy screening. Originally the zebrafish was mainly used to study embryonic development, but since the start of this century it has become a widely used model to study mechanisms of disease, genetic disorders and behavior[12]. Furthermore, many countries have accepted zebrafish as an alternative animal model to study toxicity, in an effort to reduce the number of higher vertebrates used for mandatory safety assessments of chemicals (e.g. in the EU: OECD236 2013).

The popularity of the zebrafish model is easily explained. This small sub-tropical fish can be kept in facilities capable of housing many more animals in the same space

as would be required for mammalian models. They reach a sexual reproductive age in 2 to 3 months. Zebrafish pairs can be crossed every week and a single pair can yield hundreds of eggs in one crossing. The external embryonic development makes the zebrafish highly suitable for experimental manipulation[11]. Genetic modification is performed conveniently by injecting DNA constructs or knockdown/knockout reagents into the zebrafish eggs at the one-cell stage. Owing to these advantages, the zebrafish research community has generated a large number of knock-out as well as transgenic reporter lines, and with technologies such as CRISPR-Cas, the possibilities for genetic interventions have greatly improved[11,13]. Furthermore, temporary knock-down can easily be achieved, for example using synthetic morpholino oligomers[14].

The possibilities of the zebrafish model for various applications, including drug screening, are optimal at the embryonic and larval stages. The zebrafish embryo has a functioning innate immune system as early as 1 day post fertilization (dpf), while it takes at least 3 weeks for the adaptive immune system to fully mature[15]. This means that the early life stages that are extensively used for biomedical research are representative for innate immunity only, thus providing an *in vivo* model to study this branch of the immune system in separation from adaptive immunity[16]. This is especially useful for understanding the interactions between pathogens and phagocytes during the early stages of infection. Furthermore, the transparency of the embryos and larvae, especially when combined with cell lineage-specific promotors driving fluorescent reporters, make zebrafish ideal for real-time fluorescent microscopy studies into cellular and pathogen-host dynamics *in vivo*[17–20].

The aim of this study was to utilize the zebrafish embryo model to screen for potential new host-directed therapeutics (HDTs) for infectious diseases caused by intracellular pathogens. HDTs are drugs that increase the ability of the host's immune system to combat (intracellular) pathogens[21,22]. As such, HDTs could provide an alternative for treatment of antibiotic-resistant infections or be used as adjunctive therapy to enhance the efficacy of antibiotic treatment[23,24]. In our study we infected zebrafish embryos with the intracellular pathogen *Mycobacterium marinum*, which is widely used as a model for TB, caused by its close relative *Mycobacterium tuberculosis* (*Mtb*)[25–27]. TB is a global health threat and the most common cause of death from a single infectious agent, with 1.6 million deaths in 2017 (WHO global report 2018). HDT approaches have attracted much interest in the TB field due to the worrying rise of multiple drug resistant (MDR) strains of *Mtb*, which are unresponsive to several first- and second-line antibiotics. Because of the complex host-pathogen interplay during mycobacterial infection[28–31], the context of a whole organism will be a substantial factor in the translation from *in vitro* HDT screens to clinically relevant drugs. Here, we describe the development of several approaches, as well as identifying potential pitfalls, to screen for anti-TB HDTs using the zebrafish model. Furthermore, we report on results of a pilot screen where we test potential HDTs identified in *Mtb*-infected human macrophages and identify three HDTs effective in the zebrafish model for TB.

Results

Toxicity evaluation of potential anti-TB HDTs

In this study we evaluated the suitability of several *Mycobacterium marinum* (*Mm*) infection protocols for anti-TB drug screening. The list of compounds tested during the course of this study is shown in table 1. These compounds were selected based on previously demonstrated activity against *Mtb* in human MelJuSo cells and primary macrophages (Heemskerk *et al* – in preparation). Before testing compounds under infected conditions in zebrafish, we performed dose range studies to determine the maximum dose tolerated by embryos without induction of overt developmental aberrations. Several compounds induced developmental toxicity, such as oedema

and mortality (Table 1). This precluded us from testing approximately one third of the selected compounds. When subsequently applying non-toxic doses under infected conditions, we generally observed an increase of developmental toxicity. For example, the anti-psychotic drug haloperidol, which does not induce developmental toxicity in absence of infection at doses up to 30 µM, does induce developmental toxicity at this dose when combined with *Mm* infection (Figure 1A), indicating an additive effect of cellular stress caused by drug treatment and infection. It is not surprising that certain HDTs caused toxicity in the zebrafish embryo model for TB as the putative targets of these compounds could be involved in developmental pathways.

A
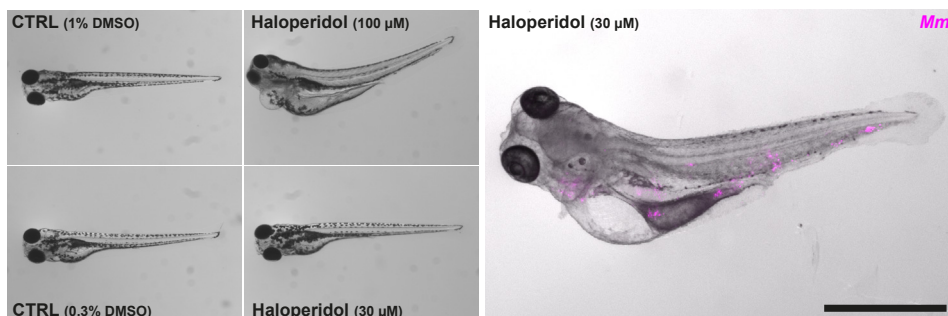
Figure 1. Toxic effects of HDTs are exacerbated by *Mm* infection.
A. Toxicity assay of uninfected and mCherry-expressing *Mm*-infected zebrafish larvae. Zebrafish larvae treated with Haloperidol at mid (30 µM) and high (100 µM) dose or control (DMSO at equal v/v). Treatment was started at 1 hpi and larvae were anesthetized at 4 dpi for imaging. Representative stereo fluorescent images of whole larvae. Right panel shows a larva infected with mCherry-expressing *Mm*. Magenta shows *Mm*. Scale bar annotates 2 mm.
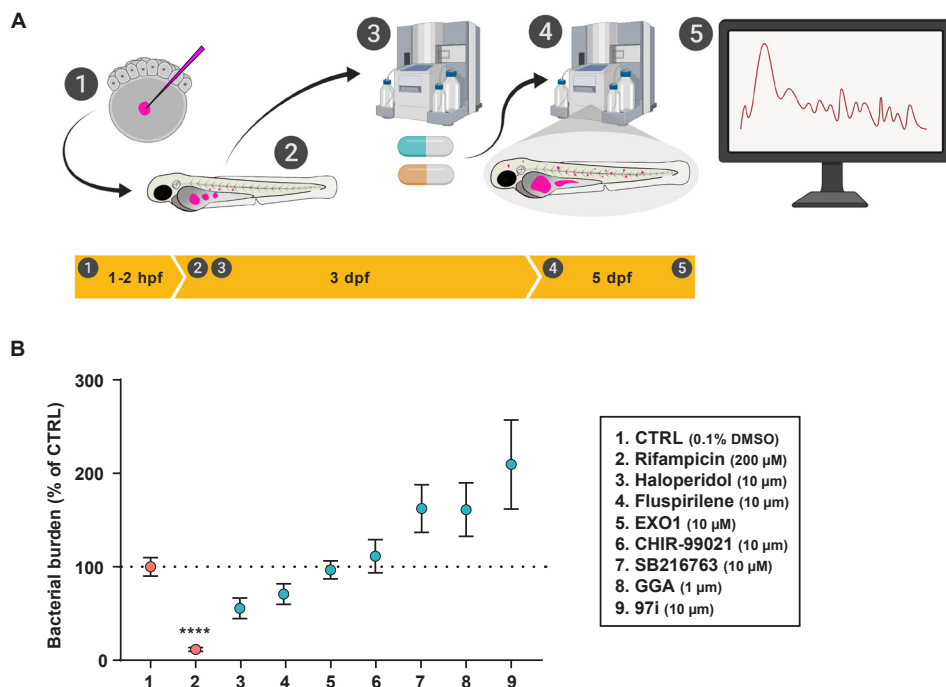
Evaluation of yolk infection and the COPAS system for HDT screens

We wanted to maximize the number of HDT compounds we could screen in a short period of time. For this purpose, we evaluated the Complex Object Parametric Analyser and Sorter (COPAS) system. This system can achieve mid- to high-throughput level in zebrafish embryo screens using fluorescent readouts[32]. Fertilized eggs were infected with *Mm* containing a fluorescent reporter construct at the 8 to 128 cell stage, using a previously described yolk injection route[33]. At 3 dpf, larvae were sorted using the COPAS system and any larvae with infection levels outside the predetermined range as measured by fluorescent readout were discarded. The range of infection level was determined based on a signal higher then background fluorescence of zebrafish larvae, while excluding larvae with a bacterial fluorescent signal above the COPAS detection limit. The remaining larvae were subsequently treated with compounds or vehicle control (DMSO solvent corresponding to the mass percent of the solvent in the final compound concentration) dissolved in the embryo medium (Instant Ocean Sea Salts in demi water). At 2 days post treatment (age 5 dpf), the larvae were again analysed with the COPAS system to quantify the fluorescent signal of *Mm*. By comparing fluorescent signal of the control treatment group to compound treated groups, we obtained a relative measure of bacterial burden and could determine effectiveness of the compound in reducing bacterial burden (Figure 2A). Using this method, we tested several compounds that were found effective in an *in vitro* screen performed on MelJuSo cells infected with *Mtb*, using the antibiotic rifampicin (200 µM) as a positive control for reduction of bacterial burden. We did not identify any compound that effectively reduced bacterial burden, while rifampicin was able to almost clear the infection (Figure 2B). This initial screen included 97i (Table 1), which *in vitro* is a more potent derivative of the kinase inhibitor H89, that has been reported as a potential HDT against *Mtb*[34].

Compound	Toxicity *in vivo* at 10µM dose	*in vivo Mm* screen
Kinase inhibitors		
H89		DoC, BI
97i		COPAS, DoC, BI
98t		
97q		
SB 216763		COPAS
CHIR-99021		COPAS
Imatinib		DoC
ENMD-2076	Oedema	DoC
Dovitinib	Slight oedema	DoC, BI
AT9283		DoC
Quizartinib	Slight oedema	DoC
PDGFR TKI III	Mortality	
GW 5074	Oedema, mortality	
Autophagy modulation		
Spautin-1	Mortality	
Carbamazepine		DoC
Tamoxifen citrate		BI
Amiodarone hydrochloride		BI
Pimozide		BI
Fluspirilene	Slight oedema	COPAS, DoC, BI
Deubiquitinase inhibitors		
M12 (quinazoline)		DoC, BI
C13		
E8		
Trifluoperazine (7994228)		DoC, BI
Chlorprothixene		
Dopamine receptor antagonist		
Haloperidol	Oedema (100n µM dose, excasterbated by *Mm*)	COPAS
Fluphenazine dihydrochloride		BI
cis-(Z)-Flupenthixol dihydrochloride	Mortality	
Golgi apparatus		
Golgicide A	Mortality	COPAS
Exo 1		COPAS
Other		
NBI-74330		DoC

Table 1. Overview of compounds tested
Abbreviations: DoC = Duct of Cuvier and BI = blood island

Figure 2. HDT screen using yolk infection and the COPAS system
A. Schematic overview of the experimental procedure of the HDT screen using the COPAS system. Injection of mCherry-expressing *Mm* in the yolk is performed at 8 to 128 cell stage (1). At 3 dpf bacterial burden of larvae are determined by fluorescent readout using the COPAS system (2). Subsequently, larvae are divided in groups and treated with compounds of interest or the control treatment (3). At 5 dpf the COPAS system is again used to determine bacterial burden based by fluorescent readout using the COPAS system (4). Fluorescent signal is obtained per larvae and is a measure of bacterial burden (5). Subsequently, the effect of different treatments on bacterial burden can be compared.
B. Bacterial burden assay of mCherry-expressing *Mm*-infected zebrafish larvae treated with compounds of interests, control treatment (DMSO at 0.1% v/v) or Rifampicin (200 µM) as a positive control for reduction of bacterial burden. Assay was performed as described in A. Normalized data of multiple experiments was included (n = 17-43 per group) and 1 representative control treatment (for both DMSO and Rifampicin) is shown. Dots show mean of each group and error bars indicate standard error of the mean. Statistical analysis was performed per experiment using a Kruskal-Wallis with Dunn's multiple comparisons test. (**** = $p < 0.0001$).

Establishment of Duct of Cuvier injection of *Mm* at 2 dpf

While the COPAS system is well suited for fluorescent analysis of zebrafish eggs, embryos and larvae, we did not detect positive effects of any of the HDTs we tested using the yolk infection model. We therefore decided to adopt the more frequently used intravenous infection route for HDT screening using injection into the duct of Cuvier, which leads to rapid phagocytosis of bacteria by macrophages and initiation of TB granuloma formation. Because this procedure is more time consuming than injection into the yolk, quantifying infection using stereo fluorescent microscopy was no longer the bottleneck of the experiment. We therefore replaced the COPAS system and reverted to the use of stereo fluorescent microscopy and fluorescent pixel-count analysis, which has previously been established as a reliable method to quantify infection burden[35]. In this manner we combined bacterial burden analysis with a visual inspection of the larvae for developmental toxicity. To minimize potential developmental toxicity, we decided on an infection timepoint at 2 dpf as opposed to the blood island infection method at 1 dpf used customly in the zebrafish embryo model for TB[36]. We infected 2 dpf embryos in the duct of Cuvier with *Mm*, divided them randomly over treatment groups and treated

with control or compound 1 hour post infection (hpi). At 3 dpi (5 dpf) we imaged the larvae and quantified fluorescent signal using pixel-count analysis (Figure 3A). The experimental end point was set at 5 dpf because of animal experimentation regulation. In light of the relatively short time frame available to assess the effect of a drug on the infection burden, we first assessed *Mm* inoculum doses for the 3 day infection period (Figure 3B). We concluded that a high inoculum dose (400 CFU) maximizes bacterial burden and therefore the potential infection reduction window after HDT compound treatment.

A pilot HDT screen using duct of Cuvier injection did not yield any hits

Having established the screening method by duct of Cuvier injection at 2 dpf, we tested several HDTs that reduced bacterial burden in an *in vitro* screen of MelJuSo cells infected with *Mtb* (Table 1). None of 12 compounds tested reduced bacterial burden in our *in vivo* model, while the antibiotic rifampicin was able to do so (Figure 3C). As H89 and 97i show a synergistic effect with antibiotics *in vitro* (Heemskerk *et al* - in preparation), we hypothesized that these HDTs could potentiate the host in a manner that weakened the bacteria but did not lead to a direct reduction in bacterial burden in our model. We decided to study if a synergistic effect with antibiotics could be achieved using these compounds in our *in vivo* model. Therefore, we treated infected embryos with H89 and 97i alone or in combination with a sub-optimal dose of rifampicin (10-fold lower; 20 μM). We tried a low and high dose of both H89 and 97i. To reduce potential toxic effects of the high doses in combination with Rifampicin, we reduced the treatment window to 2 days and measured bacterial burden at 2 dpi. Both doses of H89 (10 & 50 μM) alone did not reduce bacterial burden compared to control treatment. While a combinatorial treatment of H89 and rifampicin did reduce bacterial burden, the reduction was no greater than treatment with the low-dose rifampicin alone and both treatments did not reduce infection significantly (Figure 3D). Similarly, both doses of 97i (10 & 25 μM) did not reduce bacterial burden significantly, and the reduction in bacterial burden observed in the combinatorial treatment with rifampicin did not exceed treatment with low-dose rifampicin alone (Figure 3D). Although we screened compounds with known *in vitro* HDT potential, we could not confirm the anti-mycobacterial effects of these compounds in our *in vivo* model using the 2 dpf duct of Cuvier infection method.
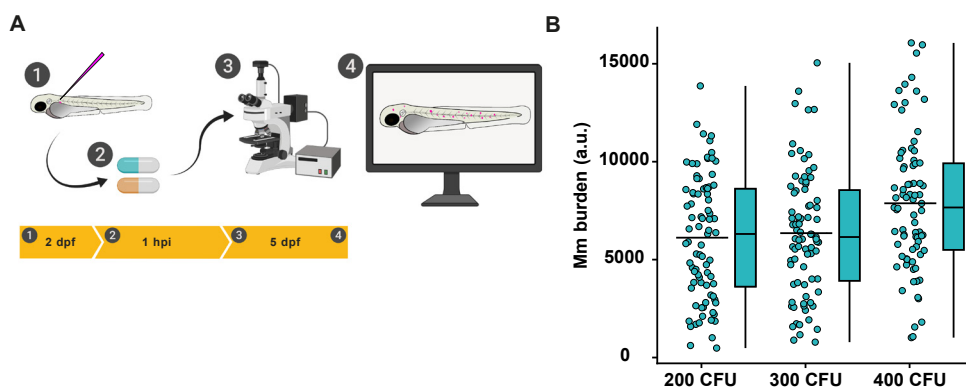
Figure 3. HDT screen using Duct of Cuvier infection
A. Schematic overview of the experimental procedure of the HDT screen using DoC infection. Infection of mCherry-expressing *Mm* in the DoC is performed at 2 dpf (1). Treatment was started at 1 hpi (2) and at 3 dpi larvae were anesthetized and subsequently imaged using a stereo fluorescent microscope (3). Fluorescent signal is obtained per larvae and is a measure of bacterial burden (4). Quantification of fluorescent signal is performed using pixel count analysis.
B. Quantification of bacterial burden as described in A. Infection was performed using an inoculum with increasing CFU. Data of 4 experimental repeats were combined (n = 80-83 per group). Each dot represents a single larva. Boxplots with 95% confidence intervals are shown and the black line in the boxplots and percentage indicates the group median, while the black line in the dot plot indicates the group mean.

C

1. CTRL (0.25% DMSO)
2. Rifampicin (200 µM)
3. Dovitinib (10 µM)
4. Imatinib (25 µM)
5. ENMD-2076 (10 µM)
6. AT9283 (10 µM)
7. Fluspirilene (6.5 µM)
8. NBI-74330 (25 µM)
9. Quizartinib (10 µM)
10. Carbamazepine (10 µM)
11. 7994228 (10 µM)
12. M12 (10 µM)
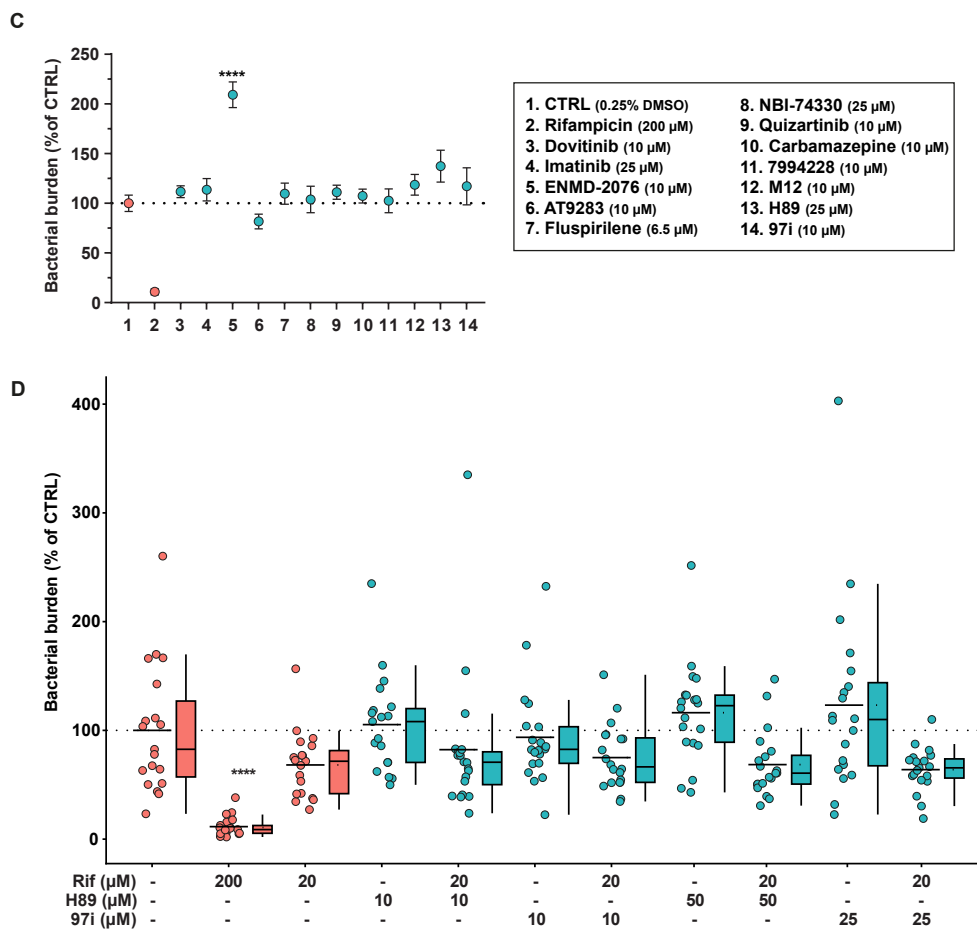13. H89 (25 µM)
14. 97i (10 µM)

D

Figure 3. (continued)
C. Bacterial burden assay of mCherry-expressing *Mm*-infected zebrafish larvae treated with compounds of interests, control treatment (DMSO at 0.25% v/v) or Rifampicin (200 µM) as a positive control for reduction of bacterial burden. Assay was performed as described in A. Normalized data of multiple experiments was included (n = 20-31 per group) and 1 representative control treatment (for both DMSO and Rifampicin) is shown. Dots show mean of each group and error bars indicate standard error of the mean. Statistical analysis was performed per experiment using a Kruskal-Wallis with Dunn's multiple comparisons test.
D. Bacterial burden assay of mCherry-expressing *Mm*-infected zebrafish larvae treated with compounds of interests (H89 and 97i) combined with a low dose of Rifampicin (20 µM), control treatment (DMSO at 0.5% v/v) or Rifampicin (200 µM) as a positive control for reduction of bacterial burden. Assay was performed as described in A except the endpoint of the experiment is 2 dpi. Each dot represents a single larva (n = 19-20 per group). Boxplots with 95% confidence intervals are shown and the black line in the boxplots and percentage indicates the group median, while the black line in the dot plot indicates the group mean. Statistical analysis was performed per experiment using a Kruskal-Wallis with Dunn's multiple comparisons test. (**** = p<0.0001).

H89 and 97i do not reduce *Stm* burden in zebrafish

As H89 and 97i did not reduce *Mm* bacterial burden in our zebrafish embryo model for TB, we decided to look at *Salmonella* Typhimurium (*Stm*), another intracellular pathogen causing human disease for which zebrafish embryos and larvae are used as an animal model[37–39]. Previously, H89 and 97i were described to also be effective against *Stm* infection (Heemskerk *et al* – in preparation)[34]. We infected 2 dpf zebrafish embryos with 150 CFU of *Stm*, divided the embryos randomly in treatment groups and treated with control or H89 (25 µM) by adding it to the embryo medium. At 24 and 48 hpi we plated

diluted embryo extractions to get a readout of *Stm* infection burden as measured by colony counting (Figure 4A). We did not find any differences in the number of grown colonies after treatment with H89 at 24 hpi (Figure 4B). Although we did find a significant difference at 48 hpi, at this timepoint most larvae had succumbed to the infection and subsequently died in both the control treated and H89 treated group (Figure 4B). We also injected the compounds directly into the duct of Cuvier to see if this compound delivery method would be more effective than immersion treatment, using a similar approach as described above (Figure 4A). We injected H89 and 97i at high doses (5mM) in the infected zebrafish embryos to get to a tissue concentration around the desired
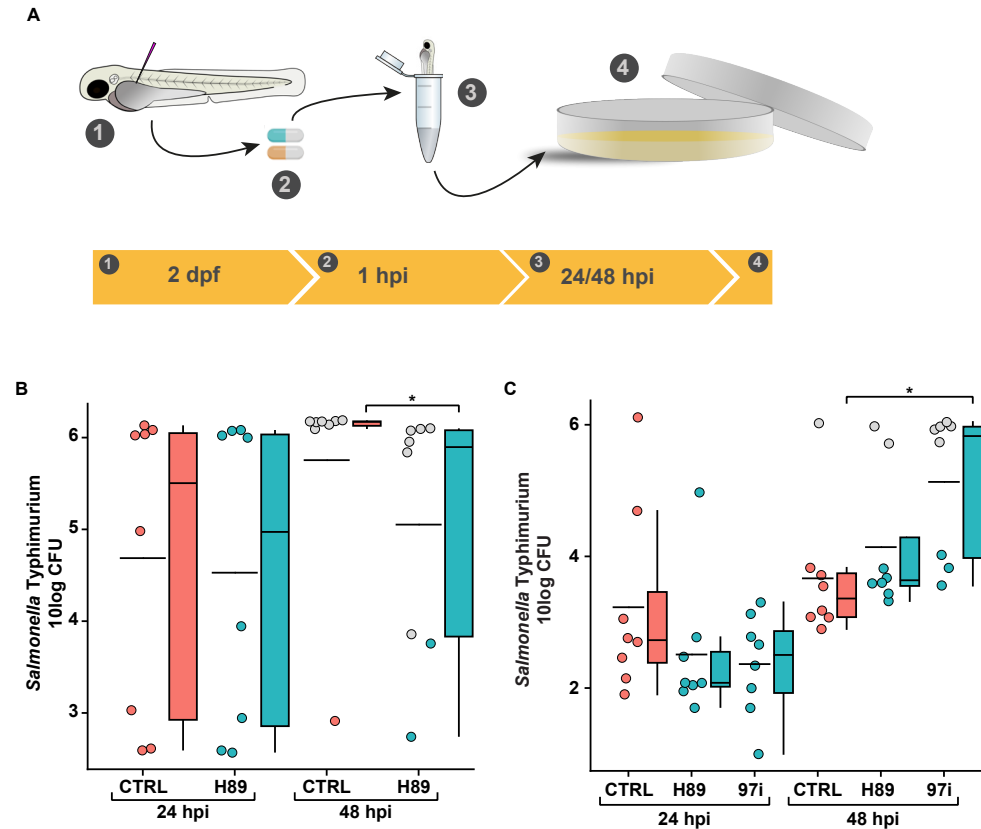
**Figure 4. Effect of HDTs on *Stm* burden**

A. Schematic overview of the experimental procedure of the HDT screen using *Stm*. Infection of mCherry-expressing *Stm* in the DoC is performed at 2 dpf (1) and treatment was started at 1 hpi (2). At both 24 and 48 hpi larvae (n = 8) were anesthetized and homogenized (3). The resulting homogenates were serial diluted and plated (4). After overnight incubation of the plate, the number of colonies were counted and calculated back to CFU in the original homogenate giving a readout for bacterial burden.

B. CFU assay of mCherry-expressing *Stm*-infected zebrafish larvae treated with H89 (25 μM) or control treatment (DMSO at 0.25% v/v). Assay was performed as described in A. Each dot represents a single larva (n = 8 per group). Boxplots with 95% confidence intervals are shown and the black line in the boxplots and percentage indicates the group median, while the black line in the dot plot indicates the group mean. Grey dots indicate dead larvae. Statistical analysis was performed per experiment using a Mann-Whitney test.

C. CFU assay of mCherry-expressing *Stm*-infected zebrafish larvae treated with H89 or 97i (10 μM) or control treatment (DMSO at 0.1% v/v). Assay was performed as described in A except the treatment was not added to the embryo medium but injected in the DoC. Each dot represents a single larva (n = 8 per group). Boxplots with 95% confidence intervals are shown and the black line in the boxplots and percentage indicates the group median, while the black line in the dot plot indicates the group mean. Grey dots indicate dead larvae. Statistical analysis was performed per experiment using a Kruskal-Wallis with Dunn's multiple comparisons test. (* = p<0.05).

treatment dose (10µM). We found similar or higher infection burdens for the H89 and 97i treatment groups compared to the control treatment group at both timepoints and observed high mortality at the 48 hpi timepoint (Figure 4C). We concluded that neither H89 nor 97i are effective in reducing *Stm* burden in our *in vivo* model.
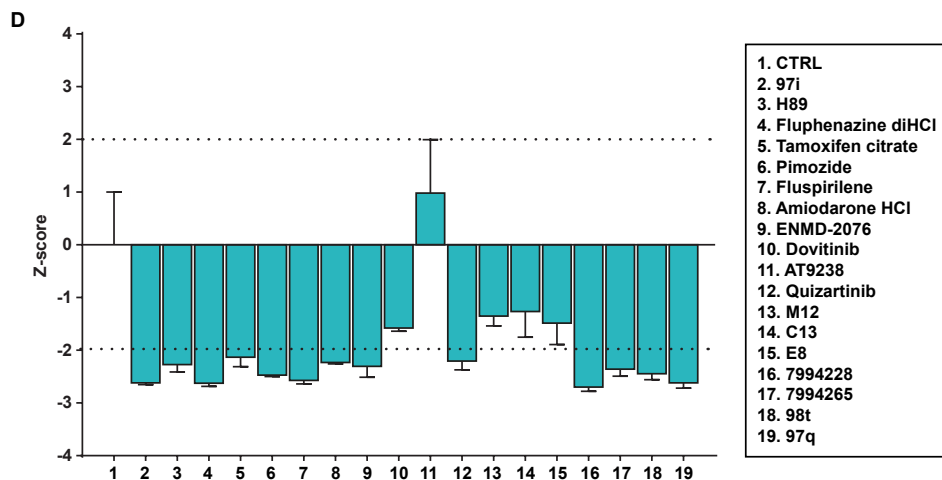
Intracellular infection dynamics

As the HDTs tested in our *in vivo* model were all capable of reducing bacterial load *in vitro* in MelJuSo cells infected with *Mtb*, we analysedintracellular infection dynamics, such as intracellular bacterial load. For this, we utilized the intra-macrophage killing model[40]. Embryos were infected with the less virulent *Mm* ERP mutant strain, and at 24 hpi confocal laser scanning microscopy was used to quantify the number of bacteria
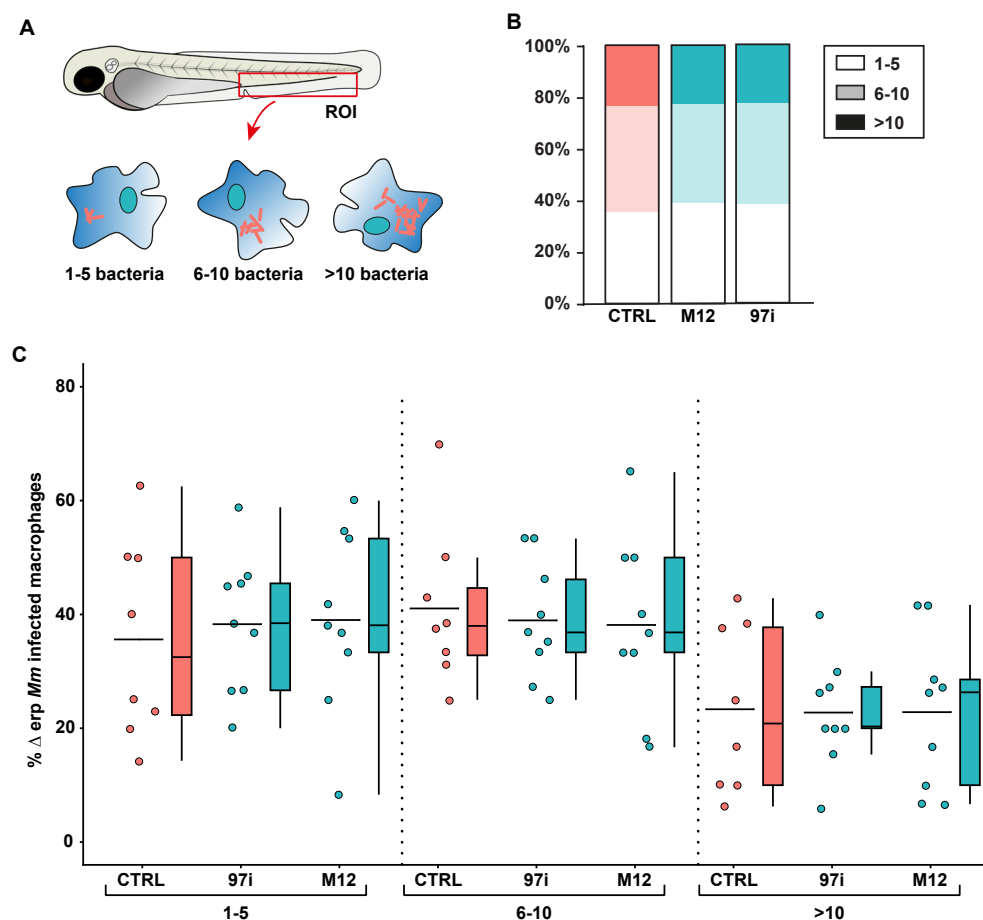
Figure 5. Effect of HDTs on intracellular dynamics of *Mm in vivo* and *in vitro*
A. Schematic overview of the intra-macrophage killing model. A wasabi-expressing *Mm* ERP-mutant-strain was used to infect 30 hpf zebrafish larvae. Treatment was started at 1 hpi and at 2 dpi larvae were fixed using 4% paraformaldehyde and imaged in the CTH region using a confocal microscope. Infected macrophages were classified in low (1-5 bacteria), mid (6-10 bacteria) or high (>10 bacteria) intracellular load.
B. Enumeration of bacteria per macrophage at 2 dpi as described in B comparing larvae treated with M12 (10 µM), 97i (10 µM) or control treatment (DMSO at 0.1% v/v).
C. Quantification of intracellular bacterial load as described in A. Each dot represents a single larva (n = 8-9 per group). Boxplots with 95% confidence intervals are shown and the black line in the boxplots and percentage indicates the group median, while the black line in the dot plot indicates the group mean. Statistical analysis was performed per experiment using a Kruskal-Wallis with Dunn's multiple comparisons test.

D

Legend:
1. CTRL
2. 97i
3. H89
4. Fluphenazine diHCl
5. Tamoxifen citrate
6. Pimozide
7. Fluspirilene
8. Amiodarone HCl
9. ENMD-2076
10. Dovitinib
11. AT9238
12. Quizartinib
13. M12
14. C13
15. E8
16. 7994228
17. 7994265
18. 98t
19. 97q

Figure 5. (continued)

D. Bacterial load of mCherry expressing *Mm*-infected MelJuSo cells, expressed as z-scores. Cells were treated with compound of interest (10 µM) or control treatment (DMSO at 0.1% v/v). Bars show average z-score of 3 replicates and error bars indicate standard deviation. The dashed line depicts a cutoff at a z-score of +/−2.

residing in single macrophages in the CHT region of the larvae (Figure 4A). By dividing the intracellular bacterial load of macrophages in three classes of low (1-5 bacteria), mid (6-10 bacteria) or high (>10 bacteria), differences in intracellular survival can be observed. We did not find any effect of 97i or M12 treatment on the number of macrophages distributed over the three classes of bacterial load (Figure 5B-C). We therefore concluded that neither 97i nor M12 increased intracellular killing or inhibited intracellular bacterial growth. We then asked whether differences between *Mm* and *Mtb* pathogenesis and pathogen-host interactions could be the reason why we did not observe reduction of bacterial burden in our *in vivo* model as opposed to the *in vitro* model. Therefore, we infected MelJuSo cells with *Mm* and treated them with a range of compounds known to work in this system with *Mtb* infection. We found almost all compounds to be able to reduce *Mm* bacterial load *in vitro*, including 97i and H89 (Figure 5D). We concluded that differences between the *in vivo* whole organism model and the *in vitro* cell systems were responsible for differences in observed HDT effectiveness, and not differences in the pathogen used.

Back to basics: the blood island infection model yields three hits

As none of the above methods proved effective in screening for HDTs, we decided to return to the blood island infection model commonly used in our laboratory and the zebrafish community[38]. In this model, 30 hpf embryos are infected in the blood island, leading to a systemic infection, similar to that resulting from duct of Cuvier injection. The younger age of the embryos in the blood island method compared to the duct of Cuvier method prohibits testing part of the potential HDT compounds due to developmental toxicity as described earlier (Table 1). However, the younger age at the onset of infection provides a longer time window for evaluation of HDT effects on bacterial burden. After infection via the blood island, embryos were randomly divided in groups. At 1 hpi, treatment was performed by immersion in embryo medium containing the compounds. Stereo fluorescent imaging at 4 dpi and subsequent pixel-count analysis was used to quantify bacterial burden of the different treatment groups (Figure 6A). We decided to test selected compounds from an autophagy modulating library and a deubiquitinase inhibitor library. These compounds were identified as hits *in vitro* in *Mtb*-infected MelJuSo cells as well as in *Mtb*-infected human primary macrophages

(Heemskerk *et al* – in preparation). While neither H89 nor 97i showed marked activity in the blood island infection model, we found 1 compound from the DUB inhibitor library (Trifluoperazine) and 2 compounds from the autophagy modulating library (Amiodarone-HCl and Tamoxifen-citrate) to be effective in initial screens (Figure 6B). Therefore, we conclude that the 1 dpi blood island infection method, which provides a window of 4 days to assess drug efficacy, is a practical procedure for HDT screening, resulting here in the identification of several promising candidates for further research.
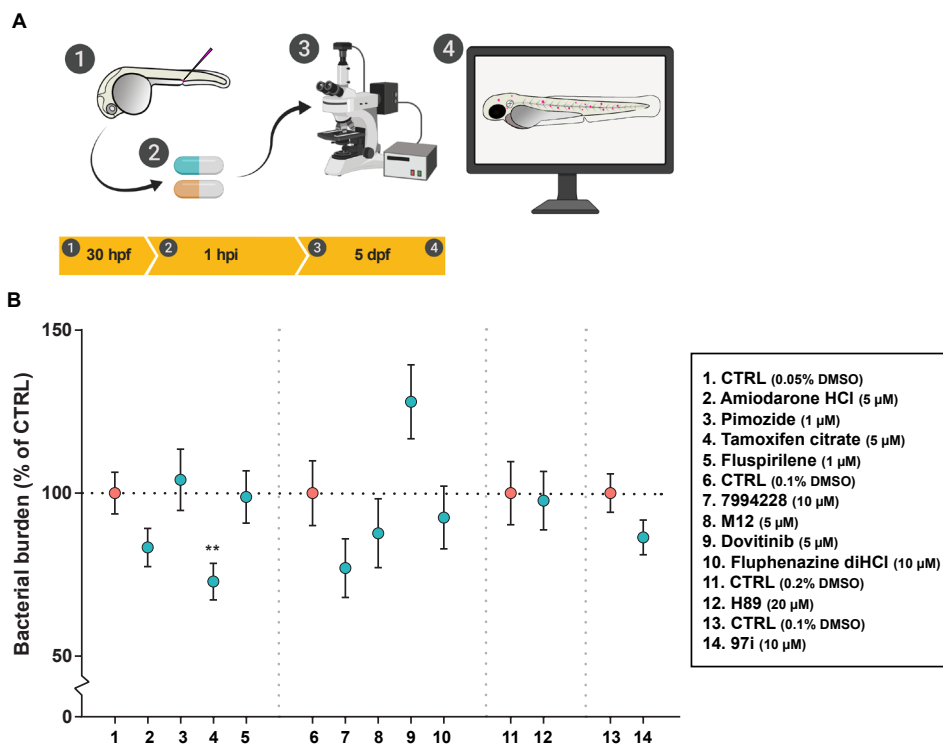
Figure 6. HDT screen using blood island infection model
A. Schematic overview of the experimental procedure of the HDT screen using blood island infection. Injection of mCherry-expressing *Mm* in the blood island is performed at 30 hpf (1). Treatment was started at 1 hpi (2) and at 4 dpi larvae were anesthetized and subsequently imaged using a stereo fluorescent microscope (3). Fluorescent signal is obtained per larvae and is a measure of bacterial burden (4). Quantification of fluorescent signal is performed using pixelcount analysis.
B. Bacterial burden assay of mCherry-expressing *Mm*-infected zebrafish larvae treated with compounds of interests or control treatment (DMSO at equal v/v). Assay was performed as described in A. Normalized data of multiple experiments for each treatment was included (n = 2-4). Dots show mean of each group and error bars indicate standard error of the mean. Black dotted line indicates control mean set at 100%. Grey vertical dotted lines indicate multiple experiments. Statistical analysis was performed per normalized dataset using either a Kruskal-Wallis with Dunn's multiple comparisons test for experiments or a Mann-Whitney test for datasets with more than 2 treatment groups or datasets with 2 treatment groups respectively. (** = $p < 0.01$).

Discussion

Large scale screening using cell-based assays is increasingly utilized to identify potential new therapeutic approaches[1]. Many screens aim at repurposing of FDA-approved drugs or compounds that have not passed phase-II clinical trials for their originally intended use[7,8]. However, cell-based assays cannot mimic all aspects of a disease and it is difficult to assess developmental toxicity and tissue-relevant effects using cell cultures. While screens using three-dimensional culture models aim to address these limitations, animal models will remain a vital step towards new therapeutics[10]. The zebrafish has filled the gap between cell-based assays and mammalian models as a medium throughput and cost-effective animal model to identify new therapeutic approaches[41–44]. Our aim was to screen for anti-TB HDTs using the well-established zebrafish embryo model for TB[25–27].

We initially attempted an approach that could potentially be scaled up and partly automated by using robotic injection[32,33]. However, the yolk infection approach did not yield any HDT hits, contrary to the antibiotic rifampicin that was used as a positive control for reduction of bacterial burden. For HDTs to work effectively, the host immune system must interact with the pathogen. This interaction is not needed when testing antibiotics that target bacteria directly regardless of the tissue environment of the infection. In the yolk infection model, interaction between pathogen and the innate immune system only starts at 2 to 3 dpf (2 to 3 dpi) when *Mm* is able to infect tissues in the developing embryo[33]. As a consequence, the yolk remains a safe reservoir for *Mm* throughout the experimental window, as immune cells do not migrate in the yolk and the yolk provides a rich source of nutrients for *Mm*[45]. We therefore abandoned the use of the yolk infection model and turned to intravenous injection routes that are known to result in rapid phagocytosis of *Mm* by macrophages[19,38,46].

We compared two types of intravenous infection, the duct of Cuvier infection route at 2 dpf, and blood island infection route at 1 dpf. By imaging the larvae using stereo fluorescence microscopy, we could assess bacterial burden and potential developmental toxicity at the same time in both methods. This led us to conclude that embryos are more sensitive to developmental toxicity when drugs are applied from 1 dpf compared with 2 dpf. Thus, developmental toxicity can be minimized using the duct of Cuvier method. However, the duct of Cuvier method provides only a 3 day experimental window, while the blood island method allows us to follow the disease progression over 4 days. This is due to the fact that the end point of both methods is set at 5 dpf because of animal experimentation regulation. We used both methods to test kinase inhibitors (H89, 97i), shown to be effective in human cells against not only *Mtb* but also *Mm* and *Stm* (this study)[34]. These drugs could not reduce overall bacterial burden of *Mm*-infected or *Stm*-infected zebrafish. More detailed analysis of intracellular pathogen-host dynamics using a zebrafish *in vivo* intra-macrophage killing model also did not reveal an effect of the kinase inhibitor 97i or the deubiquitinase inhibitor M12. We decided to use the 1 dpf blood island infection model to perform pilot screens of potential HDT candidates with demonstrated effectivity against *Mtb* and *Mm* in human cells. Using this model, we found the HDTs Trifluoperazine, Tamoxifen and Amiodarone to reduce bacterial burden.

Tamoxifen targets the estrogen receptor either as an agonist or as an antagonist, depending on the tissue. It is widely used in the clinic for breast cancer therapy. Furthermore, it has been studied in the context of various infections, such as Cryptococcus, toxoplasma and Leishmania[47–49]. There is also previous evidence for a link with TB, since Tamoxifen was found to have direct anti-mycobacterial activity, also on drug-resistant strains, as well as a synergistic effect with first-line anti-TB drugs[50,51]. The question remains if the effect we observe on mycobacterial burden is host-directed and related to the estrogen receptor, or if different host pathways are modulated for the anti-mycobacterial effect. Tamoxifen was identified by screening an autophagy-modulating compound library and indeed autophagy can be modulated by Tamoxifen treatment[52]. Autophagy is an intracellular degradation pathway vital to maintaining

homeostasis by removing unwanted elements from the cell, such as misfolded protein aggregates and damaged organelles but it has also been shown to be a defense mechanism against microbial invaders[53–55]. Modulation of the autophagy pathway could be the reason for the observed effect of Tamoxifen and this will be investigated in future research (Chapter 4).

Amiodarone is an adrenergic receptor inhibitor and it blocks myocardial calcium, sodium and potassium channels. Furthermore, Amiodarone induces nitric oxide (NO) production, which is known to play a role in combating mycobacterial infection via production of reactive nitrogen species[56–58]. Like Tamoxifen, Amiodarone was identified by screening an autophagy-modulating compound library and has been shown to induce autophagy[59,60]. In contrast to Tamoxifen, Amiodarone has not been previously linked to TB. Amiodarone could work in a similar manner as Tamoxifen by modulating the autophagy pathway or alternative a host directed effect, such as NO production, could be the mechanism behind the anti-mycobacterial effect. Further research efforts will be required to elucidate its mechanism of action (Chapter 5).

Trifluoperazine was identified by screening a library of deubiquitinase inhibitors (Heemskerk *et al* – in preparation). In general, ubiquitin is attached to intracellular cargo such as proteins to mark them for degradation and deubiquitinases facilitate deubiquitination, the removal of this ubiquitin signal[61,62]. During TB pathogenesis, mycobacteria are capable of escaping phagosomes and can subsequently be ubiquitinated and targeted for selective autophagy via ubiquitin receptors[55]. Our lab has recently shown that this mechanism is important for host defence in zebrafish, as mutants in the ubiquitin receptors p62 and optineurin are hypersusceptible to *Mm* infection[63]. As a survival mechanism, intracellular pathogens will benefit from deubiquitination. Indeed, *Stm* has been shown to excretes the deubiquitinase SseL and is thereby able to inhibit selective autophagy[64]. In the case of Trifluoperazine it remains to be investigated which deubiquitinase(s) is (are) inhibited and if these are host or pathogen derived.

We show that the zebrafish model for TB can be used to identify HDTs with anti-mycobacterial effects, however we found that in several cases results obtained by cell-based culture assays did not translate to *in vivo* anti-mycobacterial effects in the zebrafish model. There are several possible explanations for differences between human cell-based and zebrafish *in vivo* screens. Some drugs identified in cell-based screens using *Mtb* might fail to reduce *Mm* burden in zebrafish for example because of differences between the pathogens or lack of conservation of the drug target site. However, a screen in zebrafish could identify drugs that act at later stages of diseases progression, for example acting on targets involved in granuloma development. Such drugs would never be identified in a cell-based screen. Furthermore, it cannot be excluded that many of the hits from cell-based screens are simply not relevant due to the phenotypic changes that mycobacteria undergo during the process of granuloma formation[25,65,66]. Proper evaluation of different screening methods awaits translation of results from cell-based screens to animal models, including the zebrafish and mammalian models.

Developmental toxicity prevented us in several cases from validating HDTs in zebrafish. For example, haloperidol was shown to reduce intracellular *Mtb* survival in human cells[67], while treatment of *Mm*-infected zebrafish embryos led to massive oedema (this study). We were also unable to confirm the antibacterial effects of Imatinib and H89, drugs that target kinases. H89 was shown to work on both *Mtb* and *Stm* in cell-based and mouse models[34], but did not restrict *Mm* or *Stm* infection burden in the zebrafish model. Similarly, imatinib did not show reduction of *Mm* bacterial burden in the zebrafish model, though it was found effective in cell-based and mouse models against *Mm* and *Mtb*[68]. Differences in these results from cell-based and mouse models compared to the zebrafish model might be attributed to side effects due to roles of the target kinases in developmental processes. For instance, Imatinib is thought to target ABL family tyrosine

kinases and these have been shown to have important roles in zebrafish development[69]. In contrast, compounds that putatively target ubiquitination and autophagy processes (Trifluoperazine, Tamoxifen and Amiodarone) worked in cell-based assays against *Mtb* as well as against *Mm* in the zebrafish model, providing *in vivo* validation for these compounds (this study). Another successful example of a screen performed in zebrafish resulted in the identification of HDT Clemastine, which is capable of restricting *Mm* infection *in vivo* in zebrafish larvae and *ex vivo* in zebrafish granuloma explants, possibly by affecting inflammasome signaling[44]. It remains to be established if this drug also works in human cell based or mammalian models and if this drug could go to clinical trials for use in TB patients.

Drug uptake and metabolism is another important aspect to take into consideration. A great advantage of the zebrafish model is the simplicity of treatment by adding drugs to the embryo medium. However, for this to work HDTs need to be water soluble, while metabolites or the HDTs themselves might alter pH of the embryo medium. To prevent this, we replaced normal embryo medium with a buffered embryo medium (1X E2). Characteristics of HDTs, such as size, molecular weight and lipophilicity, will influence the potential uptake of HDTs by the zebrafish embryo[70]. Because the mouth of zebrafish embryos opens around 3 dpf, initial uptake of nutrients, oxygen and subsequently any drug treatment is mediated mostly by diffusion through the skin. It remains unclear how concentrations in the embryo medium relate to *in vivo* concentrations, although it is assumed to reach similar levels. Advances in deducing pharmacokinetics of the zebrafish model will shine more light on this aspect. For instance, it has been shown that uptake and metabolism of paracetamol in the zebrafish model translates well to what is known of human pharmacokinetics of paracetamol[71,72]. Nevertheless, inefficient uptake or inactivation of the drug through metabolism could have been a cause of false negatives in our screen.

The zebrafish model has distinct advantages as an intermediate whole organism screening model between cell-based systems and mammalian models. Although predicted HDT targets or described effects can be indicators of the mechanistic function of an HDT, it remains unclear how the hits obtained in our screen exert their anti-mycobacterial effects and further studies into the mechanism of action are required. The zebrafish model is useful not only for the drug screening process but also for subsequent mechanistic studies, which will benefit from efficient genetic tools and excellent possibilities for intravital imaging of host-pathogen interactions.

Materials & methods

Ethics statement
Zebrafish were maintained and handled in compliance with the local animal welfare regulations as overseen by the Animal Welfare Body of Leiden University (license number: 10612). All practices involving zebrafish were performed in accordance with European laws, guidelines and policies for animal experimentation, housing and care (European Directive 2010/63/EU on the protection of animals used for scientific purposes). The present study did not involve any procedures within the meaning of Article 3 of Directive 2010/63/EU and as such it is not subject to authorization by an ethics committee.

Zebrafish husbandry and handling
Wild type zebrafish (AB/TL) were maintained according to standard protocols (www.zfin.org). Zebrafish eggs were obtained by natural spawning of single crosses to achieve synchronized developmental timing. Eggs from at least 5 couples were combined to achieve heterogeneous groups. Eggs and embryos were kept in egg water (60 µg/ml

sea salt, Sera Marin, Heinsberg, Germany) or E2 buffered embryo medium (composition: 15 mM NaCl, 0.5 mM KCl, 1 mM $MgSO_4$, 150 µM KH_2PO_4, 1 mM $CaCl_2$ & 0.7 mM $NaHCO_3$) at ~28.5 °C for the duration of experiments, with the exception of necessary handling for experimental procedures.

Bacterial strains and inoculum preparation

Mycobacterium marinum (*Mm*) M-strain or ERP-mutant strain containing a construct with a green (Wasabi) or red (mCherry) fluorescent reporter and resistance for selection (hygromycin) was used for infections[40,46]. Fresh inoculum was prepared for every infection experiment as described[38]. Briefly, the inoculum was created from 10 ml of overnight liquid culture (7H9 containing ADC and 50µg/ml hygromycin) grown at ~28.5 °C. Final inoculum was resuspended in 1X PBS containing 2% (w/v) polyvinylpyrrolidone (PVP40). Injection dose in colony forming units (CFU) was determined by optical density measurement (OD_{600} of 1 corresponds to ~100 CFU/nl) of a 1:10 dilution to ensure accurate measurements (OD_{600} < 1). In the case of the ERP-mutant strain, where single-use aliquots containing single cell suspensions were necessary, these were prepared as previously described and kept at -80 °C[40].

***Salmonella* Typhimurium** (*Stm*) SL1344-strain containing a construct with a red (mCherry) fluorescent reporter and resistance for selection (streptomycin and kanamycin) was used for infections[73,74]. Fresh inoculum was prepared for every infection experiment as described[39]. Briefly, the inoculum was created from resuspending a colony from an overnight agar plate (LB containing 90µg/ml streptomycin and 50µg/ml kanamycin) in 1X PBS containing 2% PVP40. Injection dose in CFU was determined by optical density measurement (OD_{600} of 0.5 corresponds to ~200 CFU/nl).

Zebrafish embryo infections

Below is a brief description of previously published injection techniques that were used for infection experiments[33,38,40]. All injections were performed using borosilicate glass microcapillary injection needles (Harvard Apparatus, 300038, 1 mm O.D. x 0.78 mm I.D.) prepared using a micropipette puller device (Sutter Instruments Flaming/Brown P-97). Needles were mounted on a micromanipulator (Sutter Instruments MM-33R) connected to a stand (World Precision Instruments M10L) and positioned under a stereo microscope (Leica M50). Prior to injection, embryos were anesthetized using 200 µg/ml buffered 3-aminobenzoid acid (Tricaine, Sigma-Aldrich) in egg water. After infection, embryos were incubated at ~28.5 °C in fresh egg water or E2.

*Yolk infection***:** eggs between the 8 and 128 cell stage were positioned on a 1% agarose (in egg water) plate containing slots and injected in the centre of the yolk with an inoculum of 1 nl containing ~30 (CFU). Any damaged eggs were discarded 2 to 6 hours post infection (hpi).

*Duct of Cuvier infection***:** 2 days post fertilization (dpf) old embryos were positioned on a 1% agarose (in egg water) plate prior to injection in the duct of Cuvier with an inoculum of 1 nl containing ~200 to ~400 CFU *Mm* or *Stm* (CFU dose is described for each individual experiment).

*Blood island infection***:** 30 hours post fertilization (hpf) embryos were positioned on a 1% agarose (in egg water) plate prior to injection in the blood island with an inoculum of 1 nl containing ~200 CFU *Mm*. For the intra-macrophage killing model, blood island injection was performed similarly except the inoculum of single-cell *Mm* ERP-mutant strain was obtained from single-use aliquots kept at -80 °C as described above.

Compound treatment of zebrafish embryos

All compounds were dissolved in 100% DMSO (D8418, Sigma Aldrich) in stock concentrations of 10 mM, aliquoted and kept at -80 °C. Treatment of embryos was performed by immersion with exception of the *Stm* injection experiment (Figure 4C). Stock concentrations were diluted to treatment doses in egg water (Figure 1-4), which was replaced during the course of the study by 1X E2 (Figure 6). As a solvent control treatment, 100% DMSO was diluted to the same concentration of the compound treatment in either egg water or E2. If multiple compound treatment doses were used

in the same experiment, the solvent control concentration corresponding to the highest compound treatment dose was used. Exact doses of compound treatment and solvent control concentration are described for each individual experiment. For the yolk infection experiments, treatment was performed 3 days post infection (dpi) until the endpoint of the experiment at 5 dpi. For the duct of Cuvier *Mm* infection experiments, treatment was performed 1 hour post infection (hpi) until the endpoint of the experiment at 2 or 3 dpi. For the blood island infection experiments, treatment was performed 1 hpi until the endpoint of the experiment at 4 dpi. For toxicity assessment, treatment was performed at 1 hpi or 2 dpf. For the intra-macrophage killing model, treatment was performed at 1 hpi until the endpoint of the experiment at 2 dpi. For *Stm* infection experiments, treatment was performed 1 hpi either by immersion or by injecting PBS diluted stock concentrations 1 hpi in the duct of Cuvier, assuming a 500X dilution in the tissue to achieve the desired treatment dose.

Bacterial burden assessment of infected zebrafish embryos

Yolk infection: larvae were anesthetized using tricaine at 3 dpi and run through the Complex Object Parametric Analyzer and Sorter (COPAS) system to measure bacterial fluorescent signal. Any larvae having too little or too high infection as measured by fluorescent readout were discarded. At 5 dpi treated larvae were anesthetized using tricaine and run through the COPAS system again to measure bacterial fluorescent signal[33].

Duct of Cuvier and blood island infection: larvae were anesthetized using tricaine at 3 dpi (duct of Cuvier) or 4 dpi (blood island), positioned on a 1% agarose (in egg water) plate and imaged using a Leica M205 FA stereo fluorescence microscope equipped with a DFC345 FX monochrome camera. Bacterial burden was assessed using dedicated pixel quantification software[35].

Intra-macrophage killing: larvae were fixed using 4% paraformaldehyde in PBS at 44 hpi and subsequently intra-macrophage mycobacterial sites of growth were counted using a Zeiss Observer 6.5.32 confocal microscope with a C-Apochromat 63x/1.20 W Korr UV-VIR-IR M27 objective.

CFU counts: At each timepoint 8 embryos/larvae were put in individual Eppendorf tubes in 100 µl of 1X PBS with beads (1.0 mm zirconium oxide, Next Advance) and homogenized using a tissue homogenizer (Bullet Blender, Next Advance). Homogenates were serial diluted and 10 µl of each dilution was spotted twice on an agar plate (LB containing 90 µg/ml streptomycin and 50 µg/ml kanamycin) that was incubated at 37 °C overnight. Spots of the dilution level resulting in distinguishable single colonies were counted and averaged and the number of colonies was calculated back to CFU in the original homogenate.

MelJuSo cell culture conditions

MelJuSo cell line was maintained at 37 °C/5% CO2 in Gibco Iscove's Modified Dulbecco's Medium (IMDM, Life Technologies-Invitrogen) supplemented with 10% fetal bovine serum (FBS, Greiner Bio-One, Alphen a/d Rijn, The Netherlands), 100 units/ml Penicillin and 100 µg/ml Streptomycin (Life Technologies-Invitrogen).

Infection of MelJuSo cells

MelJuSo cells were seeded in 96-well flat-bottom plates at a density of 10.000 cells/well one day prior to infection and subsequently inoculated with 100 µl of bacterial suspension at multiplicity of infection (MOI) 20, centrifuged for 3 minutes at 800 rpm and incubated at 37 °C/5% CO2 for 60 minutes. Accuracy of bacterial density measurements was verified by a standard colony-forming unit (CFU) assay. Plates were subsequently washed with culture medium containing 30 µg/ml gentamicin sulfate (Lonza BioWhittaker, Basel, Switzerland), incubated for 10 minutes, washed, and incubated at 37 °C/5% CO2 in medium containing 5 µg/ml gentamicin and indicated compounds until readout.

Compound treatment of infected MelJuSo cells

Infected cells were treated overnight with chemical compounds at a 10 µM concentration in medium containing 5 µg/ml gentamicin.

Flow cytometry

Mm infected MelJuSo cells were washed with PBS after 24 hours of compound treatment, harvested using 50 µl of Trypsin-EDTA 0.05% (ThermoFisher Scientific, Waltham, MA, USA) and added to 100 µl of 1% para-formaldehyde (PFA) (Pharmacy LUMC, the Netherlands). Cells were fixed for 1 hour prior to acquisition on a FACSCalibur using a High Throughput Sampler (HTS) (BD BioSciences).

Statistical analysis and data transformation

Due to experimental variation caused by biological variation, data of multiple experiments was combined. When data was combined, it was normalized to the mean of the control group of that experiment and normalized data of multiple experiments was combined. The number of experiments combined is described for each experiment. In the case of *Stm,* CFU count data was log-transformed. For all analysis a non-parametric distribution was assumed. The statistical test performed for each experiment is described in the figure legend. All statistical tests were performed using GraphPad Prism version 7.0.

Acknowledgements

References

1. An, W. F. & Tolliday, N. Cell-based assays for high-throughput screening. *Mol. Biotechnol*. **45**, 180–186 (2010).

2. Kumar, D. *et al*. Genome-wide analysis of the host intracellular network that regulates survival of Mycobacterium tuberculosis. *Cell* **140**, 731–43 (2010).

3. Korbee, C. J. *et al*. Combined chemical genetics and data-driven bioinformatics approach identifies receptor tyrosine kinase inhibitors as host-directed antimicrobials. *Nat. Commun*. **9**, 358 (2018).

4. Wang, L. *et al*. High-Throughput Functional Genetic and Compound Screens Identify Targets for Senescence Induction in Cancer. *Cell Rep*. **21**, 773–783 (2017).

5. Wilkinson, G. F. & Pritchard, K. In vitro screening for drug repositioning. *J. Biomol. Screen*. **20**, 167–179 (2015).

6. Madrid, P. B. *et al*. A Systematic Screen of FDA-Approved Drugs for Inhibitors of Biological Threat Agents. *PLoS One* **8**, e60579 (2013).

7. Younis, W., Thangamani, S. & Seleem, M. N. Repurposing Non-Antimicrobial Drugs and Clinical Molecules to Treat Bacterial Infections. *Curr. Pharm. Des*. **21**, 4106–11 (2015).

8. Barrows, N. J. *et al*. A Screen of FDA-Approved Drugs for Inhibitors of Zika Virus Infection. *Cell Host Microbe* **20**, 259–270 (2016).

9. Amoedo, N. D., Obre, E. & Rossignol, R. Drug discovery strategies in the field of tumor energy metabolism: Limitations by metabolic flexibility and metabolic resistance to chemotherapy. *Biochim. Biophys. Acta - Bioenerg*. **1858**, 674–685 (2017).

10. Costa, A., Sarmento, B. & Seabra, V. An evaluation of the latest in vitro tools for drug metabolism studies . *Expert Opin. Drug Metab. Toxicol*. **10**, 103–119 (2013).

11. Patton, E. E. & Tobin, D. M. Spotlight on zebrafish: the next wave of translational research. *Dis. Model. Mech*. **12**, dmm039370 (2019).

12. Lieschke, G. J. & Currie, P. D. Animal models of human disease: Zebrafish swim into view. *Nat. Rev. Genet*. **8**, 353–367 (2007).

13. Cornet, C., Di Donato, V. & Terriente, J. Combining Zebrafish and CRISPR/Cas9: Toward a more efficient drug discovery pipeline. *Front. Pharmacol*. **9**, 1–11 (2018).

14. Stainier, D. Y. R. *et al*. Guidelines for morpholino use in zebrafish. *PLoS Genet*. **13**, 6–10 (2017).

15. Page, D. M. *et al*. An evolutionarily conserved program of B-cell development and activation in zebrafish. *Blood* **122**, 1–12 (2013).

16. Meijer, A. & Spaink, H. Host-pathogen interactions made transparent with the zebrafish model. *Curr. Drug Targets* 1000–1017 (2011).

17. Cui, C. *et al*. *Infectious disease modeling and innate immune function in zebrafish embryos*. *Methods in cell biology* vol. 105 (Elsevier Inc., 2011).

18. Tobin, D. M., May, R. C. & Wheeler, R. T. Zebrafish: A See-Through Host and a Fluorescent Toolbox to Probe Host–Pathogen Interaction. *PLoS Pathog*. **8**, e1002349 (2012).

19. Torraca, V., Masud, S., Spaink, H. P. & Meijer, A. H. Macrophage-pathogen interactions in infectious diseases: new therapeutic insights from the zebrafish host model. *Dis. Model. Mech*. **7**, 785–97 (2014).

20. Yoshida, N., Frickel, E. M. & Mostowy, S. Macrophage-microbe interactions: Lessons from the Zebrafish model. *Front. Immunol.* **8**, (2017).

21. Hawn, T. R., Matheson, A. I., Maley, S. N. & Vandal, O. Host-directed therapeutics for tuberculosis: can we harness the host? *Microbiol. Mol. Biol. Rev.* **77**, 608–27 (2013).

22. Guler, R. & Brombacher, F. Host-directed drug therapy for tuberculosis. *Nat. Chem. Biol.* **11**, 748–751 (2015).

23. Hawn, T. R., Shah, J. A. & Kalman, D. New tricks for old dogs: Countering antibiotic resistance in tuberculosis with host-directed therapeutics. *Immunol. Rev.* **264**, 344–362 (2015).

24. Zumla, A., Rao, M., Dodoo, E. & Maeurer, M. Potential of immunomodulatory agents as adjunct host-directed therapies for multidrug-resistant tuberculosis. *BMC Med.* **14**, 1–12 (2016).

25. Davis, J. M. *et al.* Real-time visualization of Mycobacterium-macrophage interactions leading to initiation of granuloma formation in zebrafish embryos. *Immunity* **17**, 693–702 (2002).

26. Ramakrishnan, L. The Zebrafish Guide to Tuberculosis Immunity and Treatment. *Cold Spring Harb. Symp. Quant. Biol.* **78**, 179–192 (2013).

27. Meijer, A. H. Protection and pathology in TB: learning from the zebrafish model. *Semin. Immunopathol.* **38**, 261–273 (2016).

28. Ramakrishnan, L. Revisiting the role of the granuloma in tuberculosis. *Nat. Rev. Immunol.* **12**, 352–366 (2012).

29. Hmama, Z., Peña-Díaz, S., Joseph, S. & Av-Gay, Y. Immunoevasion and immunosuppression of the macrophage by Mycobacterium tuberculosis. *Immunol. Rev.* **264**, 220–232 (2015).

30. McClean, C. M. & Tobin, D. M. Macrophage form, function, and phenotype in mycobacterial infection: Lessons from tuberculosis and other diseases. *Pathog. Dis.* **74**, 1–15 (2016).

31. Cadena, A. M., Fortune, S. M. & Flynn, J. L. Heterogeneity in tuberculosis. *Nat. Rev. Immunol.* **17**, 691–702 (2017).

32. Veneman, W. & Stockhammer, O. A zebrafish high throughput screening system used for Staphylococcus epidermidis infection marker discovery. *BMC …* 1–15 (2013).

33. Carvalho, R. *et al.* A high-throughput screen for tuberculosis progression. *PLoS One* **6**, e16779 (2011).

34. Kuijl, C., Savage, N., Marsman, M. & Tuin, A. Intracellular bacterial growth is controlled by a kinase network around PKB/AKT1 (supplementary figures). *Nature* 1–27 (2007) doi:10.1038/nature0.

35. Stoop, E. J. M. *et al.* Zebrafish embryo screen for mycobacterial genes involved in the initiation of granuloma formation reveals a newly identified ESX-1 component. *Dis. Model. Mech.* **4**, 526–536 (2011).

36. Benard, E. L., Rougeot, J., Racz, P. I., Spaink, H. P. & Meijer, A. H. *Transcriptomic Approaches in the Zebrafish Model for Tuberculosis—Insights Into Host- and Pathogen-specific Determinants of the Innate Immune Response. Advances in Genetics* vol. 95 (Elsevier Ltd, 2016).

37. van der Sar, A. M. *et al.* Zebrafish embryos as a model host for the real time analysis of Salmonella typhimurium infections. *Cell. Microbiol.* **5**, 601–611 (2003).

38. Benard, E. L. *et al.* Infection of zebrafish embryos with intracellular bacterial pathogens. *J. Vis. Exp.* 1–8 (2012) doi:10.3791/3781.

39. Masud, S. *et al.* Macrophages target Salmonella by Lc3-associated phagocytosis in a systemic infection model. *Autophagy* **00**, 1–17 (2019).

40. Takaki, K., Davis, J. M., Winglee, K. & Ramakrishnan, L. Evaluation of the pathogenesis and treatment of Mycobacterium marinum infection in zebrafish. *Nat. Protoc.* **8**, 1114–24 (2013).

41. Yang, R. *et al.* Miconazole protects blood vessels from MMP9-dependent rupture and hemorrhage. *Dis. Model. Mech.* **10**, 337–348 (2017).

42. Tseng, W.-C. *et al.* Modeling Niemann-Pick disease type C1 in zebrafish: a robust platform for in vivo screening of candidate therapeutic compounds. *Dis. Model. Mech.* **11**, dmm034165 (2018).

43. Delgadillo-Silva, L. F. *et al.* Modelling pancreatic β-cell inflammation in zebrafish identifies the natural product wedelolactone for human islet protection. *Dis. Model. Mech.* **12**, dmm036004 (2019).

44. Matty, M. A. *et al.* Potentiation of P2RX7 as a host-directed strategy for control of mycobacterial infection. *Elife* **8**, 1–27 (2019).

45. Traver, D. *et al.* The zebrafish as a model organism to study development of the immune system. *Adv. Immunol.* **81**, 253–330 (2003).

46. van der Sar, A. M. *et al.* Mycobacterium marinum Strains Can Be Divided into Two Distinct Types Based on Genetic Diversity and Virulence. *Infect. Immun.* **72**, 6306–6312 (2004).

47. Butts, A. *et al.* Estrogen receptor antagonists are anti-cryptococcal agents that directly bind EF hand proteins and synergize with fluconazole in vivo. *MBio* **5**, 1–11 (2014).

48. Dittmar, A. J., Drozda, A. A. & Blader, I. J. Drug Repurposing Screening Identifies Novel Compounds That Effectively Inhibit Toxoplasma gondii growth. *mSphere* **1**, 1–15 (2016).

49. Miguel, D. C., Yokoyama-Yasunaka, J. K. U. & Uliana, S. R. B. Tamoxifen is effective in the treatment of Leishmania amazonensis infections in mice. *PLoS Negl. Trop. Dis.* **2**, (2008).

50. Chen, F. C. *et al.* Pros and cons of the tuberculosis drugome approach - An empirical analysis. *PLoS One* **9**, (2014).

51. Jang, W. S. *et al.* Anti-mycobacterial activity of tamoxifen against drug-resistant and intra-macrophage Mycobacterium tuberculosis. *J. Microbiol. Biotechnol.* **25**, 946–950 (2015).

52. Pattingre, S., Bauvy, C., Levade, T., Levine, B. & Codogno, P. Ceramide-induced autophagy: To junk or to protect cells? *Autophagy* **5**, 558–560 (2009).

53. Gutierrez, M. G. *et al.* Autophagy is a defense mechanism inhibiting BCG and Mycobacterium tuberculosis survival in infected macrophages. *Cell* **119**, 753–766 (2004).

54. Yang, Z. & Klionsky, D. J. Mammalian autophagy: Core molecular machinery and signaling regulation. *Curr. Opin. Cell Biol.* **22**, 124–131 (2010).

55. Deretic, V., Saitoh, T. & Akira, S. Autophagy in infection, inflammation and immunity. *Nat. Rev. Immunol.* **13**, 722–37 (2013).

56. MacMicking, J. D. *et al.* Identification of nitric oxide synthase as a protective locus against tuberculosis. *Proc. Natl. Acad. Sci.* **94**, 5243–5248 (1997).

57. Elks, P. M., Renshaw, S. a., Meijer, a. H., Walmsley, S. R. & van Eeden, F. J. Exploring the HIFs, buts and maybes of hypoxia signalling in disease: lessons from zebrafish models. *Dis. Model. Mech.* **8**, 1349–1360 (2015).

58. Jamaati, H. *et al*. Nitric oxide in the pathogenesis and treatment of tuberculosis. *Front. Microbiol.* **8**, 1–11 (2017).

59. Lin, C. W. *et al*. Amiodarone as an autophagy promoter reduces liver injury and enhances liver regeneration and survival in mice after partial hepatectomy. *Sci. Rep.* **5**, 1–13 (2015).

60. Jacquin, E. *et al*. Pharmacological modulators of autophagy activate a parallel noncanonical pathway driving unconventional LC3 lipidation. *Autophagy* **13**, 854–867 (2017).

61. Komander, D., Clague, M. J. & Urbé, S. Breaking the chains: Structure and function of the deubiquitinases. *Nat. Rev. Mol. Cell Biol.* **10**, 550–563 (2009).

62. Harrigan, J. A., Jacq, X., Martin, N. M. & Jackson, S. P. Deubiquitylating enzymes and drug discovery: Emerging opportunities. *Nat. Rev. Drug Discov.* **17**, 57–77 (2018).

63. Zhang, R. *et al*. The selective autophagy receptors Optineurin and p62 are both required for zebrafish host resistance to mycobacterial infection. *PLOS Pathog.* **15**, e1007329 (2019).

64. Mesquita, F. S. *et al*. The Salmonella deubiquitinase SseI inhibits selective autophagy of cytosolic aggregates. *PLoS Pathog.* **8**, (2012).

65. Ramakrishnan, L., Federspiel, N. A. & Falkow, S. Granuloma-Specific Expression of Mycobacterium Virulence Proteins from the Glycine-Rich PE-PGRS Family Lalita Ramakrishnan, Nancy A. Federspiel, and Stanley Falkow Supplementary Material DFI Methods: **288**, 300 (2000).

66. Chan, K. *et al*. Complex pattern of Mycobacterium marinum gene expression during long-term granulomatous infection . *Proc. Natl. Acad. Sci.* **99**, 3920–3925 (2002).

67. Sundaramurthy, V. *et al*. Integration of chemical and RNAi multiparametric profiles identifies triggers of intracellular mycobacterial killing. *Cell Host Microbe* **13**, 129–42 (2013).

68. Napier, R. J. *et al*. Imatinib-Sensitive tyrosine kinases regulate mycobacterial pathogenesis and represent therapeutic targets against tuberculosis. *Cell Host Microbe* **10**, 475–485 (2011).

69. Challa, A. K. & Chatti, K. Conservation and Early Expression of Zebrafish Tyrosine Kinases Support the Utility of Zebrafish as a Model for Tyrosine Kinase Biology. *Zebrafish* **10**, 264–274 (2012).

70. de Koning, C. *et al*. Visualizing Compound Distribution during Zebrafish Embryo Development: The Effects of Lipophilicity and DMSO. *Birth Defects Res. Part B - Dev. Reprod. Toxicol.* **104**, 253–272 (2015).

71. Kantae, V. *et al*. Pharmacokinetic Modeling of Paracetamol Uptake and Clearance in Zebrafish Larvae: Expanding the Allometric Scale in Vertebrates with Five Orders of Magnitude. *Zebrafish* **13**, 504–510 (2016).

72. van Wijk, R. C. *et al*. Impact of post-hatching maturation on the pharmacokinetics of paracetamol in zebrafish larvae. *Sci. Rep.* **9**, 2149 (2019).

73. Hoiseth, S. K. & Stocker, B. A. Aromatic-dependent Salmonella typhimurium are non-virulent and effective as live vaccines. *Nature* **291**, 238–239 (1981).

74. Burton, N. A. *et al*. Disparate impact of oxidative host defenses determines the fate of salmonella during systemic infection in mice. *Cell Host Microbe* **15**, 72–83 (2014).

4

Repurposing Tamoxifen as potential host-directed therapeutic for tuberculosis

Ralf Boland[1*], Matthias T. Heemskerk[2*], Gabriel Forn-Cuní[1], Cornelis J. Korbee[2], Kimberley V. Walburg[2], Jeroen J. Esselink[2], Carina Carvalho dos Santos[2,3], Amy de Waal[1], Daniel C.M. van der Hoeven[1], Elisa van der Sar[1], Herman P. Spaink[1], Michiel van der Vaart[1], Annemarie H. Meijer[1#], Tom H. M. Ottenhoff[2#]

1.   Institute of Biology Leiden, Leiden University, Leiden, The Netherlands
2.   Department of Infectious Diseases, Leiden University Medical Center, Leiden, The Netherlands
3.   Laboratório Especial de Desenvolvimento de Vacinas, Instituto Butantan, São Paulo, Brazil
*#   Equal contribution

Abstract

The global burden of Tuberculosis (TB) is aggravated by the continuously increasing emergence of drug resistance, urging for innovative therapeutic options. The concept of host-directed therapy (HDT) as adjunctive to classical antibacterial therapy with antibiotics represents a novel and promising approach for treating TB. Here, we have focused on repurposing the clinically used anti-cancer drug Tamoxifen, which was identified as a molecule with strong host-directed activity against intracellular *Mycobacterium tuberculosis* (*Mtb*). Using a primary human macrophage *Mtb* infection model, we demonstrate the potential of Tamoxifen against drug sensitive as well as drug resistant *Mtb* bacteria. The therapeutic effect of Tamoxifen was confirmed in an *in vivo* TB model, based on *Mycobacterium marinum* infection of zebrafish larvae. Tamoxifen had no direct antimicrobial effects at the concentrations used, confirming that Tamoxifen acted as a HDT drug. Furthermore, we demonstrate that the anti-mycobacterial effect of Tamoxifen is independent of its well-known target, the estrogen receptor (ER) pathway, but instead acts by modulating autophagy and in particular the lysosomal pathway. Through RNA sequencing and microscopic colocalization studies, we show that Tamoxifen stimulates lysosomal activation and increases the localization of mycobacteria in lysosomes both *in vitro* and *in vivo*. Thus, our work highlights the HDT potential of Tamoxifen and proposes it as a repurposed molecule for the treatment of TB.

Introduction

It is estimated that 1.7 billion people are latently infected with *Mycobacterium tuberculosis (Mtb)*, the infectious agent causing tuberculosis (TB)[1]. In 2020, there were 10 million new cases and 1.4 million people died from the disease[2]. There is an alarming contribution of multidrug-resistant (MDR-TB) and extensively drug-resistant (XDR-TB) infections to the global antimicrobial resistance (AMR) disease burden[2]. Currently, there is no effective TB vaccine available, and the only licensed vaccine in use, Bacille Calmette-Guérin (BCG) has limited protective efficacy[3]. Although in the last decade a few new antibiotics have been approved for the treatment of MDR and XDR TB, including Bedaquiline[4], Delamanid[5], Linezolid[6] and Pretomanid[7], mutations conferring resistance against these drugs have already been found[8]. Therefore, novel tools and strategies are needed to combat this global threat, including more effective therapeutics that shorten the prolonged regimens of TB treatment (currently 6 months or more) and help preventing *de novo* resistance and TB relapse.

Intracellular bacteria such as *Mtb* manipulate cellular signaling pathways to promote their own survival in human cells, by creating a replicative niche or by subverting the immune system[9,10]. As a complement to classical antibiotics, host-directed therapy (HDT) has recently emerged as a novel concept in TB: HDT aims to enhance host defense by modulating processes in the host that restrict growth and survival of bacteria in their intracellular niches[11-15]. Large-scale chemical and genetic screens of molecular libraries targeting *Mtb*-infected cells have revealed a variety of potential HDT candidates that could be repurposed to combat TB, including groups of anti-inflammatory drugs, anti-psychotic drugs, and kinase inhibitors. These compounds affecting inflammatory pathways, lipid metabolism, and autophagy could be effective against both antibiotic-sensitive and -resistant bacteria, including MDR and XDR TB[11-15].

Autophagy is an intracellular degradation pathway vital to maintaining homeostasis by removing unwanted elements from the cytosol, such as misfolded protein aggregates, damaged organelles, and microbial invaders[16]. Due to the pro-homeostatic function of autophagy, drugs that modulate this process are currently being investigated as novel therapeutics for a wide variety of diseases[17]. Autophagy can inhibit intracellular infection by promoting the delivery of pathogens to lysosomes[18]. Although virulence mechanisms of pathogens may counteract autophagy to some extent, several studies have shown that induction of autophagy restricts *Mtb* intracellular growth and promotes its lysosomal degradation[16,19,20]. For these reasons, autophagy has become a priority target for anti-(myco)bacterial HDT development[13,15,18,21].

Tamoxifen, widely known for its use as a breast-cancer therapeutic[22-24], was identified as a promising molecule for host-directed inhibition of intracellular *Mtb* when we previously screened an autophagy-modulating compound library *in vitro* in human cells[25]. The main known targets of Tamoxifen are estrogen receptors (ERs). Tamoxifen can function either as an agonist or antagonist of the ER, depending on the presence of co-regulatory transcription factors[23]. Besides its use in breast-cancer therapy, Tamoxifen has more recently been studied in the context of various microbial infections and was found to possess direct antimicrobial effects against *Cryptococcus* and *Leishmania*[26,27]. In addition, it was reported that Tamoxifen had a direct anti-bacterial effect on *Mtb*, synergizing with first-line TB-antibiotics[28,29]. In contrast to these reported direct anti-microbial effects, there is evidence that the inhibitory effect of Tamoxifen on intracellular *Toxoplasma* growth is mediated in a host-directed manner by inducing autophagic degradation of the parasite-containing vacuole[30]. However, the role of Tamoxifen-induced autophagy and possibly other Tamoxifen-modulated host pathways in controlling *Mtb* or other bacterial infections remains incompletely defined.

In this study we have used *in vitro* and *in vivo* TB models to investigate the anti-bacterial and host-directed effects of Tamoxifen, and to elucidate the potential host-directed mechanisms involved. Lung-resident macrophages, consisting mainly of alveolar macrophages, represent the predominant host cell in the initial stages of *Mtb* infection[31,32]. The different functional responses of these cells can be represented by differentiating primary human macrophages *in vitro* into pro- and anti-inflammatory polarization states[33], which proved an effective approach to explore drug efficacy[34-36]. To investigate the *in vivo* therapeutic potential of Tamoxifen, we used the zebrafish TB model, which reiterates many features of human TB pathogenesis[37-39]. Specifically, the infection of zebrafish embryos with *Mycobacterium marinum* (*Mm*), which shares major virulence factors with *Mtb*, results in the development of granulomatous aggregates of leukocytes, the hallmark pathology of TB. Moreover, we have previously demonstrated that autophagy is a critical host defense mechanism of zebrafish to *Mm* infection, which makes this model well suited to investigate the autophagy-modulating properties of Tamoxifen in relation to mycobacterial pathogenesis[40-43].

Using *in vitro* infected human macrophages, we demonstrate a clear HDT effect of Tamoxifen against both drug-susceptible and MDR-*Mtb* strains. Furthermore, we found that Tamoxifen's HDT effect against intracellular mycobacteria is independent of ER signaling, both *in vitro* and *in vivo*. Complementary transcriptome profiling of zebrafish larvae revealed significant effects of Tamoxifen on pathways related to autophagy and lysosomal processes, both in the absence and presence of infection. Colocalization analyses of *Mtb* and *Mm* with autophagosomal and lysosomal markers showed that the HDT effect of Tamoxifen could not be directly attributed to its autophagy-inducing properties, but appears linked to modulation of lysosomal function and increased

delivery of mycobacteria to lysosomes. In conclusion, our results suggest that Tamoxifen inhibits intracellular mycobacteria primarily by promoting the efficacy of the lysosomal pathway, which was cross-validated across different hosts and different mycobacterial pathogens. Our findings position this clinically approved drug as a strong candidate for repurposing as an HDT molecule against TB, especially MDR- and XDR-TB.

Results

In vitro identification of Tamoxifen as a novel repurposed host-directed therapeutic

For *de novo* discovery of drugs with potential activity against intracellular *Mtb* we previously screened the Screen-Well Autophagy Library of clinically approved molecules, which identified Tamoxifen as a promising candidate[25]. To validate this initial screening result we tested Tamoxifen in our previously described primary human macrophage model system: we compared Tamoxifen's effects on intracellular infection in two polarized macrophage subsets, pro-inflammatory (Mφ1) and anti-inflammatory (Mφ2) macrophages[34,44,45]. Classical colony forming unit assays (CFU) were used to measure the effect of 24-hour treatment on *Mtb*-infection (Figure 1A). Tamoxifen treatment showed a significant decrease of *Mtb* outgrowth in both Mφ1 and Mφ2 (median reduction of detectable bacteria of 29% and 44%, respectively). To test whether Tamoxifen could also target another intracellular pathogen, we infected Mφ1 and Mφ2 with *Salmonella enterica* serovar Typhimurium (*Stm*) (Figure 1B). Tamoxifen showed high efficacy against intracellular *Stm* outgrowth (in several donors we observed up to 99% reduction of detectable bacteria).

To confirm that Tamoxifen acts in a host-directed and not direct antibacterial manner, we treated both *Mtb* and *Stm* in liquid broth with Tamoxifen at the same concentration (10 µM). *Mtb* growth was unaffected by the presence of Tamoxifen compared to negative control solvent DMSO, whereas the positive control anti-*Mtb* antibiotic rifampicin inhibited *Mtb* growth as expected (Figure 1C). Similarly, 10 µM of Tamoxifen
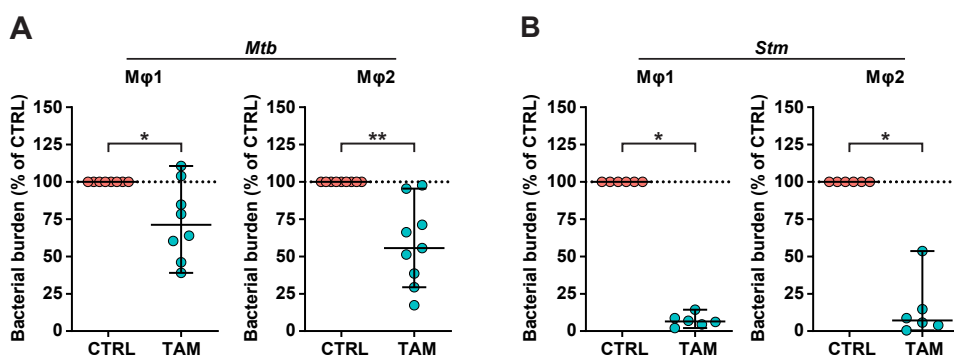
Figure 1. *In vitro* identification of Tamoxifen as a novel repurposed host-directed therapeutic
A-B. CFU assay of Mφ1 (left) and Mφ2 (right) infected with H37Rv-*Mtb* (A) or *Stm* (B) and treated with 10 µM of Tamoxifen or control (DMSO at equal v/v) for 24 hours. Each dot represents a single donor (8 and 9 donors for Mφ1 and Mφ2 respectively in A and 6 donors in B) and depicts the mean of 3 or 4 replicates. Dotted lines indicate control set at 100% and median + 95% confidence intervals are shown for every condition. Statistical significance was tested using Wilcoxon matched-pairs signed rank test.
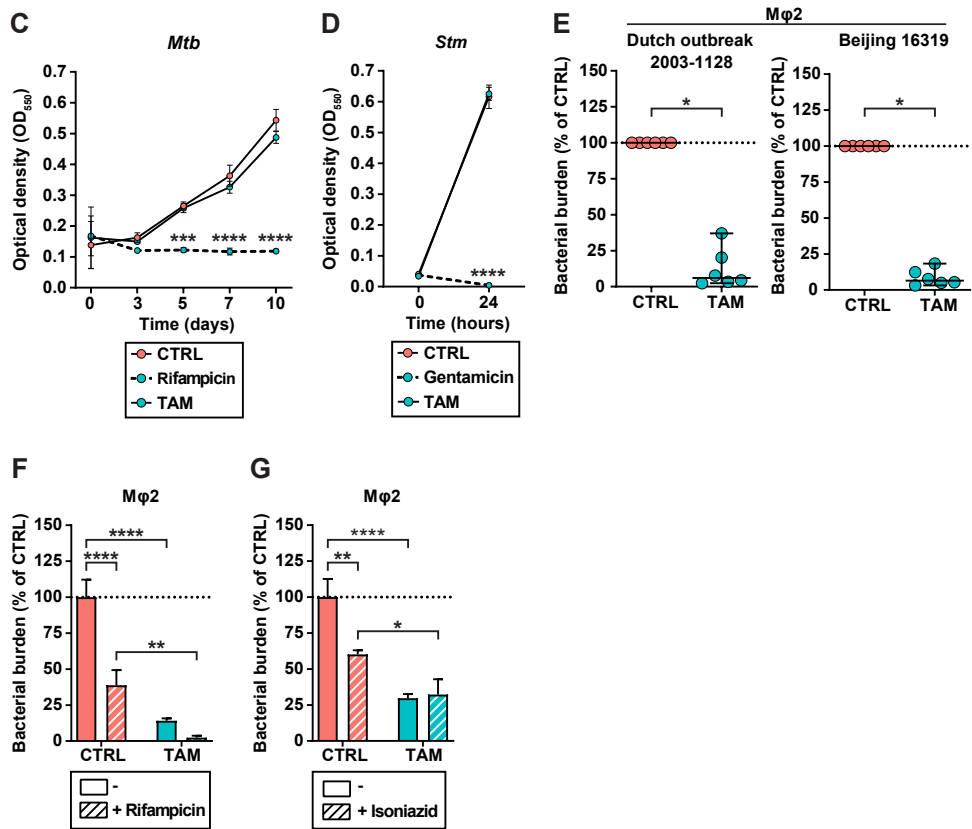
4

Figure 1. (continued)
C-D. H37Rv-*Mtb* growth (C) or *Stm* growth (D) in liquid culture during treatment with 10 μM of Tamoxifen or control (DMSO at equal v/v) up to assay endpoint, day 10 (C) or overnight (D). Rifampicin (20 μg/ml) (C) or Gentamicin (50 μg/ml) (D) was used as a positive control for growth inhibition. Each line depicts the mean ± standard deviation of 3 replicates. Experiment shown is a representative of 3 independent experiments. Statistical significance of treatment versus control treatment was tested using a two-way ANOVA with Dunnett's multiple comparisons test.
E. CFU assay of Mφ2 infected with MDR-*Mtb* strain Dutch outbreak 2003-1128 (left panel) or *Mtb* Beijing strain 16319 (right panel) and treated with 10 μM of Tamoxifen or control (DMSO at equal v/v) for 24 hours. Each dot represents a single donor (6 donors in total) and depicts the mean of 3 replicates. Dotted lines indicate control treatment set at 100% and median + 95% confidence intervals are shown for every condition. Statistical significance was tested using Wilcoxon matched-pairs signed rank test.
F-G. CFU assay of Mφ2 infected with H37Rv-*Mtb* and treated for 24 hours with 10 μM of Tamoxifen or control (DMSO at equal v/v) in combination with suboptimal doses of the antibiotics Rifampicin (F, 0.05μg/ml) or Isoniazid (G, 0.4 μg/ml). Each bar depicts the mean ± standard deviation of 3 replicates from a representative donor (out of 4 donors tested in F and 3 donors in G), expressed as a percentage of the control treatment in the absence of antibiotic. Bars with solid colors represent Tamoxifen or control treatment only, bars with pattern represent the combination with antibiotic. Statistical significance was tested using a two-way ANOVA with Tukey's multiple comparisons test comparing Tamoxifen treatment (in the absence or presence of antibiotic) to the corresponding control treatment. (* = p<0.05, ** = p<0.01, *** = p<0.001 and **** = p<0.0001).

did not affect *Stm* growth, while the control anti-*Stm* antibiotic gentamicin completely prevented bacterial proliferation (Figure 1D).

Host-directed drugs are expected to work irrespective of the exact mycobacterial substrain targeted, including drug-susceptible and multi-drug resistant (MDR) *Mtb* strains. Since Tamoxifen demonstrated similar efficacy in both Mφ1 and Mφ2 we decided to

focus further on Mφ2 cells. Tamoxifen treatment of Mφ2 infected with two MDR-*Mtb* strains, *Mtb* Dutch outbreak strain 2003-1128 and *Mtb* Beijing strain 16319, significantly inhibited bacterial outgrowth in both cases (Figure 1E).

Additionally, since HDT molecules and classical antibiotics by definition target different molecules, positive interactivity might be anticipated during combined treatment. Indeed, Tamoxifen combined with a suboptimal dose of rifampicin (0.05 µg/ml) inhibited bacterial outgrowth more effectively than either molecule individually (Figure 1F). However, this effect was not observed when Tamoxifen was combined with a suboptimal dose of Isoniazid (0.4 µg/ml) (Figure 1G), suggesting that the effect of interactivity depends on the particular combination of Tamoxifen with antibiotics.

Taken together, we report strong HDT activity of Tamoxifen against both intracellular *Mtb* and *Stm*, in primary human macrophages regardless of their M1 or M2 polarization state. Furthermore, we demonstrate that Tamoxifen shows efficacy against both drug sensitive (DS)-*Mtb* and MDR-bacteria (*Mtb),* and that it might be used as adjunctive to classical antibiotics like Rifampicin.

In vivo validation of Tamoxifen as HDT

To investigate the efficacy of Tamoxifen *in vivo*, we employed the well characterized zebrafish TB model, in which embryos are infected with their natural pathogen *Mycobacterium marinum*. We first validated Tamoxifen's efficacy on *Mm* employing the
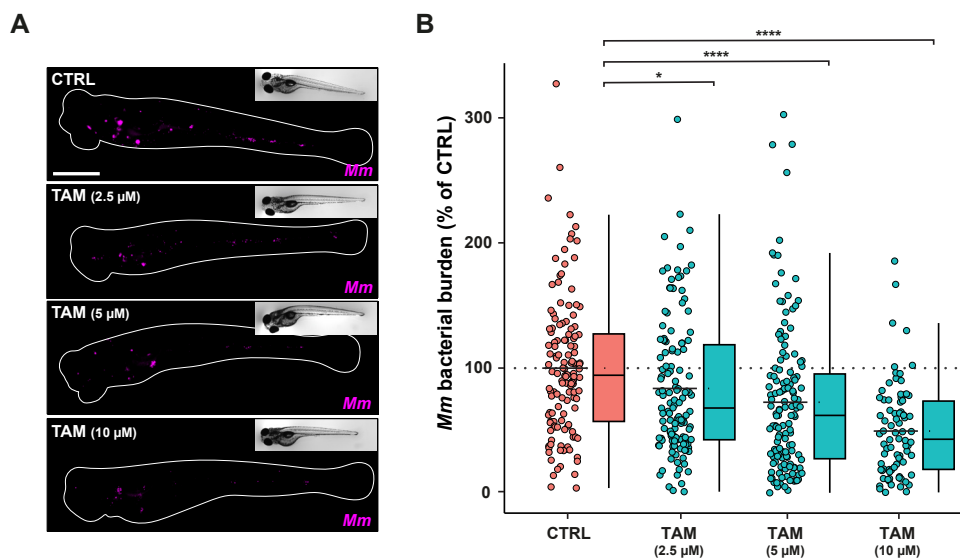
Figure 2. *In vivo* validation of Tamoxifen as HDT
A. Bacterial burden assay of mWasabi-expressing *Mm*-infected zebrafish larvae treated with increasing doses of Tamoxifen (2.5, 5 and 10 µM) or control (DMSO at 0.1% v/v). Treatment was started at 1 hpi and larvae anesthetized at 4dpi for imaging. Representative stereo fluorescent images of whole larvae infected with mWasabi-expressing *Mm*. Magenta shows *Mm*. Scale bar annotates 1 mm.
B. Quantification of bacterial burden shown in A. Bacterial burden was normalized to mean of the control, set at 100% and indicated with the dotted line. Data of 4 experimental repeats were combined (n = 132-139 per group). Each dot represents a single larva. Boxplots with 95% confidence intervals are shown and the black line in the boxplots indicates the group median, while the black line in the dot plot indicates the group mean. Statistical analysis was performed using a Kruskal-Wallis with Dunn's multiple comparisons test.
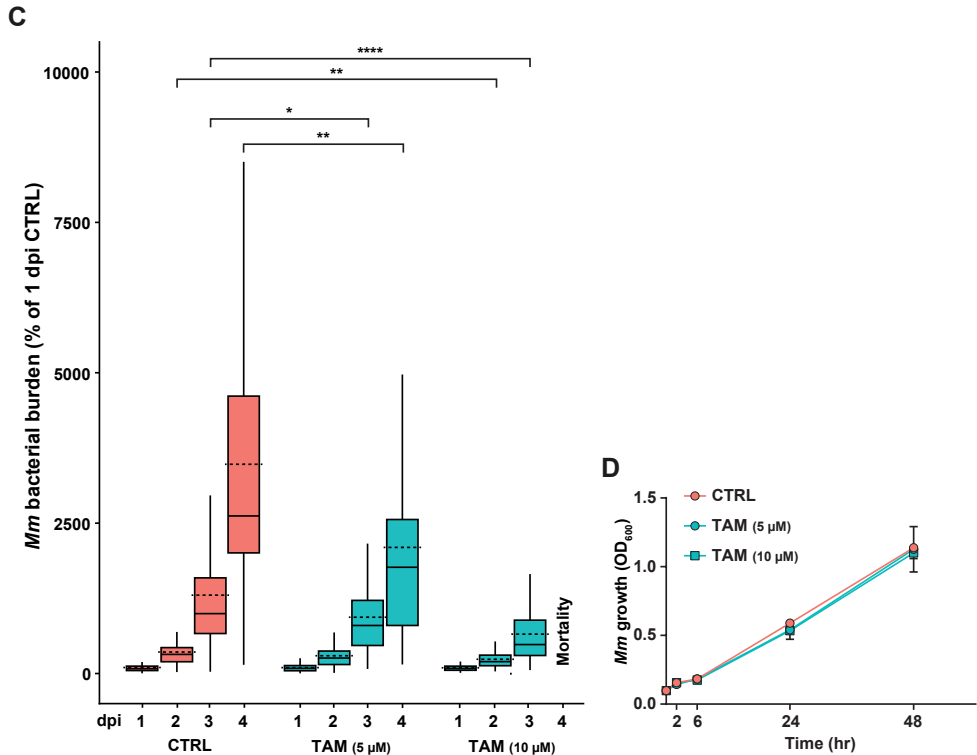
C

Figure 2. (continued)

C. Bacterial burden assay of mWasabi-expressing *Mm*-infected zebrafish larvae treated with 5 and 10 µM of Tamoxifen or control (DMSO at 0.1% v/v). Treatment was started at 1 hpi and larvae were anesthetized at 1, 2, 3 and 4 dpi for imaging. Bacterial burden was normalized to the control (DMSO at 1dpi) and data of 2 experimental repeats were combined (n = 65-70 per group). All larvae in the 10 µM group died between 3-4 dpi. Boxplots with 95% confidence intervals are shown and the black line in the boxplots indicates the group median, while the dotted line indicates the group mean. Statistical analysis was performed between treatment groups per timepoint using a Kruskal-Wallis with Dunn's multiple comparisons test.

D. *Mm* growth in liquid culture during treatment with 5 or 10 µM of Tamoxifen or control (DMSO at equal v/v) up to assay endpoint, day 2. Lines depict mean ± standard deviation of 2 experiments. Statistical significance of treatment versus control treatment was tested using a two-way ANOVA with Dunnett's multiple comparisons test.

($* = p<0.05$, $** = p<0.01$, $*** = p<0.001$ and $**** = p<0.0001$).

same flow-cytometry-based assay as used in the initial screen of HDT candidates for *Mtb*. As anticipated, Tamoxifen reduced *Mm* burden in human cells (Supplementary Figure 1). Next, we infected zebrafish embryos with mWasabi-labelled *Mm* and treated the infected embryos for 4 days with an increasing dose (2.5, 5 and 10 µM) of Tamoxifen or with vehicle (DMSO) control. Treatment with the highest dose (10 µM) resulted in developmental toxicity (e.g. oedema and lethality) in one third of the larvae, while no toxicity was observed at the lower doses. Bacterial burden was assessed by quantifying the bacterial fluorescence signal of infected larvae at 4 days post infection (dpi). All doses of Tamoxifen treatment reduced bacterial burden significantly compared to the control treatment in a dose-dependent manner (Figure 2A,B).

Next, we investigated the infection dynamics during treatment. We infected and treated embryos with Tamoxifen (5 and 10 µM) and imaged them daily for 4 days to monitor the establishing infection. Tamoxifen treatment reduced bacterial burden compared to

the control treatment from 2 dpi onward (Figure 2C). While drug-induced mortality was observed in the 10 μM group at experimental end point (4 dpi), Tamoxifen treatment with 5 μM resulted in an approximately 2-fold lower infection burden compared to the control treatment (DMSO) at 4 dpi (Figure 2C). Nonetheless, we observed that the infection burden increased between 2 and 4 dpi irrespective of treatment, indicating that Tamoxifen limits but does not fully inhibit bacterial growth.

Although we had found Tamoxifen to work as HDT on *Mtb*-infected cells *in vitro*, we sought to exclude that its effect in the zebrafish TB model was due to a direct antibacterial reduction of *Mm* growth as opposed to a host-directed effect. Therefore, we added Tamoxifen at doses of 5 and 10 μM to a liquid culture of *Mm* and assessed bacterial replication by measuring optical density (OD_{600}) at 5 time points starting from 2 hours until experimental endpoint (48 hours). No change in *Mm* growth rate could be observed (Figure 2D), confirming that the observed reduction of bacterial burden in zebrafish larvae is due to a host-directed and not a direct anti-bacterial effect of Tamoxifen. For further experiments in our *in vivo* TB model, we used Tamoxifen at 5 μM as this dose consistently lowered bacterial burden in zebrafish larvae in a host-directed manner, without causing developmental toxicity.

Tamoxifen alters leukocyte-specific gene expression without affecting macrophage or neutrophil migration *in vivo*

We decided to use the zebrafish TB model to investigate the host transcriptomic response to Tamoxifen treatment at a systemic level to obtain mechanistic insight into the observed inhibition of mycobacterial infection. Using RNA sequencing analysis, we compared the effects of Tamoxifen or DMSO control treatments on the transcriptomes of infected larvae at 2 dpi (3 dpf) and non-infected control larvae. Following quality control analysis and data processing (Supplementary Figure 2A-G), we analyzed the differential expression of transcripts in infected compared to non-infected larvae, in the absence of Tamoxifen. We found 204 genes to be differentially expressed during mycobacterial infection at 2 dpi (Supplementary Data File 1), including upregulation of the matrix metalloproteinase genes *mmp13a* and *mmp9* (Supplementary Figure 3A), which is consistent with earlier transcriptomic data of *Mm*-infected zebrafish at the same time point after infection[46]. Tamoxifen treatment of non-infected larvae caused differential expression of 141 genes, including genes involved in ER signaling and autophagy and other cellular stress pathways, consistent with known effects of Tamoxifen exposure[23,24,30,47-49] (Supplementary Data File 1)

Next, we analyzed the genes that showed interaction between Tamoxifen treatment and infection – that is genes whose expression during infection was altered by Tamoxifen treatment – and found 28 significant up- or down-regulated genes (Supplementary Table S2). These differential transcriptomic responses could be due to the lower bacterial burden in Tamoxifen-treated larvae during infection compared to the control group. For example, the lower upregulation of *mmp9* and *mmp13a* during Tamoxifen treatment is in line with a reduced inflammatory response in larvae with lower infection burden (Supplementary Figure 3A). However, we also found alterations in leukocyte-specific marker genes that were dependent on Tamoxifen treatment, such as *marco* and *mfap4*, suggesting that the number of leukocytes or their behavior during infection could be altered due to Tamoxifen treatment (Supplementary Figure 3B). Furthermore, we found 14 genes that were differentially regulated by both Tamoxifen treatment and infection compared to their respective control larvae (Supplementary Figure 3C and Supplementary Table S3). Interestingly, several of these 14 genes were related to immune processes (*cp*, *ccl34a*) (Supplementary Figure 3D) or highly expressed in leukocytes

(*mpx*, *grna*, *mfap4*) (Supplementary Figure 3E). This indicated that Tamoxifen treatment could modulate the cellular immune response even in the absence of infection. Together, these data correlate the decrease in bacterial burden in Tamoxifen-treated larvae with modulation of inflammatory responses and leukocyte development or behavior.

The development of *Mm* infection in zebrafish larvae depends strongly on migratory responses of macrophages and neutrophils, which aggregate to form the initial stages of TB granulomas[50-52]. In addition to transcriptional effects on leukocyte markers detected in our study, Tamoxifen has been reported to both inhibit and stimulate neutrophil migration[53-55]. Therefore, we asked if leukocyte migration was altered upon Tamoxifen treatment in our model. To this end we used an established injury-based migration assay, the tail amputation assay[56] in a double transgenic neutrophil and macrophage marker line and assessed the number of neutrophils and macrophages that migrated to the wound-induced site of inflammation. We did not find a significant difference between control or Tamoxifen treated groups in both neutrophil and macrophage numbers that migrated towards the injury (Supplementary Figure 3F-H). In conclusion, despite transcriptional changes in leukocyte-specific genes caused by Tamoxifen treatment, we did not detect altered leukocyte behavior in response to an inflammatory stimulus. Therefore, we decided to focus next on analysing the broad systemic effects of Tamoxifen treatment detected in the RNA sequencing analysis, specifically in relation to estrogen receptor (ER)-signaling and autophagy, processes both known to be modulated by Tamoxifen.
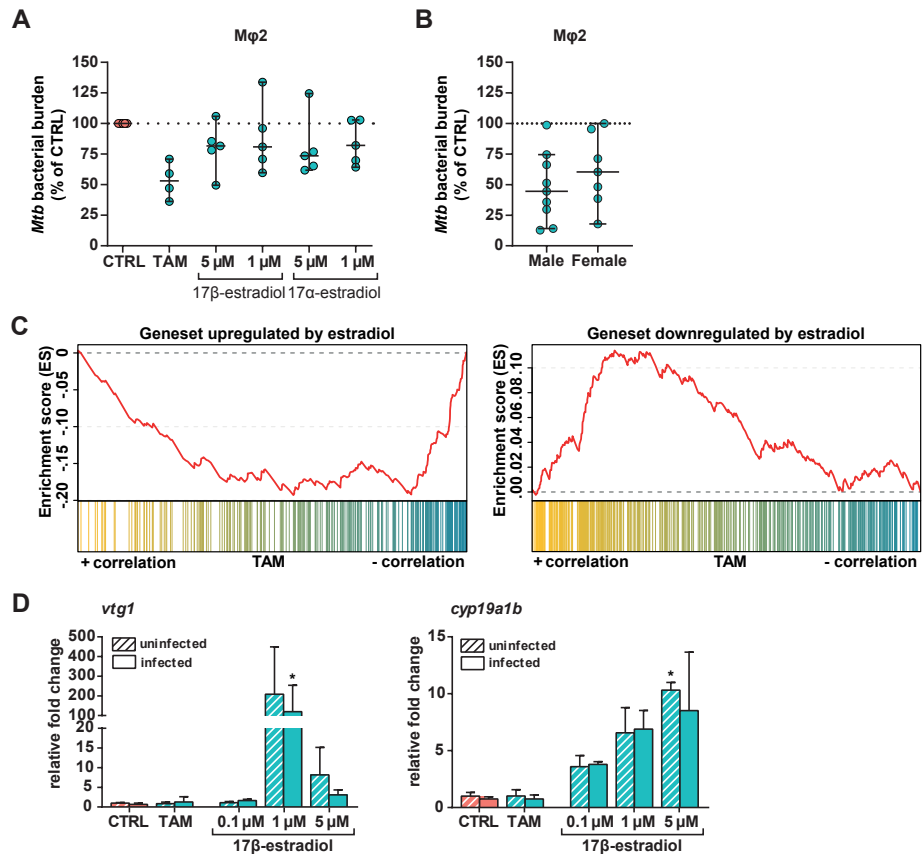
The host-directed effect of Tamoxifen is independent of ER signaling

The ER is the most well-characterized target of Tamoxifen. Tamoxifen is known to have a dual role, and can act both as an agonist and as an antagonist of ER signaling[23]. We therefore investigated whether modulating ER signaling by selective ER-agonistic and antagonistic compounds would affect bacterial burden, and in which direction. Human Mφ2 cells were infected with *Mtb* and treated with the ER agonists 17α-estradiol or 17β-estradiol, and bacterial outgrowth was measured by CFU. While Tamoxifen reduced *Mtb* growth by approximately 50% compared to control DMSO, neither ER agonist consistently affected *Mtb* growth, regardless of the concentration used (Figure 3A). Since Tamoxifen effects may depend on sex differences[57], and macrophage ER receptor levels differ between sexes[58], we investigated whether human donor sex influenced Tamoxifen HDT activity in primary macrophages from male vs. female donors. No significant differences in Tamoxifen's efficacy against intracellular bacteria were observed between male and female primary macrophages (Figure 3B).

Next, we studied if ER signaling is responsible for the effect of Tamoxifen on *Mm* infection *in vivo*. First, we used our zebrafish transcriptome data to identify classes of differentially expressed genes associated with Tamoxifen treatment by performing Gene Set Enrichment Analysis (GSEA)[59]. Tamoxifen-treated larvae showed downregulation of genes normally upregulated by 17β-estradiol, while genes that are normally downregulated by this ER agonist were upregulated after Tamoxifen treatment (Figure 3C). Considering this large effect of Tamoxifen on ER target genes, we investigated whether activating or blocking ER signaling *in vivo* would result in a similar reduction of bacterial burden as Tamoxifen treatment. We first used 17β-estradiol to activate ER signaling during *Mm* infection. To verify the effect of this agonist, we analyzed the expression level of two ER target genes, *vtg1* and *cyp19a1b*, by qPCR. After 17β-estradiol treatment (0.1, 1 and 5 μM), both infected and non-infected larvae showed markedly increased expression levels of *cyp19a1b* (reaching approx. 10-fold at the highest 17β-estradiol dose) and *vtg1* (approx. 100-fold at the 1 μM dose), while upregulation of these genes was not detected following treatment with Tamoxifen compared to

the control treatment (Figure 3D). Despite activation of ER signaling, no reduction in bacterial burden could be observed following 17β-estradiol treatment, while treatment with Tamoxifen reduced bacterial burden significantly compared to the control (Figure 3E). These results led us to consider the possibility that the effect on bacterial burden after Tamoxifen treatment might be due to the ER antagonistic role of Tamoxifen. Therefore, we investigated whether we could reproduce the effect of Tamoxifen using

Figure 3. The host-directed effect of Tamoxifen is independent of ER-signaling

A. CFU assay of Mφ2 infected with H37Rv-*Mtb* and treated with Tamoxifen (10 μM), 17β-Estradiol (1 or 5 μM), 17α-Estradiol (1 or 5 μM) or control (DMSO at equal v/v) for 24 hours. Each dot represents a single donor (4 to 5 donors were tested) and depicts the mean of 3 replicates normalized to control. Dotted line indicates control set at 100% and median + 95% confidence intervals are shown for every condition. Statistical significance was tested using Wilcoxon matched-pairs signed rank test with post-hoc Benjamini-Hochberg correction.

B. CFU assay of Mφ2 infected with H37Rv-*Mtb* and treated with 10 μM of Tamoxifen for 24 hours, separated for donor sex. The graph includes data points from Figure 1A and Figure 3A. Each dot represents a single donor (9 in male group, 7 in female group) and depicts the mean of 3 replicates normalized to control. Dotted line indicates control set at 100% and median + 95% confidence intervals are shown for every condition. Statistical significance was tested using a Mann-Whitney U test.

C. GSEA enrichment plots of downregulated (left panel) and upregulated (right panel) estradiol-responding genes in zebrafish larvae treated with 5 μM of Tamoxifen for 2 days (3 dpf). All estradiol-responding genes in the Tamoxifen-treated larval transcriptome were ranked according to their statistical significance and direction of regulation, from left (most significant, upregulated in yellow) to right (most significant, downregulated in blue). Each column depicts the position of an individual gene belonging to the gene set of estradiol-responding genes in the ranked list.

E *Mm* bacterial burden (% of CTRL)

CTRL, TAM, 0.1 µM, 1 µM, 5 µM — 17β-estradiol

*** (between CTRL and TAM)

F *Mm* bacterial burden (% of CTRL)

CTRL, TAM, 5 µM, 10 µM — Fulvestrant

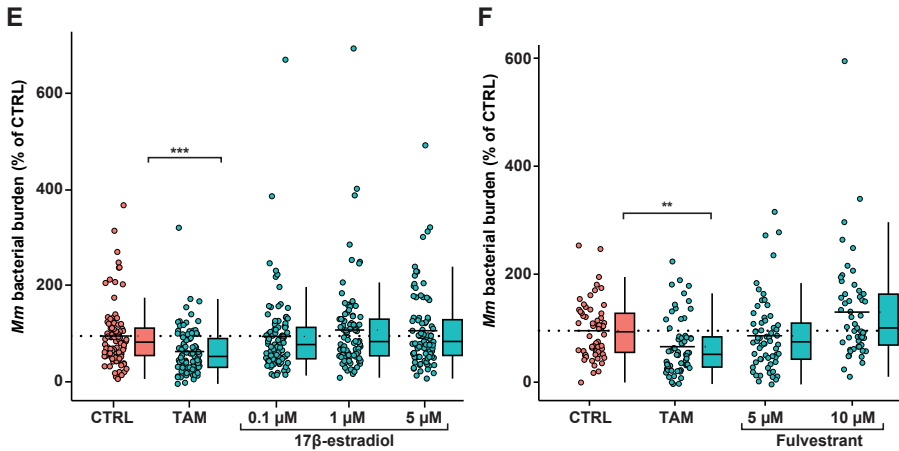** (between CTRL and TAM)

4

Figure 3. (continued)

D. Non-infected and mWasabi-expressing *Mm*-infected zebrafish larvae were treated with 5 µM of Tamoxifen, increasing doses of ER agonist 17β-estradiol (0.1, 1 and 5 µM) or control (DMSO at 0.05% v/v) starting 1 hpi. Transcript levels of two β-estradiol-responsive genes, *vtg1* (left graph) and *cyp19a1b* (right graph) were determined by qPCR analysis at 4 dpi. Data were normalized to the expression of the housekeeping gene TATA box binding protein (*tbp*) and data of 3 biological replicates were combined (n = 10 larvae per replicate). Each bar depicts the average fold change (FC) of transcript levels relative to non-infected or infected control treated zebrafish larvae and the error bar indicates SEM. Statistical analysis was performed using a Kruskal-Wallis with Dunn's multiple comparisons test. Effect of treatment compared to control was analyzed within the non-infected and infected group separately.

E. Bacterial burden assay of mWasabi-expressing *Mm*-infected zebrafish larvae treated as in D. Treatment was started at 1 hpi and larvae anesthetized at 4 dpi for imaging. Bacterial burden was normalized to the control and data of 3 experimental repeats were combined (n = 93-95 per group). Each dot represents a single larva. Boxplots with 95% confidence intervals are shown and the black line in the boxplots indicates the group median, while the black line in the dot plot indicates the group mean. Dotted line indicates control mean set at 100%. Statistical analysis was performed using a Kruskal-Wallis with Dunn's multiple comparisons test.

F. Bacterial burden assay of mWasabi-expressing *Mm*-infected zebrafish larvae treated with of 5 µM of Tamoxifen, increasing doses of ER antagonist Fulvestrant (5 and 10 µM) or control (DMSO at 0.05% v/v). Treatment was started at 1 hpi and larvae were anesthetized at 4 dpi for imaging. Bacterial burden was normalized to control and data of 2 experimental repeats were combined (n = 53-63 per group). Each dot represents a single larva. Boxplots with 95% confidence intervals are shown and the black line in the boxplots indicates the group median, while the black line in the dot plot indicates the group mean. Dotted line indicates control mean set at 100%. Statistical analysis was performed using a Kruskal-Wallis with Dunn's multiple comparisons test.
(* = p<0.05, ** = p<0.01 and *** = p<0.001).

the ER antagonist Fulvestrant. However, we did not detect an effect on bacterial burden using two different doses of Fulvestrant (Figure 3F). In contrast, we even observed a trend towards an increase of bacterial burden with the higher dose of Fulvestrant (10 µM). These data indicate that even though Tamoxifen treatment alters the host transcriptome related to ER signaling, activating or blocking ER signaling does not enhance the host-response to mycobacterial infection, suggesting Tamoxifen controls bacterial burden via alternative mechanisms than ER signaling.

To provide further evidence that Tamoxifen indeed functions independently of ER signaling, we followed a genetic approach. Two ER subtypes, ERα and ERβ, are conserved in vertebrate evolution. In zebrafish, *esr1* encodes for the ERα subtype, while due to a gene duplication event, two ER-genes; *esr2a* and *esr2b,* encode for ERβ[60,61]. For our study, we took advantage of an available *esr2b* loss-of-function mutant, which previously has been shown to be impaired in its response to viral infection[62]. We observed reduced *Mm* bacterial burdens in all Tamoxifen treated groups compared

to the DMSO control treated groups independently of the *esr2b*^{+/+}, *esr2b*^{+/-} or *esr2b*^{-/-} genotype (Supplementary Figure 4). Together, the pharmacological and genetic data show that neither activating nor blocking ER signaling in zebrafish leads to reduction of bacterial burden, and that Esr2b is not required for the effect of Tamoxifen on bacterial burden.

Collectively, these data suggest that Tamoxifen's HDT-effect against intracellular bacteria is independent from ER signaling. In line with this result, ER agonists do not consistently affect intracellular *Mtb* growth, the activity of the ER pathway in zebrafish is not required for Tamoxifen's HDT-effect and its efficacy in primary macrophages is not affected by the sex of the donor.

Tamoxifen treatment modulates autophagy in infected human macrophages and zebrafish

Because Tamoxifen induces and modulates autophagy, and because autophagy contributes to host defense against TB, we next investigated the role of Tamoxifen-induced autophagy in inhibiting bacterial outgrowth[30,49,63]. We first employed CYTO-ID, a tracer for autophagy related vesicles offering the advantage of staining all intracellular autophagy-related vesicles independent of proteins such as LC3. Mφ2 were infected with *Mtb,* subsequently treated for 4 hours with Tamoxifen, stained with the CYTO-ID tracer and visualized using confocal microscopy (Figure 4A). Although differences did not reach the statistical significance threshold due to well-known variation between human donors, a clearly increasing trend in both area of Cyto-ID vesicles and the colocalization of *Mtb* with these vesicles was observed in response to Tamoxifen (Figure 4B).
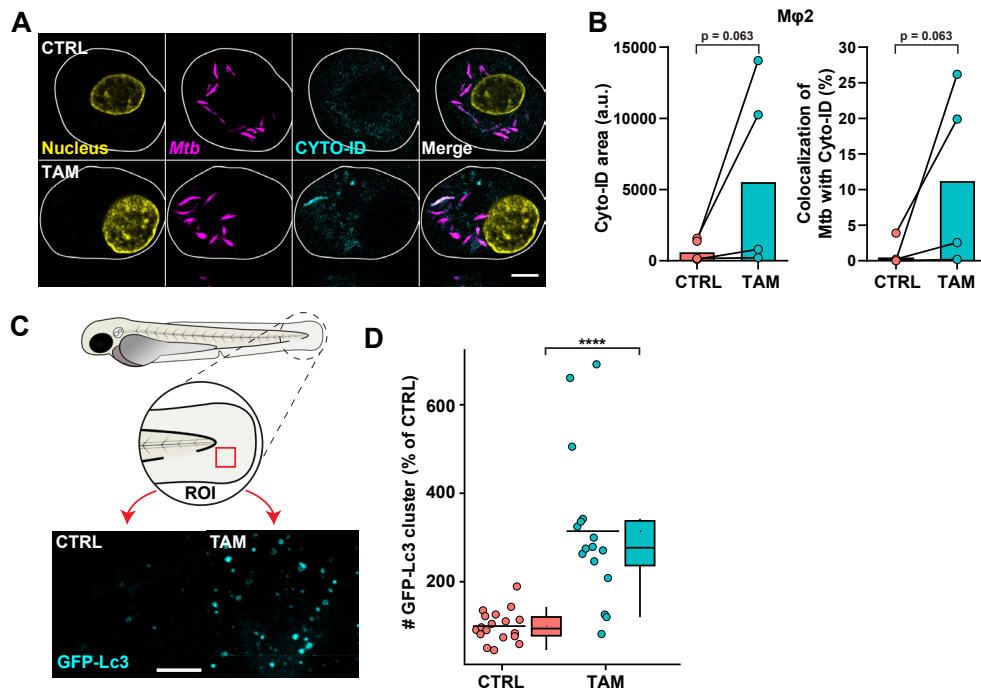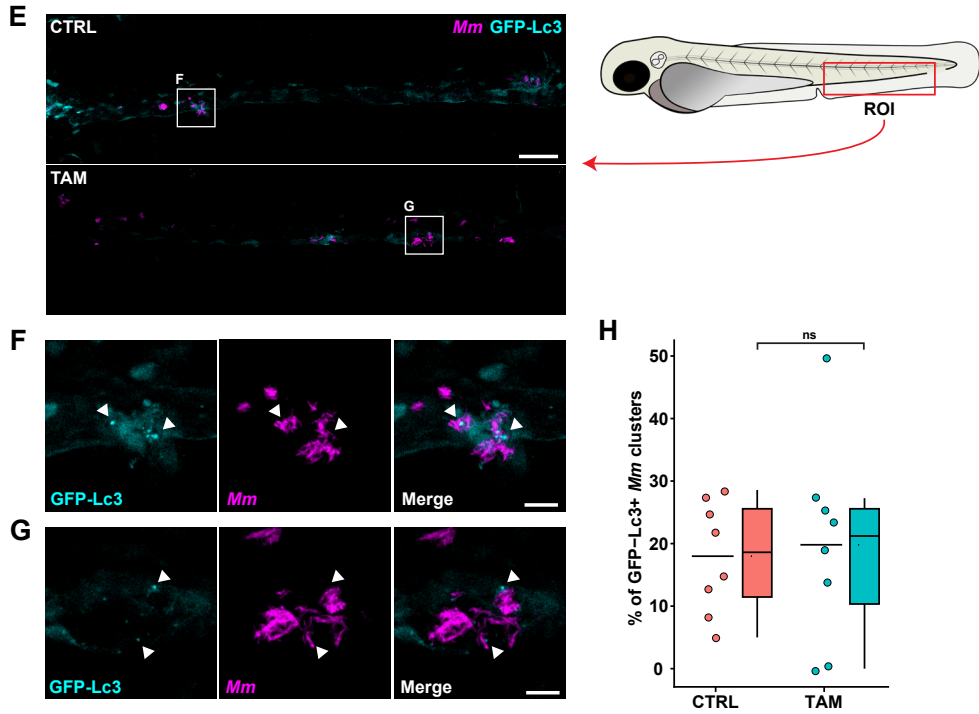

Figure 4. Tamoxifen treatment modulates autophagy in infected human macrophages and zebrafish
Figure and figure legend continued on next page.
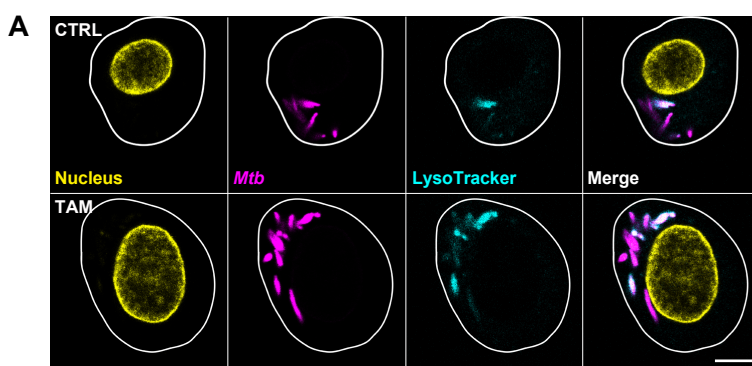
Figure 4. (continued)

A. Confocal microscopy of DsRed-expressing H37Rv-*Mtb*-infected Mφ2 treated with 10 µM of Tamoxifen or control (DMSO at equal v/v) for 4 hours. 30 min prior to the experimental endpoint cells were incubated with CYTO-ID to stain for autophagy related vesicles, fixed with 1% paraformaldehyde and counterstained for the nucleus using Hoechst 33342. In the representative images, yellow shows the nucleus, magenta shows *Mtb*, cyan shows autophagy related vesicles and the scale bar annotates 5 µm.

B. Quantification of Cyto-ID signals in A. The left panel displays Cyto-ID positive area, while the right panel displays *Mtb* colocalization with Cyto-ID positive vesicles. Each dot displays the mean of 3 or 4 replicates and represents a single donor (4 donors in total) with median indicated by colored bars. Statistical significance was tested using Wilcoxon matched-pairs signed rank test.

C. Confocal microscopy of transgenic GFP-Lc3 zebrafish larvae treated with 5 µM of Tamoxifen or control (DMSO at equal v/v). Treatment was started at 3 dpf and larvae were fixed with 4% paraformaldehyde at 4 dpf for imaging. Representative max projection images of GFP-Lc3 positive vesicles in the indicated region of imaging (ROI) in the tail fin are shown. Cyan shows GFP-Lc3 positive vesicles. Scale bar annotates 10 µm.

D. Quantification of GFP-Lc3 structures shown in C. Data were normalized to the control and data of 2 experimental repeats were combined (n = 16-18 per group). Each dot represents a single larva. Boxplots with 95% confidence intervals are shown and the black line in the boxplots indicates the group median, while the black line in the dot plot indicates the group mean. Statistical analysis was performed using a Mann Whitney test.

E. Confocal microscopy of mCherry-expressing *Mm*-infected transgenic GFP-Lc3 zebrafish larvae treated with 5 µM of Tamoxifen or control (DMSO at equal v/v). Treatment was started at 1 hpi and at 2 dpi larvae were fixed with 4% paraformaldehyde for imaging. Representative max projection images of the ROI in the caudal hematopoietic tissue (CHT) region are shown. Cyan shows GFP-Lc3 positive vesicles and magenta shows *Mm*. Scale bar annotates 50 µm.

F-G. Enlargement of areas indicated in E. Cyan shows GFP-Lc3 positive vesicles and magenta shows *Mm*. Arrowheads indicate GFP-Lc3-positive *Mm* clusters. Scale bar annotates 10 µm.

H. Quantification of GFP-Lc3 positive *Mm* clusters in the CHT region shown in E normalized to the control (n = 8 per group). Each dot represents a single larva. Boxplots with 95% confidence intervals are shown and the black line in the boxplots indicates the group median, while the black line in the dot plot indicates the group mean. Statistical analysis was performed using a Mann Whitney test. (**** = $p < 0.0001$).

We further explored the role of autophagy using a fluorescent zebrafish reporter line for Lc3[64]. Zebrafish larvae (3dpf) were treated with Tamoxifen for 24 hours and theGFP-Lc3 response was visualized in the thin tissue of the larval tail fin, which is well suited for using confocal microscopy (Figure 4C)[41]. We observed a significant increase in GFP-Lc3 positive structures in the Tamoxifen treated group compared to control treatment (Figure 4D), consistent with an autophagy modulating effect of Tamoxifen. In contrast, neither the ER agonist 17β-estradiol nor the ER antagonist Fulvestrant showed an increase in GFP-Lc3 positive structures (Supplementary Figure 5A,B). Therefore, we conclude that Tamoxifen modulates autophagy in the zebrafish model by an ER-independent mechanism. Next, to study whether Tamoxifen increased co-localization between GFP-Lc3 structures and *Mm*, we infected 1 dpf embryos of the GFP-Lc3 reporter line and imaged them at 2 dpi in their caudal hematopoietic tissue (CHT), a preferred location for aggregation of infected macrophages, the initial step in tuberculous granuloma formation[50]. We observed *Mm* clusters distributed from the injection site to the end of the tail and various GFP-Lc3 positive structures colocalized with these clusters (Figure 4E-G). However, we found no significant differences in the percentage of *Mm* clusters positive for GFP-Lc3 structures between control and Tamoxifen treatment (Figure 4H).

In summary, Tamoxifen treatment increased the abundance of autophagy vesicles both *in vitro* and *in vivo*, but the effects on colocalization of these vesicles with mycobacteria were modest or undetectable. This suggests that the autophagy induction by Tamoxifen might play a secondary or temporary role in decreasing mycobacterial infection.

Tamoxifen treatment alters lysosomal function and increases mycobacterial lysosomal localization *in vitro* and *in vivo*

Since mycobacteria can be targeted to lysosomes both dependent and independent of autophagy, we investigated whether vesicle maturation was affected by Tamoxifen. Therefore, a tracer for lysosomes, LysoTracker, was used to quantify acidic vesicles. Mφ2 were infected with *Mtb,* subsequently treated for 4 hours with Tamoxifen, stained with LysoTracker, and visualized using confocal microscopy (Figure 5A). Tamoxifen consistently and significantly increased both LysoTracker area and the colocalization of

Figure 5. Tamoxifen treatment alters lysosomal function and increases mycobacterial lysosomal localization *in vitro* and *in vivo*

A. Confocal microscopy of DsRed-expressing H37Rv-*Mtb*-infected Mφ2 treated with 10 µM of Tamoxifen or DMSO at equal v/v for 4 hours. 30 min prior to the experimental endpoint cells were incubated with LysoTracker Deep Red to stain for acidic vesicles, fixed with 1% paraformaldehyde and counterstained for the nucleus using Hoechst 33342. In the representative images, yellow shows the nucleus, magenta shows *Mtb*, cyan shows acidic vesicles and the scale bar annotates 5 µm.
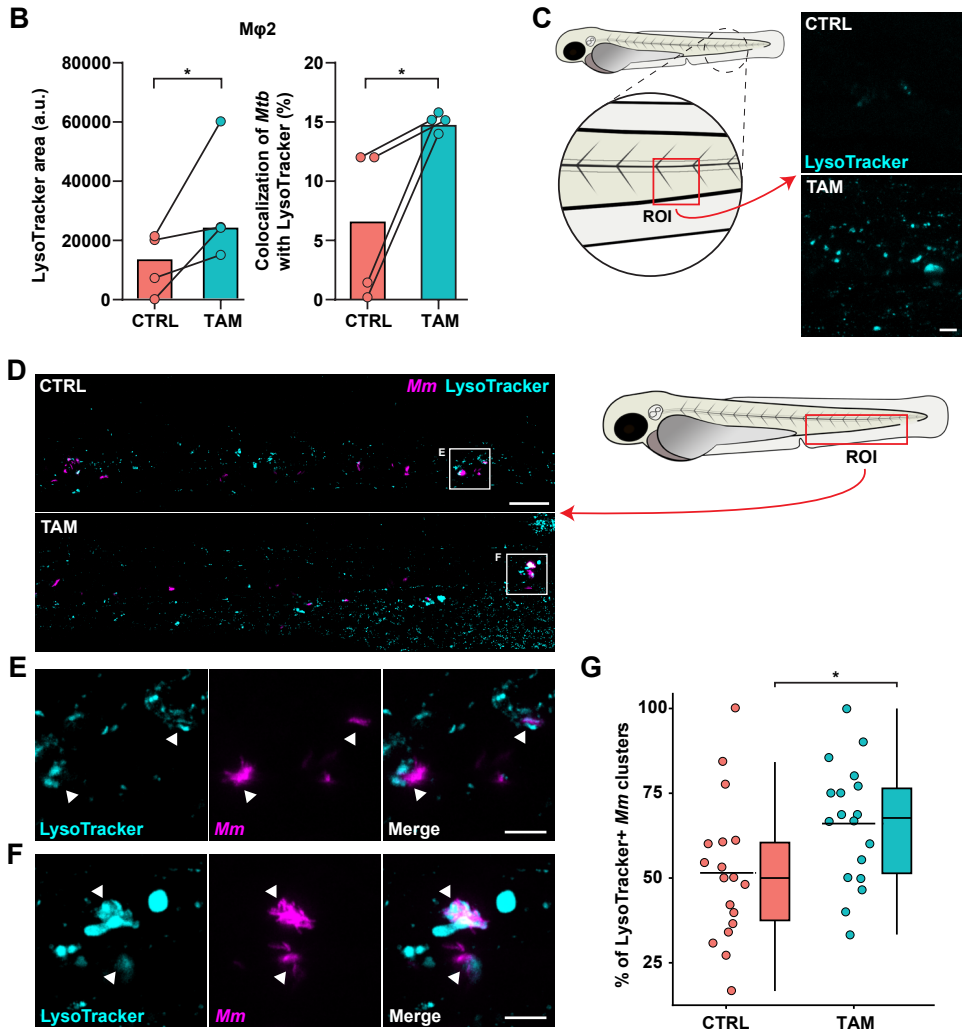
Figure 5. (continued)

B. Quantification of LysoTracker signal in A. The left panel displays Lysotracker positive area, while the right panel displays *Mtb* colocalization with Lysotracker positive vesicles. Each dots displays the mean of 3 or 4 replicates and represents a single donor (4 donors in total) with median indicated by colored bars. Statistical significance was tested using a paired T test.

C. Confocal microscopy max projection of the indicated ROI in zebrafish larvae treated with 5 μM of Tamoxifen or control (DMSO at equal v/v). Treatment was started at 31 hpf and at 3 dpf larvae were immersed in 5 μM of LysoTracker Red DND-99 for 1 hour and subsequently anesthetized for imaging. Cyan shows acidic vesicles. Scale bar annotates 10 μm.

D. Confocal microscopy max projection of mWasabi-expressing *Mm*-infected zebrafish larvae treated with 5 μM of Tamoxifen or control (DMSO at equal v/v). Treatment was started at 1 hpi and at 2 dpi larvae were immersed in 5 μM of LysoTracker Red DND-99 for 1 hour and subsequently anesthetized for imaging. Representative max projection images of LysoTracker positive *Mm* clusters in the CHT region are shown. Cyan shows acidic vesicles and magenta shows *Mm*. Scale bar annotates 50 μm.

E-F. Enlargement of areas indicated in D. Cyan shows acidic vesicles and magenta shows *Mm*. Arrowheads indicate LysoTracker positive *Mm* clusters. Scale bar annotates 10 μm.

G. Quantification of LysoTracker-positive *Mm* clusters normalized to the control and data of 3 experimental repeats were combined (n = 18 per group). Each dot represents a single larva. Boxplots with 95% confidence intervals are shown and the black line in the boxplots indicates the group median, while the black line in the dot plot indicates the group mean. Statistical analysis was performed using a Mann Whitney test. (* = p<0.05).

Mtb with LysoTracker (Figure 5B), suggesting that Tamoxifen's effect on the lysosomal response is relevant for *Mtb* infection.

In line with these results, further analysis of our zebrafish transcriptome data by means of pathway enrichment against the KEGG database revealed phagosome and lysosome pathways as strongly enriched in response to Tamoxifen treatment (Supplementary Table S4). In addition, Gene Ontology and Gene Set Enrichment Analysis (GSEA) highlighted that genes with molecular functions such as hydrolase and peptidase activity, biological processes such as proteolysis, and genes belonging to the lysosome compartment were enriched in response to Tamoxifen treatment (Supplementary Table S4). In fact, lysosomal genes such as vATPases, cathepsins and *lamp1* were all upregulated in the transcriptome of Tamoxifen treated larvae (Supplementary Data File 1). We therefore asked whether Tamoxifen treatment could also increase the localization of *Mm* clusters in lysosomes *in vivo*. Thus, we treated embryos with Tamoxifen or DMSO starting at 1 dpf (1 hpi) for 2 days and performed LysoTracker staining at 2 dpi (3 dpf). A strong increase in LysoTracker signal intensity was observed independent of infection (Figure 5C). Furthermore, imaging of the CHT region of infected larvae (Figure 5D-F) showed an increase in the colocalization between LysoTracker signal and *Mm* clusters from 50% in the control group to 65% in Tamoxifen-treated larvae (Figure 5G), corroborating the transcriptome results that Tamoxifen modulates lysosomal activity.Taken together, both in primary human macrophages and in zebrafish we observed increased LysoTracker signal intensity following treatment with Tamoxifen. Importantly, Tamoxifen led to enhanced targeting of *Mtb* and *Mm* to LysoTracker positive vesicles in these *in vitro* and *in vivo* infection models. Finally, this effect of Tamoxifen treatment was associated with modulated lysosomal gene expression. These data lead us to propose that Tamoxifen treatment reduces infection burden during mycobacterial infection by a host-dependent increase of lysosomal activity.

Discussion

The concept of HDT, combatting infection with drugs that empower the immune system, is increasingly explored as alternative or adjunctive therapeutic approaches against *Mtb* strains that are unresponsive to classical antibiotics[13-15,21], we demonstrate that the breast-cancer therapy drug Tamoxifen, restricts bacterial outgrowth of *Mtb* in primary human macrophages of different inflammatory states and differentiation stages. Furthermore, Tamoxifen shows high efficacy against clinical isolates of MDR-TB and is also active against *Stm*. Importantly, using *Mm*-infected zebrafish larvae as an *in vivo* TB model, we further substantiated the repurposing potential of Tamoxifen as an HDT for TB. Furthermore, we showed that Tamoxifen reduces bacterial burden independent of ER signaling and propose that the HDT effect of Tamoxifen is mediated primarily by enhancing lysosomal degradation pathways.

Tamoxifen has been proposed as a new antibiotic, because it was found to have direct antibacterial effects against intracellular pathogens[26-28]. Tamoxifen antimicrobial activity against *Mtb* was found at doses ranging from 16.7 to 26.8 μM, whereas lower doses similar to the ones used in our study lacked significant effects[28,29]. In agreement with this, when using Tamoxifen in low doses up to 10 μM, we did not observe any direct effect on either *Mtb*, *Stm* or *Mm* growth in liquid cultures. Importantly, both *Mtb* and *Stm* outgrowth and *Mm* burden in infected human macrophages and zebrafish larvae, respectively, were inhibited effectively by Tamoxifen at these doses (5-

10 μM). Therefore, we propose Tamoxifen as a potential new HDT against (myco-) bacterial infection. Recently, a structurally and functionally related breast-cancer drug, Bazedoxifene, has also been proposed as an HDT for TB, supporting the therapeutic potential of this class of chemicals[65]. The therapeutic potential of these drugs may extend to a wide range of bacterial pathogens, as Tamoxifen was recently found to have an immunomodulatory effect against MDR gram-negative bacilli, including *Acetinobacter baumannii*, *Pseudomonas aeruginosa*, and *Escherichia coli*[66].

The best-known target of drugs like Tamoxifen and Bazedoxifene is the ER[23,24]. However, our data do not support a role for the ER in mediating the anti-mycobacterial function of Tamoxifen. ER agonists did not significantly affect bacterial outgrowth *in vitro* and donor sex did not affect Tamoxifen restricted *Mtb* outgrowth in our model, despite that sex-based differences both in macrophage ER receptor amounts and differential effects of Tamoxifen treatment have been reported[57,58]. Furthermore, although zebrafish transcriptome analysis showed that Tamoxifen antagonized ER-signaling, Tamoxifen reduced *Mm* burden in *esr2b* mutants, indicating that its HDT effect is independent of the Esr2b receptor. Although we cannot exclude the involvement of other zebrafish ER receptors (*esr2a* and *esr1*), we considered the Esr2b receptor a prime candidate for mediating a potential HDT effect of Tamoxifen because an *esr2b* loss-of-function mutant has previously been linked to a host defense phenotype[62]. Finally, chemical activation and inhibition of ER-signaling using 17β-estradiol and Fulvestrant, respectively, did not affect mycobacterial burden while they are known to affect ER signaling in zebrafish[67,68]. Of note, we show several other host pathways, including autophagy and lysosome function to be modulated by Tamoxifen, in addition to ER-signaling. Thus, we propose that ER-independent host-directed effects of Tamoxifen are responsible for the reduction of bacterial burden.

The autophagy-inducing function of Tamoxifen, demonstrated in several previous studies[30,49], could be a plausible explanation for its anti-mycobacterial effect, considering that activating autophagy reduces mycobacterial burden both *in vitro* and *in vivo*[19,40], while impaired autophagy during mycobacterial infection is detrimental to the host[42,69,70]. Of note, the anti-TB effect of the related drug Bazedoxifene was attributed to its autophagy inducing properties, dependent on AKT/mTOR signaling and the production of mitochondrial reactive oxygen (ROS) species[65]. The authors proposed that Bazedoxifene suppresses *Mtb* outgrowth in macrophages by enhancing autophagosome formation, as chemical or genetic inhibition of autophagy reduced the antibacterial effect. Likewise, we also observed an autophagy increasing effect of Tamoxifen, which might similarly be related to mitochondrial ROS production, as our transcriptome data indicated a mitochondrial stress response, which is a well-known effect of Tamoxifen[47,48]. However, while our results suggested increased *Mtb* localization in Cyto-ID positive vesicles *in vitro*, we were unable to demonstrate an increase in the colocalization of *Mm* with the autophagy marker GFP-Lc3 *in vivo*. This might be explained by both the transient nature of GFP-Lc3-*Mm* associations and the properties of the tracer Cyto-ID, since next to autophagosomes it also stains autophagolysosomes[71], thus possibly reflecting mature lysosomes with degraded LC3. Taken together, it remains possible that increased autophagosome formation contributes to the HDT effect of Tamoxifen but, based on our data on autophagy and on the lysosomal responses we favor the hypothesis that Tamoxifen restricts mycobacterial growth primarily by augmenting the (auto)phagosome maturation process that delivers bacteria to lysosomes.

The clearance of (auto)phagosomes, as well as the delivery of neo-antimicrobial peptides, depends on the fusion with lysosomes resulting in autophagolysosomes or

phagolysomes[16,72,73]. Even in the absence of infection, the transcriptome of Tamoxifen-treated zebrafish showed major modulation of lysosomal function. Although studies in breast cancer cells have shown that Tamoxifen inhibits lysosomal acidification early during treatment due to its lysosomotrophic behavior[74-76], importantly, this rapidly triggers lysosomal activation that within hours restores pH and increases lysosomal volume to a level higher than prior to treatment[76]. In agreement, LysoTracker signal increased after Tamoxifen treatment in both human macrophages and zebrafish larvae. This appears to have a positive effect on infection control, as we observed increased colocalization between LysoTracker signal and both *Mtb in vitro* and *Mm* clusters *in vivo*. Based on these results, we propose that the primary mechanism underlying Tamoxifen's ability to restrict mycobacterial infection is an increase of bacterial sequestration to the lysosome due to *de novo* lysosomal biogenesis.

Taken together, our results suggest that the increase in lysosomal activation by the lysosomotrophic drug Tamoxifen empowers the host to better control intracellular infection with various intracellular pathogens, including *Mtb* and *Stm*, and that this underlies the host-mediated therapeutic effect observed in mycobacterial *in vitro* and *in vivo* infection models. This therapeutic effect, which enhances the killing capacity of macrophages, may be augmented by other immunomodulatory functions of Tamoxifen, recently described, including the reduction of inflammatory cytokine release and the stimulation of neutrophil extracellular trap formation[66,77]. Treatment with Tamoxifen vastly reduced *Mtb* outgrowth in primary human macrophages, while in combination with a low dose of Rifampicin affected *Mtb* outgrowth with close to a 2-log reduction. Importantly, 4 days of Tamoxifen monotherapy in the zebrafish model for TB achieved an average reduction of the overall infection load by 30%. Tamoxifen is therefore a prime candidate for further evaluation as an adjunctive therapy to classical antibiotics, particularly for MDR- and XDR-TB.

Materials and methods

Chemicals
Tamoxifen citrate (Tamoxifen) and rifampicin were purchased from Sigma-Aldrich, Zwijndrecht, The Netherlands. Isoniazid was purchased from SelleckChem, Munich, Germany. Gentamicin sulfate was bought from Lonza BioWhittaker, Basel, Switzerland and Hygromycin B was acquired from Life Technologies-Invitrogen, Bleiswijk, The Netherlands. Fulvestrantand 17β-estradiol were bought from Sigma-Aldrich. All compounds, except Gentamicin sulfate and Hygromycin B, were dissolved in 100% dimethyl sulfoxide (DMSO, Sigma-Aldrich) in stock concentrations of 10mM, aliquoted and kept at -80 °C.

Primary macrophage culture
Buffy coats were obtained from healthy donors after written informed consent (Sanquin Blood Bank, Amsterdam, The Netherlands). Peripheral blood mononuclear cells (PBMCs) were purified using density gradient centrifugation over Ficoll-Paque and monocytes isolated with subsequent CD14 MACS sorting (Miltenyi Biotec, Bergisch Gladsbach, Germany) as described previously[34,35]. Monocytes were then differentiated into pro-inflammatory (Mφ1) or anti-inflammatory (Mφ2) macrophages with 5 ng/ml of granulocyte-macrophage colony-stimulating factor (GM-CSF; Life Technologies-Invitrogen) or 50 ng/ml macrophage colony-stimulating factor (M-CSF; R&D Systems, Abingdon, UK), respectively, for 6 days with a cytokine boost at 3 days, as previously

reported[44]. Cells were cultured at a density of 1×10^6 cells per ml in T75 flasks at 37°C/5% CO_2 in Gibco Roswell Park Memorial Institute (RPMI) 1640 medium or RPMI 1640 (Dutch modified) (Life Technologies-Invitrogen) supplemented with 10% FBS from Greiner Bio-One, Alphen a/d Rijn, The Netherlands and 2 mM L-alanyl-L-glutamine (GlutaMAX) (PAA, Linz, Austria), 100 U/ml penicillin and 100 µg/ml streptomycin (both Life Technologies-Invitrogen) (complete RPMI). Macrophages were harvested using Trypsin-EDTA 0.05% (ThermoFisher Scientific) and scraping. Macrophage differentiation was evaluated by quantification of IL-10 and IL-12p40 secretion using ELISA in the presence or absence of 24-hour stimulation with 100 ng/ml of lipopolysaccharide (LPS; InvivoGen, San Diego, United States).

Zebrafish culture
Zebrafish were maintained and handled in compliance with the local animal welfare regulations as overseen by the Animal Welfare Body of Leiden University (license number: 10612). All practices involving zebrafish were performed in accordance with European laws, guidelines and policies for animal experimentation, housing, and care (European Directive 2010/63/EU on the protection of animals used for scientific purposes). The present study did not involve any procedures within the meaning of Article 3 of Directive 2010/63/EU and as such is not subject to authorization by an ethics committee. Zebrafish lines (Supplementary Table S1) were maintained according to standard protocols (www.zfin.org). Zebrafish eggs were obtained by natural spawning of single crosses to achieve synchronized developmental timing. Eggs from at least 5 couples were combined to achieve heterogeneous groups. Eggs and embryos were kept in egg water (60 µg/ml sea salt, Sera Marin, Heinsberg, Germany) at ~28.5 °C after harvesting and in embryo medium after infection and/or treatment (E2, buffered medium, composition: 15 mM NaCl, 0.5mM KCl, 1 mM MgSO¬4, 150 µM KH2PO4, 1 mM CaCl2 and 0.7 mM NaHCO3) at ~28.5 °C for the duration of experiments.

Zebrafish genotyping
Larvae obtained by incrossing heterozygous *esr2b* mutants (*esr2b*^{+/-}) zebrafish were genotyped at the end point of infection experiments. Larvae were collected individually in 100 µl of 50 mM NaOH. Samples were heated to 95 °C for 10 min until the larvae dissolved, cooled to 4 °C and then 10 µl of 1 M Tris, pH 7.5, was added to neutralize the basic solution and centrifuged to pull down any tissue debris, essentially as described [78]. Supernatant was directly used for PCR amplification of the genetic region of interest followed by Sanger sequencing to identify the genotype (BaseClear, Netherlands). Sequences of the primers are provided in Supplementary Table S1.

Bacterial cultures
Mtb (H37Rv), DsRed-expressing H37Rv, mWasabi-or mCherry- expressing *Mm* M-strain[79,80] were cultured in Difco Middlebrook 7H9 broth (Becton Dickinson, Breda, the Netherlands) supplemented with 10% ADC (Becton Dickinson), 0.05% Tween 80 (Sigma-Aldrich) and 50 µg/ml Hygromycin B (Life Technologies-Invitrogen). *Stm* strain SL1344 was cultured in Difco lysogeny broth (LB) (Becton Dickinson). *Mtb* and *Stm* were cultured at 37°C while *Mm* was grown at ~28.5°C

Bacterial infection of human cells
Mtb and *Mm* suspensions were prepared from a running culture, which were one day prior to infection diluted to a density corresponding with early log-phase growth (optical density at 550 or 600 nm ($OD_{550/600}$) of 0.25). *Stm* was grown overnight, subsequently diluted 1:33 in fresh LB and used after approximately 3 hours of incubation, when log-phase growth was achieved (OD_{600} of 0.5). Bacteria were diluted in complete RPMI or

complete IMDM without antibiotics for infection of primary cells and MelJuSo cells, respectively, as described previously[34,35]. We consistently used a multiplicity of infection (MOI) of 10 for all *in vitro* infection experiments. Primary cells and MelJuSo cells, seeded at a density of 30,000 and 10,000 cells per well, respectively, in 96-well flat-bottom plates 1 day prior to infection, were inoculated with 100 µl of the bacterial suspension. Cells were subsequently centrifuged for 3 min at 800 rpm and incubated at 37°C/5% CO_2 for 20 min in case of *Stm* infections or 60 min in case of *Mtb* and *Mm* infections. Extracellular bacteria were then washed away with culture medium containing 30 µg/ml Gentamicin sulfate, incubated for 10 min at 37°C/5% CO2, followed by replacement with medium containing 5 µg/ml Gentamicin sulfate and, if indicated, chemical compounds until readout. MOI of the inoculum was verified by a standard colony-forming unit (CFU) assay.

Bacterial infection of zebrafish embryos

Fresh *Mm* inoculum was prepared for every infection experiment as described[81]. The final inoculum was resuspended in PBS containing 2% (w/v) polyvinylpyrrolidone (PVP40). The injection dose was determined by optical density measurement (OD_{600} of 1 corresponds to ~100 CFU/nl). Infection experiments were carried out according to previously described procedures[81]. In brief, microinjections were performed using borosilicate glass microcapillary injection needles (Harvard Apparatus, 300038, 1mm O.D. x 0.78mm I.D.) prepared using a micropipette puller device (Sutter Instruments Flaming/Brown P-97). Needles were mounted on a micromanipulator (Sutter Instruments MM-33R) positioned under a stereo microscope. Prior to injection at 30 hours post fertilization (hpf), embryos were anesthetized using 200 µg/ml buffered 3-aminobenzoid acid (Tricaine, Sigma-Aldrich) in egg water. They were then positioned on a 1% agarose plate (in egg water) and injected into the blood island with an 1 nL inoculum containing ~200 CFU *Mm*. For assessment of bacterial burden, larvae were anesthetized using tricaine at 4 days post infection (dpi), positioned on a 1% agarose (in egg water) plate and imaged using a Leica M205 FA stereo fluorescence microscope equipped with a DFC345 FX monochrome camera. Bacterial burden was determined based on fluorescent pixel quantification[82].

Chemical compound treatments

Cells were treated with chemical compound or 100% DMSO at equal v/v in medium containing 5 µg/ml gentamicin sulfate as described previously[34,35]. Treatment of zebrafish embryos was performed by immersion. Stock concentrations were diluted to treatment doses in complete IMDM or embryo medium without antibiotics, for human cells and zebrafish embryos, respectively. As a solvent control treatment, 100% DMSO was diluted to the same concentration as the compound treatment. If different tamoxifen treatment doses were used in the same zebrafish embryo experiment, the solvent control concentration corresponding to the highest tamoxifen treatment dose was used. Precise doses of compound treatments and solvent control concentrations as well as the durations of treatment are described in the figure legends for each individual experiment.

Colony-forming unit (CFU) assay

Cells were lysed in H_2O containing 0.05% SDS (ThermoFisher Scientific). Lysates of *Mtb*-infected cells were 5-fold serially diluted in 7H9 broth, and 10 µl droplets were spotted onto square Middlebrook 7H10 agar plates. Plates were incubated at 37°C for 12-14 days and bacterial colonies quantified using a microscope with a magnification of 2.5 times to enhance early detection of bacterial growth. Lysates of *Stm*-infected cells were serially diluted in 10-fold steps in LB broth, and 10 µl droplets were spotted onto

square LB agar plates and incubated overnight at 37°C.

Liquid bacterial growth assay

Stm or *Mtb* and *Mm* culture in logarithmic growth phase was diluted to an OD_{550} or OD_{600} of 0.05 in LB broth or 0.1 in complete 7H9 broth respectively, of which 200 µl per flat-bottom 96-well was incubated with chemical compound, antibiotic or DMSO at equal v/v at indicated concentrations. *Stm* growth (OD_{550}) was measured after overnight incubation at 37°C, while *Mm* growth was evaluated during 2 days of incubation at ~28.5°C and *Mtb* growth for 10 days of incubation at 37°C.

Flow cytometry

Infected cells were at experimental endpoint washed with 100 µl of PBS and detached by incubation in 50 µl of Trypsin-EDTA 0.05% for several minutes. Single cell suspensions were fixed by adding 100 µl of 1.5% paraformaldehyde with subsequent incubation for 60 min at 4°C. Acquisition was performed using a BD FACSCalibur combined with a High Throughput Sampler (HTS) (BD BioSciences). Data were analyzed using FlowJo software v9.

Immunostaining

Cells were seeded on poly-d-lysine coated glass-bottom (no. 1.5) 96-well plates (MatTek, Ashland, Massachusetts, United States) that were pre-washed with PBS, at a density of 30,000 per well. After overnight incubation, cells were infected with DsRed-expressing *Mtb* at a MOI of 10 as described above. At the indicated experimental endpoint, cells were washed three times with PBS and fixed for 60 min at RT using 1% methanol-free EM-grade formaldehyde (ThermoFisher Scientific) diluted in PBS. Cells were washed with PBS and remaining reactive formaldehyde was quenched using 100 µl of Glycine solution (1.5 mg/ml in PBS) for 10 min at RT. Fluorescent dyes LysoTracker Deep Red (ThermoFisher Scientific) (75nM) and Cyto-ID 2.0 (Enzo LifeSciences) (1:500) were added to the cells 30 minutes prior to treatment endpoint and, after the washing and fixation procedure described above, counterstained with 50 ul of 2 µg/ml Hoechst 33342 (Sigma-Aldrich) at RT in the dark. For staining using antibodies, cells were permeabilized in 0.1% Triton-X (Sigma-Aldrich) diluted in PBS for 10 min at RT and Fc-receptors were subsequently blocked using 5% human serum (HS; Sanquin Blood bank, Amsterdam, The Netherlands) for 45 min at RT. After removal of the 5% HS, cells were stained with 50 ul of primary antibody diluted in 5% HS for 30 min at RT, washed three times with 5% HS and incubated with 50 ul of secondary antibody in 5% HS for 30 min at RT in the dark. After washing three times with 5% HS, cells were counterstained with Hoechst 33342 and Phalloidin as described above. Images, at least 3 per well, were acquired using a Leica TCS SP8 X WLL confocal system and 63X oil immersion objective. Hybrid detectors were used with a time gate to switch off data collection during the pulse.

Colocalization analysis of *Mtb*-infected cells was performed as follows. Image background was subtracted using the rolling ball (20-pixel radius) algorithm with Fiji software version 1.53c[83]. CellProfiler 3.0.0[84] was used to first correct for non-homogenous illumination if necessary, then for the segmentation of both the fluorescent bacteria and marker of interest using global thresholding with intensity-based declumping[84]. For every experiment, segmentation was performed with both a range of thresholds and adaptive three-class Otsu thresholding independently to confirm segmentation results. Then per image the overlap of *Mtb* with marker of interest was calculated as percentage of object overlap. To avoid potentially confounding results, two donors were excluded from colocalization results (Figures 4A and 5B) due to extensive intensity background

levels in treated samples.

GFP-Lc3 and LysoTracker imaging in zebrafish larvae

For visualization of Lc3 dynamics, Tg(CMV:EGFP-map1lc3b) larvae were embedded in 1.5% low melting point agarose (weight per volume, in egg water) and imaged using a Leica TCS SPE confocal microscope. Imaging was performed using a 63x oil immersion objective (HC PL APO CS2, NA 1.42) in a region of the tail fin to detect EGFP-map1lc3b – further referred as GFP-Lc3 – positive vesicles. For quantification of acidic vesicles in presence and absence of infection, larvae were immersed in embryo medium containing 5 µM LysoTracker Red DND-99 solution (ThermoFisher Scientific) for 1 hour. Before mounting and imaging, larvae were washed 3 times with embryo medium. To determine colocalization between *Mm* and GFP-Lc3 or LysoTracker, fixed (GFP-Lc3) or live anesthetized (LysoTracker) larvae were embedded in 1.5% low melting agarose (in egg water) and imaged in the caudal hematopoietic tissue, using a Leica TCS SP8 confocal microscope with a 40x water immersion objective (HCX APO L U-V-I, NA 0.8). Images were obtained using Leica Las X software. For the quantification of GFP-Lc3 levels the find maxima algorithm with a noise tolerance of 50 was used in Fiji software version 1.53c. To determine association of GFP-Lc3 or LysoTracker with bacteria, manual counting was performed on the obtained confocal images using Leica Las X software.

Tail amputation of zebrafish larvae

Embryos of an Tg(mpeg1:mcherryF)/Tg(mpx;gfp) double transgenic line were anesthetized using tricaine at 3 days post fertilization (dpf), positioned on a 1% agarose (in egg water) plate and the tails were partially amputated with a 1 mm sapphire blade (World Precision Instruments) under a Leica M165C stereomicroscope[85]. After amputation larvae were incubated in embryo medium for 4 hours and fixed using 4% paraformaldehyde. After fixation, larvae were positioned on a 1% agarose (in egg water) plate and imaged using a Leica M205 FA stereofluorescence microscope equipped with a DFC345 FX monochrome camera. Macrophages were detected based on the fluorescence of their mCherry label and neutrophils were detected based on their GFP label. The number of leukocytes recruited to the wounded area were counted as described previously[85].

RNA isolation, cDNA synthesis and qPCR

Zebrafish larvae (10 per sample) were collected at the experimental endpoint in QIAzol lysis reagent (Qiagen, Hilden, Germany). RNA was isolated using miRNeasy mini kit (Qiagen, Hilden, Germany) according to the manufacturer's instructions and the iScript cDNA Synthesis Kit (BioRad, Hercules, US) was used for reverse-transcription of the extracted total RNA. Quantitative RT-PCR (qPCR) was performed on a BioRad CFX96 machine following a two-step protocol with 40 cycles with a 95 °C melting temperature for 15s and 60 °C annealing and amplification for 30s. All reactions on the 3 biological replicates (3 samples/treatment group) were performed with 3 technical replicates (3 wells/sample). Analysis of qPCR results was performed using the ΔΔCt method and data were normalized to the expression of the housekeeping gene *tbp* (TATA box binding protein). Two ER-target genes were analyzed: *cyp19a1b* (cytochrome P450, family 19, subfamily A, polypeptide 1a) and *vtg1* (vitellogenin 1). Sequences of the primers are provided in Supplementary Table S1.

RNA sequencing and data analysis

Tamoxifen treatment of zebrafish larvae was performed from 1 hour post infection (hpi) until 2 dpi (3 dpf). Next, larvae were collected (10 per sample) for RNA isolation as described above. RNA integrity was assessed by Bioanalyzer (Agilent, Santa Clara, US)

and all samples were found to have a RIN ≥ 9.5. Of the total RNA, 3µg was used to create RNAseq libraries using the Illumina TruSeq strand-specific mRNA polyA preparation kit (Illumina, San Diego, US). The resulting RNAseq library was sequenced for at least 10 million reads per sample using an Illumina HiSeq2500 with a read length of 1 × 50 nucleotides (Baseclear, Leiden, The Netherlands). Four biological replicates for each treatment and infection regime were sequenced and mapped and quantified against the *D. rerio* GRCzv11 using Salmon v0.14.1[86]. Downstream analysis of the quantified libraries was performed in RStudio 1.2.5001[87] running R 3.6.1[88]. Libraries were imported using tximport v.1.12.3[89]. Differential gene expression was assessed via pairwise comparisons using DESeq2 v1.24.0[90] following a linear model taking into account possible gene expression differences from the embryo parents, drug treatments, infections, and its interaction (design: ~genotype + treatment + infection + treatment:infection). Statistical significance was defined by s-value ≤ 0.005 using apeglm[91]. S-values are aggregate statistics that have been recently proposed as an alternative to adjusted *p*-value and false discovery rate (FDR), calculating the probability of getting the sign of an effect wrong in biological contexts[92].

Venn Diagram and enrichment analysis, including pathway and GO analysis as well as Gene Set Enrichment Analysis with the C2 "Curated Gene Sets" and C5 "GO Gene Sets" collections from the Molecular Signatures Database (MSigDB) were performed as previously described[43]. Raw data are deposited into the Gene Expression Omnibus under accession number GSE178919. The data and code to recapitulate all figures and findings in this manuscript are available at https://github.com/gabrifc/rnaseq-tamox-amio.

Data analysis and statistics

The unpaired T test or One-way ANOVA with Dunnett's or Hold-Sidak's multiple comparison test was applied when assessing differences between 2 or more groups, respectively, of unpaired data representing technical replicates. Mann-Whitney U test was applied for testing differences between unpaired data representing biological replicates. When assessing differences between 2 or more groups with paired observations of biological replicates, the Wilcoxon matched-pairs signed rank test was used, except for data that was normally distributed according to the Shapiro-Wilk test, which was assessed using a paired T test. Two-way ANOVA with Dunnett's or Tukey's multiple comparison test was used when the effect of two independent variables was tested simultaneously to either a control mean or every other mean of data representing technical replicates, respectively. Data were normalized to the mean of the control group and independent repeats were combined , unless otherwise indicated. The number of experiments combined is indicated in the figure legend for each experiment. With exception of the transcriptome profiling analysis, all analyses were performed using GraphPad Prism 8 and the statistical test performed for each experiment is described in the figure legend. Dot plot graphs of zebrafish experiments were made using the raincloud plots application at https://gabrifc.shinyapps.io/raincloudplots/[93].

References

1. Houben, R. M. G. J. & Dodd, P. J. The Global Burden of Latent Tuberculosis Infection: A Re-estimation Using Mathematical Modelling. *Plos Med* **13**, doi:ARTN e1002152, 10.1371/journal.pmed.1002152 (2016).

2. WHO. Global Tuberculosis Report 2020. *World Health Organization* (2020).

3. Davenne, T. & McShane, H. Why don't we have an effective tuberculosis vaccine yet? *Expert Rev Vaccines* **15**, 1009-1013, doi:10.1586/14760584.2016.1170599 (2016).

4. Diacon, A. H. *et al*. Randomized pilot trial of eight weeks of bedaquiline (TMC207) treatment for multidrug-resistant tuberculosis: long-term outcome, tolerability, and effect on emergence of drug resistance. *Antimicrob Agents Chemother* **56**, 3271-3276, doi:10.1128/AAC.06126-11 (2012).

5. Gler, M. T. *et al*. Delamanid for multidrug-resistant pulmonary tuberculosis. *N Engl J Med* **366**, 2151-2160, doi:10.1056/NEJMoa1112433 (2012).

6. Lee, M. *et al*. Linezolid for treatment of chronic extensively drug-resistant tuberculosis. *N Engl J Med* **367**, 1508-1518, doi:10.1056/NEJMoa1201964 (2012).

7. Keam, S. J. Pretomanid: First Approval. *Drugs* **79**, 1797-1803, doi:10.1007/s40265-019-01207-9 (2019).

8. Kadura, S. *et al*. Systematic review of mutations associated with resistance to the new and repurposed Mycobacterium tuberculosis drugs bedaquiline, clofazimine, linezolid, delamanid and pretomanid. *J Antimicrob Chemother* **75**, 2031-2043, doi:10.1093/jac/dkaa136 (2020).

9. Vergne, I., Gilleron, M. & Nigou, J. Manipulation of the endocytic pathway and phagocyte functions by Mycobacterium tuberculosis lipoarabinomannan. *Front Cell Infect Microbiol* **4**, 187, doi:10.3389/fcimb.2014.00187 (2014).

10. Bussi, C. & Gutierrez, M. G. Mycobacterium tuberculosis infection of host cells in space and time. *FEMS Microbiol Rev* **43**, 341-361, doi:10.1093/femsre/fuz006 (2019).

11. Machelart, A., Song, O. R., Hoffmann, E. & Brodin, P. Host-directed therapies offer novel opportunities for the fight against tuberculosis. *Drug Discov Today* **22**, 1250-1257, doi:10.1016/j.drudis.2017.05.005 (2017).

12. Kilinc, G., Saris, A., Ottenhoff, T. H. M. & Haks, M. C. Host-directed therapy to combat mycobacterial infections*. *Immunological Reviews*, doi:10.1111/imr.12951 (2021).

13. Wallis, R. S. & Hafner, R. Advancing host-directed therapy for tuberculosis. *Nature Reviews Immunology* **15**, 255 (2015).

14. Zumla, A. *et al*. Towards host-directed therapies for tuberculosis. *Nat Rev Drug Discov* **14**, 511-512, doi:10.1038/nrd4696 (2015).

15. Hawn, T. R., Matheson, A. I., Maley, S. N. & Vandal, O. Host-directed therapeutics for tuberculosis: can we harness the host? *Microbiol Mol Biol Rev* **77**, 608-627, doi:10.1128/MMBR.00032-13 (2013).

16. Deretic, V., Saitoh, T. & Akira, S. Autophagy in infection, inflammation and immunity. *Nat Rev Immunol* **13**, 722-737, doi:10.1038/nri3532 (2013).

4

17. Maiuri, M. C. & Kroemer, G. Therapeutic modulation of autophagy: which disease comes first? *Cell Death Differ* **26**, 680-689, doi:10.1038/s41418-019-0290-0 (2019).

18. Keller, M. D., Torres, V. J. & Cadwell, K. Autophagy and microbial pathogenesis. *Cell Death Differ* **27**, 872-886, doi:10.1038/s41418-019-0481-8 (2020).

19. Gutierrez, M. G. *et al.* Autophagy is a defense mechanism inhibiting BCG and Mycobacterium tuberculosis survival in infected macrophages. *Cell* **119**, 753-766, doi:DOI 10.1016/j.cell.2004.11.038 (2004).

20. Bradfute, S. B. *et al.* Autophagy as an immune effector against tuberculosis. *Current Opinion in Microbiology* **16**, 355-365, doi:10.1016/j.mib.2013.05.003 (2013).

21. Tobin, D. M. Host-Directed Therapies for Tuberculosis. *Cold Spring Harb Perspect Med* **5**, doi:10.1101/cshperspect.a021196 (2015).

22. Zembutsu, H. Pharmacogenomics toward personalized tamoxifen therapy for breast cancer. *Pharmacogenomics* **16**, 287-296, doi:10.2217/pgs.14.171 (2015).

23. Gallo, M. A. & Kaufman, D. Antagonistic and agonistic effects of tamoxifen: significance in human cancer. *Semin Oncol* **24**, S1-71-S71-80 (1997).

24. Shagufta & Ahmad, I. Tamoxifen a pioneering drug: An update on the therapeutic potential of tamoxifen derivatives. *Eur J Med Chem* **143**, 515-531, doi:10.1016/j.ejmech.2017.11.056 (2018).

25. Heemskerk, M. K., CJ. Esselink, J. Carvalho dos Santos, C. van Veen, S. Gordijn, IF. Vrieling, F. Walburg, KV. Engele, CG. Dijkman, D. Wilson, L. Verreck, FAW. Ottenhoff, THM. Haks, MC. Repurposing diphenylbutylpiperidine-class antipsychotic drugs for host-directed therapy of *Mycobacterium tuberculosis* and *Salmonella enterica* infections. doi:https://doi.org/10.1101/2021.06.05.447191 (2021).

26. Miguel, D. C. *et al.* Tamoxifen as a potential antileishmanial agent: efficacy in the treatment of Leishmania braziliensis and Leishmania chagasi infections. *J Antimicrob Chemoth* **63**, 365-368, doi:10.1093/jac/dkn509 (2009).

27. Butts, A. *et al.* Estrogen receptor antagonists are anti-cryptococcal agents that directly bind EF hand proteins and synergize with fluconazole in vivo. *mBio* **5**, e00765-00713, doi:10.1128/mBio.00765-13 (2014).

28. Chen, F. C. *et al.* Pros and cons of the tuberculosis drugome approach--an empirical analysis. *PLoS One* **9**, e100829, doi:10.1371/journal.pone.0100829 (2014).

29. Jang, W. S. *et al.* Anti-Mycobacterial Activity of Tamoxifen Against Drug-Resistant and Intra-Macrophage Mycobacterium tuberculosis. *J Microbiol Biotechnol* **25**, 946-950, doi:10.4014/jmb.1412.12023 (2015).

30. Dittmar, A. J., Drozda, A. A. & Blader, I. J. Drug Repurposing Screening Identifies Novel Compounds That Effectively Inhibit Toxoplasma gondii Growth. *Msphere* **1**, doi:ARTN e00042-15, 10.1128/mSphere.00042-15 (2016).

31. Corleis, B. & Dorhoi, A. Early dynamics of innate immunity during pulmonary tuberculosis. *Immunol Lett* **221**, 56-60, doi:10.1016/j.imlet.2020.02.010 (2020).

32. Rothchild, A. C. *et al.* Alveolar macrophages generate a noncanonical NRF2-driven transcriptional response to Mycobacterium tuberculosis in vivo. *Sci Immunol* **4**, doi:10.1126/sciimmunol.aaw6693 (2019).

33. Thiriot, J. D., Martinez-Martinez, Y. B., Endsley, J. J. & Torres, A. G. Hacking the host: exploitation of macrophage polarization by intracellular bacterial pathogens. *Pathog Dis* **78**, doi:10.1093/femspd/ftaa009 (2020).

34. Korbee, C. J. *et al*. Combined chemical genetics and data-driven bioinformatics approach identifies receptor tyrosine kinase inhibitors as host-directed antimicrobials. *Nat Commun* **9**, 358, doi:10.1038/s41467-017-02777-6 (2018).

35. Moreira, J. D. *et al*. Functional Inhibition of Host Histone Deacetylases (HDACs) Enhances in vitro and in vivo Anti-mycobacterial Activity in Human Macrophages and in Zebrafish. *Frontiers in Immunology* **11**, doi:ARTN 36, 10.3389/fimmu.2020.00036 (2020).

36. Keiser, T. L. & Purdy, G. E. Killing Mycobacterium tuberculosis In Vitro: What Model Systems Can Teach Us. *Microbiology Spectrum* **5**, doi:UNSP TBTB2-0028-2016, 10.1128/microbiolspec. TBTB2-0028-2016 (2017).

37. Davis, J. M. *et al*. Real-time visualization of mycobacterium-macrophage interactions leading to initiation of granuloma formation in zebrafish embryos. *Immunity* **17**, 693-702, doi:10.1016/s1074-7613(02)00475-2 (2002).

38. Meijer, A. H. Protection and pathology in TB: learning from the zebrafish model. *Semin Immunopathol* **38**, 261-273, doi:10.1007/s00281-015-0522-4 (2016).

39. Berg, R. D. & Ramakrishnan, L. Insights into tuberculosis from the zebrafish model. *Trends Mol Med* **18**, 689-690, doi:10.1016/j.molmed.2012.10.002 (2012).

40. van der Vaart, M. *et al*. The DNA damage-regulated autophagy modulator DRAM1 links mycobacterial recognition via TLR-MYD88 to autophagic defense [corrected]. *Cell Host Microbe* **15**, 753-767, doi:10.1016/j.chom.2014.05.005 (2014).

41. Hosseini, R. *et al*. Correlative light and electron microscopy imaging of autophagy in a zebrafish infection model. *Autophagy* **10**, 1844-1857, doi:10.4161/auto.29992 (2014).

42. Zhang, R. *et al*. The selective autophagy receptors Optineurin and p62 are both required for zebrafish host resistance to mycobacterial infection. *Plos Pathog* **15**, doi:ARTN e1007329, 10.1371/journal.ppat.1007329 (2019).

43. Zhang, R. *et al*. Deficiency in the autophagy modulator Dram1 exacerbates pyroptotic cell death of Mycobacteria-infected macrophages. *Cell Death Dis* **11**, 277, doi:10.1038/s41419-020-2477-1 (2020).

44. Verreck, F. A. W., de Boer, T., Langenberg, D. M. L., van der Zanden, L. & Ottenhoff, T. H. M. Phenotypic and functional profiling of human proinflammatory type-1 and anti-inflammatory type-2 macrophages in response to microbial antigens and IFN-gamma- and CD40L-mediated costimulation. *Journal of Leukocyte Biology* **79**, 285-293, doi:10.1189/jlb.0105015 (2006).

45. Verreck, F. A. *et al*. Human IL-23-producing type 1 macrophages promote but IL-10-producing type 2 macrophages subvert immunity to (myco)bacteria. *Proc Natl Acad Sci U S A* **101**, 4560-4565, doi:10.1073/pnas.0400983101 (2004).

46. Benard, E. L., Rougeot, J., Racz, P. I., Spaink, H. P. & Meijer, A. H. Transcriptomic Approaches in the Zebrafish Model for Tuberculosis-Insights Into Host- and Pathogen-specific Determinants of the Innate Immune Response. *Adv Genet* **95**, 217-251, doi:10.1016/bs.adgen.2016.04.004 (2016).

4

47. Cardoso, C. M., Custodio, J. B., Almeida, L. M. & Moreno, A. J. Mechanisms of the deleterious effects of tamoxifen on mitochondrial respiration rate and phosphorylation efficiency. *Toxicol Appl Pharmacol* **176**, 145-152, doi:10.1006/taap.2001.9265 (2001).

48. Nazarewicz, R. R. *et al.* Tamoxifen induces oxidative stress and mitochondrial apoptosis via stimulating mitochondrial nitric oxide synthase. *Cancer Res* **67**, 1282-1290, doi:10.1158/0008-5472.CAN-06-3099 (2007).

49. Pattingre, S., Bauvy, C., Levade, T., Levine, B. & Codogno, P. Ceramide-induced autophagy: to junk or to protect cells? *Autophagy* **5**, 558-560, doi:10.4161/auto.5.4.8390 (2009).

50. Davis, J. M. & Ramakrishnan, L. The role of the granuloma in expansion and dissemination of early tuberculous infection. *Cell* **136**, 37-49, doi:10.1016/j.cell.2008.11.014 (2009).

51. Yang, C. T. *et al.* Neutrophils exert protection in the early tuberculous granuloma by oxidative killing of mycobacteria phagocytosed from infected macrophages. *Cell Host Microbe* **12**, 301-312, doi:10.1016/j.chom.2012.07.009 (2012).

52. Torraca, V. *et al.* The CXCR3-CXCL11 signaling axis mediates macrophage recruitment and dissemination of mycobacterial infection. *Dis Model Mech* **8**, 253-269, doi:10.1242/dmm.017756 (2015).

53. Corriden, R. *et al.* Tamoxifen augments the innate immune function of neutrophils through modulation of intracellular ceramide. *Nat Commun* **6**, 8369, doi:10.1038/ncomms9369 (2015).

54. Ligeiro de Oliveira, A. P., Oliveira-Filho, R. M., da Silva, Z. L., Borelli, P. & Tavares de Lima, W. Regulation of allergic lung inflammation in rats: interaction between estradiol and corticosterone. *Neuroimmunomodulation* **11**, 20-27, doi:10.1159/000072965 (2004).

55. Moreland, J. G., Davis, A. P., Bailey, G., Nauseef, W. M. & Lamb, F. S. Anion channels, including ClC-3, are required for normal neutrophil oxidative function, phagocytosis, and transendothelial migration. *J Biol Chem* **281**, 12277-12288, doi:10.1074/jbc.M511030200 (2006).

56. Xie, Y., Meijer, A. H. & Schaaf, M. J. M. Modeling Inflammation in Zebrafish for the Development of Anti-inflammatory Drugs. *Front Cell Dev Biol* **8**, 620984, doi:10.3389/fcell.2020.620984 (2020).

57. Dluzen, D. E. & Mickley, K. R. Gender differences in modulatory effects of tamoxifen upon the nigrostriatal dopaminergic system. *Pharmacol Biochem Be* **80**, 27-33, doi:10.1016/j.pbb.2004.10.007 (2005).

58. Campesi, I., Marino, M., Montella, A., Pais, S. & Franconi, F. Sex Differences in Estrogen Receptor alpha and beta Levels and Activation Status in LPS-Stimulated Human Macrophages. *J Cell Physiol* **232**, 340-345, doi:10.1002/jcp.25425 (2017).

59. Subramanian, A. *et al.* Gene set enrichment analysis: a knowledge-based approach for interpreting genome-wide expression profiles. *Proc Natl Acad Sci U S A* **102**, 15545-15550, doi:10.1073/pnas.0506580102 (2005).

60. Menuet, A. *et al.* Molecular characterization of three estrogen receptor forms in zebrafish: binding characteristics, transactivation properties, and tissue distributions. *Biol Reprod* **66**, 1881-1892, doi:10.1095/biolreprod66.6.1881 (2002).

61. Griffin, L. B., January, K. E., Ho, K. W., Cotter, K. A. & Callard, G. V. Morpholino-mediated knockdown of ERalpha, ERbetaa, and ERbetab mRNAs in zebrafish (Danio rerio) embryos reveals differential regulation of estrogen-inducible genes. *Endocrinology* **154**, 4158-4169, doi:10.1210/en.2013-1446 (2013).

62. Lopez-Munoz, A. *et al.* Estrogen receptor 2b deficiency impairs the antiviral response of zebrafish. *Dev Comp Immunol* **53**, 55-62, doi:10.1016/j.dci.2015.06.008 (2015).

63. Nagelkerke, A., Bussink, J., Sweep, F. C. G. J. & Span, P. N. The unfolded protein response as a target for cancer therapy. *Bba-Rev Cancer* **1846**, 277-284, doi:10.1016/j.bbcan.2014.07.006 (2014).

64. He, C., Bartholomew, C. R., Zhou, W. & Klionsky, D. J. Assaying autophagic activity in transgenic GFP-Lc3 and GFP-Gabarap zebrafish embryos. *Autophagy* **5**, 520-526, doi:10.4161/auto.5.4.7768 (2009).

65. Ouyang, Q. *et al.* Bazedoxifene Suppresses Intracellular Mycobacterium tuberculosis Growth by Enhancing Autophagy. *Msphere* **5**, doi:10.1128/mSphere.00124-20 (2020).

66. Miro-Canturri, A. *et al.* Potential Tamoxifen Repurposing to Combat Infections by Multidrug-Resistant Gram-Negative Bacilli. *Pharmaceuticals (Basel)* **14**, doi:10.3390/ph14060507 (2021).

67. Hao, R. *et al.* Identification of estrogen target genes during zebrafish embryonic development through transcriptomic analysis. *PLoS One* **8**, e79020, doi:10.1371/journal.pone.0079020 (2013).

68. Vosges, M. *et al.* 17alpha-Ethinylestradiol and nonylphenol affect the development of forebrain GnRH neurons through an estrogen receptors-dependent pathway. *Reprod Toxicol* **33**, 198-204, doi:10.1016/j.reprotox.2011.04.005 (2012).

69. Wang, J. *et al.* Glucocorticoids Suppress Antimicrobial Autophagy and Nitric Oxide Production and Facilitate Mycobacterial Survival in Macrophages. *Sci Rep* **7**, 982, doi:10.1038/s41598-017-01174-9 (2017).

70. Yang, C. S. *et al.* The AMPK-PPARGC1A pathway is required for antimicrobial host defense through activation of autophagy. *Autophagy* **10**, 785-802, doi:10.4161/auto.28072 (2014).

71. Oeste, C. L., Seco, E., Patton, W. F., Boya, P. & Perez-Sala, D. Interactions between autophagic and endo-lysosomal markers in endothelial cells. *Histochem Cell Biol* **139**, 659-670, doi:10.1007/s00418-012-1057-6 (2013).

72. Ponpuak, M. *et al.* Delivery of cytosolic components by autophagic adaptor protein p62 endows autophagosomes with unique antimicrobial properties. *Immunity* **32**, 329-341, doi:10.1016/j.immuni.2010.02.009 (2010).

73. Alonso, S., Pethe, K., Russell, D. G. & Purdy, G. E. Lysosomal killing of Mycobacterium mediated by ubiquitin-derived peptides is enhanced by autophagy. *P Natl Acad Sci USA* **104**, 6031-6036, doi:10.1073/pnas.0700036104 (2007).

74. Altan, N., Chen, Y., Schindler, M. & Simon, S. M. Tamoxifen inhibits acidification in cells independent of the estrogen receptor. *P Natl Acad Sci USA* **96**, 4432-4437, doi:DOI 10.1073/pnas.96.8.4432 (1999).

75. Chen, Y., Schindler, M. & Simon, S. M. A mechanism for tamoxifen-mediated inhibition of acidification. *Journal of Biological Chemistry* **274**, 18364-18373, doi:DOI 10.1074/jbc.274.26.18364 (1999).

76. Lu, S. Y., Sung, T., Lin, N. W., Abraham, R. T. & Jessen, B. A. Lysosomal adaptation: How cells respond to lysosomotropic compounds. *Plos One* **12**, doi:ARTN e0173771, 10.1371/journal.pone.0173771 (2017).

77. Corriden, R. *et al.* Tamoxifen augments the innate immune function of neutrophils through modulation of intracellular ceramide. *Nature Communications* **6**, doi:ARTN 8369, 10.1038/ncomms9369 (2015).

78. Meeker, N. D., Hutchinson, S. A., Ho, L. & Trede, N. S. Method for isolation of PCR-ready genomic DNA from zebrafish tissues. *Biotechniques* **43**, 610, 612, 614, doi:10.2144/000112619 (2007).

79. van der Sar, A. M. *et al.* Mycobacterium marinum strains can be divided into two distinct types based on genetic diversity and virulence. *Infect Immun* **72**, 6306-6312, doi:10.1128/IAI.72.11.6306-6312.2004 (2004).

80. Takaki, K., Davis, J. M., Winglee, K. & Ramakrishnan, L. Evaluation of the pathogenesis and treatment of Mycobacterium marinum infection in zebrafish. *Nat Protoc* **8**, 1114-1124, doi:10.1038/nprot.2013.068 (2013).

81. Benard, E. L. *et al.* Infection of zebrafish embryos with intracellular bacterial pathogens. *J Vis Exp*, doi:10.3791/3781 (2012).

82. Stoop, E. J. M. *et al.* Zebrafish embryo screen for mycobacterial genes involved in the initiation of granuloma formation reveals a newly identified ESX-1 component. *Dis Model Mech* **4**, 526-536, doi:10.1242/dmm.006676 (2011).

83. Schindelin, J. *et al.* Fiji: an open-source platform for biological-image analysis. *Nat Methods* **9**, 676-682, doi:10.1038/nmeth.2019 (2012).

84. McQuin, C. *et al.* CellProfiler 3.0: Next-generation image processing for biology. *PLoS Biol* **16**, e2005970, doi:10.1371/journal.pbio.2005970 (2018).

85. Xie, Y. *et al.* Glucocorticoids inhibit macrophage differentiation towards a pro-inflammatory phenotype upon wounding without affecting their migration. *Dis Model Mech* **12**, doi:10.1242/dmm.037887 (2019).

86. Patro, R., Duggal, G., Love, M. I., Irizarry, R. A. & Kingsford, C. Salmon provides fast and bias-aware quantification of transcript expression. *Nature Methods* **14**, 417-419, doi:10.1038/nmeth.4197 (2017).

87. RStudio: Integrated Development for R. RStudio, PBC, Boston, MA (2020).

88. R: A language and environment for statistical computing. R Foundation for Statistical Computing, Vienna, Austria (2018).

89. Soneson, C., Love, M. & Robinson, M. Differential analyses for RNA-seq: transcript-level estimates improve gene-level inferences [version 2; peer review: 2 approved]. *F1000Research* **4:1521** (2016).

90. Love, M. I., Huber, W. & Anders, S. Moderated estimation of fold change and dispersion for RNA-seq data with DESeq2. *Genome Biol* **15**, 550, doi:10.1186/s13059-014-0550-8 (2014).

91. Zhu, A., Ibrahim, J. G. & Love, M. I. Heavy-tailed prior distributions for sequence count data: removing the noise and preserving large differences. *Bioinformatics* **35**, 2084-2092, doi:10.1093/bioinformatics/bty895 (2019).

92. Stephens, M. False discovery rates: a new deal. *Biostatistics* **18**, 275-294, doi:10.1093/biostatistics/kxw041 (2017).

93. Allen, M. A.-O., Poggiali, D. A.-O., Whitaker, K. A.-O., Marshall, T. R. & Kievit, R. A.-O. Raincloud plots: a multi-platform tool for robust data visualization. *Wellcome Open Res* **4:63** (2019).

4

Supplementary data, figures and tables

Supplementary Data File 1 can be downloaded via
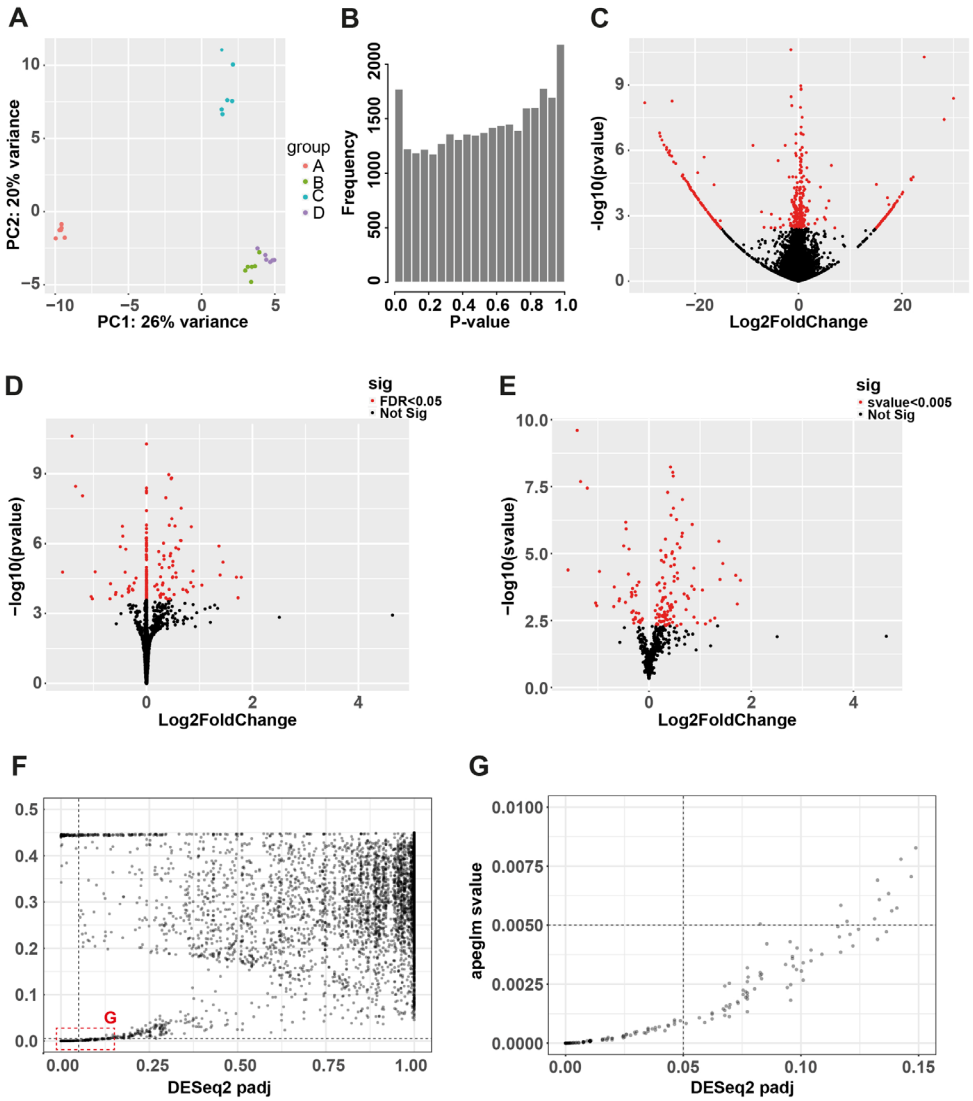https://doi.org/10.5281/zenodo.5788543
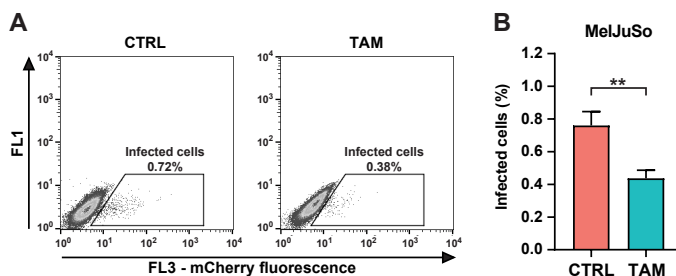
Supplementary Figure 1. Tamoxifen inhibits *Mm* burden in an *in vitro* infection model
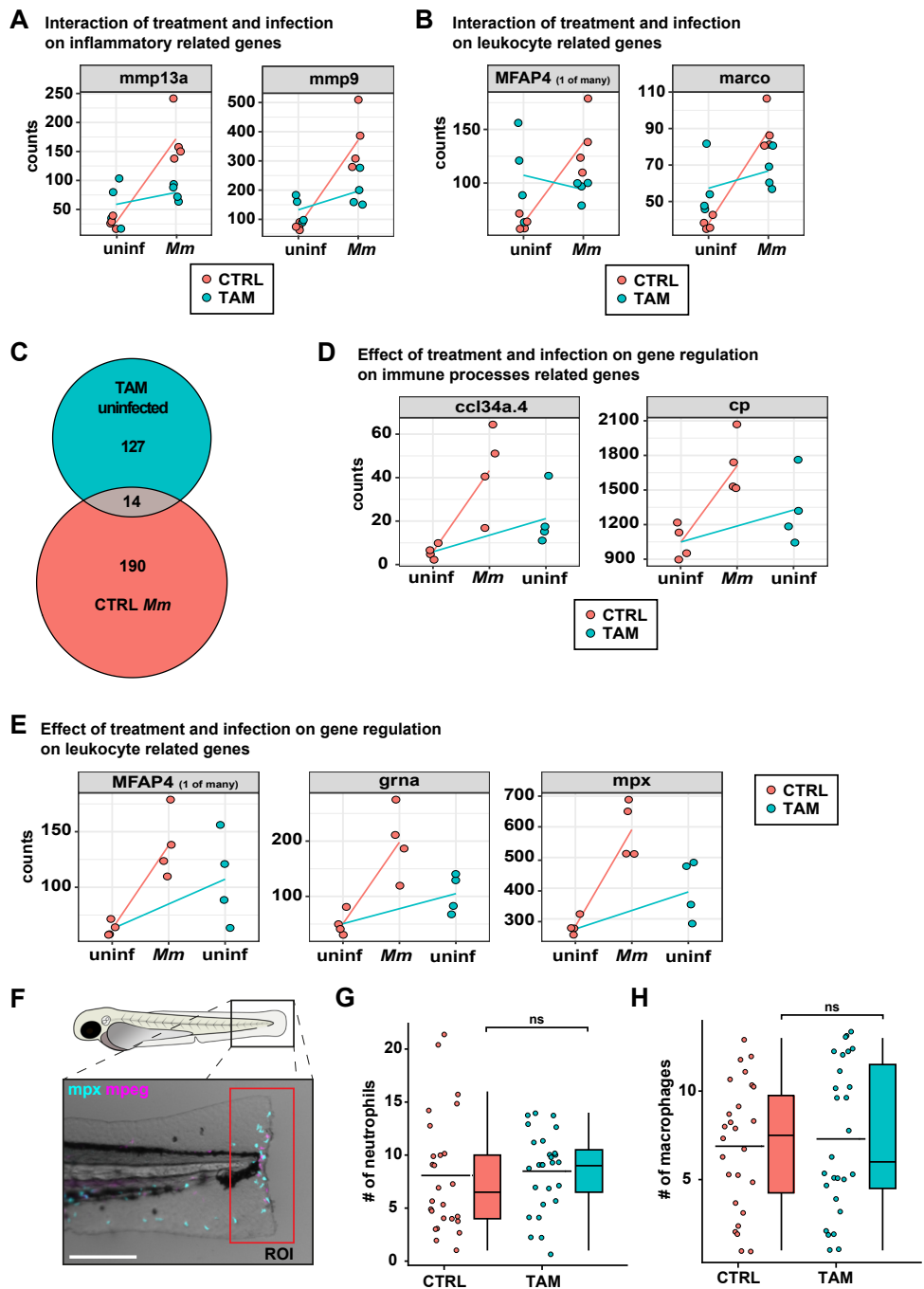**A.** Flow cytometric dot-plots of mCherry-expressing *Mm*-infected MelJuSo cells treated with 10 µM of Tamoxifen or control (DMSO at equal v/v) for 24 hours. Dot plots consist of 3 concatenated replicates and the experiment shown is a representative of 2 independent experiments.
B. Quantification of infected population shown in A. Each bar depicts the mean with standard deviation of 3 replicates. Statistical significance was tested an unpaired T test.
(** = p<0.01).

Supplementary Figure 2. Processing and quality control of zebrafish RNA sequencing data (figure on next page)
A. Principal component analysis (PCA) of transcriptomes of non-infected and *Mm*-infected zebrafish larvae treated with 5 µM of Tamoxifen or control (DMSO at equal v/v). Treatment was started at 1 hpi and isolation of RNA for RNA sequencing was performed at 2 dpi. Clustering of the different samples was driven by parent-pairs, over treatment or infection. Groups A-D indicate parent-pairs, each dot indicates a sample. Based on this result, we added the variable genotype to reflect that the major differences between samples are driven by parent-pairs in our analysis.
B. P-value histogram of the differential expression analysis of zebrafish larvae treated with 5 µM of Tamoxifen compared to treatment with control (DMSO at equal v/v), as in A. Histogram shape, which before adjusting for false discovery rates reveals test performance, showed a hill-shaped as opposed to a uniform distribution implying that the data does not fit the test assumption.
C. Volcano plot of the differential expression analysis of zebrafish larvae treated with 5 µM compared of Tamoxifen to treatment with control (DMSO at equal v/v), as in A. Red dots indicate significantly regulated genes (FDR-adjusted p-value (p.adj) ≤ 0.05), while black dots indicate non-significantly regulated genes. The subset of genes in the wings of the plot have low read counts, high inter-sample variation, and high calculated fold changes. Further analysis determined these genes as artifacts.
D. Volcano plot of the differential expression analysis as in C using apeglm to reduce variance for genes with little information while preserving large differences. The more conservative analysis method apeglm shrinks the fold-change to 0 for genes that contain insufficient information to accurately predict their fold-change. The genes with a fold change of 0 form a vertical line. Red dots indicate significantly regulated genes (p.adj) ≤ 0.05), while black dots indicate non-significantly regulated genes.
E. Volcano plot of the differential expression analysis as in D using s-values. Red dots indicate significantly regulated genes (s-value ≤ 0.005), while black dots indicate non-significantly regulated genes. By using s-values as opposed to FDR-adjusted p-values, the wings as depicted in C or vertical line as depicted in D are no longer present. Based on their s-values, these subsets of genes are deemed artifacts.
F. Correlation of transcriptome data analyzed using FDR-corrected p-values (as in D) compared to s-values (as in E). Each dot indicates a gene, the dashed lines indicate significance cut-offs. In the top left, there is a cluster of genes with low, significant adjusted p-value but high, non-significant s-value.
G. Zoom of area boxed in F, indicating the genes that are significant by both p-value (p.adj ≤ 0.05) and s-value (s ≤ 0.005).

A Interaction of treatment and infection
on inflammatory related genes

B Interaction of treatment and infection
on leukocyte related genes

C

D Effect of treatment and infection on gene regulation
on immune processes related genes

E Effect of treatment and infection on gene regulation
on leukocyte related genes


F

G

H

**Supplementary Figure 3. Tamoxifen alters leukocyte-specific gene expression without affecting macrophage
or neutrophil migration *in vivo***

*Figure legend continues on next page*

Supplementary Figure 3. (continued)

A-B. Interaction between Tamoxifen treatment and infection in genes that are differentially regulated (s-value ≤ 0.005, as in supplementary Figure 2E) and whose expression during infection was found to be dependent on Tamoxifen treatment. Panel A shows genes related to inflammation and B shows genes related to leukocyte function. Each dot represents the normalized gene read count of a single biological replicate (n = 10 larvae), while the line connects the means.

C. Venn diagram showing the total number of genes differentially regulated by Tamoxifen treatment in the absence of infection and by *Mm* infection in the absence of Tamoxifen treatment.

D-E. Normalized gene read counts of genes whose expression was regulated by both Tamoxifen treatment and *Mm* infection individually. D shows genes related to immune function and E shows genes related to leukocyte function. Each dot represents the normalized gene read count of a single group of larvae (n = 10), while the line connects the means.

F. Leukocyte migration assay of mpeg1:mcherryF/mpx;GFP double transgenic zebrafish larvae treated with 5 μM of Tamoxifen or control (DMSO at equal v/v). Treatment was started at 1 dpf and larvae were anesthetized and leukocyte migration was induced by tail amputation at 3 dpf. Representative stereo fluorescence images of leukocyte migration towards the injury (4 hours post amputation) are shown. Cyan shows neutrophils (*mpx*:GFP) and magenta shows macrophages (*mpeg1*:mCherryF). The region of interest (ROI) indicates the area for quantification of leukocyte migration. Scale bar annotates 220 μm.

G-H. Quantification of F, showing the number of migrated neutrophils (G) or macrophages (H). Each dot represents a single larva. Boxplots with 95% confidence intervals are shown and the black line in the boxplots indicates the group median, while the black line in the dot plot indicates the group mean. Statistical analysis was performed using a Mann-Whitney test.
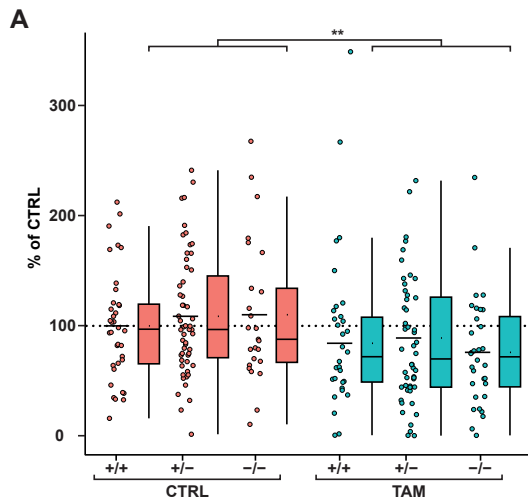
Supplementary Figure 4. The host-directed effect of Tamoxifen is independent of ER-receptor presence

A. Bacterial burden assay of mWasabi-expressing *Mm*-infected *esr2b*^{+/+}, *esr2b*^{+/-} and *esr2b*^{-/-} zebrafish larvae treated with 5 μM of Tamoxifen or control (DMSO at equal v/v). Treatment was started at 1 hpi and larvae anesthetized at 4 dpi for imaging. Bacterial burden was normalized to the control and data of 2 experimental repeats were combined (n = 25-55 per group). Each dot represents a single larva. Boxplots with 95% confidence intervals are shown and the black line in the boxplots indicates the group median, while the black line in the dot plot indicates the group mean. Dotted line indicates mean of control treated *esr2b*^{+/+} zebrafish larvae set at 100%. Statistical significance of the difference between the control and Tamoxifen-treated groups was determined using a two-way ANOVA. (** = p<0.01).
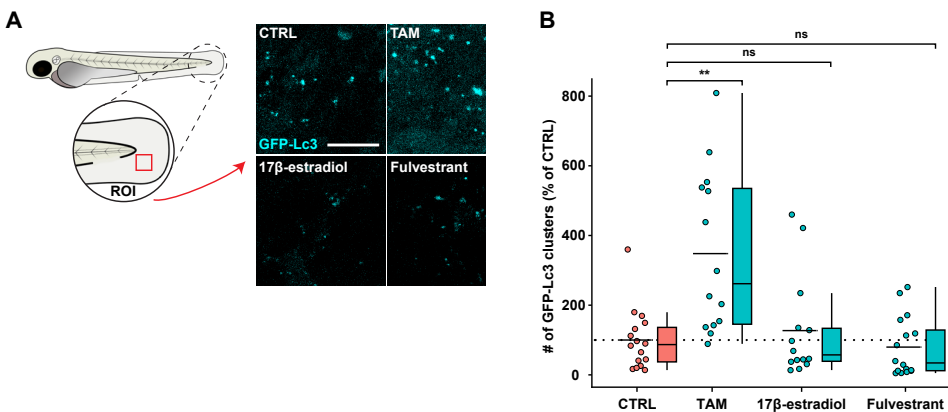
Supplementary Figure 5. Autophagy is not modulated by ER ligands in zebrafish
A. Confocal microscopy of transgenic GFP-Lc3 zebrafish larvae treated with 5 µM of Tamoxifen, 5 µM of ER agonist 17β-estradiol, 5 µM of ER antagonist Fulvestrant or control (DMSO at v/v). Treatment was started at 3 dpf and larvae were fixed with 4% paraformaldehyde at 4 dpf. Representative images of GFP-Lc3 positive vesicles in the tail fin are shown. Cyan shows GFP-Lc3 positive vesicles. Scale bar annotates 10 µm.
B. Quantification of GFP-Lc3 signal in A. Data were normalized to the control and data of 2 experimental repeats were combined (n = 14-16 per group). Each dot represents a single larva. Boxplots with 95% confidence intervals are shown and the black line in the boxplots indicates the group median, while the black line in the dot plot indicates the group mean. Dotted line indicates control mean. Statistical analysis was performed using a Kruskal-Wallis with Dunn's multiple comparisons test. (** = p<0.01).

Zebrafish lines		
Name	**Description**	**Reference**
AB/TL	Wild type strain	Zfin.org
esr2b^sa77	Loss of function *esr2b* mutant	Lopez-Munoz 2015
Tg(CMV:EGFP-map1lc3b)^zf155	GFP-tagged zebrafish Lc3	He 2009
Tg(mpeg1:mCherryF)^umsF001	Macrophage marker	Bernut 2014
Tg(mpx:EGFP)^i114	Neutrophil marker	Renshaw 2006
Tg(mpeg1:mCherryF, mpx:EGFP)^umsF001, i114	Macrophage and neutrophil marker	Bernut 2014, Renshaw 2006

Primer sequences				
Gene	**Type**	**Ensemble ID**	**Sequence**	
esr2b	PCR*	ENSDARG00000034181	FW	TCTTGGATGACATTAATAATCTGG
			RV	ATTCAACTGCAGTGTCTTGC
tbp	qPCR	ENSDARG00000014994	FW	CCTGCCCATTTTCAGTC
			RV	TGTTGTTGCCTCTGTTGCTC
cyp19a1b	qPCR	ENSDARG00000098360	FW	AAAGAGTTACTAATAAAGATCCACCGGTAT
			RV	TCCACAAGCTTTCCCATTTCA
vtg1	qPCR	ENSDARG00000092233	FW	ACTACCAACTGGCTGCTTAC
			RV	ACCATCGGCACAGATCTTC

Supplementary table S1. Supplementary materials
*The esr2b forward primer was also used for sequencing.

Gene name	Ensembl ID	s-value	Log2FC
AL935146.1	ENSDARG00000112812	0,003884	0,521512122
amd1	ENSDARG00000043856	0,000341	0,242002141
BX005175.1	ENSDARG00000112442	7,37E-05	-0,670979432
c3a.6	ENSDARG00000043719	0,002685	-0,545814275
c4b	ENSDARG00000038424	0,000121	-0,696489422
cnot2	ENSDARG00000061802	0,003033	-0,281112148
CT573383.1	ENSDARG00000097513	0,00213	-0,789054804
epg5	ENSDARG00000059846	0,001415	-0,438146512
FERMT3 (1 of many)	ENSDARG00000079267	0,004768	-1,181817384
gdi2	ENSDARG00000113039	0,0007	-0,294281106
hck	ENSDARG00000058647	0,000785	-0,732845923
hmcn2	ENSDARG00000079327	0,001891	-0,37352186
itgb2	ENSDARG00000016939	0,000284	-0,704094034
marco	ENSDARG00000059294	0,000603	-0,846209025
MFAP4 (1 of many)	ENSDARG00000088745	0,000214	-1,071839201
mfsd13a	ENSDARG00000112339	0,000522	-1,160824835
mmp13a	ENSDARG00000012395	7,33E-06	-1,905795573
mmp9	ENSDARG00000042816	1,95E-05	-1,589634402
musk	ENSDARG00000098764	0,001222	-0,637124638
psmc4	ENSDARG00000027099	0,000902	-0,507563082
ptpn13	ENSDARG00000103699	0,00347	-0,494978538
rasal2	ENSDARG00000036257	0,001658	-0,526200288
ric8b	ENSDARG00000005972	0,004342	-0,581914895
rmc1	ENSDARG00000029307	0,000445	-1,856523793
si:ch211-147m6.1	ENSDARG00000109648	4,43E-10	-1,378532336
si:ch211-194m7.3	ENSDARG00000074322	0,000388	-0,844262364
si:dkey-88l16.2	ENSDARG00000095137	0,002367	-2,336116068
trim63a	ENSDARG00000111657	0,001029	1,039071884

Supplementary table S2. Interaction of treatment and infection on gene regulation

4

Gene name	Ensembl ID	s-value (CTRL)	Log2FC (CTRL)	s-value (TAM)	Log2FC (TAM)
BX005175.1	ENSDARG00000101334	0,001093545	0,364449917	2,64E-05	0,495096771
ccl34a.4	ENSDARG00000074656	3,49E-11	2,834446032	6,52E-05	1,697390717
cfhl4	ENSDARG00000010312	0,001131535	0,218548149	0,000362287	-0,256087622
cp	ENSDARG00000090873	2,55E-13	0,687125852	0,003422273	0,257557489
ctsc	ENSDARG00000116951	9,22E-07	0,582920465	9,62E-08	0,65480504
ctss2.1	ENSDARG00000113068	3,89E-09	1,35242256	0,001239314	0,725429688
cul1a	ENSDARG00000004954	0,000260209	1,20735414	9,29E-05	1,389402743
grna	ENSDARG00000112150	1,59E-10	1,908385972	0,00237872	0,880257892
hist2h2l	ENSDARG00000019521	0,000665246	0,373924602	0,004626593	0,310629696
MFAP4 (1 of many)	ENSDARG00000112442	2,93E-07	1,031906608	0,004953604	0,545848653
mpx	ENSDARG00000109648	5,49E-13	1,058634459	0,002816962	0,417152838
si:ch211-147m6.1	ENSDARG00000105142	2,04E-46	2,342056078	8,18E-07	0,845930154
tcirg1b	ENSDARG00000006019	1,52E-08	0,548631879	0,002258719	0,284884932
tktb	ENSDARG00000088745	0,001875833	0,173521655	0,000247625	0,214566765

Supplementary table S3. Effect of treatment and infection on gene regulation

KEGG pathway		
Pathway	Number of DR genes	padj
Lysosome	16 (out of 140)	5,88E-14
Other glycan degradation	4 (out of 24)	0,00108355
Apoptosis	7 (out of 164)	0,003841255
Phagosome	6 (out of 142)	0,010176479
Glycosphingolipid biosynthesis - globo and isoglobo series	2 (out of 8)	0,028298257
Metabolic pathways	18 (out of 1286)	0,028298257
Ferroptosis	3 (out of 41)	0,048131463
Autophagy - animal	5 (out of 154)	0,05438032
mTOR signaling pathway	5 (out of 181)	0,09609386

Gene Ontology (GoSeq)				
GO term	Category	Ontology	Number of DR genes	p-adj
hydrolase activity	GO:0016787	MF	29 (out of 1268)	1,34E-07
peptidase activity	GO:0008233	MF	14 (out of 435)	0,00012964
proteolysis	GO:0006508	BP	18 (out of 752)	0,00012964
lysosome	GO:0005764	CC	7 (out of 74)	0,00012964
cysteine-type peptidase activity	GO:0008234	MF	9 (out of 147)	0,00012964
hydrolase activity, acting on glycosyl bonds	GO:0016798	MF	6 (out of 74)	0,004329959
metabolic process	GO:0008152	BP	6 (out of 82)	0,007120488
carbohydrate metabolic process	GO:0005975	BP	8 (out of 208)	0,013229959
lysosomal membrane	GO:0005765	CC	4 (out of 46)	0,078774283

Supplementary table S4. KEGG pathway and Gene Ontology (GoSeq) analysis

5

Host-directed therapy with Amiodarone restricts mycobacterial infection and enhances reactive nitrogen levels, autophagy and lysosomal activity

Ralf Boland[1], Nils Olijhoek[1], Gabriel Forn-Cuní[1], Matthias T. Heemskerk[2], Tom H. M. Ottenhoff[2], Herman P. Spaink[1], Michiel van der Vaart[1*], Annemarie H. Meijer[1*]

1.   Institute of Biology Leiden, Leiden University, Leiden, The Netherlands
2.   Department of Infectious Diseases, Leiden University Medical Center, Leiden, The Netherlands
*   Equal contribution

Abstract

There is growing concern about the rise of bacterial pathogens becoming resistant to antibiotics. Infection by the pathogen *Mycobacterium tuberculosis*, the causative agent of tuberculosis (TB), is a prime example where antibiotic treatments are losing effectivity. The loss of antibiotic effectivity has raised interest in the identification of host-directed therapeutics (HDTs) to develop novel treatment strategies for TB. In this study we investigated Amiodarone as an HDT drug candidate, which was identified by its antimicrobial effect in a screen of autophagy-modulating compounds. We used the zebrafish embryo model of TB, based on infection with its natural pathogen *Mycobacterium marinum*, to study the host mechanisms involved in the anti-mycobacterial effect of Amiodarone. We show that Amiodarone does not affect mycobacterial growth in culture at the concentrations used, thereby confirming that Amiodarone acts by a host-mediated effect in the zebrafish embryo model of TB. As Amiodarone is known to cause nitric oxide release, we investigated its effect on the reactive nitrogen host defence pathway We detected enhanced activity in both macrophages and neutrophils, although not necessarily colocalizing with mycobacteria. We then used transcriptome analysis and functional assays which indicated that Amiodarone alters host pathways related to autophagy and lysosomal function. In conclusion, we have identified Amiodarone as a strong candidate for further development as an anti-mycobacterial HDT that modulates several innate host defence processes.

Introduction

Tuberculosis (TB) is caused by the intracellular pathogen *Mycobacterium tuberculosis* (*Mtb*). During *Mtb* infection, there is an intricate interplay between the immune system and *Mtb*. On an intracellular level, *Mtb* is capable of resisting destruction by professional phagocytes by manipulation of host pathways[1–3]. On a cellular level this results in the hallmark pathology of TB, the formation of granulomatous aggregates of leukocytes[4]. TB is difficult to treat with classical antibiotics due the presence of dormant bacteria inside TB granulomas that are far less susceptible to antibiotics[5,6]. The rise of infections with multi-drug resistant (MDR) and extensively-drug resistant (XDR) *Mtb* strains is further complicating the treatment of TB[7]. Host-directed therapeutics (HDTs) offer new treatment strategies, even in the case of MDR- and XDR-*Mtb* strains, by enhancing the immune system to combat infection (chapter 1, chapter 3)[8–12]. Largescale genetic and chemical screens of *Mtb*-infected cultured cells have recently reported on a broad spectrum of potential HDTs affecting cellular processes such as lipid metabolism, inflammation and autophagy. During an *in vitro* screen of an autophagy modulating compound library using *Mtb* infected human cells, Amiodarone (Amiodarone-HCl, Sigma-Aldrich) was found to reduce bacterial burden. These results were subsequently reproduced in an *in vivo* screen using the zebrafish (*Danio rerio*) model, making Amiodarone a potentially highly interesting HDT (chapter 3). Here we aim to elucidate via which mechanism Amiodarone is able to restrict mycobacterial infection.

Amiodarone is currently used as antiarrhythmic medication and functions by blocking calcium, sodium and potassium channels as well as inhibiting alpha- and beta-adrenergic receptors. Amiodarone has never been shown to have anti-mycobacterial effects. However, Amiodarone can induce autophagy[13–15]. This intracellular degradation pathway is vital to maintaining homeostasis by removing unwanted elements from the cell, such as misfolded protein aggregates, damaged organelles, and microbial invaders[16,17]. Amiodarone accumulates in acidic organelles and therefore may interact not only with the autophagic pathway but also with other intracellular degradation

processes, like the endocytic pathway[18]. Furthermore, Amiodarone stimulates nitric oxide (NO) release[19]. NO release causes vasodilation and is argued to be an explanation for the cardiovascular protective effects exhibited by Amiodarone[19]. NO is also a key player in immunity and inflammation[20]. Consequently, the effects of Amiodarone on both autophagy and nitric oxide are highly relevant in the context of the host immune response to mycobacterial infection.

Macrophages are the main innate immune cell type that internalize and attempt to eliminate *Mtb* in a process whereby *Mtb*-containing phagosomes mature and fuse with lysosomes. This process results in degradation of the content of the formed phagolysosomes by lysosomal hydrolytic enzymes[1]. However, mycobacteria are remarkably resistant to the host immune system and can manipulate cellular signalling pathways in favour of their own survival. Mycobacteria can arrest phagosome maturation and subsequently escape into the cytosol. After escape, intracellular bacteria are targeted by the autophagy pathway. Inducing autophagy in *Mtb*-infected macrophages has been shown to restrict intracellular bacterial growth, supporting studies into autophagy as a potential target for HDTs against TB[17,21,22]. This led us to investigate if the autophagy-inducing properties of Amiodarone could be the underlying mechanism responsible for the host-directed effect of Amiodarone against TB.

It is known that Amiodarone can induce autophagy in two ways, although the precise mechanisms of action of Amiodarone on the autophagy machinery remain unclear. Firstly, Amiodarone inhibits the function of mTORC1[23]. This complex inhibits autophagy when cellular nutrients are replete by interacting directly with ULK1, which is important for initiation of autophagosome biogenesis[16]. Amiodarone potentially acts via an upstream target in the mTORC1 pathway, as the effect of Amiodarone on autophagosome biogenesis was not immediate after treatment[23]. Secondly, Amiodarone can inhibit autophagy in an mTORC-independent manner by blocking calcium channels and calcium dependent calpains[23]. Calpains inhibit autophagy via stimulation of production of cAMP, which was shown to inhibit autophagy[24,25]. Furthermore, calpains are implicated in the cleavage of Atg5, an important player in the autophagy pathway which is required for the formation of autophagosomes[26]. Interestingly, by potentially interacting with multiple players from the autophagy machinery, Amiodarone might prove to be a robust activator for autophagy in varying conditions, including during infection by mycobacterial pathogens.

Another way via which the host immune system combats intracellular bacterial infection is the formation of reactive oxygen species (ROS), as well as reactive nitrogen species (RNS) that are derived from nitric oxide (NO)[20,27]. NO is formed when L-Arginine is oxidized by nitric oxide synthases (NOS) and can react with superoxide to form peroxynitrite, which has strong antimicrobial activity. There are three NOS enzymes, two of which are constitutively active (neuronal NOS and endothelial NOS) and one is inducible (iNOS) in response to infection and inflammation[20,28]. Although mycobacteria are able to counteract ROS efficiently, they are highly susceptible to RNS[29,30]. Furthermore, it was shown that iNOS defective mice were highly susceptible to *Mtb*[28,31]. Indeed, increased production of RNS associated with increased levels of nitric oxide is host protective[32,33]. Although it is not known how Amiodarone induces NO release, this is another possible mechanism that could explain the beneficial effect of Amiodarone treatment in the context of mycobacterial infection.

In this study we used the zebrafish (*Danio rerio*) model to study the anti-mycobacterial effects of Amiodarone in an *in vivo* model and to elucidate via which host pathways this effect is exerted. The zebrafish embryo model for TB has generated considerable insight in processes involved in the early stages of TB pathogenesis, such as inflammation infection-inducible autophagy and cell death mechanisms[34,35]. In this model, zebrafish

5

embryos are infected with the close *Mtb* relative *Mycobacterium marinum* (*Mm*) that shares major virulence factors with *Mtb*. The hallmark pathology of TB, the formation of granulomatous aggregates of leukocytes, is recapitulated in zebrafish during *Mm* infection[4,35,36]. We have previously demonstrated that both autophagy and nitric oxide generation are host-protective mechanisms in zebrafish during *Mm* infection[33,37,38]. This makes the zebrafish embryo model for TB a highly suitable model to investigate a possible role for these mechanisms in the anti-mycobacterial effect of Amiodarone.

Here we show that Amiodarone treatment reduces mycobacterial infection in the zebrafish host, in the absence of any direct anti-mycobacterial effect of Amiodarone on *Mm* at doses used. Our studies into the host-mediated action of Amiodarone showed that Amiodarone treatment increased RNS production in our model but did not provide evidence for a major role for the RNS pathway in the anti-mycobacterial effect. Furthermore, while we did observe increased autophagy activity, we did not observe increased targeting of autophagosomes to mycobacteria. We performed transcriptome profiling to identify other pathways that could underly the reduction of bacterial burden after Amiodarone treatment, which revealed major effects of Amiodarone on lysosomal processes. We confirmed these findings by demonstrating that Amiodarone treatment increased levels of lysosomal acidification. These results suggest that Amiodarone treatment has a beneficial effect on defence against mycobacterial infection by modulating functions of lysosomes that contribute to host defence mechanisms, potentially in combination with modulation of autophagy. In conclusion, our results provide the first evidence that Amiodarone, an FDA-approved drug for treating arrhythmias, modulates innate host defence processes that restrict mycobacterial infection in an *in vivo* TB model. We therefore propose Amiodarone as a promising candidate drug to be further tested as HDT against TB.

Results

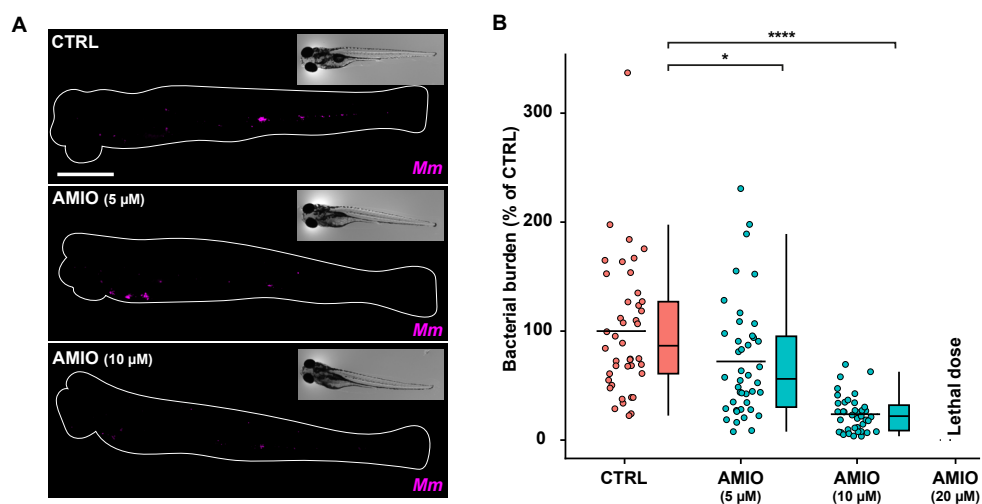### Amiodarone restricts *Mm* infection in a host-directed manner

A small scale screen of autophagy modulating FDA-approved compounds in the zebrafish embryo model for TB identified Amiodarone as a potential HDT that reduced *Mm* bacterial burden at a dosage of 5 µM (chapter 3). To further determine the optimal dose range, we infected zebrafish embryos with *Mm* at 1 day post fertilisation (dpf) and treated the infected embryos starting at 1 hour post infection (hpi) with vehicle control treatment (DMSO) or with increasing doses (5, 10 and 20 µM) of Amiodarone. Four days post infection (dpi) we assessed bacterial burden by quantifying fluorescent bacterial signal. Amiodarone was able to reduce bacterial burden compared to control treatment in a dose-dependent manner for the 5 and 10 µM groups. However, we observed developmental toxicity such as oedema and lethality in the group treated with 20 µM Amiodarone (Figure 1A-B).

Next, we looked into infection dynamics during Amiodarone treatment to better understand the effect of Amiodarone on *Mm* infection. We infected and treated embryos with Amiodarone (5 and 10 µM) or control treatment as described above. Subsequently, we imaged the embryos daily from 1-4 dpi, which allowed us to compare the development of the infection burden after control or Amiodarone treatment. As early as 2 dpi, a reduction in the Amiodarone-treated groups compared to control could be observed, though we also found developmental toxicity (e.g. oedema and lethality) in the 10 µM group from 3 dpi onward. In all treatment conditions, we observed an increase in bacterial burden. However, at the end point of the experiment Amiodarone treatment with 5 µM reduced the infection burden almost 2-fold compared to control

treatment (Figure 1C). Therefore, Amiodarone does not fully inhibit bacterial growth but does limit the infection burden.

We then wanted to assess whether Amiodarone had a direct effect on *Mm* bacterial growth or survival, as opposed to limiting bacterial burden via a host-directed effect. We thus exposed *Mm* liquid cultures to increasing doses of Amiodarone and measured optical density (OD) to assess bacterial replication at 4 different timepoints (Figure 1D). We found a growth limiting effect of Amiodarone in the *Mm* cultures exposed to 10 μM of Amiodarone, but not in the cultures exposed to 5 μM Amiodarone. These results show that while Amiodarone can have a direct effect on *Mm* growth in liquid cultures, the reduction of bacterial burden we observed in zebrafish embryos treated with 5 μM of Amiodarone can be attributed to host-dependent factors.

To exclude that the host-dependent effect of Amiodarone was associated with major alterations in leukocyte behaviour that might lower its potential application as an HDT, we determined if leukocyte migration was affected. To this end we used an established injury-based migration assay, the tail amputation assay[39,40], in a double transgenic neutrophil and macrophage marker line and assessed the number of neutrophils and macrophages that migrated to the wound-induced site of inflammation (Figure 1E). We did not find significant differences in the numbers of neutrophils and macrophages that accumulated at the site of inflammation after control or Amiodarone (5 μM) treatment (Figure 1F-G).

Figure 1. Amiodarone restricts *Mm* infection in a host-directed manner

A. Bacterial burden assay of mWasabi-expressing *Mm*-infected zebrafish larvae treated with increasing doses of Amiodarone (2.5, 5 and 10 μM) or control (DMSO at 0.1% v/v). Treatment was started at 1 hpi and larvae anesthetized at 4dpi for imaging. Representative stereo fluorescent images of whole larvae infected with mWasabi-expressing *Mm*. Magenta shows *Mm*. Scale bar annotates 1 mm.

B. Quantification of bacterial burden shown in A. Bacterial burden was normalized to mean of the control, set at 100% and indicated with the dotted line. Data of 2 experimental repeats were combined (n = 39-42 per group). Each dot represents a single larva. Boxplots with 95% confidence intervals are shown and the black line in the boxplots indicates the group median, while the black line in the dot plot indicates the group mean. Statistical analysis was performed using a Kruskal-Wallis with Dunn's multiple comparisons test.
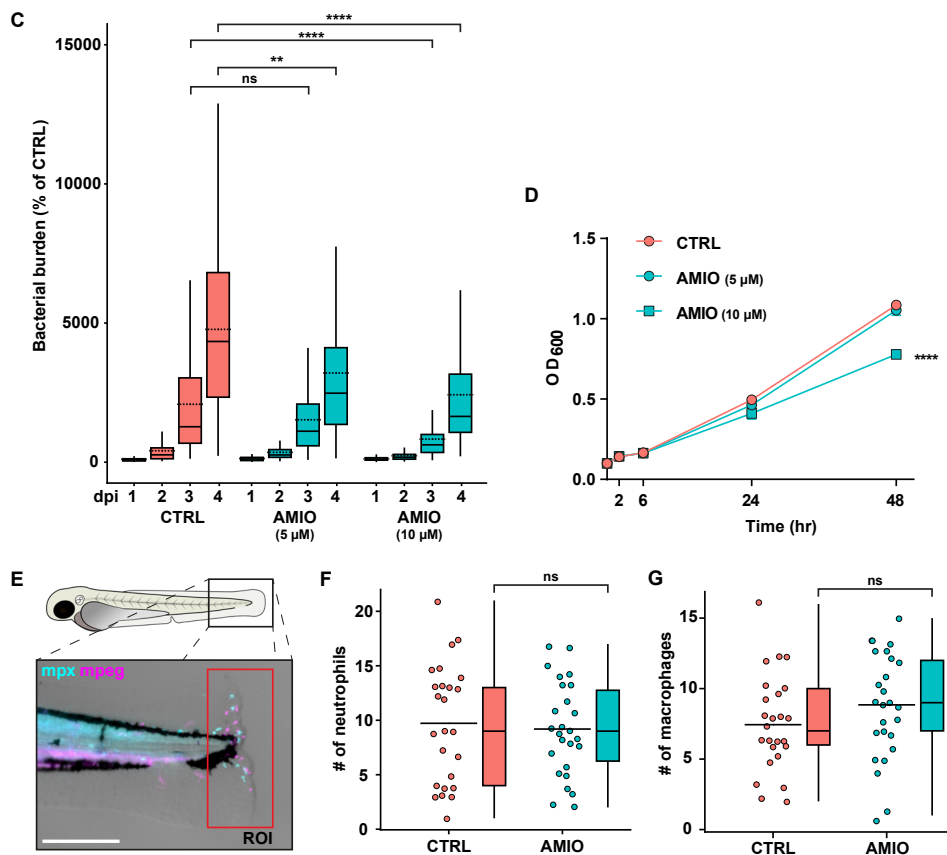
Figure 1. (continued)

C. Bacterial burden assay of mWasabi-expressing *Mm*-infected zebrafish larvae treated with 5 and 10 µM of Amiodarone or control (DMSO at 0.1% v/v). Treatment was started at 1 hpi and larvae were anesthetized at 1, 2, 3 and 4 dpi for imaging. Bacterial burden was normalized to the control (DMSO at 1dpi) and data of 2 experimental repeats were combined (n = 65-70 per group). All larvae in the 10 µM group died between 3-4 dpi. Boxplots with 95% confidence intervals are shown and the black line in the boxplots indicates the group median, while the dotted line indicates the group mean. Statistical analysis was performed between treatment groups per timepoint using a Kruskal-Wallis with Dunn's multiple comparisons test.

D. *Mm* growth in liquid culture during treatment with 5 or 10 µM of Amiodarone or control (DMSO at equal v/v) up to assay endpoint, day 2. Lines depict mean ± standard deviation of 2 experiments. Statistical significance of treatment versus control treatment was tested using a two-way ANOVA with Dunnett's multiple comparisons test.

E. Leukocyte migration assay of mpeg1:mcherryF/mpx:GFP double transgenic zebrafish larvae treated with 5 µM of Amiodarone or control (DMSO at equal v/v). Treatment was started at 1 dpf and larvae were anesthetized and leukocyte migration was induced by tail amputation at 3 dpf. Representative stereo fluorescence images of leukocyte migration towards the injury (4 hours post amputation) are shown. Cyan shows neutrophils (*mpx*:GFP) and magenta shows macrophages (*mpeg1*:mCherryF). The region of interest (ROI) indicates the area for quantification of leukocyte migration. Scale bar annotates 220 µm.

F-G. Quantification of E, showing the number of migrated neutrophils (F) or macrophages (G). Each dot represents a single larva. Boxplots with 95% confidence intervals are shown and the black line in the boxplots indicates the group median, while the black line in the dot plot indicates the group mean. Statistical analysis was performed using a Mann-Whitney test.

(* = p<0.05, ** = p<0.01, *** = p<0.001 and **** = p<0.0001).

We conclude that treatment with 5 μM Amiodarone results in reduction of bacterial burden via a host-directed effect, without apparent adverse effects on the host such as developmental toxicity or altered leukocyte migration. We therefore continued investigating the mechanism by which Amiodarone exerts its anti-mycobacterial effect.

Amiodarone increases RNS activity but not co-localisation of RNS with *Mm* clusters

We considered the possibility that the anti-mycobacterial effect of Amiodarone might be due to its ability to stimulate nitric oxide release[19]. Reactive nitrogen species (RNS), derived from nitric oxide, as well as reactive oxygen species (ROS), are well known anti-microbial molecules[27,41]. Thus, we hypothesized that induction of RNS could be the mechanism via which Amiodarone aids host-resistance to *Mm* in our model. To assess the presence and activity of RNS, we performed immunostaining with an antibody against nitrosylated tyrosine residues (α-nitrotyrosine) that has previously been used in the zebrafish embryo model for TB[33,42]. We first investigated if induction of RNS occurred in uninfected conditions after control treatment or Amiodarone treatment. For this, we used a double fluorescent marker line (*mpx*:GFP/*mpeg*:mCherry) to distinguish neutrophils and macrophages using confocal microscopy in the CHT (Figure 2A). We found an increase in α-nitrotyrosine signal in Amiodarone treated embryos (Figure 2B). Notably, the increase was only observed in neutrophils and not in macrophages without infection, consistent with previous results that demonstrated RNS to be mainly produced by neutrophils during *Mm* infection[33].
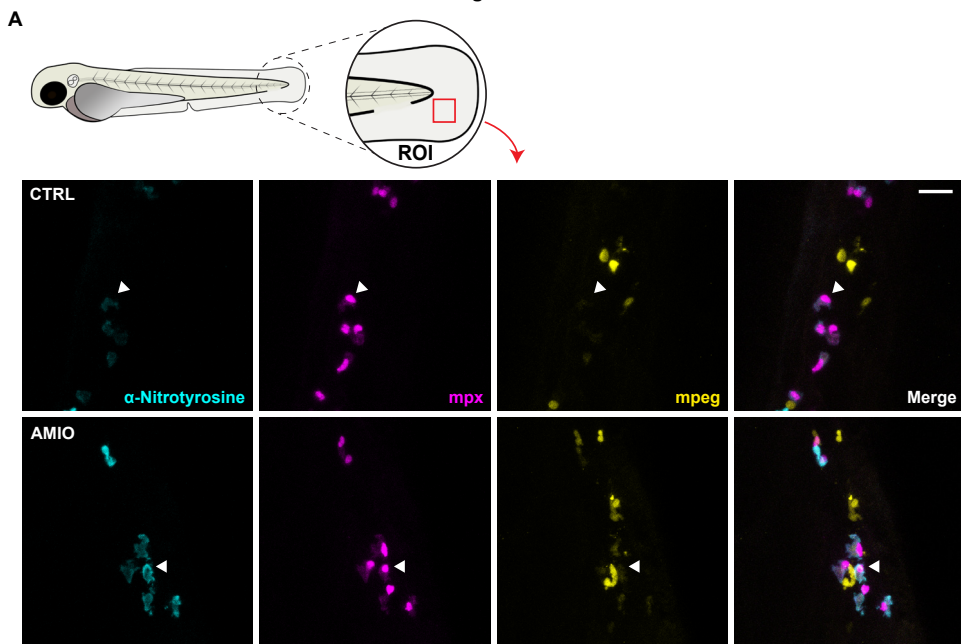
Figure 2. Amiodarone increases RNS levels in neutrophils but not macrophages in absence of infection
A.   Confocal microscopy max projection of immunostaining assay using α-nitrotyrosine of mpeg1:mcherryF/ mpx:GFP double transgenic zebrafish larvae treated with 5 μM of Amiodarone or control (DMSO et equal v/v). Treatment was started at 1 hpi and at 2 dpi larvae were fixed using 4% paraformaldehyde for imaging. Representative max projection images of the ROI in the tail fin. Cyan shows α-nitrotyrosine signal, magenta shows neutrophils (*mpx*:GFP) and yellow shows macrophages (*mpeg1*:mCherryF). White arrowheads indicate neutrophils showing α-nitrotyrosine signal, indicating RNS production. Scale bar annotates 20 μm.
Figure and figure legend continued on next page.

B
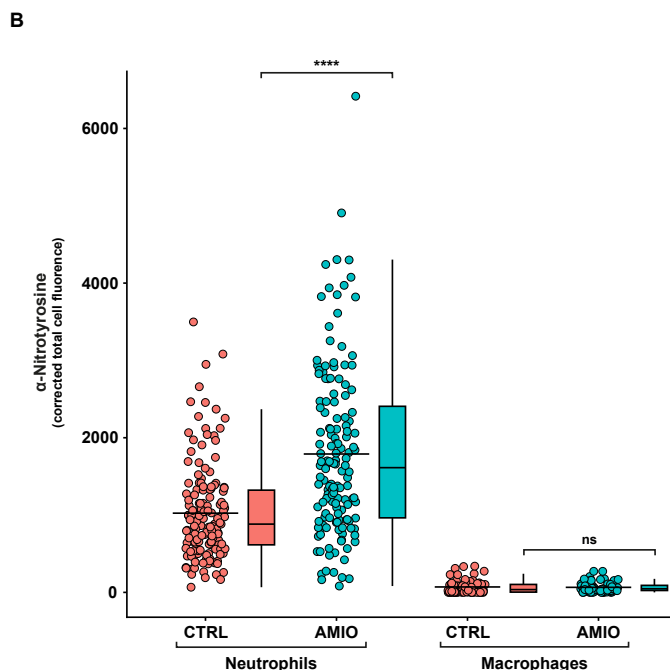
Figure 2. (continued)
B. Quantification of the corrected total cell fluorescence of α-nitrotyrosine signal shown in A per neutrophil or macrophage respectively. Data of 2 experimental repeats were combined. Each data point represents a single cell (n = 147-148 for neutrophils and n = 74 for macrophages). Error bars indicate SEM. Statistical analysis was performed using using a Mann-Whitney test
(**** = p<0.0001).

While Amiodarone treatment without infection increased RNS levels in neutrophils, *Mm* infection is mostly constricted to macrophages in the zebrafish model. Therefore, we asked if Amiodarone treatment could boost RNS levels in *Mm*-infected macrophages. To this end, we infected embryos with fluorescently labelled macrophages (*mpeg:*GFP) locally in the tail fin with labelled *Mm* bacteria. We again performed immunostaining with the α-nitrotyrosine antibody and used confocal laser scanning microscopy at 1 dpi to assess RNS activation in the presence of bacteria. As shown by representative images, we were able to detect *Mm*-infected macrophages that were α-nitrotyrosine-positive, but the majority of the α-nitrotyrosine signal was observed outside macrophages (Figure 3A). The total level of α-nitrotyrosine signal inside and outside of macrophages was increased in the Amiodarone treated group compared to control treatment, similar to non-infected conditions (Figure 3B). We then looked specifically at the α-nitrotyrosine signal inside infected macrophages and found it to be significantly increased in the Amiodarone treated group (Figure 3C). In conclusion, macrophages contribute to the increased production of RNS after treatment with Amiodarone in infected conditions, despite that the vast majority of RNS production occurs in neutrophils.

As Amiodarone is able to increase RNS production in infected macrophages as well as in bystander neutrophils, we hypothesized that this increase could be the mechanism underlying the host-protective effect of Amiodarone against *Mm* infection. To address this question, we asked if the increased RNS production was localized around *Mm* clusters. Thus, we analysed colocalization between α-nitrotyrosine signal and *Mm* clusters and macrophages. Because 2D maximum projection images of confocal

A

CTRL

α-Nitrotyrosine | *Mm* | mpeg | Merge

AMIO

B

p = 0.0566

α-Nitrotyrosine
(% total signal intensity)

CTRL   AMIO

C

**

α-Nitrotyrosine
(normalized total cell fluorence
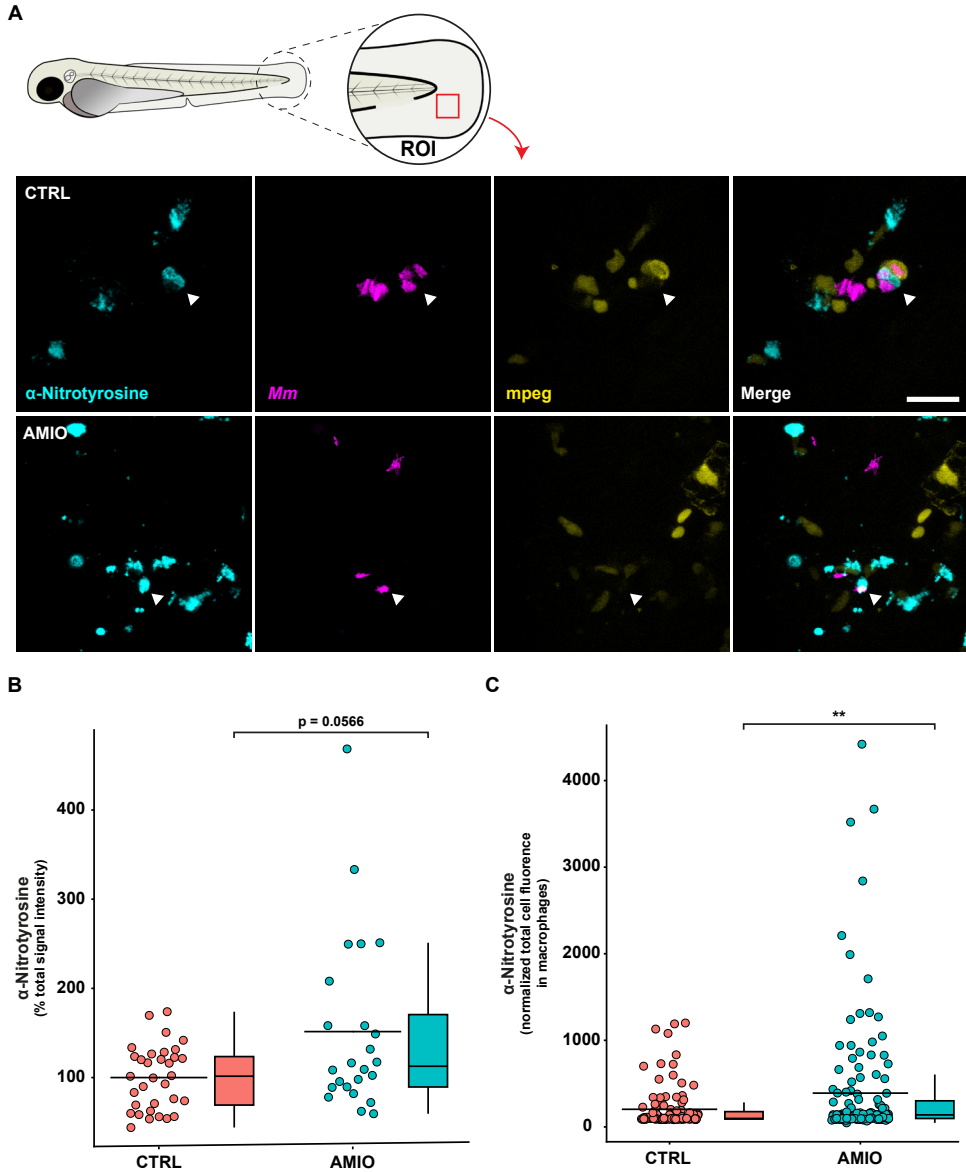in macrophages)

CTRL   AMIO

Figure 3. Amiodarone increases total and macrophage specific RNS levels in the presence of infection

A. Confocal microscopy max projection of immunostaining assay using α-nitrotyrosine of mCherryexpressing *Mm*-infected mpeg1:GFP transgenic zebrafish larvae treated with 5 μM of Amiodarone or control (DMSO et equal v/v). Treatment was started at 1 hpi and at 2 dpi larvae were fixed using 4% paraformaldehyde for imaging. Representative max projection images of the ROI in the tail fin. Cyan shows α-nitrotyrosine signal, magenta shows *Mm* and yellow shows macrophages (*mpeg1*:GFP). White arrowheads indicate interactions between *Mm* and the innate immune system. Scale bar annotates 20 μm.

B. Quantification of the total α-nitrotyrosine signal intensity shown in A. Data of 3 experimental repeats were combined. Each data point represents a single embryo (n = 24-33). Error bars indicate SEM. Statistical analysis was performed using a Mann-Whitney test.

C. Quantification of the normalized total cell fluorescence in macrophages shown in A. Data of 2 experimental repeats were combined. Each data point represents a single cell (n = 111-135). Error bars indicate SEM. Statistical analysis was performed using a Mann-Whitney test.
(** = p<0.01).

microscopy data potentially misrepresents colocalization in the Z-dimension, we used Imaris image analysis software to construct 3D images from the Z-stacks obtained in the tail fin infection experiment with confocal microscopy (Figure 4A). Quantification of the percentage of volume colocalization between macrophages and α-nitrotyrosine signal based on the 3D reconstruction, showed that only ~3.5% of the signal colocalized with macrophages. Furthermore, we found no significant difference between control treatment and Amiodarone treatment (Figure 4B). We then quantified volume colocalization of *Mm* clusters and α-nitrotyrosine signal based on the 3D reconstruction, which also revealed no significant difference between control treatment or Amiodarone-treated embryos (Figure 4C). This suggests that the observed increase in RNS production is not leading to more RNS that is specifically localized at *Mm* clusters, either intra- or extracellular. We then reasoned that limiting the analysis only to direct colocalization could overlook bacterial exposure to RNS at earlier time points that could be relevant for bacterial clearance. Thus, we quantified the number of α-nitrotyrosine spots in the vicinity of non-infected macrophages, *Mm* clusters, or infected macrophages to detect if Amiodarone treatment increased RNS around bacteria, which could explain the lower bacterial burden. We found no significant differences in the total number of α-nitrotyrosine spots between control treatment or Amiodarone treatment groups, nor in a 4 μM radius around *Mm* clusters, in a 2 μM radius around macrophages or in a 2 μM radius around infected macrophages (Figure 4D).

Taken together we conclude that, while Amiodarone induces RNS production in neutrophils and infected macrophages, there is no evidence for a specific increase of RNS at or around *Mm* clusters, either within macrophages or in the nearby extracellular environment.

A
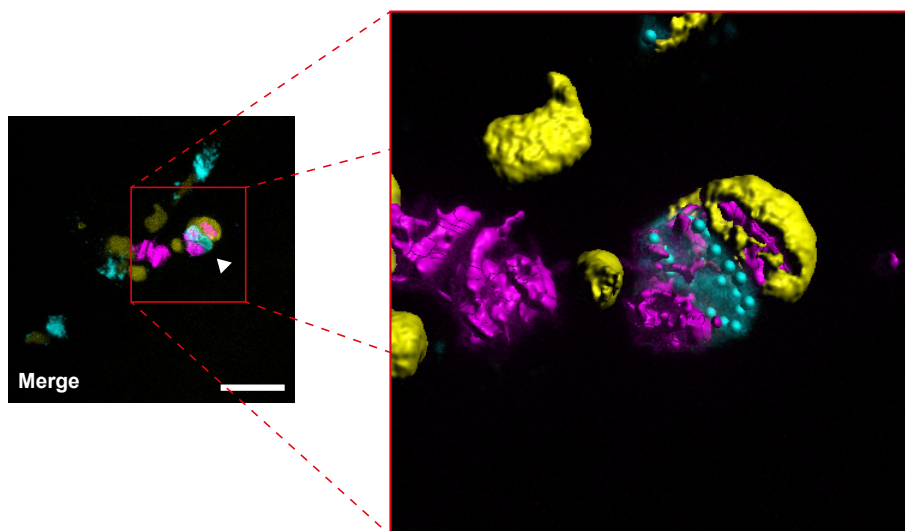
Figure 4. Amiodarone does not increase colocalization of α-nitrotyrosine signal with macrophages nor *Mm*

A. 3D rendering of confocal image shown in figure 3A made with Imaris. Cyan shows α-nitrotyrosine signal, magenta shows *Mm* and yellow shows macrophages (*mpeg1*:GFP). White arrowhead indicates interactions between *Mm* and the innate immune system. The 3D rendering was made based on the image data with Imaris software.
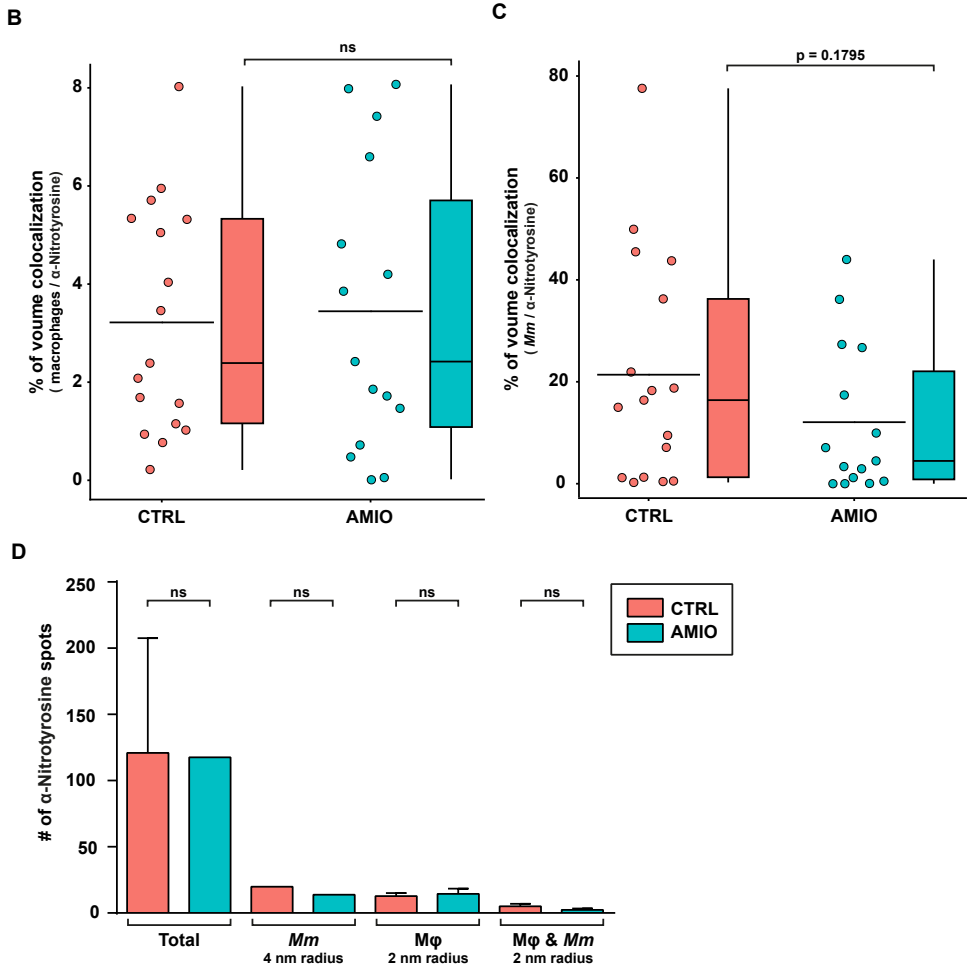
Figure 4. (continued)

B. Quantification of the colocalization of macrophage and α-nitrotyrosine signal based on volume calculated using the 3D rendering in Imaris shown in A. Data of 2 experiments were combined. Each data point represents a single embryo (n = 15-17). Error bars indicate SEM. Statistical analysis was performed using a Mann-Whitney test.

C. Quantification of the colocalization of *Mm* and α-nitrotyrosine signal based on volume calculated using the 3D rendering in Imaris shown in A. Data of 2 experiments were combined. Each data point represents a single embryo (n = 15-17). Error bars indicate SEM. Statistical analysis was performed using a Mann-Whitney test.

D. Quantification of α-nitrotyrosine signal spots in the proximity of *Mm* clusters, macrophages, or infected macrophages using the 3D rendering in Imaris shown in A. Data of 2 experiments were combined (n = 15-17 embryos in total). Error bars indicate SEM. Statistical analysis for each proximity quantification was performed separately using a Kruskal-Wallis with Dunn's multiple comparisons test.

Amiodarone restricts *Mm* bacterial burden independent of RNS production

Because of the known host protective role of RNS[20,27,28,43] and the fact that we did not observe a localized increase in RNS production around *Mm* clusters after Amiodarone treatment, we asked if Amiodarone treatment would still reduce bacterial burden if RNS production was inhibited. Therefore, we used chemical inhibition of NOS enzymes that produce RNS. We used a specific iNOS inhibitor (L-NIL) or a pan-NOS inhibitor (L-NAME) to block NOS activity. We hypothesized that inhibiting iNOS and NOS activity would abolish the effect of Amiodarone treatment on bacterial burden if increased RNS production is indeed the mechanism by which Amiodarone exerts its lowering effect on bacterial burden. Thus, we infected zebrafish embryos at 1 dpf and treated with control treatment or Amiodarone in presence or absence of L-NIL. Treatment of infected embryos with Amiodarone resulted in reduced bacterial burden compared to control treatment with or without iNOS inhibition (Figure 5A). Similarly, when infected zebrafish
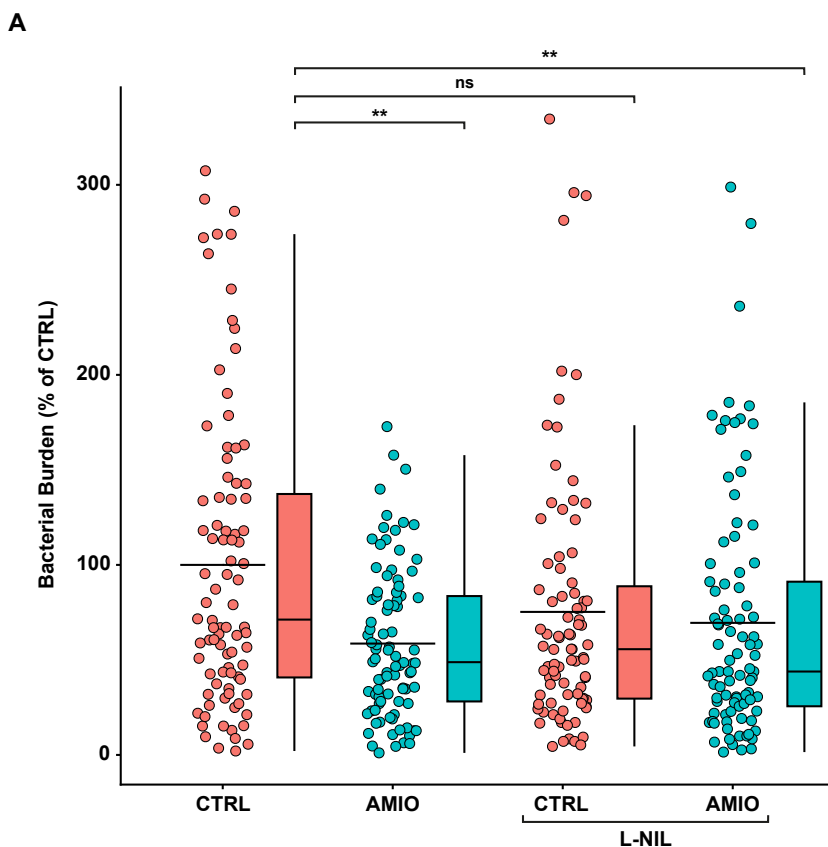
Figure 5. Amiodarone restricts *Mm* bacterial burden independent of RNS production

A. Bacterial burden assay of mWasabi-expressing *Mm*-infected zebrafish larvae treated with 5 µM of Amiodarone, 200 µM of the specific iNOS inhibitor L-NIL, a combination of 5 µM Amiodarone and 200 µM L-NIL or control (DMSO at 0.25% v/v). Treatment was started at 1 hpi and larvae anesthetized at 4dpi for imaging. Bacterial burden was normalized to mean of the control, set at 100% and indicated with the dotted line. Data of 3 experimental repeats were combined (n = 88-90 per group). Each dot represents a single larva. Boxplots with 95% confidence intervals are shown and the black line in the boxplots indicates the group median, while the black line in the dot plot indicates the group mean. Statistical analysis was performed using a Kruskal-Wallis with Dunn's multiple comparisons test.

Figure and figure legend continued on next page.

B
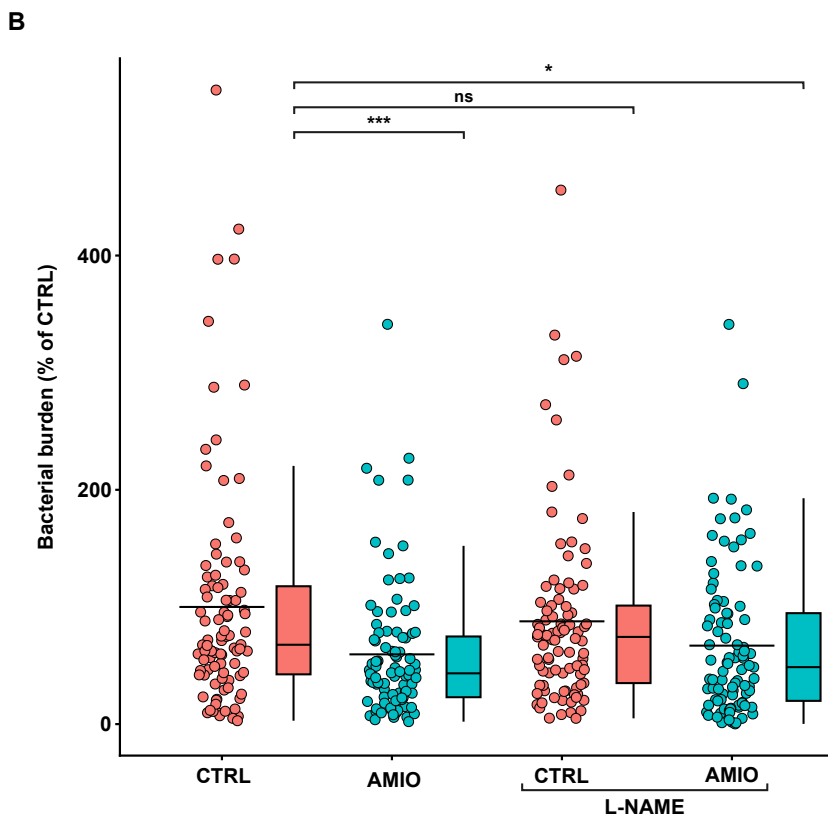
Figure 5. (continued)
B. Bacterial burden assay of mWasabi-expressing *Mm*-infected zebrafish larvae treated with 5 µM of Amiodarone, 200 µM of the pan-NOS inhibitor L-NAME, a combination of 5 µM Amiodarone and 200 µM L-NAME or control (DMSO at 0.45% v/v). Treatment was started at 1 hpi and larvae anesthetized at 4dpi for imaging. Bacterial burden was normalized to mean of the control, set at 100% and indicated with the dotted line. Data of 3 experimental repeats were combined (n = 92-94 per group). Each dot represents a single larva. Boxplots with 95% confidence intervals are shown and the black line in the boxplots indicates the group median, while the black line in the dot plot indicates the group mean. Statistical analysis was performed using a Kruskal-Wallis with Dunn's multiple comparisons test.
(* = p<0.05, ** = p<0.01 and *** = p<0.001).

embryos were treated with control treatment or Amiodarone in presence or absence of L-NAME, the effectivity of Amiodarone treatment was not affected and reduced bacterial burden compared to control treatment was observed regardless of pan-NOS inhibition (Figure 5B). This suggests that, while Amiodarone treatment leads to an increase in RNS production, the effect of Amiodarone on reduction of bacterial burden is independent of RNS production and is mediated via different host pathways.

Amiodarone induces an increase in autophagosomes but not in autophagic targeting of *Mm* clusters

Next, we investigated if the anti-mycobacterial effect of Amiodarone could be due to the autophagy-inducing activity that has been reported for this compound[13,15]. We first looked into autophagic activity in uninfected zebrafish embryos using a fluorescent reporter line for the autophagy marker Lc3[44]. We treated 3 dpf embryos for 24 hours with Amiodarone or control treatment and imaged the tail fin using confocal laser scanning

microscopy[45]. We quantified GFP-Lc3 positive structures and observed a significant increase in the number of GFP-Lc3 structures in the Amiodarone treated group (Figure 6A-B) compared to control treatment. Therefore, we conclude that Amiodarone results in an increased number of autophagic vesicles under uninfected conditions.
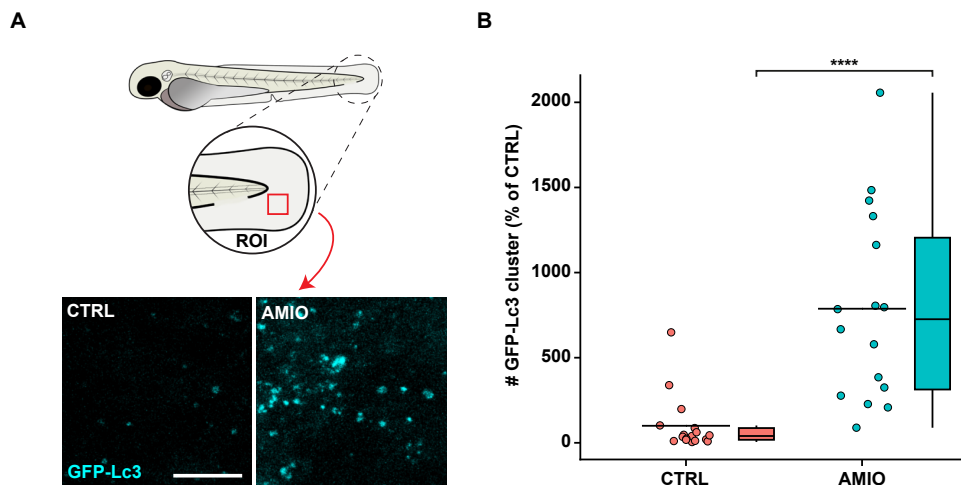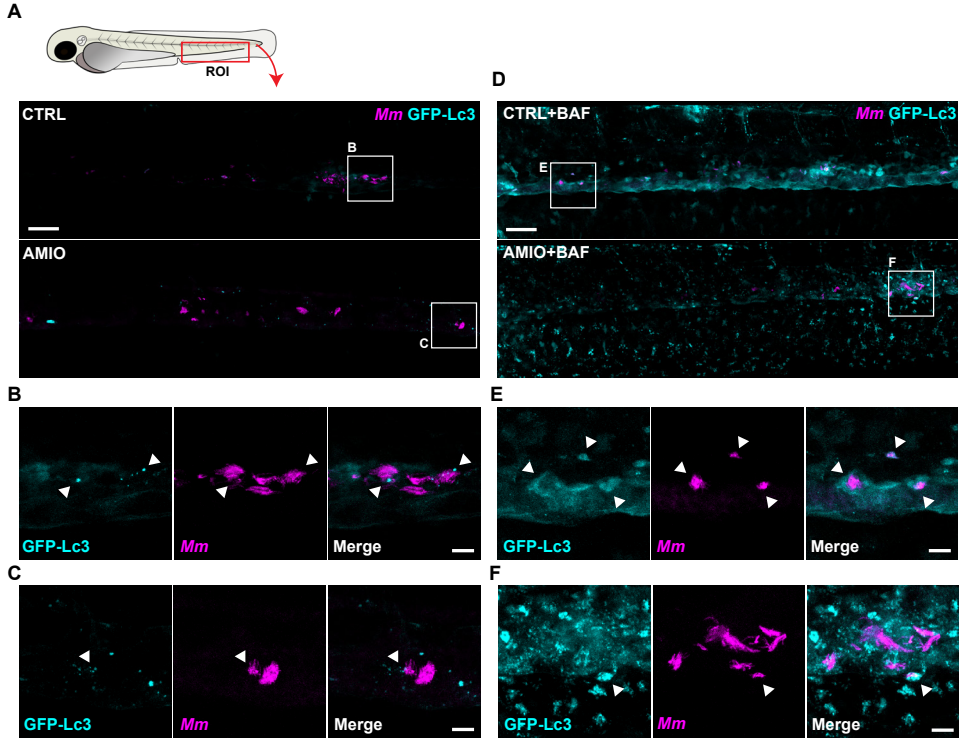

Figure 6. Amiodarone induces an increase in autophagosomes

A. Confocal microscopy max projection of transgenic GFP-Lc3 zebrafish larvae treated with 5 μM of Amiodarone or control (DMSO at equal v/v). Treatment was started at 3 dpf and larvae were fixed with 4% paraformaldehyde at 4 dpf for imaging. Representative max projection images of GFP-Lc3 positive vesicles in the indicated region of imaging (ROI) in the tail fin are shown. Cyan shows GFP-Lc3 positive vesicles. Scale bar annotates 10 μm.

B. Quantification of GFP-Lc3 structures shown in A. Data were normalized to the control and data of 2 experimental repeats were combined (n = 16-17 per group). Each dot represents a single larva. Boxplots with 95% confidence intervals are shown and the black line in the boxplots indicates the group median, while the black line in the dot plot indicates the group mean. Statistical analysis was performed using a Mann Whitney test.
(**** = p<0.0001).

Because we observed an increase in autophagic vesicles after Amiodarone treatment, we next investigated *Mm* clearance via the autophagolysosomal pathway after Amiodarone treatment. We therefore assessed co-localisation between GFP-Lc3 and *Mm* clusters by infecting 1 dpf embryos of the GFP-Lc3 reporter line and imaged the embryos at 2 dpi in the caudal hematopoietic tissue (CHT) region using confocal microscopy. We selected the CHT because it is a region where infected macrophages are known to aggregate, which is the first step in granuloma formation[36]. In both control treatment and Amiodarone treatment groups, we observed bacterial clusters that are decorated by GFP-Lc3 and bacterial clusters that are GFP-Lc3 negative (Figure 7A-B). Besides treatment with control treatment or Amiodarone, we also used the V-ATPase inhibitor bafilomycin (Bafilomycin A1, 160nM) to prevent lysosomal acidification and block autophagic flux, allowing to distinguish between effects of Amiodarone on autophagic targeting of *Mm* from effects on *Mm* degradation through the autophagolysosomal pathway. As expected, blocking flux with bafilomycin resulted in an overall increase of GFP-Lc3 signal in both control treatment and Amiodarone treatment conditions (Figure 7D-G). However, we did not observe a difference in the percentage of *Mm* clusters

positive for GFP-Lc3 structure(s) between control treatment or Amiodarone treatment in absence or presence of bafilomycin (Figure 7G). Thus, blocking autophagic flux did not reveal an increase in *Mm*-containing autophagomes due to Amiodarone treatment.

Figure 7. Amiodarone does not induce an increase in autophagic targeting of *Mm* clusters

A. Confocal microscopy max projection of mCherry-expressing *Mm*-infected transgenic GFP-Lc3 zebrafish larvae treated with 5 µM of Amiodarone or control (DMSO at equal v/v). Treatment was started at 1 hpi and at 2 dpi larvae were fixed with 4% paraformaldehyde for imaging. Representative max projection images of the ROI in the caudal hematopoietic tissue (CHT) region are shown. Cyan shows GFP-Lc3 positive vesicles and magenta shows *Mm*. Scale bar annotates 50 µm.

B-C. Enlargement of areas indicated in A. Cyan shows GFP-Lc3 positive vesicles and magenta shows *Mm*. Arrowheads indicate GFP-Lc3-positive *Mm* clusters. Scale bar annotates 10 µm.

D. Confocal microscopy max projection of mCherry-expressing *Mm*-infected transgenic GFP-Lc3 zebrafish larvae treated with 5 µM of Amiodarone and 160 nm of bafilomycin or control (DMSO at equal v/v). Treatment was started at 1 hpi and at 2 dpi larvae were fixed with 4% paraformaldehyde for imaging. Representative max projection images of the ROI in the caudal hematopoietic tissue (CHT) region are shown. Cyan shows GFP-Lc3 positive vesicles and magenta shows *Mm*. Scale bar annotates 50 µm.

E-F. Enlargement of areas indicated in D. Cyan shows GFP-Lc3 positive vesicles and magenta shows *Mm*. Arrowheads indicate GFP-Lc3-positive *Mm* clusters. Scale bar annotates 10 µm.

G
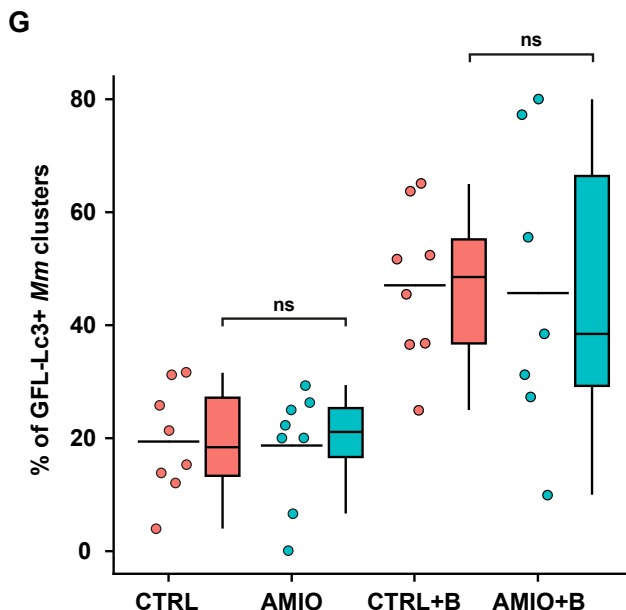
Figure 7. (continued)
G. Quantification of GFP-Lc3 positive *Mm* clusters in the CHT region shown in A and D normalized to the control (n = 8 per group). Each dot represents a single larva. Boxplots with 95% confidence intervals are shown and the black line in the boxplots indicates the group median, while the black line in the dot plot indicates the group mean. Statistical analysis was performed using a Kruskal-Wallis with Dunn's multiple comparisons test.

Amiodarone increases lysosomal staining

Considering that Amiodarone has also been reported to affect the endocytic pathway[18], we performed LysoTracker staining to detect acidified intracellular compartments. We treated uninfected embryos with control treatment or Amiodarone (5 μM) starting at 30 hpf for 2 days. At 3 dpf we performed LysoTracker staining and imaged the tail fin of the embryos using confocal microscopy. We observed a clear increase in LysoTracker signal in the embryos treated with Amiodarone (Figure 8A-B). Moreover, the LysoTracker positive vesicles were significantly enlarged (300%) compared to those in control treatment treated embryos (Figure 8C). The increase in both the number of positive vesicles combined with the increase in vesicle size in these embryos may provide an explanation for the antimycobacterial effect of Amiodarone.

RNA sequencing confirms major effects on lysosomal function *in vivo*

Finally, we performed RNA sequencing analysis to investigate the transcriptional effects of Amiodarone treatment and get more insight into the cellular pathways that are affected by Amiodarone treatment. The RNA sequencing analysis of Amiodarone was performed in conjuncture with RNA sequencing analysis of Tamoxifen, another potential HDT that was shown to be effective against *Mm* in zebrafish (chapter 4). For both Amiodarone and Tamoxifen, the same control treatment-treatment groups and analysis methods were used. When analysing the transcriptome of the control treatment treated larvae, we found consistent results with earlier transcriptomic data of *Mm* infected zebrafish, showing upregulation of genes associated with inflammation and host defence as is described in chapter 4[46]. Amiodarone treatment of non-infected larvae caused differential expression of 381 genes, including genes involved in autophagy and

lysosomal processes, such as *p62* (*sqstm1*) and *lamp1a* (Supplementary Data File 1).
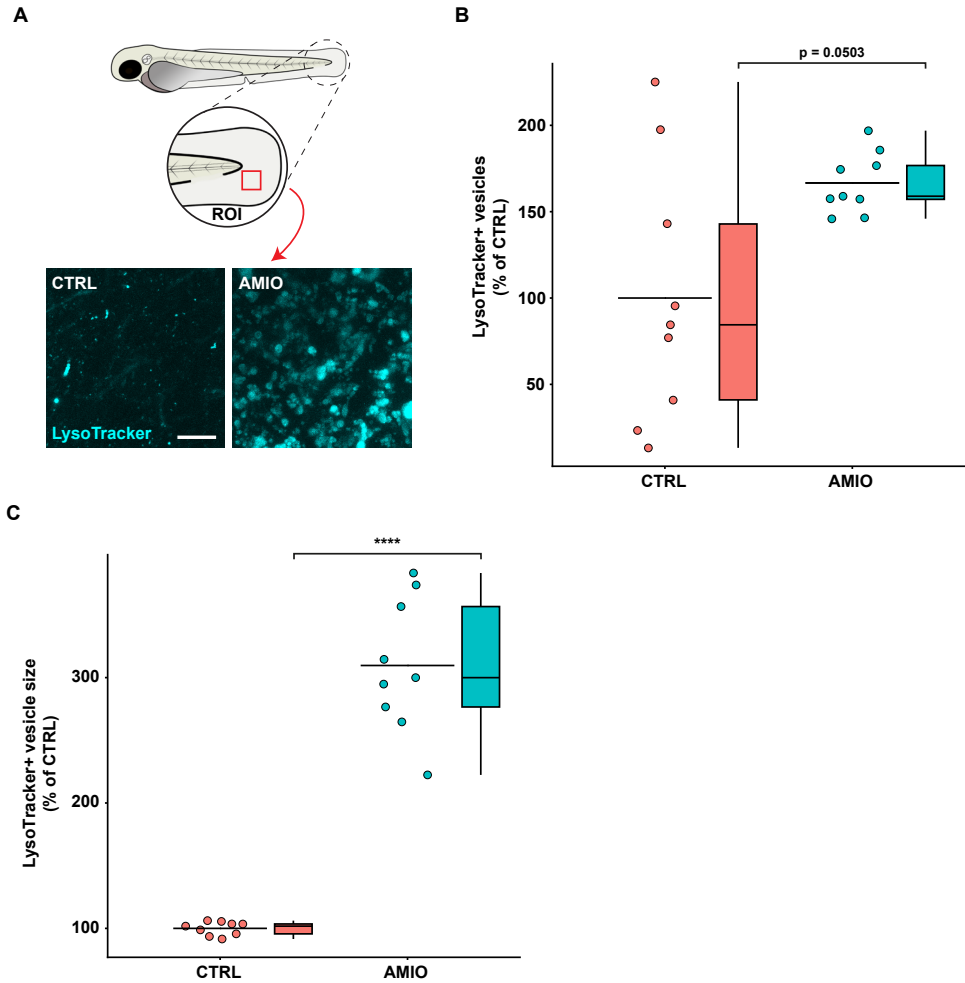
Figure 8. Amiodarone induces lysosomal activity
A. Confocal microscopy max projection of the indicated ROI in zebrafish larvae treated with 5 µM of Amiodarone or control (DMSO at equal v/v). Treatment was started at 31 hpf and at 3 dpf larvae were immersed in 5 µM of LysoTracker Red DND-99 for 1 hour and subsequently anesthetized for imaging. Cyan shows acidic vesicles. Scale bar annotates 10 µm.
B. Quantification of LysoTracker-positive vesicles shown in A normalized to the control and data of 2 experimental repeats were combined (n = 9 per group). Each dot represents a single larva. Boxplots with 95% confidence intervals are shown and the black line in the boxplots indicates the group median, while the black line in the dot plot indicates the group mean. Statistical analysis was performed using a Mann Whitney test.
C. Quantification of the size of LysoTracker-positive vesicles shown in A normalized to the control and data of 2 experimental repeats were combined (n = 9 per group). Each dot represents a single larva. Boxplots with 95% confidence intervals are shown and the black line in the boxplots indicates the group median, while the black line in the dot plot indicates the group mean. Statistical analysis was performed using a Mann Whitney test.
(****p=<.0001).

We proceeded to analyse which genes were differentially regulated in control treatment larvae by both of the two applied stimuli: Amiodarone treatment and infection. We found 10 genes whose expression was upregulated by both stimuli, independent of each other (Figure 9A-B, Supplementary Table S1). One of these genes is cathepsin C (*ctsc*), which is central in the lysosomal pathway in immune cells. Furthermore, some other genes we found to be upregulated are related to immune processes (*c4b*, *cfb*, *ncf1*, *cp*, *stat3*), suggesting Amiodarone treatment in absence of infection is able to modulate and perhaps prime the immune system. We then looked at the interaction between Amiodarone treatment and infection. We found 17 genes whose expression level was altered by Amiodarone treatment during infection (Figure 9C, Supplementary Table S2). Interestingly, we again found upregulation of immune related genes (*cfb* and *ncf1*) which are components of the complement and phagocyte NADPH oxidase systems. This result could suggest Amiodarone activates these innate immune defence mechanisms. Together with iNOS, the NADPH oxidase mediates RNS production. Notably, the upregulation of *ncf1* is in line with the observed effect of Amiodarone on increased RNS levels.

We then focused on the broad systemic effects of Amiodarone treatment and looked at the differences in the transcriptome of uninfected larvae after control treatment and Amiodarone treatment. This analysis revealed prominent differences in the expression of genes in pathways involved in (phago)lysosomal processes. Specifically, pathway enrichment against the KEGG database revealed enrichment of genes from the phagosome and lysosome pathways (Supplementary Table S3). Furthermore, Gene Ontology and GSEA highlighted that genes with molecular functions such as hydrolase activity, biological processes such as lysosomal transport, and genes belonging to the

A

Interaction of treatment and infection
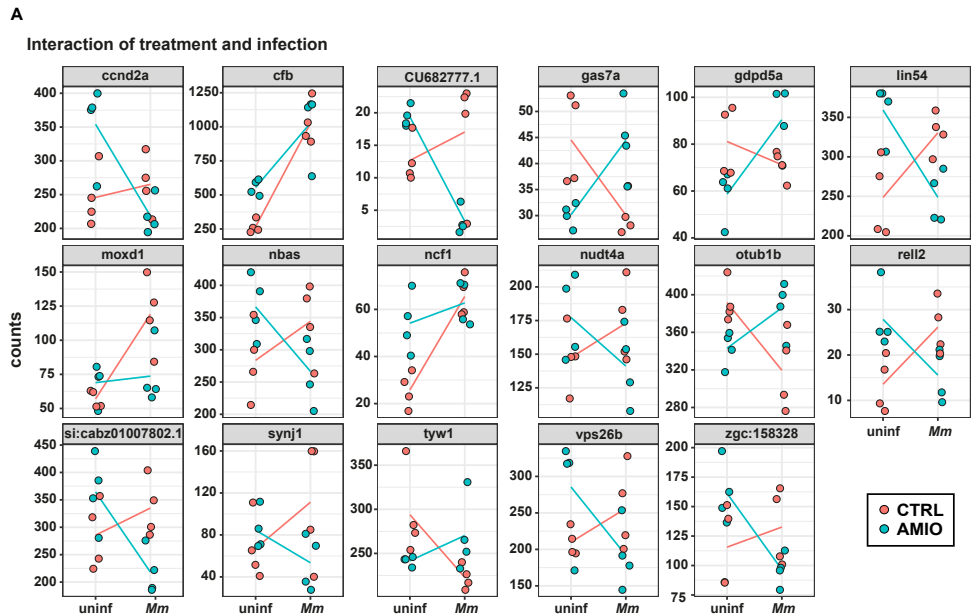
Figure 9. Amiodarone treatment modulates leukocyte gene expression
A. Interaction between Amiodarone treatment and infection in genes that are differentially regulated (s-value ≤ 0.005) and whose expression during infection was found to be dependent on Amiodarone treatment. Each dot represents the normalized gene read count of a single biological replicate (n = 10 larvae), while the line connects the means.

Figure and figure legend continued on next page.

B

AMIO uninfected: 371 | 10 | Ctrl *Mm*: 194

C

Effect of treatment and infection on gene regulation

counts

c4b | cd63 | cfb | cp | ctsc

lgals9l1 | ncf1 | stat3 | tcirg1b | zmp:0000001082

uninf *Mm* uninf (for each panel)

CTRL
AMIO
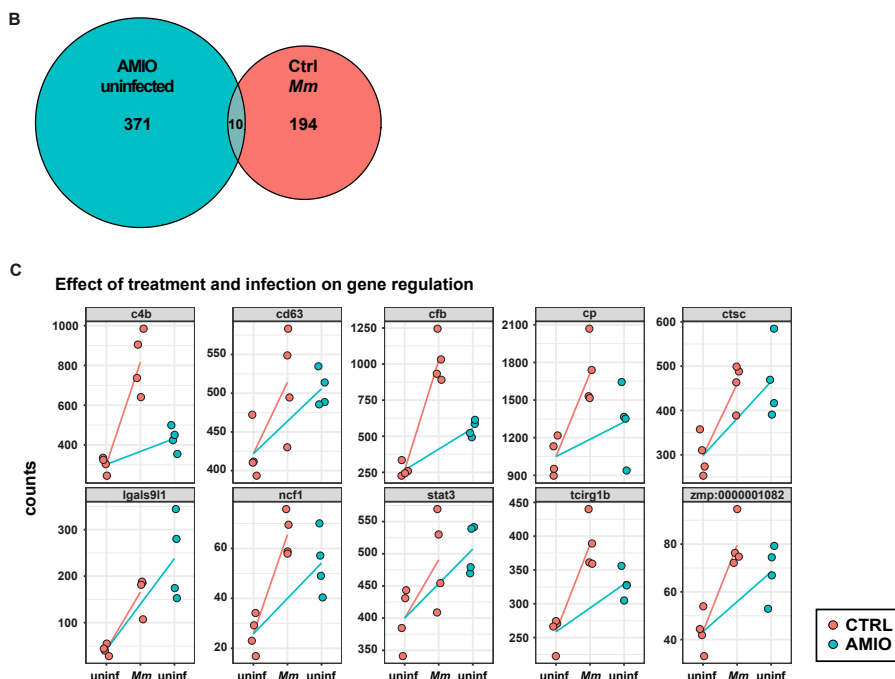
Figure 9. (continued)
B. Venn diagram showing the total number of genes differentially regulated by Amiodarone treatment in the absence of infection and by *Mm* infection in the absence of Amiodarone treatment.
C. Normalized gene read counts of genes whose expression was regulated by both Amiodarone treatment and *Mm* infection individually. Each dot represents the normalized gene read count of a single group of larvae (n = 10), while the line connects the means.

lysosome compartment were enriched in response to Amiodarone treatment. In addition, pathways associated with phototransduction and retinol metabolism were enriched (Supplementary Table S3), a possible reflection of the association of Amiodarone with optic neuropathies[47,48]. Taken together, the upregulation of the (auto)phagolysosomal pathway and the observed increase in numbers and size of lysosomal vesicles lead us to propose that Amiodarone reduces *Mm*-infection burden in a host-dependent manner by increasing (auto)phagolysosomal activity.

Discussion

Amiodarone is widely used as an antiarrhythmic drug that prolongs cardiomyocyte contraction by blocking calcium channels. In addition, via NO release, it causes vasodilation which is also believed to contribute to its cardiovascular protective effect[19,49]. Unrelated to its current therapeutic use, it is known that Amiodarone induces autophagy and affects the endocytic pathway[13,15,18], which are both crucial processes in the intracellular defence against infections with many intracellular pathogens, including *Mtb*[17,50]. In an effort to find new HDTs for TB, we performed a small screen of autophagy modulating compounds (chapter 3). Amiodarone was found to be effective against mycobacterial infection in cultured macrophages and in zebrafish. Here, we investigated the possible mechanisms underlying the anti-mycobacterial effect of

Amiodarone. Importantly, we show that Amiodarone treatment leads to an increase in RNS and (auto)phagolysosomal activity, two important mechanisms in host defence against mycobacterial infection, further substantiating the potential of repurposing Amiodarone as an HDT for TB.

We showed the effect of Amiodarone on RNS and (auto)phagolysosomal activity by utilizing the zebrafish embryo model for TB[34,35,51,52]. This model proved highly suitable for this study for several reasons. Firstly, it has been previously used to study both the RNS and autophagy pathways in relation to mycobacterial infection, showing that both processes contribute to host defence *in vivo*[33,37,38]. Secondly, the model allows us to perform treatments and co-treatments of Amiodarone and chemical inhibitors simultaneously in an easy manner by drug administration to the embryo medium (chapter 3). Thirdly, the model is highly suitable for fluorescent and confocal microscopy using both live and fixated samples[45,53]. This allowed us to visualize and quantify cellular processes in the context of a whole organism. And lastly, transcriptome analysis can be conducted at whole organism level in this model, enabling us to identify host defence pathways enhanced by Amiodarone. Transcriptional regulation by Amiodarone treatment of pathways related to phototransduction and retinol metabolism (Supplementary Tabl S3) are in line with the known clinical side effect of Amiodarone to induce optic neuropathy in humans[47,48], further supporting the translational relevance of the model. While Amiodarone is considered a relatively safe antiarrhythmic drug, it has a number of well-known and sometimes serious side-effects including lung toxicity, liver injury and vision problems. There are several case studies of lung disease associated with Amiodarone treatment[54,55]. Of note to our study, a case has also been reported where side effects of Amiodarone-induced lung injury had masked an underlying TB infection[56]. To the best of our knowledge, Amiodarone has not yet been shown to have anti-TB effects, either as an HDT or directly as an antibiotic.

Our analysis of Amiodarone on *Mm* infection in zebrafish revealed a significant increase in autophagic vesicles that led us to hypothesize that increased autophagy was responsible for the reduction of bacterial burden. The role of autophagy as a defence mechanism against intracellular pathogens, including mycobacterium, is well known[17,21,57]. However, after Amiodarone treatment we did not observe increased colocalization of the autophagy marker GFP-Lc3 with *Mm*-clusters, nor when blocking autophagic flux using bafilomycin during Amiodarone treatment. While these results did not provide evidence for increased autophagy-mediated degradation, LysoTracker analysis showed a massive increase in acidic vesicle size and numbers. Furthermore, transcriptome analysis showed upregulation of the (auto)phagolysosomal pathway. Although further elucidation of the effects of Amiodarone on (auto)phagolysosomal activity is needed, our results are in line with known effects of Amiodarone on the endocytic pathway. It has been previously shown that the accumulation of Amiodarone in endosomes and lysosomes play a role in restricting viral replication in the cases of Ebola and SARS[18]. It has even been proposed that Amiodarone could restrict SARS-CoV2 and is therefore an interesting drug candidate to treat Covid-19[58]. The mechanism by which Amiodarone restricts viral replication, could well be similar to the restriction of mycobacterial infection. For instance, viral replication is slowed after Amiodarone treatment by containing virus particles in endocytic and lysosomal compartments, preventing the release of viral particles in the cytoplasm. Likewise, containing bacteria in these compartments could lead to slower replication and less spread through the host.

The increase in acidic vesicle size and numbers in Amiodarone-treated zebrafish embryos shows parallels with the phenotypes seen in zebrafish models for lysosomal storage disorders, resulting from the accumulation of lipids in lysosomes[59]. Amiodarone is also known to induce phospholipidosis, the accumulation of phospholipids in lysosomal structures[54,60]. The relationship of these conditions with mycobacterial infections

is not well understood. The possibility is proposed, and debated, that heterozygous carriers of mutations underlying lysosomal storage disorders could provide a selective advantage for resistance against TB[61]. It has been shown that the increase in intracellular cargo, contained in lysosomes, has a negative impact on macrophage migration, and macrophage migration is known to play a role in the dissemination of bacteria[62]. Severe lysosomal storage defects have been shown to impair macrophage migration to such extent that macrophage necrosis resulted in exacerbated extracellular bacterial growth[59]. However, we did not observe reduced migration of macrophages after Amiodarone treatment. Still, it is conceivable that infected macrophages migrate less in Amiodarone-treated hosts. In contrast to the severe migration defect associated with lysosomal storage disorders, a moderate reduction of macrophage migration has been shown to have a host-protective effect because this limits spreading of bacteria through the host. Furthermore, macrophages that have reduced migration capability were observed to increase their lysosomal compartment, which augments the microbicidal capacity[63]. Therefore, the Amiodarone-induced increase in the lysosomal compartment, together with a possible reduction of infected-cell migration, could be beneficial for the host combatting intracellular bacterial infection.

In addition to the increased (auto)phagolysomal activity, our results show a marked increase of RNS production by Amiodarone in macrophages and neutrophils measured by α-nitrotyrosine signal. In line with previous observations in the zebrafish model[33], most of the RNS production occurred in neutrophils and independent of infection. We also detected increased RNS production in infected macrophages, but these RNS levels were much lower than in neutrophils despite the fact that macrophages are the main cell type carrying mycobacteria. However, we were unable to link the induction of NO production and subsequent increase in RNS activity directly to the reduction of mycobacterial burden because colocalization did not reveal a specific increase in RNS around mycobacteria in infected cells. Furthermore, we found no evidence that chemical inhibition of iNOS or the use of a pan-NOS inhibitor eliminates the anti-mycobacterial effect of Amiodarone. Together these results indicate that while RNS is increased by Amiodarone, the effect does not play a substantial role in combating mycobacterial infection. A possible explanation for the limited effect of increased RNS levels is that Amiodarone was applied after infection in our study. In agreement, activating RNS defences by stabilizing Hif-1α prior to infection led to lower bacterial burden, while no effect was observed when RNS production was blocked chemically or genetically during the course of infection[33]. Another explanation for the limited role that RNS has in the host defence response to mycobacterial infection could be that mycobacterium is able to counteract the RNS response of the host[32,42]. Based on these data, increased RNS production may contribute to the anti-mycobacterial effect of Amiodarone, but it is likely that additional innate immune effects are responsible for increased resistance of Amiodarone-treated zebrafish embryos to *Mm* infection.

Taken together, we have identified several innate host defence pathways that are enhanced by Amiodarone treatment, but have not fully elucidated the mechanism by which Amiodarone reduces mycobacterial burden. It is possible that the (auto) phagolysosomal pathway is activated by Amiodarone as a general result of cellular stress, caused by disruption of mitochondrial function[64]. In addition, Amiodarone might prime the innate immune system by upregulation of among others the NAPDH oxidase pathway, which potentially cooperates with Amiodarone-inducible nitric oxide signalling. Indeed, we show that treatment with Amiodarone alters the RNS and (auto)phagolysomal pathways, two relevant pathways in cellular defence against mycobacterial infection. Amiodarone treatment results in lower mycobacterial burden and we propose that because of the activation of these pathways, intracellular bacteria are less successful in resisting degradation. This makes Amiodarone a highly interesting compound to further study as a potential HDT against tuberculosis.

Materials and methods

Chemicals
Amiodarone-HCl (Amiodarone) was purchased from Sigma-Aldrich, Zwijndrecht, The Netherlands. L-NAME HCl (L-NAME) and L-NIL Hydrochloride (L-NIL) were purchased from Bio-Connect, Huissen, The Netherlands. All compounds were dissolved in 100% dimethyl sulfoxide (DMSO, Sigma-Aldrich) in stock concentrations of 10 mM, aliquoted and kept at -80 °C.

Zebrafish culture
Zebrafish were maintained and handled in compliance with the local animal welfare regulations as overseen by the Animal Welfare Body of Leiden University (license number: 10612). All practices involving zebrafish were performed in accordance with European laws, guidelines and policies for animal experimentation, housing, and care (European Directive 2010/63/EU on the protection of animals used for scientific purposes). The present study did not involve any procedures within the meaning of Article 3 of Directive 2010/63/EU and as such is not subject to authorization by an ethics committee. Zebrafish lines (Supplementary Table S4) were maintained according to standard protocols (www.zfin.org). Zebrafish eggs were obtained by natural spawning of single crosses to achieve synchronized developmental timing. Eggs from at least 5 couples were combined to achieve heterogeneous groups. Eggs and embryos were kept in egg water (60 µg/ml sea salt, Sera Marin, Heinsberg, Germany) at ~28.5 °C after harvesting and in embryo medium after infection and/or treatment (E2, buffered medium, composition: 15 mM NaCl, 0.5mM KCl, 1 mM MgSO¬4, 150 µM KH2PO4, 1 mM CaCl2 and 0.7 mM NaHCO3) at ~28.5 °C for the duration of experiments.

Bacterial cultures
mWasabi-or mCherry- expressing *Mm* M-strain[65,66] were cultured in Difco Middlebrook 7H9 broth (Becton Dickinson, Breda, the Netherlands) supplemented with 10% ADC (Becton Dickinson), 0.05% Tween 80 (Sigma-Aldrich) and 50 µg/ml Hygromycin B (Life Technologies-Invitrogen) at ~28.5 °C as previously described[52].

Bacterial infection of zebrafish embryos
Fresh *Mm* inoculum was prepared for every infection experiment as described above. The final inoculum was resuspended in PBS containing 2% (w/v) polyvinylpyrrolidone (PVP40). The injection dose was determined by optical density measurement (OD_{600} of 1 corresponds to ~100 CFU/nl). Infection experiments were carried out according to previously described procedures[52]. In brief, microinjections were performed using borosilicate glass microcapillary injection needles (Harvard Apparatus, 300038, 1mm O.D. x 0.78mm I.D.) prepared using a micropipette puller device (Sutter Instruments Flaming/Brown P-97). Needles were mounted on a micromanipulator (Sutter Instruments MM-33R) positioned under a stereo microscope. Prior to injection embryos were anesthetized using 200 µg/ml buffered 3-aminobenzoid acid (Tricaine, Sigma-Aldrich) in egg water. They were then positioned on a 1% agarose plate (in egg water) and injected with an 1 nL inoculum containing ~200 CFU *Mm* at 30 hpf in the blood island or at 3 dpf in the tail fin[45]. For assessment of bacterial burden, larvae were anesthetized using tricaine at 4 days post infection (dpi), positioned on a 1% agarose (in egg water) plate and imaged using a Leica M205 FA stereo fluorescence microscope equipped with a DFC345 FX monochrome camera. Bacterial burden was determined based on fluorescent pixel quantification (Stoop 2011). For confocal imaging larvae were either fixed in 4% paraformaldehyde in PBS at 20°C for 2hrs or at 4°C or anesthetized using tricaine and embedded in 1.5% low melting point agarose (in egg water) before imaging[45]. Timepoints of all confocal experiments are described in the figure legends.

Chemical compound treatments

Treatment of zebrafish embryos was performed by immersion. Stock concentrations were diluted to treatment doses in complete embryo medium without antibiotics. As a solvent control treatment, 100% DMSO was diluted to the same concentration as the compound treatment. If different compound treatment doses were used in the same zebrafish embryo experiment, the solvent control concentration corresponding to the highest compound treatment dose was used. Precise doses of compound treatments and solvent control concentrations as well as the durations of treatment are described in the figure legends for each individual experiment.

Liquid bacterial growth assay

Mm culture in logarithmic growth phase was diluted to an OD_{600} of 0.1 in complete 7H9 broth, of which 5 ml in a T25 Haynes culture flask was incubated with Amiodarone or DMSO at equal v/v at indicated concentrations. *Mm* growth was measured at 2, 6, 24 and 48 hours of incubation at ~28.5°C

Immunostaining

Immunohistochemistry was performed on fixed larvae using a rabbit polyclonal anti-nitrotyrosine antibody (Merck Milipore 06-284 MA, USA) at a 1:200 dilution of the primary antibody, the primary antibody was detected using an Alexa Fluor (Invitrogen Life Technologies NY, USA) secondary antibody in a 1:500 dilution as previously described[33].

Immunostaining imaging

For visualization of fixed 4 dpf uninfected or 1 dpi infected larvae were embedded in 1.5% low melting point agarose (weight per volume, in egg water) and imaged using a Leica TCS SPE confocal 63x oil immersion objective (HC PL APO CS2, NA 1.42) and a Leica TCS SP8 confocal microscope with a 40x water immersion objective (HCX APO L U-V-I, NA 0.8). Corrected total cell fluorescence in figure 2 was calculated using Fiji (version 1.53c) by using measurements for each individual immune-stained cell as previously described[33]. Dedicated image analysis software (Imaris, Bitplane) was used to calculate total signal intensity, normalized total cell fluorescence, volumes and co-localization in figure 3 and 4. Using Imaris, surfaces were made for the different fluorescent channels that were observed and the surface was made to fit the signal as best as possible. By masking the α-nitrotyrosine channel an estimation for background fluorescence was made. Additionally, volumes of observed macrophages were used to correct for cell size. For analysis, the total α-nitrotyrosine signal was used, divided by the volume of the cell and then divided again through the mean intensity.

GFP-Lc3 and LysoTracker imaging

For visualization of Lc3 dynamics, fixed Tg(CMV:EGFP-map1lc3b) larvae were embedded in 1.5% low melting point agarose (weight per volume, in egg water) and imaged using a Leica TCS SPE confocal microscope. Imaging was performed using a 63x oil immersion objective (HC PL APO CS2, NA 1.42) in a region of the tail fin to detect EGFP-map1lc3b – further referred as GFP-Lc3 – positive vesicles. To determine colocalization between *Mm* and GFP-Lc3 fixed larvae were embedded in 1.5% low melting agarose (in egg water) and imaged in the caudal hematopoietic tissue, using a Leica TCS SP8 confocal microscope with a 40x water immersion objective (HCX APO L U-V-I, NA 0.8). For quantification of acidic vesicles, larvae were immersed in embryo medium containing 5 µM LysoTracker Red DND-99 solution (ThermoFisher Scientific) for 1 hour. Before mounting and imaging, larvae were washed 3 times with embryo medium. Live larvae embedded in 1.5% low melting point agarose (weight per volume, in egg water) and imaged using a Leica TCS SP8 confocal microscope. Imaging was performed using a

63x oil immersion objective (HC PL APO CS2, NA 1.40) in a region of the tail fin to detect acidic vesicles. Images were obtained using Leica Las X software. For the quantification of GFP-Lc3 or LysoTracker levels the find maxima algorithm with a noise tolerance of 50 was used in Fiji software version 1.53c. To determine association of GFP-Lc3 with bacteria, manual counting was performed on the obtained confocal images using Leica Las X software.

Tail amputation of zebrafish larvae

Embryos of an Tg(mpeg1:mcherryF)/Tg(mpx;gfp) double transgenic line were anesthetized using tricaine at 3 days post fertilization (dpf), positioned on a 1% agarose (in egg water) plate and the tails were partially amputated with a 1 mm sapphire blade (World Precision Instruments) under a Leica M165C stereomicroscope[67]. After amputation larvae were incubated in embryo medium for 4 hours and fixed using 4% paraformaldehyde. After fixation, larvae were positioned on a 1% agarose (in egg water) plate and imaged using a Leica M205 FA stereo fluorescence microscope equipped with a DFC345 FX monochrome camera. Macrophages were detected based on the fluorescence of their mCherry label and neutrophils were detected based on their GFP label. The number of leukocytes recruited to the wounded area were counted as described previously[67].

RNA isolation, sequencing and sequencing data analysis

Amiodarone treatment of zebrafish larvae was performed from 1 hour post infection (hpi) until 2 dpi (3 dpf). Next, larvae were collected (10 per sample) in QIAzol lysis reagent (Qiagen, Hilden, Germany) and RNA was isolated using miRNeasy mini kit (Qiagen, Hilden, Germany) according to the manufacturer's instructions. RNA integrity was assessed by Bioanalyzer (Agilent, Santa Clara, US) and all samples were found to have a RIN ≥ 9.5. Of the total RNA, 3µg was used to create RNAseq libraries using the Illumina TruSeq strand-specific mRNA polyA preparation kit (Illumina, San Diego, US). The resulting RNAseq library was sequenced for at least 10 million reads per sample using an Illumina HiSeq2500 with a read length of 1 × 50 nucleotides (Baseclear, Leiden, The Netherlands). Four biological replicates for each treatment and infection regime were sequenced and mapped and quantified against the D. rerio GRCzv11 using Salmon v0.14.1[68]. Downstream analysis of the quantified libraries was performed in RStudio 1.2.5001[69] running R 3.6.1[70]. Libraries were imported using tximport v.1.12.3[71]. Differential gene expression was assessed via pairwise comparisons using DESeq2 v1.24.0[72] following a linear model taking into account possible gene expression differences from the embryo parents, drug treatments, infections, and its interaction (design: ~genotype + treatment + infection + treatment:infection). Statistical significance was defined by s-value ≤ 0.005 using apeglm[73]. S-values are aggregate statistics that have been recently proposed as an alternative to adjusted p-value and false discovery rate (FDR), calculating the probability of getting the sign of an effect wrong in biological contexts[74].

Venn Diagram and enrichment analysis, including pathway and GO analysis as well as Gene Set Enrichment Analysis with the C2 "Curated Gene Sets" and C5 "GO Gene Sets" collections from the Molecular Signatures Database (MSigDB) were performed as previously described[75]. Raw data are deposited into the Gene Expression Omnibus under accession number GSE178919. The data and code to recapitulate all figures and findings in this manuscript are available at https://github.com/gabrifc/rnaseq-tamox-amio.

Data analysis and statistics

Mann-Whitney test or Kruskal-Wallis with Dunn's multiple comparisons test was applied when assessing differences between 2 or more groups, respectively, of unpaired data representing technical replicates. Data were normalized to the mean of the control group

and independent repeats were combined, unless otherwise indicated. The number of experiments combined is indicated in the figure legend for each experiment. With exception of the transcriptome profiling analysis, all analyses were performed using GraphPad Prism 8 and the statistical test performed for each experiment is described in the figure legend. Dot plot graphs of zebrafish experiments were made using the raincloud plots application at https://gabrifc.shinyapps.io/raincloudplots[76].

Acknowledgements

5

References

1.   Vergne, I., Gilleron, M. & Nigou, J. Manipulation of the endocytic pathway and phagocyte functions by Mycobacterium tuberculosis lipoarabinomannan. *Front. Cell. Infect. Microbiol.* **4**, 1–9 (2015).

2.   Levitte, S. *et al.* Mycobacterial Acid Tolerance Enables Phagolysosomal Survival and Establishment of Tuberculous Infection In Vivo. *Cell Host Microbe* **20**, 250–258 (2016).

3.   Pires, D. *et al.* Role of Cathepsins in Mycobacterium tuberculosis Survival in Human Macrophages. *Sci. Rep.* **6**, 1–13 (2016).

4.   Ramakrishnan, L. Revisiting the role of the granuloma in tuberculosis. *Nat. Rev. Immunol.* **12**, 352–366 (2012).

5.   Boshoff, H. I. M. & Barry, C. E. Tuberculosis — metabolism and respiration in the absence of growth. *Nat. Rev. Microbiol. 2005 31* **3**, 70–80 (2005).

6.   Friedrich, N., Hagedorn, M., Soldati-Favre, D. & Soldati, T. Prison Break: Pathogens' Strategies To Egress from Host Cells. *Microbiol. Mol. Biol. Rev.* **76**, 707–720 (2012).

7.   WHO. *Global Tuberculosis Report 2020*. (2020).

8.   Hawn, T. R., Matheson, A. I., Maley, S. N. & Vandal, O. Host-directed therapeutics for tuberculosis: can we harness the host? *Microbiol. Mol. Biol. Rev.* **77**, 608–27 (2013).

9.   Tobin, D. M. Host-Directed Therapies for Tuberculosis. *Cold Spring Harb. Perspect. Med.* **5**, a021196 (2015).

10.   Wallis, R. S. & Hafner, R. Advancing host-directed therapy for tuberculosis. *Nat. Rev. Immunol.* 1–9 (2015) doi:10.1038/nri3813.

11.   Zumla, A., Rao, M., Dodoo, E. & Maeurer, M. Potential of immunomodulatory agents as adjunct host-directed therapies for multidrug-resistant tuberculosis. *BMC Med.* **14**, 1–12 (2016).

12.   Kilinç, G., Saris, A., Ottenhoff, T. H. M. & Haks, M. C. Host-directed therapy to combat mycobacterial infections*. *Immunological Reviews* vol. 301 62–83 (2021).

13.   Zhang, L. *et al.* Small molecule regulators of autophagy identified by an image-based high-throughput screen. *Proc. Natl. Acad. Sci. U. S. A.* **104**, 19023–19028 (2007).

14.   Balgi, A. D. *et al.* Screen for chemical modulators of autophagy reveals novel therapeutic inhibitors of mTORC1 signaling. *PLoS One* **4**, (2009).

15.   Jacquin, E. *et al.* Pharmacological modulators of autophagy activate a parallel noncanonical pathway driving unconventional LC3 lipidation. *Autophagy* **13**, 854–867 (2017).

16.   Yang, Z. & Klionsky, D. J. Mammalian autophagy: Core molecular machinery and signaling regulation. *Curr. Opin. Cell Biol.* **22**, 124–131 (2010).

17.   Deretic, V., Saitoh, T. & Akira, S. Autophagy in infection, inflammation and immunity. *Nat. Rev. Immunol.* **13**, 722–37 (2013).

18.   Stadler, K. *et al.* Amiodarone alters late endosomes and inhibits SARS coronavirus infection at a post-endosomal level. *Am. J. Respir. Cell Mol. Biol.* **39**, 142–149 (2008).

19.   Kishida, S. *et al.* Amiodarone and N-desethylamiodarone enhance endothelial nitric oxide production in human endothelial cells. *Int. Heart J.* **47**, 85–93 (2006).

20.   Bogdan, C. Nitric oxide and the immune response. *Nature Immunology* vol. 2 907–916 (2001).

21.   Gutierrez, M. G. *et al*. Autophagy is a defense mechanism inhibiting BCG and Mycobacterium tuberculosis survival in infected macrophages. *Cell* **119**, 753–766 (2004).

22.   Bradfute, S. B. *et al*. Autophagy as an immune effector against tuberculosis. *Curr. Opin. Microbiol.* **16**, 355–365 (2013).

23.   Fleming, A., Noda, T., Yoshimori, T. & Rubinsztein, D. C. Chemical modulators of autophagy as biological probes and potential therapeutics. *Nat. Chem. Biol.* **7**, 9–17 (2011).

24.   Noda, T. & Ohsumi, Y. Tor, a phosphatidylinositol kinase homologue, controls autophagy in yeast. *J. Biol. Chem.* **273**, 3963–3966 (1998).

25.   Sarkar, S., Ravikumar, B., Floto, R. A. & Rubinsztein, D. C. Rapamycin and mTOR-independent autophagy inducers ameliorate toxicity of polyglutamine-expanded huntingtin and related proteinopathies. *Cell Death Differ.* **16**, 46–56 (2009).

26.   Mizushima, N. *et al*. Dissection of autophagosome formation using Apg5-deficient mouse embryonic stem cells. *J. Cell Biol.* **152**, 657–667 (2001).

27.   Peranzoni, E. *et al*. Role of arginine metabolism in immunity and immunopathology. *Immunobiology* **212**, 795–812 (2008).

28.   Adams, L. B., Dinauer, M. C., Morgenstern, D. E. & Krahenbuhl, J. L. Comparison of the roles of reactive oxygen and nitrogen intermediates in the host response to Mycobacterium tuberculosis using transgenic mice. *Tuber. Lung Dis.* **78**, 237–246 (1997).

29.   GS, J., HJ, A. & BR, A. Killing of Mycobacterium tuberculosis by neutrophils: a nonoxidative process. *J. Infect. Dis.* **162**, 700–704 (1990).

30.   WU, G. & MORRIS, S. M. Arginine metabolism: nitric oxide and beyond. *Biochem. J.* **336**, 1–17 (1998).

31.   Yang, C.-S., Yuk, J.-M. & Jo, E.-K. The Role of Nitric Oxide in Mycobacterial Infections. *Immune Netw.* **9**, 46 (2009).

32.   Voskuil, M. I., Bartek, I. L., Visconti, K. & Schoolnik, G. K. The response of Mycobacterium tuberculosis to reactive oxygen and nitrogen species. *Front. Microbiol.* **2**, 1–12 (2011).

33.   Elks, P. M. *et al*. Hypoxia Inducible Factor Signaling Modulates Susceptibility to Mycobacterial Infection via a Nitric Oxide Dependent Mechanism. *PLoS Pathog.* **9**, 1–16 (2013).

34.   Ramakrishnan, L. The Zebrafish Guide to Tuberculosis Immunity and Treatment. *Cold Spring Harb. Symp. Quant. Biol.* **78**, 179–192 (2013).

35.   Meijer, A. H. Protection and pathology in TB: learning from the zebrafish model. *Semin. Immunopathol.* **38**, 261–273 (2016).

36.   Davis, J. M. *et al*. Real-time visualization of Mycobacterium-macrophage interactions leading to initiation of granuloma formation in zebrafish embryos. *Immunity* **17**, 693–702 (2002).

37.   van der Vaart, M. *et al*. The DNA Damage-Regulated Autophagy Modulator DRAM1 Links Mycobacterial Recognition via TLR-MYD88 to Autophagic Defense. *Cell Host Microbe* **15**, 753–767 (2014).

5

38. Zhang, R. *et al*. The selective autophagy receptors Optineurin and p62 are both required for zebrafish host resistance to mycobacterial infection. *PLOS Pathog*. **15**, e1007329 (2019).

39. Renshaw, S. a *et al*. A transgenic zebrafish model of neutrophilic inflammation. *Blood* **108**, 3976–8 (2006).

40. Xie, Y., Meijer, A. H. & Schaaf, M. J. M. Modeling Inflammation in Zebrafish for the Development of Anti-inflammatory Drugs. *Front. Cell Dev. Biol*. **8**, (2021).

41. Lambeth, J. D. NOX enzymes and the biology of reactive oxygen. *Nat. Rev. Immunol*. **4**, 181–189 (2004).

42. Elks, P. M. *et al*. Mycobacteria Counteract a TLR-Mediated Nitrosative Defense Mechanism in a Zebrafish Infection Model. *PLoS One* **9**, e100928 (2014).

43. Elks, P. M., Renshaw, S. a., Meijer, a. H., Walmsley, S. R. & van Eeden, F. J. Exploring the HIFs, buts and maybes of hypoxia signalling in disease: lessons from zebrafish models. *Dis. Model. Mech*. **8**, 1349–1360 (2015).

44. He, C., Bartholomew, C. R., Zhou, W. & Klionsky, D. J. Assaying autophagic activity in transgenic GFP-Lc3 and GFP-Gabarap zebrafish embryos. *Autophagy* **5**, 520–526 (2009).

45. Hosseini, R. *et al*. Correlative light and electron microscopy imaging of autophagy in a zebrafish infection model. *Autophagy* **10**, 1844–1857 (2014).

46. Benard, E. L., Rougeot, J., Racz, P. I., Spaink, H. P. & Meijer, A. H. *Transcriptomic Approaches in the Zebrafish Model for Tuberculosis—Insights Into Host- and Pathogen-specific Determinants of the Innate Immune Response*. *Advances in Genetics* vol. 95 (Elsevier Ltd, 2016).

47. AG, W. & HC, C. Amiodarone-Associated Optic Neuropathy: Clinical Review. *Neuroophthalmology*. **41**, 55–58 (2016).

48. Alshehri, M. & Joury, A. Ocular Adverse Effects of Amiodarone: A Systematic Review of Case Reports. *Optom. Vis. Sci*. **97**, 536–542 (2020).

49. M, G., D, D. & W, K. Amiodarone causes endothelium-dependent vasodilation in human hand veins in vivo. *Clin. Pharmacol. Ther*. **64**, 302–311 (1998).

50. Gomes, L. C. & Dikic, I. Autophagy in antimicrobial immunity. *Mol. Cell* **54**, 224–233 (2014).

51. Lieschke, G. J. & Currie, P. D. Animal models of human disease: Zebrafish swim into view. *Nat. Rev. Genet*. **8**, 353–367 (2007).

52. Benard, E. L. *et al*. Infection of zebrafish embryos with intracellular bacterial pathogens. *J. Vis. Exp*. 1–8 (2012) doi:10.3791/3781.

53. Cui, C. *et al*. *Infectious disease modeling and innate immune function in zebrafish embryos*. *Methods in cell biology* vol. 105 (Elsevier Inc., 2011).

54. Gefter, W. B., Epstein, D. M., Pietra, G. G. & Miller, W. T. Lung disease caused by amiodarone, a new antiarrythmic agent. *Radiology* **147**, 339–344 (1983).

55. Papiris, S. A., Triantafillidou, C., Kolilekas, L., Markoulaki, D. & Manali, E. D. Amiodarone: Review of pulmonary effects and toxicity. *Drug Saf*. **33**, 539–558 (2010).

56. Karinauske, E. *et al*. A case report and literature review: Previously excluded tuberculosis masked by amiodarone induced lung injury. *BMC Pharmacol. Toxicol*. **19**, 1–6 (2018).

57.   Keller, M. D., Torres, V. J. & Cadwell, K. Autophagy and microbial pathogenesis. *Cell Death Differ.* **27**, 872–886 (2020).

58.   Aimo, A., Baritussio, A., Emdin, M. & Tascini, C. Amiodarone as a possible therapy for coronavirus infection. *Eur. J. Prev. Cardiol.* 3–5 (2020) doi:10.1177/2047487320919233.

59.   Berg, R. D. *et al*. Lysosomal Disorders Drive Susceptibility to Tuberculosis by Compromising Macrophage Migration. *Cell* **165**, 139–152 (2016).

60.   Buratta, S. *et al*. A role for the autophagy regulator Transcription Factor EB in amiodarone-induced phospholipidosis. *Biochem. Pharmacol.* **95**, 201–209 (2015).

61.   SPYROPOULOS, B. Tay-Sachs carriers and tuberculosis resistance. *Nature* **331**, 666–666 (1988).

62.   Meijer, A. H. & Aerts, J. M. Linking Smokers' Susceptibility to Tuberculosis with Lysosomal Storage Disorders. *Dev. Cell* **37**, 112–113 (2016).

63.   Sommer, F. *et al*. Disruption of Cxcr3 chemotactic signaling alters lysosomal function and renders macrophages more microbicidal. *Cell Rep.* **35**, 109000 (2021).

64.   Bolt, M. W., Card, J. W., Racz, W. J., Brien, J. F. & Massey, T. E. Disruption of mitochondrial function and cellular ATP levels by amiodarone and N-desethylamiodarone in initiation of amiodarone-induced pulmonary cytotoxicity. *J. Pharmacol. Exp. Ther.* **298**, 1280–9 (2001).

65.   van der Sar, A. M. *et al*. Mycobacterium marinum Strains Can Be Divided into Two Distinct Types Based on Genetic Diversity and Virulence. *Infect. Immun.* **72**, 6306–6312 (2004).

66.   Takaki, K., Davis, J. M., Winglee, K. & Ramakrishnan, L. Evaluation of the pathogenesis and treatment of Mycobacterium marinum infection in zebrafish. *Nat. Protoc.* **8**, 1114–24 (2013).

67.   Xie, Y. *et al*. Glucocorticoids inhibit macrophage differentiation towards a pro-inflammatory phenotype upon wounding without affecting their migration. *Dis. Model. Mech.* **12**, dmm037887 (2019).

68.   Patro, R., Duggal, G., Love, M. I., Irizarry, R. A. & Kingsford, C. Salmon provides fast and bias-aware quantification of transcript expression. *Nat. Methods* **14**, 417–419 (2017).

69.   RStudio Team. RStudio: Integrated Development for R. RStudio, PBC, Boston, MA. http://www.rstudio.com/ (2020).

70.   R Core Team. R: a language and environment for statistical computing. https://www.r-project.org/ (2018).

71.   Soneson, C., Love, M. I. & Robinson, M. D. Differential analyses for RNA-seq: Transcript-level estimates improve gene-level inferences. *F1000Research* **4**, (2016).

72.   Love, M. I., Huber, W. & Anders, S. Moderated estimation of fold change and dispersion for RNA-seq data with DESeq2. *Genome Biol. 2014 1512* **15**, 1–21 (2014).

73.   Zhu, A., Ibrahim, J. G. & Love, M. I. Heavy-tailed prior distributions for sequence count data: removing the noise and preserving large differences. *Bioinformatics* **35**, 2084–2092 (2019).

74.   Stephens, M. False discovery rates: A new deal. *Biostatistics* **18**, 275–294 (2017).

75.   Zhang, R. *et al*. Deficiency in the autophagy modulator Dram1 exacerbates pyroptotic cell death of Mycobacteria-infected macrophages. *Cell Death Dis. 2020 114* **11**, 1–16 (2020).

5

76.   Allen, M. *et al.* Raincloud plots: a multi-platform tool for robust data visualization [version 2; peer review: 2 approved]. *Wellcome Open Res. 2021 463* **4**, 63 (2021).

Supplementary data and tables

Supplementary Data Table 1 can be downloaded via https://doi.org/10.5281/zenodo.5788771.

Gene name	Ensembl ID	s-value (CTRL)	Log2FC (CTRL)	s-value (AMIO)	Log2FC (AMIO)
c4b	ENSDARG00000038424	1,32E-26	1,41242232	0,000426874	0,427846742
cd63	ENSDARG00000115979	0,000783028	0,22990061	0,001721136	0,208615745
cfb	ENSDARG00000110358	6,77E-22	1,91084473	3,41E-07	0,968397619
cp	ENSDARG00000010312	2,55E-13	0,68712585	0,002866682	0,248472345
ctsc	ENSDARG00000101334	9,22E-07	0,58292046	7,99E-07	0,584656237
lgals9l1	ENSDARG00000025903	3,41E-12	1,86780544	3,14E-18	2,375554832
ncf1	ENSDARG00000033735	2,53E-09	1,29881729	6,10E-06	0,974733487
stat3	ENSDARG00000022712	0,003413588	0,22468678	0,000147126	0,301455165
tcirg1b	ENSDARG00000105142	1,52E-08	0,54863188	0,002278049	0,27273832
zmp:0000001082	ENSDARG00000098899	1,71E-07	0,81669974	0,000365082	0,559371158

Supplementary table S1. Effect of treatment and infection on gene regulation

Gene name	Ensembl ID	s-value	Log2FC
ccnd2a	ENSDARG00000051748	0,001758206	-0,6694574
cfb	ENSDARG00000110358	0,001164028	-0,8979486
CU682777.1	ENSDARG00000054207	0,001960381	-2615936
gas7a	ENSDARG00000111294	0,003391572	0,9261403
gdpd5a	ENSDARG00000077284	0,001496878	0,6968877
lin54	ENSDARG00000063194	0,000190726	-0,8305882
moxd1	ENSDARG00000031136	0,004379886	-0,7649399
nbas	ENSDARG00000008593	0,004773179	-0,604494091
ncf1	ENSDARG00000033735	0,002231734	-0,9422264
nudt4a	ENSDARG00000057767	0,002677158	-0,4509043
otub1b	ENSDARG00000011462	0,003079944	0,383625054
rell2	ENSDARG00000071876	0,00074083	-1547236
si:cabz01007802.1	ENSDARG00000068030	0,003692912	-0,7809593
tyw1	ENSDARG00000062987	0,003988326	0,4300815
vps26b	ENSDARG00000015823	0,002448688	-0,672679549
zgc:158328	ENSDARG00000005216	0,002892983	-0,764794573

Supplementary table S2. Interaction of treatment and infection on gene regulation

KEGG pathway		
Pathway	**Number of DR genes**	**padj**
Metabolic pathways	66 (out of 1458)	0,000
Lysosome	20 (out of 140)	0,000
Metabolism of xenobiotics by cytochrome P450	11 (out of 35)	0,000
Drug metabolism - other enzymes	13 (out of 62)	0,000
Glutathione metabolism	11 (out of 57)	0,000
Drug metabolism - cytochrome P450	9 (out of 32)	0,000
Other glycan degradation	7 (out of 24)	0,000
Phagosome	13 (out of 142)	0,000
Phototransduction	7 (out of 37)	0,000
Porphyrin and chlorophyll metabolism	6 (out of 28)	0,000
Amino sugar and nucleotide sugar metabolism	7 (out of 57)	0,001
Histidine metabolism	5 (out of 25)	0,001
Ferroptosis	6 (out of 41)	0,001
Ascorbate and aldarate metabolism	4 (out of 17)	0,002
Retinol metabolism	5 (out of 38)	0,004
Purine metabolism	9 (out of 151)	0,009

Gene Ontology (GoSeq)				
GO term	**Category**	**Ontology**	**Number of DR genes**	**p-adj**
transferase activity, transferring hexosyl groups	GO:0016758	MF	10 (out of 66)	0,000138178
oxidation-reduction process	GO:0055114	BP	35 (out of 891)	0,000138178
lysosome	GO:0005764	CC	10 (out of 74)	0,000141739
visual perception	GO:0007601	BP	12 (out of 119)	0,000141739
glucuronosyltransferase activity	GO:0015020	MF	8 (out of 39)	0,000165387
glutathione transferase activity	GO:0004364	MF	6 (out of 22)	0,000179239
photoreceptor activity	GO:0009881	MF	7 (out of 43)	0,001788054
oxidoreductase activity	GO:0016491	MF	25 (out of 610)	0,00280307
proton-transporting V-type ATPase, V1 domain	GO:0033180	CC	5 (out of 17)	0,002853676
hydrolase activity	GO:0016787	MF	40 (out of 1268)	0,002853676
iron ion binding	GO:0005506	MF	13 (out of 203)	0,00469861
catalytic activity	GO:0003824	MF	24 (out of 587)	0,00469861
oxidoreductase activity [...]	GO:0016705	MF	11 (out of 143)	0,005523145
carbohydrate metabolic process	GO:0005975	BP	13 (out of 208)	0,005646846
phototransduction	GO:0007602	BP	6 (out of 41)	0,007918938
protein-chromophore linkage	GO:0018298	BP	6 (out of 41)	0,007918938
ATP hydrolysis coupled proton transport	GO:0015991	BP	6 (out of 39)	0,007941036

Supplementary table S3. KEGG pathway and Gene Ontology (GoSeq) analysis

Zebrafish lines		
Name	Description	Reference
AB/TL	Wild type strain	Zfin.org
Tg(CMV:EGFP-map1lc3b)[zf155]	GFP-tagged zebrafish Lc3	He 2009
Tg(mpeg1:mCherryF)[umsF001]	Macrophage marker	Bernut 2014
Tg(mpeg1:EGFP)[gl22]	Macrophage marker	Ellett 2011
Tg(mpx:EGFP)[i114]	Neutrophil marker	Renshaw 2006
Tg(mpeg1:mCherryF, mpx:EGFP)[umsF001, i114]	Macrophage and neutrophil marker	Bernut 2014, Renshaw 2006

Supplementary table S4. Supplementary materials

5

6

Summary and discussion

Tuberculosis (TB) remains a global health problem caused by the intracellular pathogen *Mycobacterium tuberculosis*. TB is treated with classical antibiotics taken daily for up to six months[1]. Unfortunately, classical antibiotics are becoming less effective due to the rise of multi-drug resistant (MDR) and extensively-drug resistant (XDR) *Mtb* strains. Making treatment of TB even more difficult is the latent phase of *Mtb* infection, which can persist for many years before leading to active disease. It is estimated that one-third of the global population carries a latent *Mtb* infection[1]. Prevention using a vaccine is currently impossible as the available BCG-vaccine offers only partial protection. In the fight against TB, researchers are now also looking at host-directed therapeutics (HDTs) aimed to boost the host-immune system by modulating host-pathways beneficial for the immune response against *Mtb*.

In 2016, the Nobel Prize in Physiology or Medicine was awarded to Yoshinori Ohsumi for his discoveries of mechanisms of autophagy, a term describing an intracellular degradation pathway essential to maintain cellular homeostasis[2,3]. The term "autophagy" was coined in 1963 by Christian de Duve to describe intracellular vesicles containing cytoplasmic components[2,3]. These were the early days of the then newly available high resolution transmission electron microscopy techniques, which led to the first observations of autophagic structures in mammalian cells. The concept and principles of autophagy proposed at that time were proven to be accurate in recent years as researchers further unravelled the underlying molecular mechanisms[4]. Furthermore, in the last two decades it has become apparent that autophagy plays a crucial role in health and disease[5-7]. In addition to its relation to various non-infectious diseases, autophagy proved highly relevant as a host-protective pathway against intracellular pathogens causing some of the most dangerous infectious diseases[8,9]. The host-protective role of autophagy sparked a particular interest in potential HDTs that modulate autophagy in our endeavour to identify new anti-TB drugs.

Using the zebrafish model to evaluate host-directed therapeutics against tuberculosis

As a starting point for the discovery of HDTs for TB, many studies utilize drug repurposing by screening compounds that have at least passed phase-I clinical trials, and are sometimes approved drugs that are used clinically for other purposes. Most of these high-throughput screens use *in vitro* cell culture, enabling fast identification of potential HDTs[10-12]. Positive hits are then moved forward to more complex *in vitro* or *in vivo* models required for validation. To make the translation to the clinic, the use of mammalian models is essential. Zebrafish (*Danio rerio*) are a powerful intermediate model for translational research that fills the gap between *in vitro* research and mammalian models[13-15]. Furthermore, in addition to *in vitro* or *ex vivo* models such as immortalized or primary human macrophages, zebrafish offer a whole animal model that is well accessible for elucidating the molecular mechanisms mediating HDT effects. The whole organism context is of great benefit for TB research, as the interplay between mycobacteria and host cells and tissues during infection is complex, especially due to the role that granulomas (infected cell aggregates) play in TB pathology[16,17]. Zebrafish are easily genetically manipulated and a wide range of transgenic reporter lines exists that help to identify immune cell types and to analyse immune defence responses[18-20]. Due to the optical transparency, zebrafish embryos and larvae allow for extensive and detailed live imaging of cellular and intracellular mechanisms. In our study we infected zebrafish embryos with the intracellular pathogen *Mycobacterium marinum* (*Mm*), a close relative of *Mtb*, which is widely used as a model for TB[14,21,22].

Zebrafish can be used to perform chemical and genetic screens, aided by robotic injection

techniques and automated fluorescence assessment[23,24]. Microinjection of zebrafish is a powerful technique to achieve infection with pathogens, introduce cancer cells or compounds, or achieve genetic manipulation by injecting DNA constructs, mRNA, or knock-down/knock-out/knock-in reagents[14,25,26]. Efficient genetic manipulation requires injection into the cell at the one-cell-stage, and although manual injection is laborious work, this precision could not yet be achieved using robotic injection techniques that were designed to inject in the centre of the yolk. To improve automated injection efficiency for use in genetic manipulation, we used deep learning image recognition (chapter 2). This allowed for recognition of the cell and automated injection close to or in the cell. We achieved similar efficiency levels compared to manual injection and combined with a higher throughput this approach can achieve a higher yield (chapter 2). Deep learning image recognition might eventually also facilitate the development of more complex automated injections into locations desired for infection studies, including the blood circulation and body cavities. However, the robotic technology is not yet sufficiently advanced for these applications. While bacteria can be injected into the yolk using robotic injection, we found the yolk infection approach unsuitable for our study into HDTs (chapter 3). Interaction between the host immune system and the pathogen is needed for HDTs to exert their effect. In the yolk infection model interaction between injected *Mm* and the innate immune system only starts at 2 to 3 dpf when bacteria are able to infect tissues of the developing embryo[23]. Immune cells do not migrate into the yolk, which therefore remains a safe reservoir for *Mm*[27]. In contrast to robotic injection, manual zebrafish injection techniques can be done at multiple timepoints and multiple injection sites, to achieve a variety of goals. For instance, intravenous injection of pathogens into the blood island at 1 day post fertilization (dpf) or at the duct of Cuvier at 2 dpf leads to systemic infection, while localized infection can also be achieved when injection into the hindbrain ventricle or the otic vesicle[28].

We compared the blood-island method with the duct of Cuvier method and used fluorescent microscopy to assess bacterial burden and potential developmental toxicity (chapter 3). As we started drug treatment about 1 hour post infection (hpi), developmental toxicity could be minimized using the duct of Cuvier method which is performed at 2 dpf, when the embryo is more developed compared to the blood-island method at 1 dpf. However, as the end-point of the experiment is set at 5 dpf because of animal experimentation regulation, the experimental window for the duct of Cuvier method is 3 days compared to 4 days for the blood island method. While the longer experimental window of the blood island method is an advantage, it is likely that developmental toxicity prevented us from validating HDTs using this system. For instance, when we treated zebrafish embryos with Haloperidol, we observed massive oedema and this phenotype was exacerbated when treatment was performed on infected embryos, rendering Haloperidol unsuitable for experiments in the zebrafish embryo model of TB (chapter 3). However, Haloperidol was shown to reduce intracellular *Mtb* survival in human cells[29]. In addition, we were unable to confirm several other HDTs that had previously been shown to reduce mycobacterial burden in *in vitro* systems, despite that application of the duct of Cuvier method minimized developmental toxicity. We then reverted to the blood island method to do a pilot screen of potential HDTs identified in an *in vitro* screen. We chose to perform a small pilot screen so that we could test large numbers of larvae to ensure robust effects. However, it is interesting to note that application of the zebrafish embryo model for a large screen for anti-TB compounds recently also proved to be feasible. A screen of 1200 compounds yielded 8 hits of which the most effective was the compound Clemastine, which was found to act as an HDT on the purinergic receptor P2RX7 and to modulate inflammation-associated signalling[30]. This study shows that by minimizing the number of larvae assessed in the

6

primary screen it is still possible to find HDTs able to reduce bacterial burden, although this approach will obviously result in many false negatives. In our small pilot screen of 10 compounds, we found 3 compounds to reduce bacterial burden in the zebrafish TB model: Trifluoperazine, from a library of deubiquitinase inhibitors, and Tamoxifen and Amiodarone, from a library of autophagy modulating compounds (chapter 3). We subsequently focused on the two potential autophagy modulators and used the zebrafish embryo model to gain more mechanistic insights into the anti-mycobacterial effect exerted by these drugs (chapters 4 and 5).

Repurposing Tamoxifen as potential host-directed therapeutic for tuberculosis

Tamoxifen is widely known for its use in breast-cancer therapy. The main target of Tamoxifen is the estrogen receptor (ER). Tamoxifen can function as an agonist or antagonist of the ER, which is dependent of the tissue and determined by presence of co-regulatory transcription factors[31]. There is evidence that the inhibitory effect of Tamoxifen on intracellular *Toxoplasma* growth is mediated in a host-directed manner by inducing autophagic degradation of the parasite-containing vacuole[12]. Our results show that Tamoxifen inhibits mycobacterial infection in human macrophages and in the zebrafish embryo model of TB (chapter 4). Though several studies found Tamoxifen to have direct antibacterial effects against intracellular pathogens[32,33], we found no direct anti-mycobacterial effect of Tamoxifen on *Mtb* or *Mm* at doses that inhibited mycobacterial infection in macrophages or zebrafish, and therefore we propose that Tamoxifen functions as an HDT capable of modulating the immune response against mycobacteria (chapter 4). Tamoxifen was also recently found to have an immunomodulatory effect against MDR gram-negative bacteria[34]. The therapeutic potential of Tamoxifen is further supported by a recent study that proposed another breast-cancer drug, Bazedoxifene, as an HDT for TB[35]. Bazedoxifine and Tamoxifen are structurally and functionally related and both target the ER. However, our studies into the host-mediated action of Tamoxifen showed that its anti-mycobacterial effect operates independent of ER signaling and we propose that the HDT effect of Tamoxifen is mediated primarily by enhancing autolysosomal or phagolysosomal degradation pathways.

Both *in vitro* and *in vivo* functional assays and transcriptome profiling revealed major effects of Tamoxifen on autophagy and lysosomal processes (chapter 4). We found an autophagy-increasing effect of Tamoxifen treatment in human macrophages as well as in zebrafish embryos. However, although Cyto-ID staining of autophagic compartments pointed towards an increase in colocalization with *Mtb* in primary human macrophages, we were unable to demonstrate an increase in colocalization of *Mm* with the autophagy marker GFP-Lc3 in zebrafish. It remains possible that an increase of autophagosome formation and maturation contributes to the HDT effect of Tamoxifen. For example, despite our observation that Tamoxifen did not lead to a detectable increase in colocalization of GFP-Lc3 positive vesicles with *Mm*, the observed increase in Cyto-ID and GFP-Lc3 positive vesicles might indicate increased generation of neo-antimicrobial peptides[36]. Therefore, it is possible that part of the anti-mycobacterial effect of Tamoxifen could be attributed to an increase in the generation and delivery of neo-antimicrobial peptides to mycobacteria-containing compartments, a process in which GFP-Lc3 signal might be rapidly lost due to fusion with lysosomes. This process may work in concert with increased lysosome-mediated degradation of bacteria and be part of an increased killing capacity.

We further analyzed the effect of Tamoxifen by using LysoTracker dye as a fluorescent

staining method for lysosomal acidification. Importantly, we observed not only increased LysoTracker signal but also increased colocalization between mycobacteria and LysoTracker signal in both human macrophages and zebrafish larvae (chapter 4). Although mycobacteria are known to be relatively tolerant to lysosomal acidification and even capable of replication in acidic lysosomes to some extent[37–39], in our study Tamoxifen reduced bacterial burden which suggests that the increased numbers of lysosomes and colocalization with mycobacteria is related to an increased killing capacity of macrophages in both human and zebrafish assays. Based on our functional and transcriptomic data on both autophagy and lysosomal modulation we propose that Tamoxifen stimulates *de novo* lysosomal biogenesis and primarily restricts mycobacterial growth by modulation of the (auto)phagosome maturation processes that deliver bacteria to lysosomes (Figure 1A).

Host-directed therapy with Amiodarone restricts mycobacterial infection and enhances reactive nitrogen levels, autophagy and lysosomal activity

Amiodarone is currently used as an antiarrhythmic drug. It functions by blocking calcium, sodium and potassium channels and inhibiting alpha- and beta-adrenergic receptors. It also causes vasodilation via NO release, which is suggested to aid in the cardiovascular protective properties of Amiodarone[40,41]. Reactive nitrogen species (RNS) are host protective against pathogenic mycobacteria and are derived from NO[42,43]. It has been shown that Amiodarone induces autophagy and accumulates in acidic organelles, which suggests it also interacts with other intracellular degradation processes such as the endocytic pathway[44–46]. We show reduced bacterial burden and an increase in both reactive nitrogen species (RNS) and (auto)phagolysosome activity after Amiodarone treatment in the zebrafish embryo model of TB (chapter 5).

The increase in RNS production by Amiodarone was observed both in neutrophils and in macrophages of zebrafish larvae by measuring the α-nitrotyrosine signal that results from exposure to RNS. In line with previous results[47], we observed RNS production mostly in neutrophils in both non-infected as infected larvae. Though we also observed increased RNS production in infected macrophages, these levels were far below that found in neutrophils (chapter 5). However, we were unable to demonstrate increased colocalization of *Mm* and α-nitrotyrosine signal and when using inhibitors of RNS production we still observed decreased bacterial burden after Amiodarone treatment (chapter 5). It is important to note that in previous studies using the zebrafish embryo model of TB, RNS defences were activated prior to infection[47,48], while we performed Amiodarone treatment post infection. Furthermore, it has been reported that mycobacteria are able to counteract RNS host defences[48]. Taken together, the RNS increase possibly contributes to the HDT effect of Amiodarone, but is unlikely to be the main explanation.

In agreement with autophagy inducing properties reported for Amiodarone, we observed an increase in autophagic vesicles after Amiodarone treatment of zebrafish embryos. However, we were unable to demonstrate increased colocalization of *Mm* clusters and GFP-Lc3 signal. Transcriptome and LysoTracker analysis did reveal involvement of the (auto)phagolysosomal pathway. We found Amiodarone increased LysoTracker positive vesicle numbers and size (chapter 5). These results are in line with results that show Amiodarone restricts viral replication due to accumulation of Amiodarone in endosomes and lysosomes[45]. In this study Ebola and SARS viral particles were contained in endocytic and lysosomal compartments which prevented the release of these particles in the cytoplasm. This effect of Amiodarone has even been suggested to make Amiodarone a potential drug candidate to treat Covid-19[49]. That Amiodarone combines anti-viral and
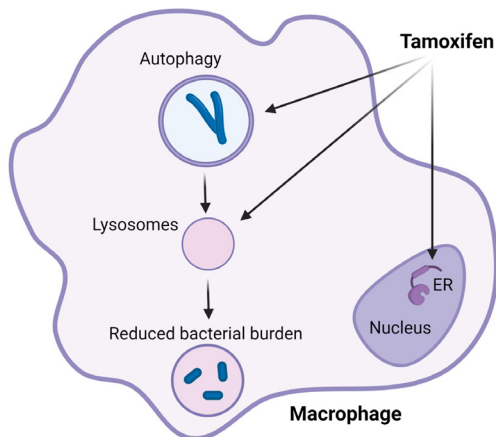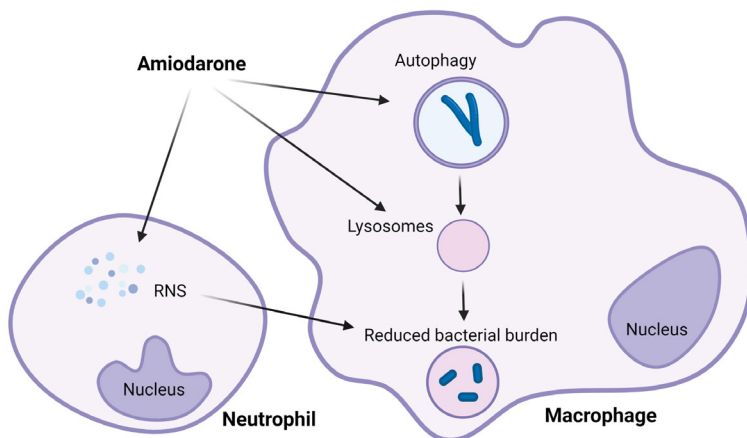
Figure 1. Model of the modes of action of Tamoxifen and Amiodarone
A. The main target of Tamoxifen is the estrogen receptor (ER). Tamoxifen can also induce autophagy and modulate lysosomal processes. Tamoxifen treatment leads to a reduced bacterial burden, which is independent of ER signalling.
B. Amiodarone can induce RNS production, autophagy and modulate lysosomal processes. Amiodarone treatment leads to a reduced bacterial burden.

anti-mycobacterial properties is of particular interest considering clinical data pointing to more severe Covid-19 disease consequences for TB patients[50].

In line with the increased lysosomal staining observed in Amiodarone-treated zebrafish, Amiodarone is known to induce the accumulation of phospholipids in lysosomal structures, called phospholipidosis[51–53]. Similar phenotypes can be observed in zebrafish models for lysosomal storage disorders[38]. Increase in intracellular cargo contained in lysosomes can be beneficial either for the host or for the mycobacteria. The key to this balance could be moderation, as severe lysosomal storage defects lead to macrophage necrosis and subsequent exacerbated extracellular bacterial growth[38], but

moderate reduction of macrophage migration and increased microbicidal capacity due to increased intracellular cargo contained in lysosomes has a host-protective effect[54]. Possibly, the drug treatment conditions used in our study induced a moderate increase in lysosomal activity and thus tipped the balance towards a host-beneficial effect.

Taken together, we show that Amiodarone modulates two relevant pathways in cellular defence, though we have not fully elucidated the mechanism by which Amiodarone treatment results in lower mycobacterial burden. We demonstrate Amiodarone increases RNS activation and (auto)phagolysosomal pathways and we propose that because of this activation intracellular bacteria are less successful in resisting degradation (Figure 1B). This makes Amiodarone a highly interesting compound to further study as a potential HDT against TB.

Prediction of potential host-directed therapeutics based on our results in the zebrafish model for tuberculosis

In this thesis two HDTs are extensively studied: Tamoxifen and Amiodarone. These compounds share a number of characteristics (chapters 4 and 5)[12,45]. First, both are known to induce autophagy. Second, both were identified as potential HDTs against *Mtb* in human cells, emerging as hits in a screen of an autophagy modulating compound library. Third, both were confirmed to reduce mycobacterial burden *in vitro* and *in vivo* in a host-directed manner. Fourth, both were found to increase not only autophagy but also the autophagolysosomal axis. However, the targets and molecular function of Tamoxifen and Amiodarone differ greatly, suggesting that the mechanisms of these two HDTs are different as well.

Despite the differences in molecular function, we were intrigued that these two compounds were both able to reduce bacterial burden, most likely via modulation of similar host pathways, particularly (auto)phagolysosomal processes. Therefore, we looked at overlap in effects on the KEGG pathways and GO categories by Gene Set Enrichment Analysis (GSEA) score in zebrafish treated after Tamoxifen and Amiodarone treatment (Figure 2). Interestingly both compounds also have activity against SARS-
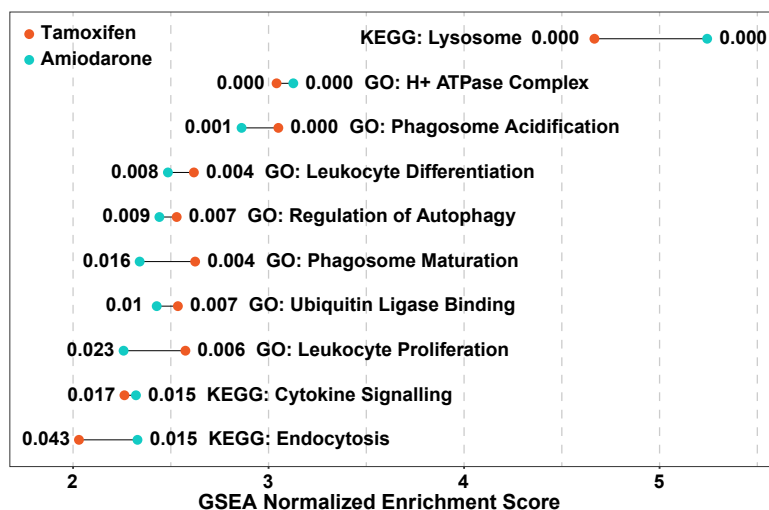

Figure 2. Overlap in the enrichment of KEGG Pathways and Gene Ontology (GO) categories in zebrafish following treatment with Tamoxifen and Amiodarone

CoV-2, which has been attributed to lysosomal effects such as phospholipidosis. To analyse these similarities, we compared the overlapping Tamoxifen/Amiodarone transcriptomic signature to publicly available transcriptomic signatures of drug-studies. This comparison resulted in a list of close to 1800 compounds that show strong effects on pathways related to lysosomal function, and modulate the same genetic pathways as Tamoxifen and Amiodarone. This prediction of potentially effective compounds against mycobacteria includes for instance Dovitinib, which has been shown to be effective against *Mtb* and even MDR-*Mtb*[55]. Interestingly, Dovitinib was identified using a similar *in silico* predictive approach, though this approach was based on drug targets identified in *in vitro* human cell cultures. The list also includes the compound YM-201636, which inhibits PIKfyve kinase, recently shown to be involved in Dram1-dependent vesicle delivery to lysosomes[56]. These examples show the potential of using the transcriptomic data obtained after Tamoxifen and Amiodarone treatment in the zebrafish embryo model of TB to predict potential HDTs of interest as anti-TB drugs.

Conclusion

New therapeutic approaches for TB are needed and HDTs can function as adjunctive drugs to first-line antibiotics to shorten treatment time and combat MDR- and XDR-*Mtb*. Screening for potential HDTs can be done rapidly *in vitro*, but in this thesis we show that the zebrafish embryo model for TB can combine screening and validation with mechanistic analysis. The improvements on robotic injection of zebrafish eggs using deep learning described in **chapter 2** offer an insight into the possibilities for future steps in automation of zebrafish research, especially for large-scale screens. The methods using zebrafish evaluated in **chapter 3** provide an overview of approaches that can be used for drug-screens. We highlight potential pitfalls for future drug-screens using zebrafish and validate three HDTs in a pilot screen using our chosen approach of the blood island injection method. We subsequently analysed the underlying mechanisms of the two autophagy-modulating HDTs Tamoxifen and Amiodarone in **chapters 4 and 5**. This thesis shows that both these drugs, which have been used in the clinic for years, can potentially be repurposed for TB treatment due to their stimulatory effects on autolysosomal or phagolysosomal degradration pathways that are important to control infection. Our studies also revealed that these drugs have broad effects on the transcriptome, which could be host beneficial via various mechanisms when used for infectious diseases. These findings underscore the importance of investigating the underlying mechanisms of action of drugs identified in chemical screens. Although further research in mammalian models is necessary to translate the results on Tamoxifen and Amiodarone to the clinic, this thesis shows the relevance of using zebrafish larvae as an intermediate translational vertebrate model.

References

1.   WHO. *Global Tuberculosis Report 2020*. (2020).

2.   Frake, R. & Rubinsztein, D. Yoshinori Ohsumi's Nobel Prize for mechanisms of autophagy: from basic yeast biology to therapeutic potential. *J. R. Coll. Physicians Edinb.* **46**, 228–233 (2016).

3.   Tooze, S. A. & Dikic, I. Autophagy Captures the Nobel Prize. *Cell* **167**, 1433–1435 (2016).

4.   Eskelinen, E.-L., Reggiori, F., Baba, M., Kovács, A. L. & Seglen, P. O. Seeing is believing: The impact of electron microscopy on autophagy research. *Autophagy* **7**, 935–956 (2011).

5.   Levine, B., Mizushima, N. & Virgin, H. W. Autophagy in immunity and inflammation. *Nat. 2011 4697330* **469**, 323–335 (2011).

6.   Castillo, E. F. *et al.* Autophagy protects against active tuberculosis by suppressing bacterial burden and inflammation. *Proc. Natl. Acad. Sci.* **109**, E3168–E3176 (2012).

7.   Deretic, V., Saitoh, T. & Akira, S. Autophagy in infection, inflammation and immunity. *Nat. Rev. Immunol.* **13**, 722–37 (2013).

8.   Gutierrez, M. G. *et al.* Autophagy is a defense mechanism inhibiting BCG and Mycobacterium tuberculosis survival in infected macrophages. *Cell* **119**, 753–766 (2004).

9.   Nakagawa, I. *et al.* Autophagy defends cells against invading group A Streptococcus. *Science (80-.).* **306**, 1037–1040 (2004).

10.   An, W. F. & Tolliday, N. Cell-based assays for high-throughput screening. *Mol. Biotechnol.* **45**, 180–186 (2010).

11.   Wilkinson, G. F. & Pritchard, K. In vitro screening for drug repositioning. *J. Biomol. Screen.* **20**, 167–179 (2015).

12.   Dittmar, A. J., Drozda, A. A. & Blader, I. J. Drug Repurposing Screening Identifies Novel Compounds That Effectively Inhibit Toxoplasma gondii growth. *mSphere* **1**, 1–15 (2016).

13.   Lieschke, G. J. & Currie, P. D. Animal models of human disease: Zebrafish swim into view. *Nat. Rev. Genet.* **8**, 353–367 (2007).

14.   Meijer, A. H. Protection and pathology in TB: learning from the zebrafish model. *Semin. Immunopathol.* **38**, 261–273 (2016).

15.   Patton, E. E. & Tobin, D. M. Spotlight on zebrafish: the next wave of translational research. *Dis. Model. Mech.* **12**, dmm039370 (2019).

16.   Volkman, H. E. *et al.* Tuberculous granuloma formation is enhanced by a Mycobacterium virulence determinant. *PLoS Biol.* **2**, (2004).

17.   Ramakrishnan, L. Revisiting the role of the granuloma in tuberculosis. *Nat. Rev. Immunol.* **12**, 352–366 (2012).

18.   Rafferty, S. A. & Quinn, T. A. A beginner's guide to understanding and implementing the genetic modification of zebrafish. *Prog. Biophys. Mol. Biol.* **138**, 3–19 (2018).

19.   Prykhozhij, S. V. & Berman, J. N. Zebrafish knock-ins swim into the mainstream. *Dis. Model. Mech.* **11**, (2018).

6

20.   Zhou, W. *et al*. Neutrophil-specific knockout demonstrates a role for mitochondria in regulating neutrophil motility in zebrafish. *Dis. Model. Mech*. **11**, dmm033027 (2018).

21.   Davis, J. M. *et al*. Real-time visualization of Mycobacterium-macrophage interactions leading to initiation of granuloma formation in zebrafish embryos. *Immunity* **17**, 693–702 (2002).

22.   Ramakrishnan, L. The Zebrafish Guide to Tuberculosis Immunity and Treatment. *Cold Spring Harb. Symp. Quant. Biol*. **78**, 179–192 (2013).

23.   Carvalho, R. *et al*. A high-throughput screen for tuberculosis progression. *PLoS One* **6**, e16779 (2011).

24.   Veneman, W. J. *et al*. Establishment and optimization of a high throughput setup to study Staphylococcus epidermidis and Mycobacterium marinum infection as a model for drug discovery. *J. Vis. Exp*. e51649 (2014) doi:10.3791/51649.

25.   Albadri, S., Del Bene, F. & Revenu, C. Genome editing using CRISPR/Cas9-based knock-in approaches in zebrafish. *Methods* **121**–**122**, 77–85 (2017).

26.   Stainier, D. Y. R. *et al*. Guidelines for morpholino use in zebrafish. *PLoS Genet*. **13**, 6–10 (2017).

27.   Traver, D. *et al*. The zebrafish as a model organism to study development of the immune system. *Adv. Immunol*. **81**, 253–330 (2003).

28.   Benard, E. L. *et al*. Infection of zebrafish embryos with intracellular bacterial pathogens. *J. Vis. Exp*. 1–8 (2012) doi:10.3791/3781.

29.   Sundaramurthy, V. *et al*. Integration of chemical and RNAi multiparametric profiles identifies triggers of intracellular mycobacterial killing. *Cell Host Microbe* **13**, 129–42 (2013).

30.   Matty, M. A. *et al*. Potentiation of P2RX7 as a host-directed strategy for control of mycobacterial infection. *Elife* **8**, 1–27 (2019).

31.   Gallo, M. A. & Kaufman, D. Antagonistic and agonistic effects of tamoxifen: significance in human cancer. *Semin. Oncol*. **24**, S1-71-S1-80 (1997).

32.   Chen, F. C. *et al*. Pros and cons of the tuberculosis drugome approach - An empirical analysis. *PLoS One* **9**, (2014).

33.   Jang, W. S. *et al*. Anti-mycobacterial activity of tamoxifen against drug-resistant and intra-macrophage Mycobacterium tuberculosis. *J. Microbiol. Biotechnol*. **25**, 946–950 (2015).

34.   Miró-Canturri, A. *et al*. Potential Tamoxifen Repurposing to Combat Infections by Multidrug-Resistant Gram-Negative Bacilli. *Pharmaceuticals* **14**, (2021).

35.   Ouyang, Q. *et al*. Bazedoxifene Suppresses Intracellular Mycobacterium tuberculosis Growth by Enhancing Autophagy. *mSphere* **5**, (2020).

36.   Ponpuak, M. *et al*. Delivery of Cytosolic Components by Autophagic Adaptor Protein p62 Endows Autophagosomes with Unique Antimicrobial Properties. *Immunity* **32**, 329–341 (2010).

37.   Vandal, O. H., Pierini, L. M., Schnappinger, D., Nathan, C. F. & Ehrt, S. A membrane protein preserves intrabacterial pH in intraphagosomal Mycobacterium tuberculosis. *Nat. Med*. **14**, 849–854 (2008).

38.   Berg, R. D. *et al.* Lysosomal Disorders Drive Susceptibility to Tuberculosis by Compromising Macrophage Migration. *Cell* **165**, 139–152 (2016).

39.   Levitte, S. *et al.* Mycobacterial Acid Tolerance Enables Phagolysosomal Survival and Establishment of Tuberculous Infection In Vivo. *Cell Host Microbe* **20**, 250–258 (2016).

40.   M, G., D, D. & W, K. Amiodarone causes endothelium-dependent vasodilation in human hand veins in vivo. *Clin. Pharmacol. Ther.* **64**, 302–311 (1998).

41.   Kishida, S. *et al.* Amiodarone and N-desethylamiodarone enhance endothelial nitric oxide production in human endothelial cells. *Int. Heart J.* **47**, 85–93 (2006).

42.   GS, J., HJ, A. & BR, A. Killing of Mycobacterium tuberculosis by neutrophils: a nonoxidative process. *J. Infect. Dis.* **162**, 700–704 (1990).

43.   WU, G. & MORRIS, S. M. Arginine metabolism: nitric oxide and beyond. *Biochem. J.* **336**, 1–17 (1998).

44.   Zhang, L. *et al.* Small molecule regulators of autophagy identified by an image-based high-throughput screen. *Proc. Natl. Acad. Sci. U. S. A.* **104**, 19023–19028 (2007).

45.   Stadler, K. *et al.* Amiodarone alters late endosomes and inhibits SARS coronavirus infection at a post-endosomal level. *Am. J. Respir. Cell Mol. Biol.* **39**, 142–149 (2008).

46.   Jacquin, E. *et al.* Pharmacological modulators of autophagy activate a parallel noncanonical pathway driving unconventional LC3 lipidation. *Autophagy* **13**, 854–867 (2017).

47.   Elks, P. M. *et al.* Hypoxia Inducible Factor Signaling Modulates Susceptibility to Mycobacterial Infection via a Nitric Oxide Dependent Mechanism. *PLoS Pathog.* **9**, 1–16 (2013).

48.   Elks, P. M. *et al.* Mycobacteria Counteract a TLR-Mediated Nitrosative Defense Mechanism in a Zebrafish Infection Model. *PLoS One* **9**, e100928 (2014).

49.   Aimo, A., Baritussio, A., Emdin, M. & Tascini, C. Amiodarone as a possible therapy for coronavirus infection. *Eur. J. Prev. Cardiol.* 3–5 (2020) doi:10.1177/2047487320919233.

50.   Irfani, T. H., Siburian, R., Nabila, R. & Umar, T. P. Tuberculosis and Coronavirus disease 2019 (COVID-19) From Clinical Perspective: A Systematic Review. *Medeni. Med. J.* **35**, 338–343 (2020).

51.   Gefter, W. B., Epstein, D. M., Pietra, G. G. & Miller, W. T. Lung disease caused by amiodarone, a new antiarrythmic agent. *Radiology* **147**, 339–344 (1983).

52.   Buratta, S. *et al.* A role for the autophagy regulator Transcription Factor EB in amiodarone-induced phospholipidosis. *Biochem. Pharmacol.* **95**, 201–209 (2015).

53.   Tummino, T. A. *et al.* Drug-induced phospholipidosis confounds drug repurposing for SARS-CoV-2. *Science* **373**, (2021).

54.   Sommer, F. *et al.* Disruption of Cxcr3 chemotactic signaling alters lysosomal function and renders macrophages more microbicidal. *Cell Rep.* **35**, 109000 (2021).

55.   Korbee, C. J. *et al.* Combined chemical genetics and data-driven bioinformatics approach identifies receptor tyrosine kinase inhibitors as host-directed antimicrobials. *Nat. Commun.* **9**, 358 (2018).

6

56.   Vaart, M. van der *et al*. DRAM1 requires PI(3,5)P2 generation by PIKfyve to deliver vesicles and their cargo to endolysosomes. *bioRxiv* 2020.12.15.422832 (2020) doi:10.1101/2020.12.15.422832.

A

Addendum

Nederlandse samenvatting

De wetenschap speelt een belangrijke rol in de vooruitgang van de mensheid. Een belangrijk aspect van die vooruitgang is dat deze de gehele mensheid bedient, niet slechts zij die de wetenschap kunnen doorgronden. Uitvindingen zoals de smartphone en het internet zijn niet meer weg te denken uit de hedendaagse maatschappij, maar waren niet mogelijk geweest zonder wetenschappelijke ontdekkingen. Zo ook de ontwikkeling van meerdere goed werkende vaccins tegen Covid-19 in een tijdsbestek van minder dan een jaar: wat mij betreft een prachtig voorbeeld van hoe wetenschappers, met voldoende middelen en samenwerking, grote problemen voor de mensheid het hoofd kunnen bieden. Evenwel zoekt de wetenschap nog altijd oplossingen voor veel oudere levensbedreigende infectieziekten, waaronder tuberculose, het onderwerp van mijn proefschrift. Naast vertrouwen is er ook scepsis over wetenschap en wordt deze steeds vaker in twijfel getrokken. Hierom, en ook omdat wetenschap doorgaans betaald wordt uit publieke middelen, ligt er voor wetenschappers een belangrijke taak om hun werk breed te delen. Zo kunnen zij ook aan het grote publiek uitleggen welke resultaten zij behaald hebben en hoe die de mensheid verder kunnen helpen. In deze samenvatting van mijn proefschrift wil ik mijn werk breder delen en vertellen hoe wetenschappelijk onderzoek naar tuberculose kan bijdragen aan nieuwe behandelmethoden.

Iedere dag worden we blootgesteld aan tal van mogelijke ziekteverwekkers zoals bacteriën, virussen en schimmels. Gelukkig worden we daar zelden ziek van, een verdienste van ons immuunsysteem. Het menselijk immuunsysteem bestaat uit twee belangrijke routes: de aangeboren immuniteit en de adaptieve immuniteit. In eerste instantie zullen ziekteverwekkers die ons lichaam weten binnen te dringen, te maken krijgen met het aangeboren immuunsysteem. Cellen en eiwitten proberen zo snel mogelijk de ziekteverwekkers onschadelijk te maken. Als de reactie van het aangeboren immuunsysteem niet afdoende is om een infectie te neutraliseren, dan komt het adaptieve immuunsysteem in actie. Dit immuunsysteem bestaat uit gespecialiseerde cellen die een grote diversiteit aan ziekteverwekkers specifiek kunnen herkennen en neutraliseren. Ook bezit het adaptieve immuunsysteem een geheugen. Hierdoor wordt een volgende infectie met dezelfde ziekteverwekker sneller door het immuunsysteem aangepakt. Dit is het principe achter vaccinaties: hiermee trainen we ons adaptieve immuunsysteem om een ziekteverwerker waar we nog niet mee in aanraking zijn gekomen te herkennen. Als deze ziekteverwerker op een later moment toch ons lichaam weet binnen te dringen, dan is de immuunreactie door dit geheugen een stuk sneller gemobiliseerd. Vrijwel alle organismen bezitten een vorm van het aangeboren immuunsysteem, maar alleen gewervelde dieren zoals de mens bezitten ook een adaptief immuunsysteem.

Tuberculose, waarnaar ik in dit proefschrift onderzoek doe, is een infectieziekte die wordt veroorzaakt door een bacterie die zich voornamelijk nestelt in de longen. Deze bacterie verspreidt zich via de lucht en is bijzonder goed in staat om zowel het aangeboren als het adaptieve immuunsysteem om de tuin te leiden. Ingeademde bacteriën zullen in eerste instantie door een bepaald type cellen van het aangeboren immuunsysteem worden aangevallen. Macrofagen, zoals dit type cel heet en wat Grieks is voor grote eters, omsluiten daarbij de bacteriën en nemen deze vervolgens op, als ware het ze de bacterie opeten. Dit proces leidt uiteindelijk tot de vorming van structuren van geïnfecteerde macrofagen en andere cellen in de longen en andere organen van geïnfecteerde mensen. In deze structuren, waar een soort schild omheen zit, blijven de bacteriën afgeschermd van andere gezonde cellen. Deze structuren, die granulomen genoemd worden, beschermen aan de ene kant de gastheer door de ziekteverwerkers af te schermen, maar aan de andere kant worden deze granulomen door de bacteriën

gebruikt als een veilige plek om te verblijven en zich verder te verspreiden. Het is een evenwicht tussen de bacterie en het immuunsysteem. Bacteriën in granulomen kunnen maanden of zelfs jaren niet actief zijn. Er wordt geschat dat er zo'n 2 miljard mensen een niet-actieve tuberculose-infectie hebben. Iemand kan jaren rondlopen met een infectie zonder hier last van te hebben. Als het evenwicht verstoord wordt, bijvoorbeeld omdat iemand een verzwakt immuunsysteem ontwikkelt door een HIV-besmetting, dan kan de infectie weer oplaaien en leiden tot actieve tuberculose. Jaarlijks krijgen zo'n 10 miljoen mensen actieve tuberculose en overlijden er 1,4 miljoen aan deze ziekte.

Tegen tuberculose is het zogenaamde BCG-vaccin beschikbaar. Dit vaccin is inmiddels al een eeuw oud en biedt slechts gedeeltelijke bescherming. Ondanks inzet van de wetenschap om nieuwe vaccins tegen tuberculose te ontwikkelen, bestaat er tot op heden nog geen effectief vaccin. De bacterie die tuberculose veroorzaakt is daarbij ook steeds vaker minder gevoelig voor antibiotica. Dit maakt dat tuberculose moeilijk te behandelen is: een kuur tegen tuberculose bestaat uit vier verschillende antibiotica die men zes maanden moet slikken. Omdat antibiotica steeds minder effectief zijn tegen de tuberculosebacterie en er nog geen effectieve vaccins zijn, wordt veel onderzoek gedaan naar nieuwe medicijnen. Een bijzondere interesse is er voor medicijnen die op de gastheer zelf gericht zijn. Deze medicijnen vallen niet direct de bacterie aan, zoals antibiotica dat wel doen, maar proberen het evenwicht te laten doorslaan in het voordeel van het immuunsysteem. In het bijzonder is daarbij aandacht voor medicijnen die werken op het aangeboren immuunsysteem, zoals op macrofagen, waardoor die beter in staat worden de bacterie te doden.

Het werk in dit proefschrift beschrijft het gebruik van een klein subtropisch visje uit zuidoost Azië om nieuwe medicijnen tegen tuberculose te onderzoeken: de zebravis. Deze vis is zeer bekend onder aquarium-enthousiastelingen en is in vrijwel iedere dierenwinkel te vinden. In de wetenschap wordt dankbaar gebruik gemaakt van dit visje als modelorganisme. Een modelorganisme wordt gebruikt om bijvoorbeeld ziekten te onderzoeken. De zebravis heeft een aantal eigenschappen die dit dier bijzonder geschikt maken als modelorganisme. Zo zijn de embryo's en larven van dit visje transparant, waardoor we met moleculair celbiologische technieken en gereedschappen zoals fluorescentiemicroscopie op subcellulair niveau kunnen zien wat er gebeurt. Een tweede belangrijke eigenschap is dat het aangeboren immuunsysteem in zebravisembryo's direct actief is, terwijl het adaptieve immuunsysteem pas actief wordt in larven van zo'n twee weken oud. Hierdoor kunnen we tijdens de eerste dagen van de ontwikkeling de complexe interactie tussen ziekteverwekkers en het aangeboren immuunsysteem bijzonder goed bestuderen. Hoewel een vis geen longen heeft, is er een natuurlijke ziekteverwekker voor vissen die nauw verwant is aan de bacterie die tuberculose veroorzaakt. Injectie met deze bacterie leidt tot vergelijkbare granuloomachtige structuren als die bij tuberculosepatiënten in bijvoorbeeld longweefsel te vinden zijn. De zebravis is daarom bij uitstek geschikt voor het werk dat in dit proefschrift gedaan is.

In **hoofdstuk 1** wordt een overzicht gegeven van enkele reeds bestaande medicijnen voor verschillende aandoeningen, waarvan nu getracht wordt deze te gebruiken tegen tuberculose. Het voordeel hiervan is dat deze medicijnen vaak al jaren in de kliniek gebruikt worden, waardoor de veiligheid al bekend is. De werking van deze medicijnen kan ook effectief zijn tegen infecties met de tuberculosebacterie als bepaalde immuun-gerelateerde mechanismen door deze medicijnen kunnen worden versterkt. Ook worden in **hoofdstuk 1** de voordelen van de zebravis als modelorganisme besproken.

In **hoofdstuk 2** wordt beschreven hoe door automatisering het onderzoek met het

zebravismodel vergemakkelijkt kan worden. Door gebruik te maken van robots die de zebravisembryo's injecteren met stoffen die gebruikt worden voor genetische manipulatie kan een grotere doorvoersnelheid behaald worden ten opzichte van manuele injectie. Deze genetische manipulatie stelt ons bijvoorbeeld in staat om specifieke genen uit te schakelen, waardoor we de werking van dat gen kunnen bestuderen. Dat maakt het bijvoorbeeld mogelijk om meer over het immuunsysteem te leren door genen gerelateerd aan het immuunsysteem uit te schakelen. In het bijzonder wordt in **hoofdstuk 2** de efficiëntie van de injectierobot verbeterd door gebruik te maken van beeldherkenningssoftware om preciezer te kunnen injecteren. De injectierobot die gebruikt is voor deze studie, is ook in staat om zebravisembryo's te injecteren met de tuberculosebacterie, een noodzakelijke stap voor het onderzoek met het zebravismodel voor tuberculose. Helaas was de injectierobot nog niet precies genoeg om een succesvolle infectie in de bloedbaan te bewerkstelligen wat een vereiste was voor het werk in dit proefschrift.

In **hoofdstuk 3** wordt gekeken wat de beste methode is om de zebravisembryo's te infecteren om effectieve screens (onderzoeken waarbij veel medicijnen getest worden) voor medicijnen tegen tuberculose te kunnen uitvoeren. Hiervoor worden verschillende manuele infectietechnieken met elkaar vergeleken. Na infectie wordt een behandeling gestart met potentiële nieuwe medicijnen die op de gastheer gericht zijn. We gebruiken daarbij medicijnen waarvan we, door experimenten waarbij gebruik gemaakt is van menselijke cellen, al verwachten dat ze effectief zijn. Nadat de beste methode werd gevonden, zijn verschillende nieuwe medicijnen geprobeerd in een kleine pilot studie. Dat resulteert in drie medicijnen die effectief zijn in het verlagen van de tuberculose-infectie in het zebravismodelorganisme. Dit zijn Trifluorperazine, Tamoxifen en Amiodarone.

Een belangrijk cellulair mechanisme dat de balans in onze cellen bewaart is autofagie. Dit mechanisme ruimt ongewenste deeltjes in cellen op, zo ook bacteriën die zich in onze cellen bevinden. Deze ongewenste deeltjes worden in blaasjes opgenomen waarna ze samengaan met lysosomen, blaasjes met een zeer zure inhoud, waardoor de ongewenste deeltjes worden afgebroken. Deze afbraakmachinerie is daardoor een interessant mechanisme dat bij activering het evenwicht tussen immuunsysteem en bacterie in het voordeel van het immuunsysteem kan doen kantelen. Van de drie gevonden medicijnen worden Tamoxifen en Amiodarone in wetenschappelijke vakliteratuur al gelinkt aan het activeren van autofagie.

Tamoxifen is een medicijn dat gebruikt wordt in de behandeling van borstkanker. In **hoofdstuk 4** onderzoeken wij of Tamoxifen ook gebruikt kan worden als een gastheer-gericht medicijn in de behandeling van tuberculose. We testen of Tamoxifen niet mogelijk direct op bacteriën werkt als een antibioticum, wat niet het geval is bij de behandeldosis waarin we nog steeds een verlaging van de bacteriële infectie zien. Vervolgens proberen we uit te zoeken welke cellulaire mechanismen precies door Tamoxifen geactiveerd worden. Het is bekend dat Tamoxifen werkt via de oestrogeenreceptor. Een receptor bevindt zich doorgaans in het celmembraan en kan daar moleculaire signalen van buiten de cel opvangen. Receptoren zijn zeer precies, het is een puzzelstukje dat niet zomaar overal op past. Ook in een zebravislijn waarin de oestrogeenreceptor deels is uitgeschakeld, blijkt behandeling met Tamoxifen nog steeds te werken tegen de tuberculosebacterie. Dit duidt erop dat Tamoxifen via een ander mechanisme effect uitoefent op het immuunsysteem. We komen erachter dat Tamoxifen niet alleen in staat is om autofagie te activeren, maar ook het aantal lysosomen doet toenemen. De werking van Tamoxifen kan daardoor mogelijk verklaard worden door een toename van de afbraak van tuberculosebacteriën.

Vervolgens behandelen we in **hoofdstuk 5** met tuberculosebacteriën geïnfecteerde zebravis-embryo's met Amiodarone. Dit medicijn, dat al jaren gebruikt wordt bij de behandeling van hartritmestoornissen, activeert net als Tamoxifen autofagie en leidt tot een toename van het aantal stikstofradicalen in cellen. Stikstofradicalen zijn ook een belangrijk mechanisme waarmee bacteriën gedood kunnen worden. We kijken daarom eerst of deze toename in stikstofradicalen de verklaring kan zijn van de verminderde bacteriële infectie. Dit blijkt echter geen volledige verklaring te bieden voor het effect van Amiodarone: ook als we de stikstofradicalen met een tweede medicijn onschadelijk maken, blijft Amiodarone de bacteriële infectie verlagen. Nadere studie laat zien dat ook Amiodarone, net als Tamoxifen, het aantal lysosomen doet toenemen, zodat verhoogde afbraak van tuberculosebacteriën in lysosomen mogelijk de werking van Amiodarone verklaart.

Voordat Tamoxifen of Amiodarone gebruikt kunnen worden voor de behandeling van tuberculose is meer onderzoek nodig. Maar samen laten de resultaten uit **hoofdstuk 4** en **hoofdstuk 5** zien dat autofagie en de lysosomale afbraak bijzonder interessante mechanismen zijn om te activeren met gastheer-gerichte medicijnen om tuberculose te behandelen. Hoewel de moleculaire mechanismen van Tamoxifen en Amiodarone verschillen, weten ze beiden hetzelfde effect te sorteren. Die kennis kan gebruikt worden om te zoeken naar andere medicijnen die vergelijkbare mechanismen activeren. In **hoofdstuk 6** worden de resultaten en inzichten uit dit proefschrift in het perspectief geplaatst van de huidige kennis over gastheer-gerichte medicijnen.

A

Curriculum vitae

Ralf Boland was born on the 27th of October, 1986 in Katwijk, The Netherlands. He grew up in Katwijk and finished his high school education at the Northgo College in Noordwijk. In 2006 he started studying for his BSc in Biology at Leiden University. During his BSc studies he did an internship in the Leiden Malaria Research Group at the Leiden University Medical Center under supervision of dr. Blandine M.D. Franke-Fayard. After obtaining his BSc degree in 2011 he proceeded with his MSc studies at Leiden University, with a specialisation in Molecular and Cellular BioScience. He did a one-year internship supervised jointly by prof. dr. Annemarie H. Meijer of the Animal Sciences cluster of the Institute of Biology at Leiden University and dr. Marco H. Siderius of the Medicinal Chemistry group at the Vrije Universiteit Amsterdam. After obtaining his MSc degree in 2013 he worked briefly as Lab Manager at Mymetics B.V. Leiden, was elected in the city council of Katwijk in 2014 and started his PhD-study in 2014 in the Immunobiology group of prof. dr. Annemarie Meijer, co-supervised by prof. dr. Herman P. Spaink and dr. Michiel van der Vaart. During his PhD-training he used the zebrafish embryo as a model organism to identify new host-directed therapeutics for tuberculosis, which resulted in the work before you. After publishing chapter 2, he and his co-authors are currently working on publishing chapters 4 and 5 of this thesis. In 2019 he started as programme officer at the Dutch Research Council in The Hague.

A

List of publications

1. Torraca, V., Cui, C., **Boland, R.**, Bebelman, J.-P., van der Sar, A. M., Smit, M. J., Siderius, M., Spaink, H. P., & Meijer, a. H. (2015). *The CXCR3-CXCL11 signaling axis mediates macrophage recruitment and dissemination of mycobacterial infection*. Disease Models & Mechanisms, 8, 53–269. https://doi.org/10.1242/dmm.017756

2. Cordero-Maldonado, M. L., Perathoner, S., Kolk, K.-J. van der, **Boland, R.**, Heins-Marroquin, U., Spaink, H. P., Meijer, A. H., Crawford, A. D., & Sonneville, J. de. (2018). *Deep learning image recognition enables efficient genome editing in zebrafish by automated injections*. PLoS ONE 14(1): e0202377. https://doi.org/10.1371/journal.pone.020237

3. **Boland, R.**, Heemskerk, M. T., Forn-Cuní G., Korbee, C. J., Walburg, K. V., Esselink, J. J., Carvalho dos Santos, C., de Waal, A., van der Hoeven, D. C. M., van der Sar, E., Spaink, H. P., van der Vaart, M., Meijer, A. H., Ottenhoff, T. H. M.. *Repurposing Tamoxifen as potential host-directed therapeutic dor tuberculosis*. Under revision.

4. **Boland, R.**, Olijhoek, N., Forn-Cuní G., Heemskerk, M. T., Ottenhoff, T. H. M., Spaink, H. P., van der Vaart, M., Meijer, A. H.. *Host-directed therapy with Amiodarone restricts mycobacterial infection and enhances reactive nitrogen levels, autophagy and lysosomal activity*. In preparation.

A